

Nonlinear Laser Propagation Phenomena in Transparent Media

Thesis by

Daryoush Abdollahpour

In Partial Fulfillment of the Requirements
for the Degree of
Doctor of Philosophy



Department of Physics
University of Crete
Heraklion, Crete

November 2011

© 2011

Daryoush Abdollahpour

All Rights Reserved

In the name of God, Most Gracious, Most Merciful

To my parents

Acknowledgements

First and foremost, I am really grateful to my parents and my family for their continuous love, encouragement and patience. Without their support, I have no doubt that I would not have been able to complete my education. I am also grateful to my wife for her love, understanding, and patience.

I would like to express my gratitude to my thesis supervisor, Stelios Tzortzakis, not only for his valuable guidance throughout this work but also for many direct and indirect lessons about being a good scientist. Although very serious and demanding about work, his concern extends beyond just work and he is interested in how his students and group members are doing in their personal life.

Besides having the opportunity to have Stelios as a supervisor, in the last four years, I had the chance to work with knowledgeable researchers within our group, UNIS. I would like to thank Dimitris Papazoglou for giving me valuable knowledge and discussions of my research and the experiments. I am also grateful to Takis Loukakos, with whom I started my work in the UNIS group, and Sergiy Suntsov with whom we performed various experiments together and obtained plenty of interesting results.

Thanks to Savas Georgiou, from IESL-FORTH, for our collaboration on a part of this work.

I am grateful to Arnaud Couairon and Daniele Faccio and his group for our collaboration in several parts of this work.

Thanks to my fellow student, Paris Panagiotopoulos, for a great collaboration making it possible to have direct comparisons between experiments and numerical simulations of nonlinear propagation phenomena.

I would like to thank Michael Loulakis for providing us a laser chain always running at its optimum and Michael Galanakis for providing us with electronic automation support.

Together with the colleagues already mentioned, I am grateful to my other colleagues, Maria Massaouti, Despina Adamidou, Jean-Michel Manceau, and Matthieu Bellec for their kind help on various issues during the last few years.

Many Thanks to R. Karali, L. Papadopoulou, and M. Stakianakis for their great help with the administrative issues.

Abstract

This thesis is focused on investigations of unanswered questions in the filamentation field. Two techniques for measuring electron plasma densities in light filaments are presented in detail. Pump-probe in-line holographic microscopy technique as a powerful and accurate method for retrieving very small perturbations on the wavefront of the probe beam, caused by the filamentation of the pump beam is presented. Plasma conductivity technique, as a simple method for measuring plasma densities in gases and an easy approach to calibrate this method for quantitative measurements are presented.

We present our measurement of the electron plasma densities in fused silica under the conditions, which lead to nanograting formation in the bulk of fused silica glass. Moreover, the dynamics of nonlinear propagation of femtosecond laser pulses in the bulk of PMMA, over a wide temporal range is investigated. Based on our measurements, it is shown that filamentation in PMMA is followed by fast excitation of electrons and excited states, which decay quickly and lead to material modification that in turn leads to a pressure wave formation and creation of voids at latter times.

Third-harmonic generation in air is investigated and it is shown that by inserting a plasma string in the path of a light filament, the third-harmonic generation efficiency can be significantly enhanced (by two-orders of magnitude). This enhancement is attributed to enhanced third-order nonlinearity of plasma and a physical model for third-harmonic generation in plasmas is presented. Moreover, it is shown that two intersecting filaments can form a plasma grating in air and the attributes of such grating are characterized.

It is shown that the filamentation tailoring can be achieved by introducing a periodic refractive index lattice in the medium or by modifying the input beam characteristics. The results of filamentation tailoring using periodic plasma lattice are presented. It is shown that by using non-diffracting Bessel beams and utilizing a linear technique, the filament attributes can be tuned. The linear propagation characteristics of Airy beams are studied and an easy approach to generate tunable Airy beams is presented. It is shown that by combining an Airy pulse in time with a 2D Airy beam in space, Airy³ light bullets can be generated, which are robust and resist spreading in all spatiotemporal dimensions. Moreover, propagation of Airy beams in different nonlinear regimes is studied.

Contents

Acknowledgements	vi
Abstract.....	viii
CHAPTER 1: Introduction.....	1
1.1 Ultrashort laser pulse propagation -----	1
1.1.1 Gaussian beam optics.....	1
1.1.2 Linear pulse propagation.....	4
1.1.3 Linear pulse propagation in dispersive media	8
1.1.4 Nonlinear polarization	14
1.1.5 Nonlinear index of refraction.....	18
1.1.6 Self-focusing.....	20
1.1.7 Self-phase modulation	21
1.1.8 Optical Solitons and light bullets.....	23
1.1.9 Photoionization and Plasma formation	24
1.1.10 Plasma defocusing and plasma absorption	25
1.2 Filamentation and its application -----	26
1.2.1 Model equation for filamentation	28
1.2.2 Main attributes of light filaments.....	30
1.2.3 Applications of filamentation	34
1.3 Thesis outline -----	38
CHAPTER 2: Development of Diagnostic Tools for Studying Filamentation	41
2.1 Introduction -----	41
2.2 Overview of present methods -----	41
2.2.1 Interferometric Techniques.....	42
2.2.2 Shadowgraphy, diffractometry and holography	43
2.2.3 Non-optical techniques: Plasma conductivity technique	44
2.3 In-line holographic microscopy -----	45
2.3.1 Principles of in-line holographic microscopy.....	46

2.3.2	Experimental Implementation.....	51
2.3.3	Experimental results.....	55
2.3.4	Investigation of multiple filaments using in-line holographic microscopy	57
2.4	Calibrated plasma conductivity technique-----	62
2.4.1	Experimental setup and physical model	63
2.4.2	Experimental results and discussion	66
2.5	Conclusion	71
CHAPTER 3: Filamentation in Transparent Solids		72
3.1	Introduction	72
3.2	Formation of self-organized nanogratings in the bulk of fused silica	72
3.3	Dynamics of filamentation in polymers	80
3.4	Conclusion	93
CHAPTER 4: Filamentation in Gases		94
4.1	Introduction	94
4.2	Enhancement of filamentation-induced third-harmonic (TH) generation	94
4.2.1	TH generation from a single filament.....	95
4.2.2	Enhancement of TH generation with a plasma slab.....	95
4.2.3	Enhancement of TH emission from a filament screened by an obstacle	103
4.2.4	Physical mechanism of TH generation enhancement in the presence of the Pump plasma slab.....	104
4.3	Plasma Diffraction Gratings-----	112
4.3.1	Experimental setup and theoretical background	114
4.3.2	Experimental results and discussion	115
4.4	Conclusion	123
CHAPTER 5: Filamentation Tailoring and Exotic Optical Beams		125
5.1	Introduction	125
5.2	Filamentation tailoring by a plasma lattice-----	126
5.3	Filamentation tailoring using exotic beams	133

5.3.1	Filamentation of Bessel beams	134
5.3.2	Airy beams: generation, linear and nonlinear propagation	141
5.3.3	Airy ³ light bullets	160
5.4	Conclusion -----	187
References		189
List of Publications		202

List of Figures

Figure 1.1-1	(a) Intensity of a typical Gaussian beam propagating along z-axis and (b) on axis intensity of a Gaussian beam. -----	2
Figure 1.1-2	Normalized beam intensity I / I_0 as a function of the radial distance r at different axial distance: $z = 0$; $z = z_0$ and $z = 2z_0$. -----	3
Figure 1.1-3	Temporal and spectral representation of an optical pulse. (a) The real part of the wave function $\text{Re}[E(t)] = \mathcal{E}(t) \cos[\omega_0 t + \varphi(t)]$, the magnitude of the envelope $ \mathcal{E}(t) $, the intensity $I(t)$. (b) Spectral intensity $I(\omega)$ and spectral phase $\varphi(\omega)$ (from [1]). -----	5
Figure 1.1-4	A chirped Gaussian pulse with the indicated parameters for temporal width, chirp, and central angular frequency. -----	6
Figure 1.1-5	Typical wavelength dependence of the absorption coefficient and refractive index for a dielectric medium with resonant absorption bands in the ultraviolet and infrared spectral regions (from [1]).	9
Figure 1.1-6	(a) Potential energy functions of a harmonic oscillator (linear regime) and noncentrosymmetric and centrosymmetric medium (nonlinear regime). (b) P-E relations for a linear (dashed line) and a nonlinear dielectric medium (solid line).-----	16
Figure 1.1-7	Third-harmonic generation. (a) Geometry of interaction, and (b) energy-level description. -----	18
Figure 1.1-8	Sketch showing the distortion of the wavefront and self-focusing of a laser beam in a nonlinear medium (from [7]). -----	20
Figure 1.1-9	(a) Nonlinear phase shift, and (b) nonlinear frequency shift of a Gaussian pulse after propagating a distance in a nonlinear medium. (c) Spectral intensity of a Gaussian pulse before and after propagating in the nonlinear medium. -----	22
Figure 1.1-10	Schematic showing the spatial beam profiles for (a) beam self-focusing, (b) normal beam diffraction, and (c) soliton propagation.-----	23
Figure 1.1-11	Photoionization mechanisms. (a) Multiphoton ionization (MPI) and (b) tunnel ionization. -----	25
Figure 1.2-1	Schematic representation of focusing-defocusing cycles during filamentary propagation. The solid curves indicate the diameter of the intense core. The filamentation length is the distance covered by these cycles. The dashed line indicates the root mean square radius of the full beam (from [5]). -----	27
Figure 1.2-2	(a) Numerical result of filament propagation with the core blocked at $z = 18$ cm, and (b) experimental results of self-healing of a filaments in water (from [55]).-----	31
Figure 1.2-3	Spectrum of fs laser beam after propagation over a distance of 10 m in air (from [5]). -----	32
Figure 1.2-4	Photograph of conical emission after 30 m of filamentary propagation in air. The diameter of green ring is ~ 10 cm (from [63]). -----	33
Figure 1.2-5	Multiple filamentation of $700 P_{cr}$ beam (from [75]).-----	34
Figure 1.2-6	Schematic of a white-light LIDAR (from [80])-----	35

Figure 1.2-7	Experimental setup for local and remote LIBS using femtosecond UV laser filaments (from [83]). -----	36
Figure 1.2-8	(a): (i) Experimental configuration of the discharge circuit using a filament, (ii) photograph of a guided discharge between two electrodes; (from [84]). (b): Photographs of a guided discharge (i), and a partially guided discharge (ii); (from [85]).-----	36
Figure 1.2-9	(a) SEM image of microfluidic channel fabricated by HF-etching fs-micromachined area inside fused silica (from [88]). (b) Image of fabricated periodic structure with period of 10 μm in bulk PMMA and diffraction pattern by illuminated the fabricated structure (from [89]).-----	37
Figure 1.2-10	Diffraction of one of the white light created by one of the grating forming filaments, diffracted by the formed plasma grating. The blue spot is the projection of the second beam.-----	38
Figure 2.2-1	Experimental layout of single-shot chirped-probe pulse spectral interferometry.-----	43
Figure 2.2-2	Experimental scheme for the time-resolved diffractometry. The modified image of the probe beam crossing the filament is recorded at various delays. Also shown is the central dark fringe in the probe far-field image for zero time delay. From [105].-----	44
Figure 2.2-3	Experimental scheme of plasma conductivity technique. From [120].-----	45
Figure 2.3-1	Typical holographic diffraction images for a probe perturbed by a cylindrical structure with (a) $\Delta n > 0$, ($\Delta\kappa = 0$); (b) $\Delta n < 0$, ($\Delta\kappa = 0$), and (c) $\Delta\kappa \neq 0$, ($\Delta n = 0$).-----	46
Figure 2.3-2	Schematic representation of the wavefront reconstruction algorithm (see text).-----	48
Figure 2.3-3	(a) Simulated input amplitude distributions (in-line holograms) corresponding to the phase object shown in (b) and (d); (b-e) simulated (initial) and retrieved phase and amplitude distributions by using i-HOM technique at two different propagation distances $z = 0$ and $z = 2 \text{ mm}$. (f) Simulated (initial) and retrieved phase change by using only one diffraction pattern at $z = 2 \text{ mm}$.-----	50
Figure 2.3-4	(a) Simulated input amplitude distributions (in-line holograms) for various propagation distances with the addition of 2% random noise, (b-e) simulated (initial) and retrieved phase and amplitude distributions at two different propagation distances $z = 0$ and $z = 2 \text{ mm}$.-----	51
Figure 2.3-5	(a) Imaging in a typical microscope system. Plane waves are transformed to spherical waves. (b) Imaging using a bi-telecentric optical system; Plane waves are still plane after exiting the system. (c) Experimental setup of the pump-probe in-line holographic microscopy utilizing a cascade of bi-telecentric optical system.-----	53
Figure 2.3-6	(a) Experimental in-line holograms remotely captured along the propagation of the probe beam; (b) retrieved phase and corresponding refractive index change (Abel transform), and respective electron density distribution in the plasma string.-----	55
Figure 2.3-7	(a) Experimental in-line holograms of a propagating filament for various pump-probe delays (k denotes the pump wavevector) (b) retrieved refractive index distribution.-----	57
Figure 2.3-8	(a) Retrieved phase information as a function of the number of input in-line holograms. (b) Number of iterations to reach convergence (under the same constrain) versus the number of input in-line holograms.-----	58
Figure 2.3-9	(a) The simulated and retrieved phase changes, corresponding to low refractive structures, located on the same plane along z -axis and separated by 10 (a), 15 (b) and 20 μm (c) along y -axis.-----	59

Figure 2.3-10	(a) In-line holograms recorded at $z=1.5$ mm, corresponding to two filaments located on the same plane along the propagation direction of the probe beam, z , separated by ~ 145 μm (a) and ~ 72 μm (b), along the y -axis. (c)-(d) Retrieved phase change profiles corresponding to (a) and (b), respectively. -----	60
Figure 2.3-11	(a) Two filaments separated along the propagation direction of the probe beam. -----	61
Figure 2.3-12	(a) Phase distribution of the numerically propagated wavefront as a function of the propagation distance z and (b) normalized phase change as a function of propagation distance. The peaks indicated the position of the filaments along the z -axis. -----	61
Figure 2.4-1	PCo experimental setup schematic. -----	63
Figure 2.4-2	(a) Typical signal of plasma conductivity (PCo) technique recorded by an oscilloscope, (b) peak signal of PCo along a plasma string created by a focusing the laser pulses by an $f=500$ mm lens, and (c) peak plasma (PCo) signal at the position of maximum plasma fluorescence for different pulse energies ($f=100$ mm). -----	64
Figure 2.4-3	(a) Schematic of the microscopic model representing the role of plasma dimensions on the conductivity signal; before (left) and after (right) the charge separation due to the external electric field. -----	65
Figure 2.4-4	(a) Transverse CCD images of plasma fluorescence for different laser pulse energies, and (b) corresponding retrieved spatial distribution of the electron density using i-HOM. -----	67
Figure 2.4-5	(a) i-HOM and calibrated PCo-measured electron densities versus input pulse energy for plasma strings created by an $f=100$ mm lens. -----	68
Figure 2.4-6	i-HOM- and calibrated PCo-measured electron densities versus pulse energy for plasma strings created by an $f=300$ mm; two different reference electron densities are used for the calibration of the PCo: electron density measured at 3.2 mJ in a plasma string created by an $f=100$ mm and the same created by an $f=300$ mm (see text). -----	69
Figure 2.4-7	Estimated electron density from calibrated PCo measurement in plasma strings using different laser pulse durations and energies ($f=100$ mm). -----	70
Figure 2.4-8	Comparing plasma conductivity signals of plasma strings as a function of energy for filamentation of transform limited pulses and chirped pulses. -----	70
Figure 3.2-1	Different regimes of fs laser induced-modifications in the bulk of fused silica. Regime 1: smooth modification; regime 2: nano-grating formation embedded into smooth modification, and regime 3: complex morphology comprising of disrupted regions, nanogratings, and smooth modifications. From [132]. -----	73
Figure 3.2-2	Side views of modified region. (a) Microscope image of the birefringence from the modified region, (b) low-magnification, and (c) high-magnification SEM image of nanogratings from a side view. In the schemes, E , S , and k denote the polarization, scanning and propagation directions of the incident beam, respectively. -----	74
Figure 3.2-3	Top view SEM images of nanogratings formed in by irradiating a single spot in the bulk of fused silica (a), and by scanning the beam along a path ((b) and (c)). From [132]. -----	74

Figure 3.2-4	Two models for the nanograting formation in the bulk of fused silica. (a) Coupling between plasma waves and electric field of the incident beam [90], and (b) conversion from plasma nano-spheres to plasma nano-planes due to electric field enhancement after multiple laser shots [91]. - 75
Figure 3.2-5	(a) Spatial distribution of the imaginary part of the refractive index at central longitudinal section for various delays. (b) Spatial distribution of maximal electron density of the plasma string. ----- 77
Figure 3.2-6	Ratio of changes in the real part to the imaginary part of the complex refractive index, with inverse sign, for various delays. These results are used for estimation of the collision time in fused silica using the Drude model. ----- 78
Figure 3.2-7	(a) Electron density distribution in the focal region for various pump pulse energies. (b) Peak electron density as a function of pulse energy.----- 79
Figure 3.2-8	Measurement of the induced birefringence in comparison with the electron density distribution.- 80
Figure 3.3-1	(a) Pump-probe setup, (b) Transmission images of the probe beam as it traverses the pump-irradiated volume at various delays. ----- 83
Figure 3.3-2	(a) Spatiotemporal distribution and evolution of the imaginary part of the refractive index induced during the nonlinear propagation of ultrafast laser pulses in PMMA for short delays; at the bottom is shown the maximal (in time) electron density in the focal area. (b) Spatial distribution of the estimated maximal free carrier density. (c) Temporal evolution of the free carrier density (Norm units).----- 84
Figure 3.3-3	Temporal evolution of mean absorption (normalized values) in the center of the focal volume. (b) Diffraction pattern as a function of time. The emergence of an expanding acoustic wave is clearly visible at ~ 1 ns (velocity: 2.94 km/sec or ~ 1.03 Mach).----- 85
Figure 3.3-4	Spatiotemporal distribution of the refractive index changes (real and imaginary parts) for long delays (>200 ps). (b) Graphical representation of a transverse section of the focal volume (the pump beam propagation is perpendicular to the figure). ----- 86
Figure 3.3-5	Refractive index change distribution profiles along the transverse dimension, perpendicular to the pump beam propagation direction, for various long pump-probe delays. ----- 88
Figure 3.3-6	(a) Experimental setup for measuring transmission of PMMA as a function of pulses energy, and (b)-(c) transmission and absorption of the PMMA sample as a function of input pulse energy. Solid curve is an exponential fit with a decay constant of $0.67 \mu\text{J}^{-1}$. ----- 89
Figure 3.3-7	(a) Experimental scheme for recording diffraction images of probe beam from the pump beam-induced modifications in the focal region in the bulk of PMMA. (b) Typically acquired diffraction image using.----- 90
Figure 3.3-8	(a) A montage of $\sim 7\text{-}\mu\text{m}$ -wide horizontal slices from the central part of the CCD images shown in Figure 3.3-7(b), corresponding to different pump-probe delays, and (b) measured radius of the modified region at different delays for the indicated input pulse energy. ----- 91
Figure 3.3-9	Expansion speeds of the modified volume as a function of input pulse energy and absorbed energy at (a) first expansion region before 3 ns, and (b) third expansion region after 5 ns. ----- 91
Figure 3.3-10	Expansion speed at the second region (~ 3 ns- ~ 5 ns) as a function of (a) input energy, and (b) absorbed energy. The dashed straight lines indicate 1 Mach and the solid curves are the fits (see text). ----- 92

Figure 3.3-11	(a) Shock startup time as a function of input pulse energy, (b) the length of the modified region (structure) as a function of input pulse energy, (c) speed at the second region as a function of absorbed energy per unit length.-----	92
Figure 4.2-1	(a) TH images taken by an ICCD camera at different pump energies using 100 cm focal length lens, and (b) Experimental measurements of total energy of the TH generated in air as a function of the fundamental energy and the TH energy contained in the rings structure and central spot using the same lens. Both from [167]. -----	95
Figure 4.2-2	(a) Schematic of the experimental setup; here: BS, beamsplitter; L1, L2, lenses; P, prism; D, photodetector. (b) Scheme of the spatial arrangement of the plasma slab (Pump beam) and the filament (Signal beam). -----	96
Figure 4.2-3	Spatial distribution of the fundamental and TH beams at several delays between Signal and Pump pulses. Negative delay means that the pump pulse reaches the crossing point after the Signal pulse. -----	97
Figure 4.2-4	Far-field images of the TH (blue ring) and of the fundamental (red central spot) beams taken with a digital camera on a paper screen placed at 1.4 m from the filament for (a) negative τ , and (b) $\tau = 200$ fs. In (a), the fundamental beam spot is partially shadowed by the TH ring. (c) TH intensity profiles, versus divergence angle, measured with a linear CCD, dashed and solid curves for (a) and (b), respectively.-----	98
Figure 4.2-5	Conversion efficiency and spatial distribution of the TH beam at several positions for the pump slab along the Signal filament.-----	99
Figure 4.2-6	Far-field and near field of the TH beam. The near-field profile is simply achieved by a two-dimensional Fourier transformation of the far-field profile. -----	100
Figure 4.2-7	TH energy as a function of the delay between the Pump and Signal pulses. Two lower curves: Pump energy 0.5 mJ, open and solid triangles for co-polarized and cross-polarized beams, respectively. Two upper curves: Pump energy 2 mJ, open and solid circles for co-polarized and crossed-polarized beams, respectively. Inset: the same plot with the delay scale extended to 40 ps. -----	101
Figure 4.2-8	(a) Measured dependence of TH signal on Pump energy for Signal pulse energy 0.15 mJ (squares), 0.7 mJ (circles), and 1.5 mJ (triangles). (b) TH energy versus Signal pulse energy in the absence of Pump (triangles) and at Pump energy 2 mJ/pulse (circles). The ratio of these two curves represents the TH enhancement factor shown with open circles in (b).-----	102
Figure 4.2-9	Reshaping and enhancement of TH by introducing a piece of 125 μm -thick optical fiber (top) and a 90 μm -thick copper wire in the middle of the Signal filament. The images of the separated fundamental and TH beams are captured on piece of paper by a photographic camera.-----	104
Figure 4.2-10	Experimental setup: L1, L2, lenses; CL, plano-convex cylindrical lens (cylindrical axis is parallel to the plane of the figure); P, prism; IF, interface filter at 266 nm; D, calibrated photodetector. -----	106
Figure 4.2-11	(a) TH energy as a function of the delay between the Pump and Filament pulses for Pump plasma channel thickness of 0.4 mm (circles), 0.7 mm (triangles), and 1mm (squares). The locations of the harmonic signal maxima are indicated by vertical arrows. (b) Schematic of the relative position of the Pump and Filament pulses at different timing in the experimental geometry. -----	107
Figure 4.2-12	(a) Total wave-vector mismatch Δk between 800 and 267 nm wavelengths as a function of plasma density. (b) Maximum TH intensity in normalized units (left vertical scale) and minimum	

	plasma thickness L needed to reach it (right vertical scale) versus electron density. (c) False color two-dimensional map of TH intensity versus plasma density and plasma thickness (normalized units).-----	109
Figure 4.2-13	Theoretical (circles) and experimentally measured (diamonds) normalized TH intensity as a function of the plasma density in the Pump channel. -----	111
Figure 4.3-1	Laser pulse cleaning by a double plasma mirror (a) CPA generated temporal profile, which usually has a prepulse and a wider pedestal. (b) The same pulse after reflection from the first plasma mirror. (c) Reflecting this off a second plasma mirror cleans the pulse still further. From [188].	113
Figure 4.3-2	Schematic of the experimental setup to create and study plasma diffraction gratings in the air. L1, L2, and L3 lenses; BS, beam splitter.-----	115
Figure 4.3-3	Wavevectors of Beam 1 and Beam 2 and the plasma diffraction grating. The dashed-dotted lines represent the refractive index planes.-----	116
Figure 4.3-4	(a) Experimental setup, (b) wavevectors of the Beam 1 and Beam 2 and grating vector and, (c) diffracted SC of the Beam 1 from the grating (Beam 2 is the white-bluish spot). -----	117
Figure 4.3-5	Simulated intensity patterns of the diffracted SC for different values of the grating thickness. In all pictures, Beam 2 appears as a bright white-bluish spot. -----	117
Figure 4.3-6	Measured diffraction angle of various SC components from the plasma grating (red solid circles) and theoretical fit used to calculate the period of the plasma grating (solid curve).-----	118
Figure 4.3-7	Spectral selectivity curves (diffraction efficiency vs wavelength) for a plasma grating with $\Delta n = 1.5 \times 10^{-3}$, $n_{av} = 1$, $\Lambda = 566$ nm at $\lambda_0 = 540$ nm for various grating thicknesses.-----	119
Figure 4.3-8	(a) Schematic of the experimental setup to form the plasma diffraction grating and find its dimensions. (b) Incident SC on the plasma grating at incidence angle of $\theta_i = 28.7^\circ$ (dashed-dotted curve), diffracted spectrum (red solid curve) and spectral selectivity curve for $\lambda_0 = 540$ nm for which the Bragg condition is held.-----	120
Figure 4.3-9	(a) Diffracted SH signal as a function of the delay of SH probe pulse with respect to the Beam 1/ Beam 2 pulses. (b) Diffracted SH signal vs the delay between Beam 1 and Beam 2 pulses at a fixed SH pulse delay of 1 ps.-----	121
Figure 4.3-10	Normalized diffraction efficiency of the SH wave as a function of the ratio of the Beam 2 energy to the Beam 1 energy: Experimental data (dots) and theoretical fit (solid curve) assuming an eight-photon ionization process.-----	122
Figure 4.3-11	(a) Schematic of the experimental setup for diffraction of a light filament, and (b) diffraction efficiency versus the filament beam energy. -----	123
Figure 5.2-1	Comparison of peak intensities $I_{\text{peak}}(r, z)$ for propagation (a,b) and (c,d) in a cylindrical lattice. Left column: linear propagation regime ($P_{\text{in}} = 10^{-6} P_{\text{cr}}$). Right column: nonlinear propagation and filamentation regime ($P_{\text{in}} = 1.25 P_{\text{cr}}$). Lattice parameters: $\Lambda = 350$ μm , $w = 100$ μm , and $\Delta n_0 = -3.3 \times 10^{-7}$. Insets are graphic representations of the cylindrical lattice. Darker rings show lower refractive index. From [196].-----	127
Figure 5.2-2	Beam width as a function of the propagation distance z , without lattice (a), and with lattice (b). Peak intensity I_{peak} as a function of the propagation distance z for (c) lattice strengths Δn_0 of 0 (curve i), -2×10^{-7} (curve ii), -2.5×10^{-7} (curve iii), -3.3×10^{-7} (curve iv), and -5.0×10^{-7} (curve v) and	

	(d) lattice periodicities Λ of ∞ (curve 1), 450 μm (curve 2), 400 μm (curve 3), 350 μm (curve 4), and 300 μm (curve 5). From [196]. -----	128
Figure 5.2-3	(a) Schematic of the experimental setup: BS1, BS2, beam-splitters; L1, L2, L3, lenses; P, polarizer, (b) Gray-scale image of the phase mask (black and white colors denote 0 and 2π phase, respectively). A zoomed view of the central part of the mask is shown in the inset. -----	129
Figure 5.2-4	The simulated (a) and measured (b) double Bessel distribution of the pump beam. (c) xz -plane cut of the pump intensity. (d) Magnified image of the two brightest pump fringes with a yellow spot indicating the launching position of the filament. -----	130
Figure 5.2-5	(a) Experimental xz -plane intensity distribution of the filament without the lattice (top), and in the presence (bottom) of the plasma lattice. (b) 1D filament peak intensity without (black solid) and with (red solid) lattice. Blue dashed and green dashed-dotted curves represent the respective widths of the filaments. (c) The simulated intensity of the filament without (top) and in the presence (bottom) of the lattice. -----	132
Figure 5.3-1	(a) Spatial intensity distribution in the Bessel beam, (b) Generation of Bessel beam by an axicon. -----	134
Figure 5.3-2	Schematic representation of the Bessel zone of a single axicon (a) and an axicon preceded by a negative spherical lens (b). (c) Ray tracing comparison of the Bessel zones of an axicon (dashed lines) and the system of axicon-negative lens (solid line), and (d) Bessel zone vs the incident beam height for an axicon (dashed curve) and the system of axicon negative lens (solid curve). 136	
Figure 5.3-3	Electron density ρ versus propagation distance for 248 nm, UV Bessel beams. (Squares) 7.5 mJ, 0.5 ps, (circles) 10.25 mJ, 5 ps, (a) axicon only (base angle $\gamma = 5^\circ$), (b) axicon with diverging lens ($f = -200$ mm).-----	138
Figure 5.3-4	The measured spectra of the pulse before (solid curve) and after (dashed line) formation of the plasma channel; (a) for 5 ps pulse duration and (b) for 0.5 ps pulse duration. -----	138
Figure 5.3-5	Simulated on axis intensity and electron density profile for 7.5 mJ, 248 nm, 0.5 ps pulses illuminating an axicon (base angle of $\gamma = 5^\circ$) preceded by a diverging lens ($f = -200$ mm) (solid line)-Intensity (circles) –Intensity values for a 7.5 nJ pulses ($\times 10^{-6}$), (dashed line) – on axis electron density.-----	140
Figure 5.3-6	Profile of Airy function (a) and its intensity (b).-----	142
Figure 5.3-7	Intensity profile of 2D Airy beam with $x_0 = y_0 = 300$ μm . -----	143
Figure 5.3-8	Propagation dynamics of an ideal (untruncated) Airy beam with $x_0 = 300$ μm and $\lambda_0 = 800$ nm over a propagation distance of $z = 500$ cm. -----	144
Figure 5.3-9	Intensity profile of an exponentially truncated Airy beam (with $x_0 = 300$ μm) for different values of truncation parameter, a .-----	145
Figure 5.3-10	Propagation dynamics of a truncated Airy beam with $a = 0.05$, $x_0 = 300$ μm , $\lambda_0 = 800$ nm over a propagation distance of $z = 500$ cm. -----	146
Figure 5.3-11	The ballistic dynamics of an Airy beam with $a = 0$, $x_0 = 200$ μm , $\lambda_0 = 800$ nm and different launching angle (a) $\theta = -1.6$ mrad, (b) $\theta = -31.4$ mrad, (c) $\theta = 31.4$ mrad, and (d) $\theta = 1.16$ mrad. These launching angles correspond to $\eta = -2.47$ (a), -0.49 (b), 0.49 (c) and 2.47 (d). ----	147

Figure 5.3-12	Self-healing of an Airy beam with the main lobe obstructed. Observed intensity pattern at (a) the input $z = 0$, (b) $z = 11$ cm, and (c) $z = 30$ cm. From Ref. [241].-----	148
Figure 5.3-13	Transverse energy flow in a 2D Airy beam.-----	149
Figure 5.3-14	Experimentally synthesizing an Airy beam: (a) Input Gaussian beam, (b) wrapped (modulo 2π) cubic phase map imprinted and the input Gaussian beam, and (c) obtained Airy beam after Fourier transformation by a spherical lens.-----	150
Figure 5.3-15	(a) Ray-tracing simulation of a tilted spherical lens, and (b) CCD image of a curved plasma channel fluorescence by focusing the laser beam with a tilted lens.-----	151
Figure 5.3-16	(a) Ray-tracing simulation of a conventional cylindrical beam expander without tilt, (b) calculated spatial phase imprinted on the input beam using a conventional untilted cylindrical beam expander, (c) tilted cylindrical beam expander; arrows denote the degrees of freedom to control the aberration induced spatial phases and (d) calculated imprinted cubic spatial phase on the input beam using the optimized (for cubic spatial phase only) tilted cylindrical beam expander. -----	153
Figure 5.3-17	Configuration for the generation of the 2D cubic phase modulation (along the x and y axes)----	154
Figure 5.3-18	Simulated phase modulation at the exit of the optical system. (a) 1D phase modulation of the two-lens system and respective cubic fits αx^3 for two tilt angles φ_1 : open squares, simulation results for $\varphi_1=25^\circ$; dashed line, cubic fit with $\alpha=0.16$ waves/mm ³ ; open circles, simulation results for $\varphi_1=35^\circ$; and dotted line, cubic fit with $\alpha=0.27$ waves/mm ³ . (b) Contour plots of the 2D phase modulation (in waves) for the four-lens system ($\varphi_1 = \varphi_2 = 35^\circ$) and respective cubic phase fit $\alpha(x^3+y^3)$: solid line, simulation results; dotted lines, contour curves of the 2D cubic fit with $\alpha=0.25$ waves/mm ³ . ---	155
Figure 5.3-19	(a) Experimental setup to generate 1D Airy beams and (b) generated 1D Airy beam. The focal length of the titled cylindrical beam expander, used to induce spatial cubic phase in 1D were ∓ 50 mm and an $f=100$ mm cylindrical lens is used for Fourier transformation. -----	156
Figure 5.3-20	(a) Experimental setup to generate 2D Airy beams and (b) generated Airy beam beams with two sets of titled cylindrical beam expanders with lenses of focal length of ∓ 50 mm used to induce spatial cubic phase modulation and a spherical lens with $f=100$ mm used for spatial Fourier transformation. -----	156
Figure 5.3-21	Transverse acceleration Δ_d of the 2D Airy beam main lobe (along the x -axis) for two Fourier transforming lenses as a function of the distance Δz from their Fourier plane. Circles, experimental points; dotted line, quadratic fit, for the $f = 100$ mm lens; and Squares, experimental points; dashed line, quadratic fit for the $f = 500$ mm lens. -----	157
Figure 5.3-22	(a) FWHM of the 2D Airy peak intensity lobe as a function of the propagation distance z for three Fourier transforming lenses with $f = 100, 200,$ and 500 mm. The evolution of equivalent Gaussian beam is also presented. (b) Calibrated intensity profiles on the Fourier plane of each of the three Fourier transforming lenses. -----	158
Figure 5.3-23	Microscope images of damage spots generated by Airy beams (35 fs, 1mJ) using an $f = 100$ mm Fourier transforming lens. Δz refers to the distance from the Fourier plane. (a) Single shot-burn spots on Cr of a 2D Airy beam. (b) Microscope images of ablation spots on glass generated from the 2D Airy beam. -----	159
Figure 5.3-24	Formation of nonlinearly generated spatiotemporal soliton due the simultaneous balance of diffraction and dispersion by nonlinear self-focusing. From [14].-----	161

- Figure 5.3-25 Iso-intensity plots of Gaussian-Gaussian (initial profile), Airy-Gaussian (after adding a large cubic phase), and Airy-Bessel (after the axicon) wave packets. From [26].----- 162
- Figure 5.3-26 Graphical representation of an Airy³ light bullet generation; (a) a spatiotemporal Gaussian pulse (Gaussian in time and Gaussian in transverse dimensions) is transformed to a temporal Airy pulse with a Gaussian spatial distribution by a grating-telescope compressor, (b) The Gauss-Airy spatiotemporal wavepacket is transformed to a spatiotemporal Airy³ wavepacket by a cascade of two orthogonally-oriented tilted cylindrical telescope systems. ----- 163
- Figure 5.3-27 Normalized spatial and temporal profiles of the Airy³ wavepacket. (a) Initial and (b)-(e) after propagation through $(1.2 L_R, 0.8 L_D)$, $(3.6 L_R, 2.3 L_D)$, $(6 L_R, 3.9 L_D)$ and $(8.3 L_R, 5.4 L_D)$, respectively. L_R and L_D denote the diffraction and dispersion lengths, respectively.----- 165
- Figure 5.3-28 Effect of quadratic and quantic phase terms on the intensity profile of an Airy pulse. The cubic phase coefficient is set to $b = 9000 \text{ fs}^3$, while the other coefficients were changed as the following: $(a = 0, b = 9000 \text{ fs}^3, c = 0)$: Solid curve; $(a = 1000 \text{ fs}^2, b = 9000 \text{ fs}^3, c = 0)$: dashed curve; $(a = 2000 \text{ fs}^2, b = 9000 \text{ fs}^3, c = 0)$: dashed-dotted curve; $(a = 2000 \text{ fs}^2, b = 9000 \text{ fs}^3, c = 10000 \text{ fs}^4)$: dotted curve. ----- 166
- Figure 5.3-29 (a) Intensity iso-surface of the experimentally realized Airy³ light bullet (to assist visualization, the z -axis, time, is stretched by 5 times). (b) Temporal and spatial widths of the main lobe of the Airy³ light bullet vs propagation distance. ----- 167
- Figure 5.3-30 Spatial profiles, representing the fluence distribution, of the Airy³ light bullet at the exit surface of a 2.5-cm-long PMMA sample for (a) 0.4, (b) 0.64, (c) 1.1 mJ total energies. (d) Respective temporal profiles at a distance of 20 cm from the sample exit. ----- 168
- Figure 5.3-31 Spatial profiles, representing the fluence distribution, of the Airy³ light bullet with total energy of 0.4 mJ (a) at the exit surface of the sample and (b) after $z = 9$ cm of propagation in air. (c) Respective temporal profiles at $z = 20$ cm (\circ) and $z = 80$ cm (\square) after the exit surface of the sample.----- 170
- Figure 5.3-32 Nonlinear Airy wave forms for (a) a pure Kerr focusing (green dotted line) and defocusing (red dashed line) nonlinearity with no NLLs; (b) NLLs alone with $K=5$ (red dashed line) and Kerr + NLLs (blue dotted line). (c) Domain of existence (shaded region) of the NAB solution in the case of water at $\lambda_0 = 800$ nm as a function of peak intensity and width of the linear solution. The circles indicate the peak intensities at which numerical simulations were performed (Figure 5.3-33).----- 174
- Figure 5.3-33 Numerical results: propagation in water with focal length $f = 20$ cm. Solid blue line, linear Airy profile; dashed red line, nonlinear Airy profile; black dotted line, nonlinear case with artificially increased NLLs. All profiles are shown in the focal plane of the lens $f(z = 20 \text{ cm})$. ----- 176
- Figure 5.3-34 Experimental results: (a) Schematics of the experimental setup. (b)-(e) Output Airy beam fluence profiles in logarithmic scale. (b) Water at three input energies 25 nJ (solid line), 350 μJ (dashed line), and 530 μJ (dotted line) and for input Airy pulse with a main lobe FWHM of 159 μm . (c) Water at same energies as in (b) and main lobe FWHM of 182 μm . (d) PMMA at three different input energies of 25 nJ (solid line), 78 μJ (dashed line), and 196 μJ (dotted line) and for an input Airy main lobe FWHM of 78 μm . (e) PMMA at same energies as (d) and a main lobe FWHM of 136 μm . ----- 177

Figure 5.3-35	Simulation results of nonlinear propagation of intense Airy beams with main lobe width of 100 μm ((a)-(b)), 200 μm ((c)-(d)) and 300 μm ((e)-(f)). (a), (c) and (e): Peak intensity (solid blue curve, left-axis), electron density (dashed curve, right axis). (b), (d) and (f): iso-intensity of the intensity distribution shown the trajectories of the main and secondary lobes of the Airy beam. -----	180
Figure 5.3-36	Projection of the main lobe trajectory and FWHM of the Airy beam along the x -direction for Input Airy beam with $w_0 = 100 \mu\text{m}$ (a), $w_0 = 200 \mu\text{m}$ (b) and $w_0 = 300 \mu\text{m}$ (c). Dashed red curve shows the trajectory of the linear Airy beam with the same characteristics. -----	182
Figure 5.3-37	Transverse energy flux plots at two different propagation distances $z = 2 \text{ cm}$ (first column) and $z = 16 \text{ cm}$ (second column) for a 2D Airy beam with the main lobe FWHM of 200 μm . (a)-(b) for $n_2 = 3.2 \times 10^{-19} \text{ cm}^2/\text{W}$, and (c)-(d) $n_2 = 3.2 \times 10^{-18} \text{ cm}^2/\text{W}$.-----	184
Figure 5.3-38	Normalized fluence distribution of 2D Airy beam with $w_0 = 235 \mu\text{m}$ as a function of main lobe energy content; (a) 1.6 nJ, (b) 0.5 μJ , (c) 1.3 μJ , and (d) 5.4 μJ . (e) Normalized line-outs of the 2D profiles depicted in (a)-(d) along x -axis. -----	185
Figure 5.3-39	Reconstruction of 2D Airy beam profile in highly nonlinear regime.-----	186

CHAPTER 1

Introduction

1.1 Ultrashort laser pulse propagation

1.1.1 Gaussian beam optics

Most of the widely used laser systems have a spatial distribution that can be approximately considered as Gaussian profile (fundamental transverse mode, TEM_{00}). Gaussian distribution of a laser beam is preserved upon reflection from a mirror or transmission through a lens, with different parameters of Gaussian distribution. The mathematical function describing the Gaussian distribution is a solution to paraxial wave equation (Helmholtz equation). A paraxial wave is a plane wave travelling along the z -direction $\exp[-ikz]$ (with wavenumber $k = 2\pi / \lambda$ and wavelength λ), modulated by a complex envelope $\mathcal{E}(r, z)$ that is slowly varying function of position, so that its complex amplitude is

$$U(r, z) = \mathcal{E}(r, z) \exp[-ikz] \quad (1.1-1)$$

In order that the complex amplitude $U(r, z)$ satisfy the Helmholtz equation, $\nabla^2 U + k^2 U = 0$, which can be directly achieved from the Maxwell equations (see for example [1]), the complex envelope $\mathcal{E}(r, z)$ must satisfy the paraxial Helmholtz equation:

$$\nabla_T^2 \mathcal{E} - i2k \frac{\partial \mathcal{E}}{\partial z} = 0, \quad (1.1-2)$$

where $\nabla_T^2 = \partial^2 / \partial x^2 + \partial^2 / \partial y^2$ is the transverse Laplacian operator. It can be easily proved that a simple solution for the paraxial wave equation is as (see for example, Chapter 6 of Ref. [2])

$$U(r, z) = \mathcal{E}_0 \frac{w_0}{w(z)} \exp\left[-\frac{r^2}{w^2(z)}\right] \exp\left[-ikz - ik \frac{r^2}{2R(z)} + i\zeta(z)\right] \quad (1.1-3)$$

with

$$w(z) = w_0 \sqrt{1 + \frac{z^2}{z_0^2}} \quad (1.1-4)$$

$$R(z) = z \left(1 + \frac{z_0^2}{z^2} \right) \quad (1.1-5)$$

where $\zeta(z) = \tan^{-1}(z / z_0)$, $w_0 = \sqrt{\lambda z_0 / \pi}$ and $\mathcal{E}_0 = \mathcal{E}_1 / iz_0$. The optical intensity $I(r, z) = |U(r, z)|^2$ of a Gaussian beam thus depends on the axial and radial positions.

$$I(r, z) = I_0 \left[\frac{w_0}{w(z)} \right]^2 \exp \left[-\frac{2r^2}{w^2(z)} \right] \quad (1.1-6)$$

where $I_0 = |\mathcal{E}_0|^2$. Optical intensity $I(r, z)$ of a Gaussian beam is shown in Figure 1.1-1(a).

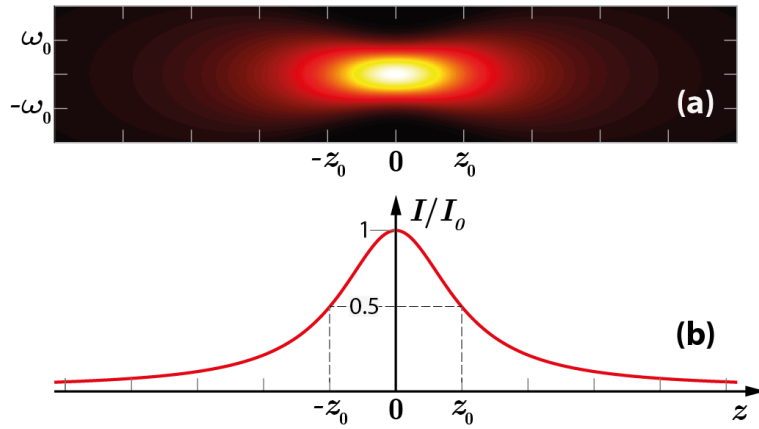


Figure 1.1-1 (a) Intensity of a typical Gaussian beam propagating along z-axis and (b) on axis intensity of a Gaussian beam.

At any value of z , the intensity is a Gaussian function of the radial (transverse) distance, and that is why such beams are called *Gaussian beams*. The Gaussian function has its peak on the z -axis at $r = 0$ as it is shown in Figure 1.1-1, and monotonically reduces by increasing r .

The beam width $w(z)$ of the Gaussian distribution increases with the axial distance z as illustrated in Figure 1.1-2.

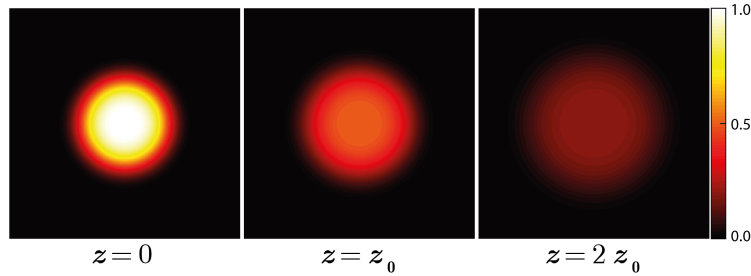


Figure 1.1-2 Normalized beam intensity I / I_0 as a function of the radial distance r at different axial distance: $z = 0$; $z = z_0$ and $z = 2z_0$.

Conventionally, the propagation distance at which the beam waist is increased by a factor of $\sqrt{2}$ with respect to the minimal waist w_0 is called Rayleigh range or diffraction length, z_0 ; which is found as:

$$z_0 = \frac{1}{2} k w_0^2 \quad (1.1-7)$$

where $k = 2\pi n_0 / \lambda$ is the wavenumber (n_0 is the refractive index of the propagation medium and here it is considered to be equal to 1). At any transverse plane along the propagation axis, z , the beam radius is given by Eq. (1.1-4), and its minimum value that is known as waist radius is w_0 . The waist diameter $2w_0$ is also called the spot size. The beam width increases monotonically with z , and becomes equal to $\sqrt{2} w_0$ at $z = \pm z_0$ that is the Rayleigh range. For $z \gg z_0$ the first term of (1.1-4) can be neglected, which results in the linear relation

$$w(z) = \frac{w_0}{z_0} z = \theta_0 z \quad (1.1-8)$$

Therefore, the angular divergence of the beam is

$$2\theta_0 = \frac{4}{\pi} \frac{\lambda}{2w_0} \quad (1.1-9)$$

The divergence angle is directly proportional to the wavelength and inversely proportional to the spot size. Clearly, the best focus occurs and thus the minimal waist occurs at $z = 0$. Moreover, Eq. (1.1-3) clearly shows that the phase of the Gaussian beam can be written as:

$$\varphi(r, z) = kz - \zeta(z) + \frac{kr^2}{2R(z)} \quad (1.1-10)$$

where the first term is the phase of a plane wave. The second term represents a phase delay $\zeta(z) = \tan^{-1}(z / z_0)$, which ranges from $-\pi / 2$ at $z = -\infty$ to $+\pi / 2$ at $z = \infty$. This phase delay corresponds to excess retardation of the wavefront in relation to a plane wave or a spherical wave and the third term causes a wave front bending. It represents a deviation of the phase at off-axis points in a given transverse plane from that at the axial point.

1.1.2 Linear pulse propagation

- **Temporal and spectral representation of an optical pulse**

The electric field of any optical pulse with a central angular frequency of ω_0 can be written as $E(t) = \mathcal{E}(t) \exp(i\omega_0 t)$, where $\mathcal{E}(t)$ is a complex envelope which can be expressed in terms of its magnitude $|\mathcal{E}(t)|$ and phase $\varphi(t) = \arg[\mathcal{E}(t)]$, hence, the electric field can be written as

$$E(t) = |\mathcal{E}(t)| \exp(i[\omega_0 t + \varphi(t)]) \quad (1.1-11)$$

The optical intensity of an optical pulse is $I(t) = |E(t)|^2 = |\mathcal{E}(t)|^2$. Most known intensity profiles of common pulsed laser systems are Gaussian $I(t) \propto \exp[-2(t/a)^2]$, Lorentzian $I(t) \propto 1/[1 + (t/a)^2]$, or hyperbolic secant $I(t) \propto \text{sech}^2(t/a)$ functions of time; where a is proportional to the temporal width of the pulse and the proportionality constant depends to the chosen criterion. For instance, in the case of the Gaussian pulse, relation between a and temporal width with different criterions are

$$\begin{aligned}
 a &= \frac{1}{\sqrt{2 \ln 2}} \tau_{\text{FWHM}} \\
 a &= \frac{1}{\sqrt{2}} \tau_{1/e} \\
 a &= \frac{1}{2} \tau_{1/e^2}
 \end{aligned}
 \tag{1.1-12}$$

where τ_{FWHM} , $\tau_{1/e}$ and τ_{1/e^2} are full temporal widths at 1/2, 1/e and 1/e² of maximum intensity, respectively.

The spectral representation of the pulse can be obtained by the Fourier transformation of its temporal electric field. This results in a complex function $E(\omega) = |E(\omega)| \exp[i\varphi(\omega)]$. The squared magnitude $I(\omega) = |E(\omega)|^2$ is called spectral intensity and $\varphi(\omega)$ is the spectral phase. The function $E(\omega)$ is centered at the central frequency ω_0 . If the pulse has a narrow spectral width, then the complex envelope is a slowly varying function of time (i.e. changes slightly within an optical cycle, $2\pi/\omega_0$), but for very narrow pulses in time that have a very broad spectral width, the variation of complex envelope in time is considerable.

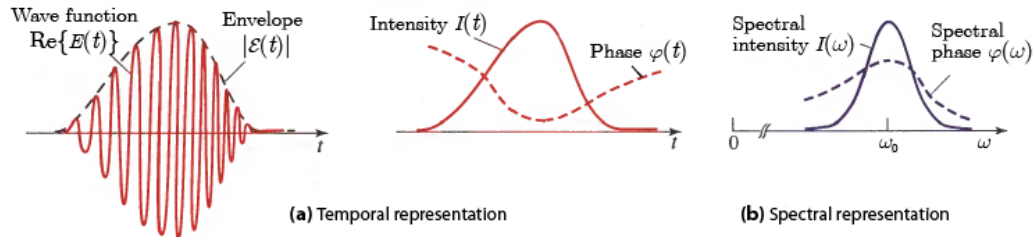


Figure 1.1-3 Temporal and spectral representation of an optical pulse. (a) The real part of the wave function $\text{Re}[E(t)] = |\mathcal{E}(t)| \cos[\omega_0 t + \varphi(t)]$, the magnitude of the envelope $|\mathcal{E}(t)|$, the intensity $I(t)$. (b) Spectral intensity $I(\omega)$ and spectral phase $\varphi(\omega)$ (from [1]).

The temporal and spectral widths of a pulse are the width of intensity $I(t)$ and spectral intensity $I(\omega)$, respectively. Temporal and spectral representations of an optical pulse are shown in Figure 1.1-3.

Since in practice many laser systems produce Gaussian pulses, it will be helpful to study these pulses in more detail. For a Gaussian pulse with a quadratic phase in time as $\varphi(t) = bt^2$, the complex envelope $\mathcal{E}(t)$ can be written as:

$$\mathcal{E}(t) = \exp\left[-(t/a)^2\right] \exp\left[ibt^2\right] \quad (1.1-13)$$

Using Eq. (1.1-11), the electric field of the pulse is found to be

$$E(t) = \exp\left[-\eta t^2\right] \exp\left[i\omega_0 t\right] \quad (1.1-14)$$

$$\eta = 1/a^2 - ib$$

The instantaneous intensity for such a pulse is

$$I(t) = \exp\left[-2(t/a)^2\right] \quad (1.1-15)$$

On the other hand, by using the Eq. (1.1-11), it can be seen that the total instantaneous phase is $\varphi_{\text{tot}} = \omega_0 t + bt^2$. Therefore, the instantaneous angular frequency of the electric field, the rate at which the total phase changes with time, can be written as

$$\omega_1(t) = \frac{d\varphi_{\text{tot}}(t)}{dt} = \omega_0 + 2bt \quad (1.1-16)$$

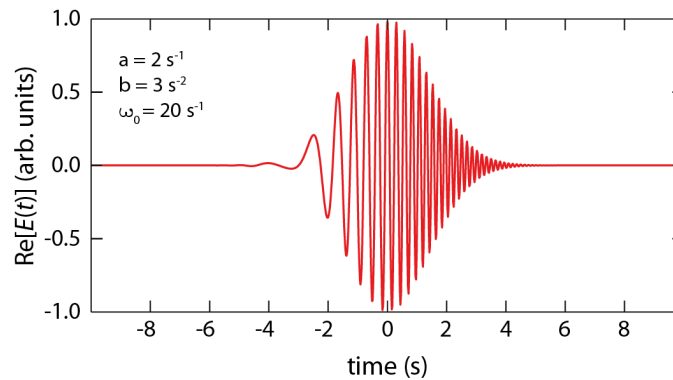


Figure 1.1-4 A chirped Gaussian pulse with the indicated parameters for temporal width, chirp, and central angular frequency.

Thus, a Gaussian pulse with a nonzero imaginary part b , has linearly time-varying instantaneous frequency. Such a signal is referred to as a *chirped Gaussian pulse*, with the parameter b being the chirp parameter. A chirped Gaussian pulse with $a = 2 \text{ s}^{-1}$, $b = 3 \text{ s}^{-2}$ and $\omega_0 = 30 \text{ s}^{-1}$ is illustrated in Figure 1.1-4.

Fourier transformation of the electric field in time domain (given by Eq. (1.1-14)), results in the electric field in the positive angular frequency side as:

$$\begin{aligned}\tilde{E}(\omega) &= \left[-\frac{(\omega - \omega_0)^2}{4\eta} \right] \\ &= \exp \left[-\frac{1}{4} \left(\frac{a^2}{1 + b^2 a^4} \right) (\omega - \omega_0)^2 - i \frac{1}{4} \left(\frac{b a^4}{1 + b^2 a^4} \right) (\omega - \omega_0)^2 \right]\end{aligned}\quad (1.1-17)$$

It can be seen that the linear frequency chirp (or equivalently a quadratic phase chirp) in time, results in a quadratic phase shift in the spectral domain, as given by $b a^4 / (1 + b^2 a^4)$ factor in the Eq. (1.1-17). The power spectrum, of this pulse is given as:

$$\begin{aligned}|\tilde{E}(\omega)|^2 &= \exp \left[-\frac{1}{2} \left(\frac{a^2}{1 + b^2 a^4} \right) (\omega - \omega_0)^2 \right] \\ &= \exp \left[-4 \ln 2 \left(\frac{\omega - \omega_0}{\Delta\omega_{FWHM}} \right)^2 \right]\end{aligned}\quad (1.1-18)$$

where $\Delta\omega_{FWHM}$ is the FWHM of the spectral intensity. By using Eq. (1.1-12) and Eq. (1.1-18), the relation between the spectral and temporal widths of a Gaussian pulse are found as

$$\Delta\omega_{FWHM} = \frac{4 \ln 2}{\tau_{FWHM}} \sqrt{1 + \left(\frac{b}{2 \ln 2} \right)^2 \tau_{FWHM}^4}\quad (1.1-19)$$

Instead of angular frequency width, the frequency width $\Delta\nu_{FWHM}$ can be simply found by $\Delta\nu = \Delta\omega / 2\pi$. The preceding equation indicates that in the absence of chirp factor b , the spectral bandwidth is inversely proportional to the temporal width and for big chirp factors, the

spectral width is proportional to the temporal width. Moreover, Eq. (1.1-19) shows the fact that for a chirped Gaussian pulse time-bandwidth product is given by

$$\tau\Delta\nu = 0.44\sqrt{1 + \left(\frac{b}{2\ln 2}\right)^2 \tau^4} \quad (1.1-20)$$

where the FWHM subscripts for temporal and spectral widths are omitted. The minimum value for time-bandwidth product is $\tau\Delta\nu = 0.44$, which is satisfied for unchirped Gaussian pulses. The time-bandwidth product value depends also on exact pulse shape and criterion of measuring widths (e.g. $1/e$, $1/e^2$, or $1/2$ of maximum intensity, etc.). However, pulses whose time-bandwidth product is close to 0.5 are referred to as *transform-limited pulses*. Such pulses are unchirped or they have very little chirp.

It is mostly desired to express the spectral intensity $I(\omega)$ as a function of the wavelength, $I_\lambda(\lambda)$. Such a conversion can be obtained by using the relation $I_\lambda(\lambda) = I(\nu)|d\nu/d\lambda|$. The spectral width $\Delta\nu$ may also be converted into wavelength units. If $\Delta\nu \ll \nu_0$, then the spectral width in wavelength units is approximately $\Delta\lambda \approx |d\lambda/d\nu|\Delta\nu$, or

$$\Delta\lambda \approx \frac{\lambda_0^2}{c} \Delta\nu \quad (1.1-21)$$

where $\lambda_0 = c/\nu_0$ is the wavelength corresponding to the central frequency.

1.1.3 Linear pulse propagation in dispersive media

It is known that a polychromatic light wave splits to different colors upon refraction in optical media. This is because the refractive index of an optical material depends on the frequency of the light wave. In other words, since the speed of light is $v = c/n$, different components of a polychromatic wave propagate with different speeds. The dependency of the refractive index on wavelength was first formulated by Cauchy as:

$$n(\lambda) = A + \frac{B}{\lambda^2} + \frac{C}{\lambda^4} + \dots \quad (1.1-22)$$

where A, B, C , are empirical constants for a given material. Equation (1.1-22) shows that, for a certain material, by increasing the wavelength the refractive index decreases. This behavior is known as *normal dispersion*. However, the dispersion behavior of optical materials close to the resonance transitions (absorption lines) cannot be explained by Cauchy's dispersion relation. In this region, the refractive index of material grows for longer wavelengths and it is known as so-called *anomalous dispersion*. Typical dependency of the absorption coefficient and refractive index of dielectric materials are shown in Figure 1.1-5 [1]. Later on, the dispersion relation was generalized and extended by Sellmeier as

$$n^2 = 1 + \sum_i \frac{A_i \lambda^2}{\lambda^2 - \lambda_i^2} \quad (1.1-23)$$

where $\lambda_i, i = 1, 2, 3, \dots$ are the possible resonance frequencies and A_i are empirical coefficients. In fact, Sellmeier's equation can be derived from the electromagnetic theory with some assumptions (see for instance [3]).

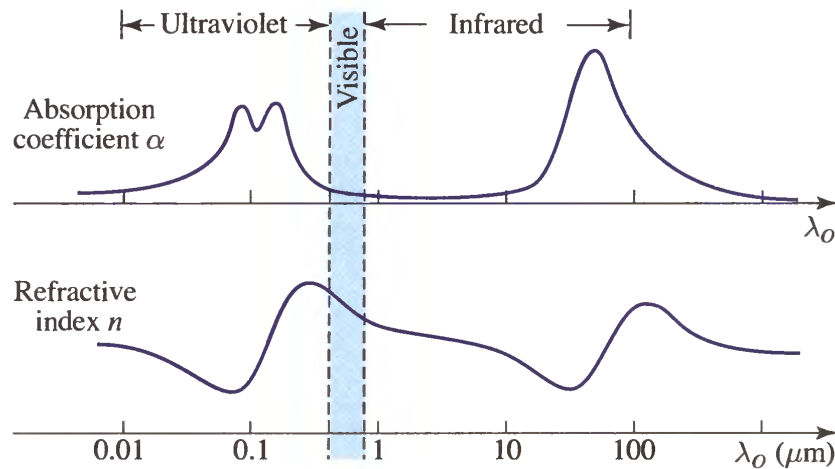


Figure 1.1-5 Typical wavelength dependence of the absorption coefficient and refractive index for a dielectric medium with resonant absorption bands in the ultraviolet and infrared spectral regions (from [1]).

Now, knowing that the dispersion should be taken into account for laser pulse comprised of multiple wavelengths, let us investigate how a Gaussian pulse evolves during the propagation in

a dispersive medium. The electric field of the chirped Gaussian optical pulse before propagation in the dispersive is considered as

$$E(t)_{z=0} = \exp(-\eta_0 t^2) \exp(-i\omega_0 t) \quad (1.1-24)$$

with

$$\eta_0 = 1 / a_0^2 - ib_0 \quad (1.1-25)$$

where η_0 is the initial pulse parameter, a_0 is proportional to the initial pulse duration (Eq. (1.1-12)) and b_0 is proportional to the amount of initial chirp. The spectral representation of the electric field of this optical pulse before entering the dispersive material is given by Eq. (1.1-17) as

$$\mathcal{E}_0(\omega) = \exp\left[-\frac{(\omega - \omega_0)^2}{4\eta_0}\right] \quad (1.1-26)$$

After propagating a distance z in the dispersive medium, the pulse spectrum changes to

$$E(\omega, z) = \mathcal{E}_0(\omega) \exp[-ik(\omega)z] \quad (1.1-27)$$

where $k(\omega) = n\omega / c$ is the frequency-dependent wavenumber. The frequency dependency of the wavenumber is a result of the material dispersion. To find an analytical solution for the propagation equation, assuming that $\Delta\omega \ll \omega_0$ (this assumption is not valid for few-cycle ultrashort pulses), the wavenumber $k(\omega)$ can be rewritten using a Taylor expansion as a function of angular frequency deviation around the central angular frequency ω_0 .

$$k(\omega) = k(\omega_0) + k' \cdot [\omega - \omega_0] + \frac{1}{2} k'' \cdot [\omega - \omega_0]^2 + \dots, \quad (1.1-28)$$

where the primes denote the derivatives with respect to ω , at the central frequency ω_0 . By placing Eq. (1.1-28) in Eq.(1.1-27), and using Eq.(1.1-26) the electric field in the spectral domain can be written as

$$E(\omega, z) = \exp \left[-ik(\omega_0)z - ik'z(\omega - \omega_0) - \left(\frac{1}{4\eta_0} + \frac{i}{2}k''z \right) (\omega - \omega_0)^2 \right] \quad (1.1-29)$$

The respective time-representation of this pulse can be calculated by performing an inverse Fourier transform. Thus, the time-domain representation is found as

$$E(t, z) = \exp \left[j\omega_0 \left(t - \frac{z}{v_\varphi(\omega_0)} \right) \right] \exp \left[-\eta(z) \left(t - \frac{z}{v_g(\omega_0)} \right)^2 \right] \quad (1.1-30)$$

where $v_\varphi(\omega_0) = \omega_0 / k$ is the phase velocity, $v_g(\omega_0) = d\omega / dk |_{\omega_0}$ is the group velocity (at the central angular frequency), and $\eta(z) = 1 / \eta_0 + 2ik''z$ is the distance-dependent Gaussian pulse parameter.

The first exponential term in Eq. (1.1-30) shows that the phase of the central angular frequency ω_0 is delayed by an amount of z / v_φ (phase delay) after propagation through distance z . The phase velocity is the speed of the plane wave components of the pulse in the medium. The phase velocity, in general, can be greater than the speed of light in vacuum; however, this does not contradict the special relativity because the phase velocity is not the speed at which energy is transferred. In fact, these plane waves do not carry any information since they have an infinite duration. The second term in Eq. (1.1-30) indicates that after propagation over a distance z , the pulse keeps a Gaussian envelope, with a modified pulse parameter $\eta(z)$, and the envelope is delayed by an amount z / v_g (group delay time).

The relation between initial pulse parameter η_0 (defined in Eq.(1.1-25)) and the pulse parameter at a distance z reveals more information about the evolution of the pulse. The pulse parameter at propagation distance of z can be written as:

$$\frac{1}{\eta(z)} = \frac{a_0^2}{1 + a_0^4 b_0^2} + j \left(\frac{b_0 a_0^4}{1 + a_0^4 b_0^2} + 2k''z \right) \quad (1.1-31)$$

It can be seen $k'' = 0$ results in $\eta(z) = \eta_0$; this means that in the absence of dispersion, the pulse shape is preserved over the propagation. If $k'' \neq 0$, the medium possesses *group velocity dispersion (GVD)*. The relation between the group velocity and the dispersion parameter k'' is given by

$$k'' = \frac{d}{d\omega} \left(\frac{1}{v_g(\omega_0)} \right) = - \frac{1}{v_g(\omega_0)} \frac{dv_g(\omega)}{d\omega} \quad (1.1-32)$$

Hence, the group velocity $v_g(\omega)$ can be written as a function of the frequency deviation from the central frequency ω_0 as

$$v_g(\omega) \simeq v_g(\omega_0) - k''v_g(\omega_0) \cdot [\omega - \omega_0] \quad (1.1-33)$$

This equation clearly shows that the different frequency components around the central frequency will have different speeds and thus k'' is indeed representing the effect of dispersion. By assuming $\eta(z) \equiv 1 / a^2(z) - ib(z)$, we have

$$a(z) = \frac{1}{a_0} \left[a_0^4 (1 + 4b_0 k'' z) + 4k''^2 z^2 (1 + a_0^4 b_0^2) \right]^{1/2} \quad (1.1-34)$$

$$b(z) = \frac{a_0^4 b_0 + 2k'' z (1 + a_0^4 b_0^2)}{a_0^4 (1 + 4b_0 k'' z) + 4k''^2 z^2 (1 + a_0^4 b_0^2)} \quad (1.1-35)$$

where parameters $a(z)$ and $b(z)$ are related to pulse duration and chirp at a distance z , respectively. In an analogy to Eq. (1.1-12), $a(z)$ is proportional to the pulse duration at a distance z , depending on the measuring criterion. For instance, the pulse duration at the FWHM of the intensity at z is $\tau_{\text{FWHM}}(z) = \sqrt{2 \ln 2} a(z)$. Furthermore, it can be shown that group

velocity dispersion can compress or broaden a pulse depending on the initial chirp. However, when the input pulse is initially unchirped, it accumulates chirp and thus gradually broadens through the propagation in dispersive media. For an initially unchirped pulse ($b_0 = 0$), Eq. (1.1-34) and Eq. (1.1-35) are reduced to

$$a(z) = \frac{1}{a_0} \left(a_0^4 + 4k''^2 z^2 \right)^{1/2} \quad (1.1-36)$$

$$b(z) = \frac{2k''z}{a_0^4 + 4k''^2 z^2} \quad (1.1-37)$$

Obviously, an unchirped pulse broadens during the propagation in the dispersive medium. In an analogy to the Rayleigh range (diffraction length) as a characteristic length determining the spatial broadening of a beam, a characteristic length is also defined in the time domain that is called *dispersion length*. Dispersion length is a range over which a pulse broadens by a factor $\sqrt{2}$. Assuming that $a(z) \equiv \alpha \tau(z)$, where α is a proportionality factor which is defined by the pulse duration measurement criterion (see Eq. (1.1-12)), the dispersion length is

$$z_D = \frac{\alpha^2 \tau_0^2}{2k''} \quad (1.1-38)$$

As an example, for the pulse duration at the FWHM of the intensity ($\alpha = 1/\sqrt{2 \ln 2}$), the dispersion length is $z_D = \tau_0^2 / (4 \ln 2 k'')$. By replacing the definition of the dispersion length in Eq. (1.1-36), the pulse duration at a distance z can be written as

$$\tau(z) = \tau_0 \left[1 + \left(\frac{z}{z_D} \right)^2 \right]^{1/2} \quad (1.1-39)$$

1.1.4 Nonlinear polarization

So far in this chapter, we have considered the linear propagation of optical beams, however, when the power carried by an optical beam is high enough, optical materials do not behave in a linear fashion anymore. This may cause significant changes in the medium and in the optical pulse. This regime of propagation is very rich regarding involved physical phenomena and applications. Since the invention of lasers, this field has been a subject of enormous amount of research both for understanding the physics of nonlinear propagation and its applications in many different fields.

From the classical physics point of view, many optical phenomena (such as dispersion, absorption, etc.), can be explained by the harmonic oscillator model (Lorentz oscillator model). This purely classical model gives the simplest picture of atom-field interaction. It assumes an atom as a mass (the nucleus) connected to another mass (electron) by a spring that behaves according to Hook's law. The restoring force of this system is $-kx$, where x is displacement from the balance positions and k is the spring coefficient. Therefore, the potential energy of the system is $U=(1/2)kx^2=(1/2)\omega_0^2x^2$, where ω_0 is the angular frequency of the harmonic oscillator. The spring would be set into motion by an electric field interacting with the charge of the electron with the electric force $\mathbf{F}_E = -e\mathbf{E}$. The field would either repel or attract the electron that leads to either compression or expansion of the spring. This system can be considered as a dipole with a dipole moment of $\mathbf{p} = -ex$. Thus an ensemble of N atoms in similar conditions would generate a total dipole moment of $\mathbf{P} = -Nex$.

Any oscillatory behavior of the external electric field results in harmonic oscillation of the electron. The external electric field can be of an incident electromagnetic field and the effect of the magnetic field can be neglected since it is very small in comparison to the effect of the electric field. In other words, the effect of the external field on a dielectric material is to induce a polarization. The motion equation of this system is found as $\ddot{x}+2\gamma\dot{x}+\omega_0^2x=(e/m)E(t)$, where dots denote the time derivatives, ω_0 is the central angular frequency of oscillation, γ is the damping factor and e, m are the electric charge and mass of the electron, respectively. Assuming the incident field as $E(t) = E \exp(-i\omega t) + c.c.$, the time-dependent polarization is found as $P(t) = \varepsilon_0\chi^{(1)}(\omega)E \exp(-i\omega t) + c.c.$; where $\chi^{(1)}$ is the linear complex susceptibility given by

$$\chi^{(1)} = \chi'^{(1)}(\omega) + i\chi''^{(1)}(\omega)$$

The linear susceptibility is related to the linear refractive index $n = \sqrt{1 + \chi}$. The real and imaginary parts of linear susceptibility are

$$\chi'^{(1)}(\omega) = \frac{Ne^2}{2m\omega_0} \frac{(\omega_0 - \omega)}{(\omega_0 - \omega)^2 + \gamma^2} \tag{1.1-40}$$

$$\chi''^{(1)}(\omega) = \frac{Ne^2}{2m\omega_0} \frac{\gamma}{(\omega_0 - \omega)^2 + \gamma^2}$$

It can be seen that the susceptibility and thus the refractive index have frequency dependency and the damping factor in the numerator of the imaginary part of the susceptibility stands for absorption. Therefore, it is obviously seen that this simple model can indeed explain dispersion and absorption of atomic vapors and nonmetallic solids.

However, the simple harmonic oscillator model cannot be used for explaining nonlinear optical phenomena. From the microscopic point of view, when the incident field is intense enough, displacement of electron from the balance position (minimum potential) is big. The harmonic oscillator potential is only an approximation for small displacements of electron around the balance point. In reality, the potential energy that binds an electron to the nucleus or even the potential energy for a simple diatomic molecule is not necessarily analogous to potential energy of the harmonic oscillator. Extension of this model depends on whether or not the medium has inversion symmetry. The potential energy of a simple harmonic oscillator and other classical oscillators for describing nonlinear optics in the centrosymmetric and non-centrosymmetric materials are shown in Figure 1.1-6(a).

It is clearly seen that for small displacement from the balance point, all potentials functions shown in Figure 1.1-6 coincide. This is simply, classical representation of the limits of linear optics regime; however, for large displacements, that appear when the acting force is strong enough, the deviation from the harmonic oscillator potential is significant and the restoring forces cannot be considered linearly dependent to the displacement anymore.

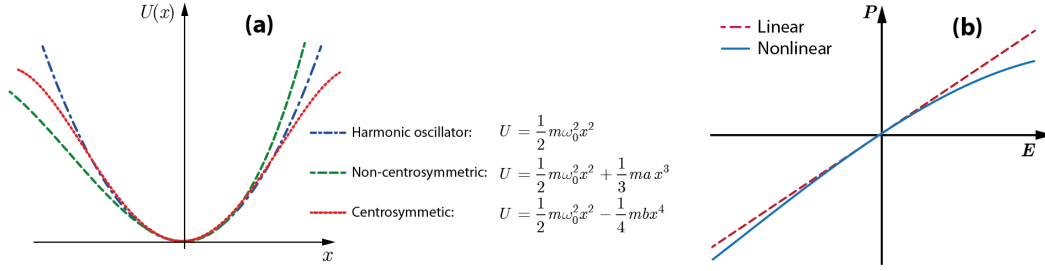


Figure 1.1-6 (a) Potential energy functions of a harmonic oscillator (linear regime) and noncentrosymmetric and centrosymmetric medium (nonlinear regime). (b) P-E relations for a linear (dashed line) and a nonlinear dielectric medium (solid line).

In other words, in a linear dielectric medium the polarization density is proportional to the applied electric field, $\mathbf{P} = \epsilon_0\chi\mathbf{E}$, where ϵ_0 is the permittivity of free space and χ is the electric susceptibility of the medium. However, in a nonlinear dielectric medium, the relation between the electric field and the polarization density is nonlinear, as depicted in Figure 1.1-6(b). The polarization density $\mathbf{P} = N\mathbf{p}$ is a result of individual dipole moments \mathbf{p} induced by the applied electric field \mathbf{E} and the number density of dipole moments N .

Since the applied electric fields of optical beams are typically small in comparison with the characteristic interatomic or crystalline fields, the nonlinearity is usually weak. The relation between P and E is then approximately linear for small E , deviating slightly from the linearity as E increases. Under these considerations, the polarization density P can be expanded in a Taylor series about $E=0$,

$$P = \epsilon_0(\chi^{(1)}E + \chi^{(2)}E^2 + \chi^{(3)}E^3 + \dots), \quad (1.1-41)$$

where ϵ_0 is the permittivity of free space, $\chi^{(1)}$ is the linear susceptibility and $\chi^{(2)}, \chi^{(3)}$ are second- and third-order nonlinear susceptibilities, respectively. It can be seen that for small E the first term which describes the linear response is dominant. It should be mentioned that P and E here are considered as scalar quantities, but in general, they are vectors and thus $\chi^{(1)}$ is a second-rank tensor, $\chi^{(2)}$ is a third-order rank tensor and so forth.

Since the first term in Eq.(1.1-41), $\epsilon_0\chi^{(1)}E$, represents the linear part of polarization, in the absence of free charges and currents, nonlinear wave equation can be simply derived from the Maxwell equations as:

$$\nabla^2\mathbf{E} - \left(\frac{n}{c}\right)^2 \frac{\partial^2}{\partial t^2}\mathbf{E} = \frac{1}{c^2} \frac{\partial^2}{\partial t^2}\mathbf{P}^{\text{NL}} \quad (1.1-42)$$

where $\mathbf{P}^{\text{NL}} = \epsilon_0(\chi^{(2)}\mathbf{E}^2 + \chi^{(3)}\mathbf{E}^3 + \dots)$. A trivial result of the nonlinear term in the nonlinear wave equation is the wave mixing. For instance, if we consider only the second-order nonlinearity as $P^{(2)}(t) = \epsilon_0\chi^{(2)}E(t)^2$ and the incident field composed of two frequencies $E(t) = \mathcal{E}_1 \exp(-i\omega_1 t) + \mathcal{E}_2 \exp(-i\omega_2 t) + c.c.$, the resultant nonlinear polarization will be found as:

$$\begin{aligned} P(2\omega_1) &= \epsilon_0\chi^{(2)}\mathcal{E}_1^2 \quad (\text{SHG}) \\ P(2\omega_2) &= \epsilon_0\chi^{(2)}\mathcal{E}_2^2 \quad (\text{SHG}) \\ P(\omega_1 + \omega_2) &= \epsilon_0\chi^{(2)}\mathcal{E}_1\mathcal{E}_2 \quad (\text{SFG}) \\ P(\omega_1 - \omega_2) &= \epsilon_0\chi^{(2)}\mathcal{E}_1\mathcal{E}_2^* \quad (\text{DFG}) \\ P(0) &= 2\epsilon_0\chi^{(2)}(\mathcal{E}_1\mathcal{E}_1^* + \mathcal{E}_2\mathcal{E}_2^*) \quad (\text{OR}) \end{aligned} \quad (1.1-43)$$

where different components of the second order polarizations are separated and labeled by the names of physical processes which are results of each component. SHG stands for second harmonic generation, SFG and DFG indicate sum- and difference-frequency generation, respectively, and OR stands for optical rectification (generation of DC field -zero-frequency component).

We should note here that usually only one of these processes would be dominant in nonlinear optical interactions, because the nonlinear polarization can efficiently produce an output signal only if a certain phase-matching condition is satisfied and this condition cannot be satisfied for more than one frequency component of the nonlinear polarization at a time. In practice, a desired frequency is chosen and then by selecting the polarization of the input field

and the orientation of the nonlinear crystal, phase matching for that specific frequency is satisfied.

Now, let us consider the third-order optical nonlinearities. The third-order polarization components is $P^{(3)}(t) = \epsilon_0 \chi^{(3)} E(t)^3$. For the general case where the applied electric field is composed of multiple frequency components, the expression for the third-order polarization is quite complex. Thus, for simplicity, now we consider a monochromatic incident field given by $E(t) = \mathcal{E} \cos(\omega t)$. Therefore, the nonlinear polarization in this case is found as:

$$P^{(3)}(t) = \frac{1}{4} \epsilon_0 \chi^{(3)} \mathcal{E}^3 \cos(3\omega t) + \frac{3}{4} \epsilon_0 \chi^{(3)} \mathcal{E}^3 \cos(\omega t) \quad (1.1-44)$$

where the first term on the RHS describes the response at frequency 3ω that is created by an applied field at frequency ω . In fact, this term describes the third-harmonic generation process, which is illustrated in Figure 1.1-7. As it is depicted in photon description (Figure 1.1-7(b)), three photons of frequency ω are eliminated and one photon of frequency 3ω is created. The second term in on the RHS is associated to the nonlinear refractive index, which is described in the following.

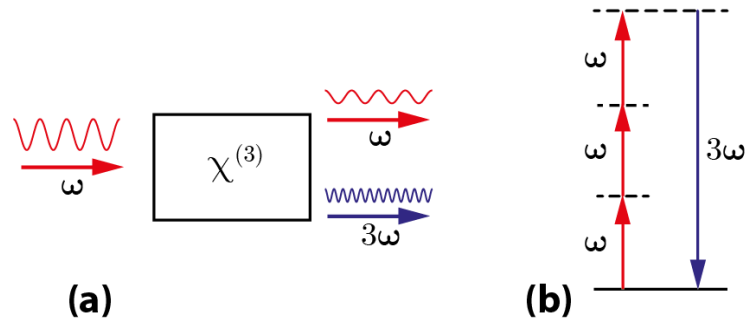


Figure 1.1-7 Third-harmonic generation. (a) Geometry of interaction, and (b) energy-level description.

1.1.5 Nonlinear index of refraction

Using Eqs. (1.1-41) and (1.1-44) in a material with an inversion symmetry (that results in $\chi^{(2)} = 0$), the polarization can be written as:

$$P = \epsilon_0 \left(\chi^{(1)} + \frac{3}{4} \chi^{(3)} |\mathcal{E}|^2 \right) E \quad (1.1-45)$$

By defining the total refractive index of the medium as $n = \sqrt{1 + \chi}$, where $\chi = \chi_L + \chi_{NL} = \chi^{(1)} + \frac{3}{4} \chi^{(3)} |\mathcal{E}|^2$ and $n_0 = \sqrt{1 + \chi^{(1)}}$, the total refractive index composed of linear and nonlinear parts is derived as:

$$n = n_0 + \frac{3}{8n_0} \chi^{(3)} |\mathcal{E}|^2 \quad (1.1-46)$$

Since the intensity of an optical field is $I = \frac{1}{2} \epsilon_0 n_0 c |\mathcal{E}|^2$, where c is the speed of light in vacuum. Thus, the refractive index can be written as:

$$n(r, t) = n_0 + n_2 I(r, t) \quad (1.1-47)$$

with

$$n_2 = \frac{3\chi^{(3)}}{4\epsilon_0 c n_0^2} \quad (1.1-48)$$

Equation (1.1-47), clearly indicates that the total refractive index is composed of a linear part n_0 , which is constant and a nonlinear part $n_2 I$, which is intensity dependent. However, the value of n_2 is small in the known optical materials; for instance $n_2 = 3.2 \times 10^{-16} \text{ cm}^2/\text{W}$ in fused silica glass [4], $n_2 = 4.1 \times 10^{-16} \text{ cm}^2/\text{W}$ in water [4] and $n_2 = 3.2 \times 10^{-19} \text{ cm}^2/\text{W}$ in air [5]. Therefore, for low intensities the nonlinear part of the refractive index will be negligible. Equation (1.1-47) shows the importance of the laser intensity $I(r, t)$; as the refractive index seen by the pulse follows the local and temporal intensity profile. Hence, for the high laser intensities the nonlinear part of the refractive index is significant and plays an essential role in nonlinear optical phenomena that will be discussed in the following subsections.

1.1.6 Self-focusing

Self-focusing is a direct result of the nonlinear refractive index. Since the nonlinear part of the refractive index is intensity dependent, an intense beam of light modifies the optical properties of a medium in such a way that the beam focuses within the material [6]. In other words, self-focusing is an induced lens effect. If we assume a single-mode laser beam with a Gaussian transverse profile propagating into a medium with a refractive index $n = n_0 + n_2 I$, where $n_2 I$ is the optical-field-induced refractive index change. For positive n_2 , the central part of the beam experiences a larger refractive index than the edges, because the central part of the beam has higher intensity. Thus, the central part of the beam travels slower than the edges and this leads to a curvature of the wavefront of the beam in a progressive manner as shown in Figure 1.1-8.

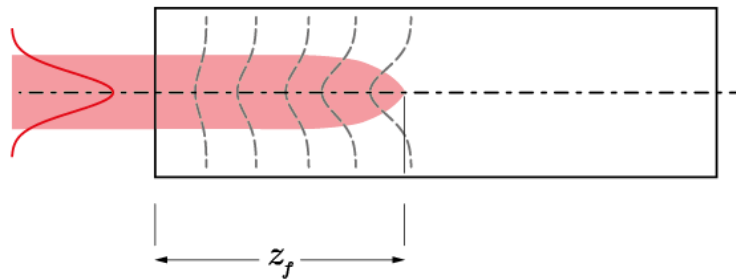


Figure 1.1-8 Sketch showing the distortion of the wavefront and self-focusing of a laser beam in a nonlinear medium (from [7]).

In fact, in self-focusing, the material acts as if it were a positive lens, causing the beam to come to a focus within the material. This phenomenon is also widely known as optical Kerr effect and this kind of nonlinearity is often referred to as Kerr nonlinearity. The self-focusing effect is an accumulative effect and can lead, without the presence of other saturating effects, to a catastrophic collapse of the beam on itself. Obviously, it is expected that the self-focusing length would depend on the input beam power P_{in} . Self-focusing can dominate the diffraction and result in the collapse of the beam only if the P_{in} exceeds a critical threshold [5]:

$$P_{cr} = \frac{3.72\lambda_0^2}{8\pi n_0 n_2} \quad (1.1-49)$$

This expression for the critical power can be simply derived by considering *self-trapping* wherein the effects of the diffraction and self-focusing are balanced [4, 8]. The threshold power of self-focusing given by Eq. (1.1-49) is valid for a specific beam shape (Townes beam) for which the diffraction and self-focusing are balanced. Beams with other shapes will undergo collapse when their power exceeds a threshold, which is usually larger than the one given by Eq. (1.1-49) [9]. For instance, for a Gaussian beam the factor 3.72 should be replaced with 3.77 [5].

The self-focusing distance until collapse, z_f , for non-paraxial propagation is numerically approximated as [5, 10, 11]:

$$z_f = \frac{0.367z_0}{\sqrt{[(P_{in} / P_{cr})^{1/2} - 0.852]^2 - 0.0219}} \quad (1.1-50)$$

where z_0 is the Rayleigh length (Eq. (1.1-7)). Equation (1.1-50) is valid for moderate input powers in purely Kerr media. [11].

1.1.7 Self-phase modulation

Intensity-dependent nonlinear refractive index given by Eq. (1.1-47) has not only spatial effects on the propagating intense beam but also temporal effects since the temporal variations of the intensity causes temporal changes in the refractive index. For instance, for an intense laser pulse with a Gaussian temporal profile, the refractive index for the central part of the pulse will be higher than the periphery. The propagation through a length z results in a phase given by:

$$\varphi = kz - \omega_0 t = \frac{2\pi}{\lambda_0} n(I)z - \omega_0 t = \frac{2\pi}{\lambda_0} [n_0 + n_2 I(t)]z - \omega_0 t \quad (1.1-51)$$

where ω_0 and λ_0 are the central carrier angular frequency and central wavelength, respectively. The total phase described by Eq. Introduction can be split into the linear and nonlinear phases $\varphi = \varphi_L + \varphi_{NL}$ where

$$\begin{aligned}\varphi_L &= \frac{2\pi n_0}{\lambda_0} z - \omega_0 t \\ \varphi_{NL} &= \frac{2\pi}{\lambda_0} z n_2 I(t)\end{aligned}\tag{1.1-52}$$

Therefore, the instantaneous frequency that is the rate at which the total phase of electric field changes with time, given by $\omega_i = -d\varphi / dt$, for a Gaussian temporal intensity profile $I = I_0 \exp[-2(t/a)^2]$, where a is proportional to the pulse duration depending on the chosen criterion given by Eq.(1.1-12), is found as:

$$\omega_i(t) = \omega_0 + \delta\omega = \omega_0 + \frac{8\pi}{\lambda_0 a^2} n_2 z t I_0 e^{-2(t/a)^2}\tag{1.1-53}$$

where $\delta\omega$, which is time dependent, is the nonlinear angular frequency shift. In materials with $n_2 > 0$ the central part of a Gaussian pulse, will encounter larger refractive index and hence will be retarded and consequently a red shift in the leading part and a blue shift in the trailing part of the pulse will occur. In Figure 1.1-9(a) is depicted the nonlinear phase acquired by a Gaussian pulse after propagating a distance in a nonlinear medium. Figure 1.1-9(b) illustrates the frequency shift resulted from the nonlinear phase and in Figure 1.1-9(c) are shown the spectral intensity of the same pulse before and after nonlinear propagation. It can be seen that new frequency components are created.

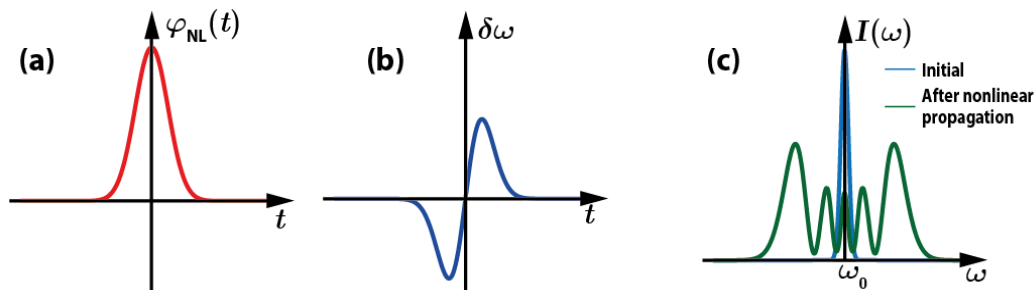


Figure 1.1-9 (a) Nonlinear phase shift, and (b) nonlinear frequency shift of a Gaussian pulse after propagating a distance in a nonlinear medium. (c) Spectral intensity of a Gaussian pulse before and after propagating in the nonlinear medium.

1.1.8 Optical Solitons and light bullets

Optical solitons are localized electromagnetic wavepackets that propagate in nonlinear media without spreading in nonlinear media with dispersion, diffraction or both. Solitons are categorized in three classes: spatial solitons, temporal solitons, and spatiotemporal solitons. Spatial solitons are a result of perfect balance between nonlinear self-focusing and linear diffraction as illustrated in Figure 1.1-10 (see for instance [12] and references therein). Likewise, in temporal solitons the effect of pulse broadening caused by group velocity dispersion (GVD) is precisely counterbalanced by the pulse shortening that can be achieved by self-phase modulation. In spatiotemporal solitons, which are also known as light bullets [13], the effects of dispersion and diffraction are simultaneously balanced by a single nonlinear effect that is the Kerr self-focusing and its temporal counterpart. However, the balance is unstable in more than one dimension because it leads to collapse or breakup [14]. Moreover, when an optical beam is sufficiently intense, additional defocusing mechanisms such as plasma defocusing or higher-order saturation of the nonlinear index compete with Kerr self-focusing [5]. Thus, if the precise balance between these effects is held, stable solitons can be achieved.

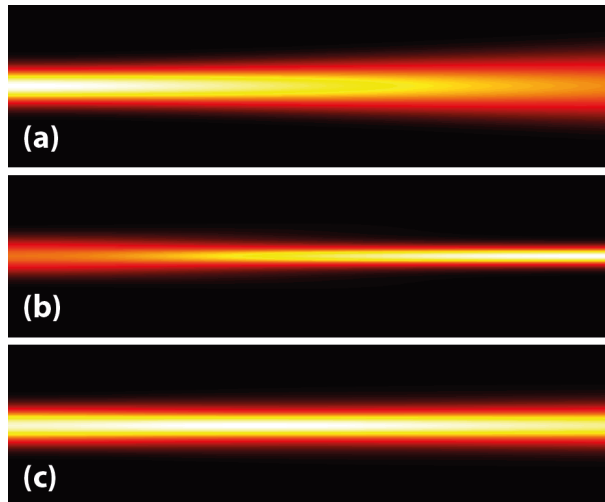


Figure 1.1-10 Schematic showing the spatial beam profiles for (a) beam self-focusing, (b) normal beam diffraction, and (c) soliton propagation.

In the case of spatiotemporal solitons, though the original idea was proposed about two decades ago [13], they have not been observed experimentally yet. Modulational instability that can occur in one or several dimensions is a major limiting parameter for the generation of these

solitons [6]. Another limiting parameter is energy dissipation through nonlinear absorption along the propagation.

Many investigations have been made on the possibility of creating stable light bullets by introducing different mechanisms such as higher order dispersion [15], competing higher order [16] or saturating nonlinearities [17] and filamentation [18]. For discrete light bullets introducing a periodic waveguide configuration has been also suggested for stabilization [19] and more recently it has been shown that filamentation in a proper periodic lattice can lead to generation of intense light bullets [20].

On the other hand, in the linear regime several non-spreading solutions have been demonstrated, such as Bessel [21], Mathieu [22] and Airy beams [23] in the spatial domain. These non-spreading beams however, though propagate without diffraction, do not resemble solitons since their formation does not rely on the competing of nonlinear focusing mechanism and diffraction. Also, in the spatiotemporal domain linear light bullets such as X-waves [24] and O-waves [25] for normal and anomalous dispersions respectively have been demonstrated. These light bullets demand a precise equalization of dispersion and diffraction lengths for their formation. However, owing to the non-spreading behavior of the Airy function, recently it has been shown that by combining a spatial non-diffracting beam with an Airy pulse in time, robust linear light bullets can be formed. Chong *et al.*, [26] have demonstrated the formation of Bessel-Airy light bullets in the linear regime and we have demonstrated the formation of Airy³ light bullets that are Airy wave packets in all spatial and temporal dimensions [27].

1.1.9 Photoionization and Plasma formation

The typical energy gap in transparent media is of the order of few electron volts. Hence, a photon of visible light does not have enough energy for direct excitation of an electron in these media. However, when the light field is strong or equivalently the intensity is very high, photoionization can take place through nonlinear mechanisms. In this case, depending on the laser frequency and intensity there are two different regimes of photoionization, multiphoton ionization regime, and tunneling.

For higher laser frequencies (less than frequencies that would result in single photon absorption), the dominant nonlinear ionization mechanism is the multiphoton ionization (MPI). As illustrated in Figure 1.1-11(a) in the MPI, an electron simultaneously absorbs several photons

and as a result, it is prompted from the valance band to the conduction band. Considering a single photon energy as $\hbar\omega_0$, the MPI will take place when $K\hbar\omega_0 > E_g$. In this case, the process is referred to as K photon absorption and the MPI rate scales as I^K .

For relatively lower frequencies but higher intensities, the Coulomb potential barrier is suppressed in a way that the bound electron can tunnel through the short barrier and becomes free, as depicted in Figure 1.1-11(b).

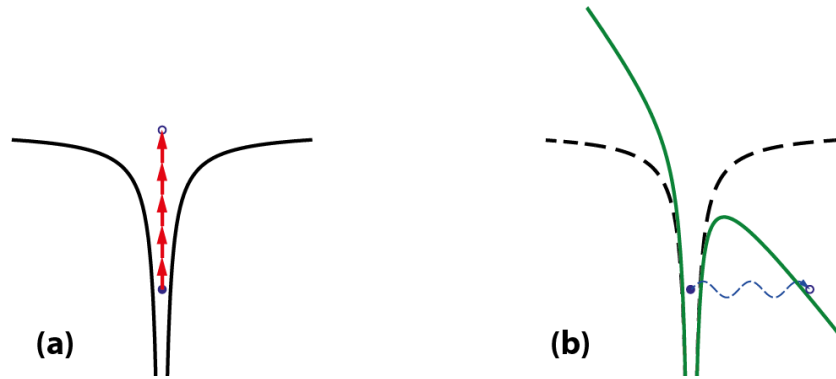


Figure 1.1-11 Photoionization mechanisms. (a) Multiphoton ionization (MPI) and (b) tunnel ionization.

1.1.10 Plasma defocusing and plasma absorption

Photoionization of the propagation medium by the strong laser field results in the formation of a plasma, that in turn results in a local reduction of refractive index [5, 28], according to

$$n \simeq n_0 - \frac{\rho(r,t)}{2\rho_c} \quad (1.1-54)$$

where $\rho(r,t)$ is the density of free electrons and $\rho_c \equiv \epsilon_0 m_e \omega_0^2 / e^2$ denotes the value of the critical plasma density above which the plasma becomes opaque (m_e and e denote the electron mass and charge, respectively). The reduction in the refractive index acts as a negative lens that defocuses the beam and therefore prevents the collapse.

On the other hand, free electrons generated through MPI or tunnel ionization can be further accelerated by the electric field of the remaining part of the pulse in an inverse Bremsstrahlung effect (i.e., absorbed photons from the field are converted to kinetic energy of the free electron).

When a free electron acquire enough kinetic energy by linear absorption of m photons in such a way that $m\hbar\omega \geq E_g$, it can ionize another bound electron through impact ionization and if the optical pulse is long enough, this procedure can continue in an avalanche process [29].

Plasma absorption can be formulated by the Drude model [30]. The absorption coefficient is related to the imaginary part of the refractive index. The complex dielectric function $\tilde{\epsilon}$, which according to the Drude model can be expressed by [30, 31]

$$\tilde{\epsilon} = 1 - \omega_p^2 \left[\frac{\tau_c^2}{1 + \omega^2 \tau_c^2} + i \frac{\tau_c^2}{\omega \tau_c (1 + \omega^2 \tau_c^2)} \right] \quad (1-1-55)$$

where τ_c the Drude collision time typically in the femtosecond range in solids depending on the conduction electron energy [29, 31] and $\omega_p = \sqrt{e^2 \rho / \epsilon_0 m_e}$ is the plasma frequency.

1.2 Filamentation and its application

For a beam of ultrashort laser pulses with a peak power above P_{cr} , self-focusing leads to the collapse of the optical pulse in transparent media. However, when the intensity becomes sufficiently high, multiphoton absorption (MPA) attenuates the core of the beam and leads to plasma generation near the collapse location, which defocuses the beam core. As illustrated in Figure 1.2-1, if the beam still carries enough power (above critical), self-focusing occurs again followed by plasma defocusing and so forth. The repetition of this process leads to filamentary propagation over lengths much longer than the corresponding Rayleigh length with intensities clamped at $\sim 10^{13}$ - 10^{14} W/cm² and leaving a low-density plasma channel. This propagation regime is called *filamentation* and it is very complex due to the contribution of various linear and nonlinear effects.

Indeed, the above-given picture (which is known as *self-guiding* or *self-channeling*) is very simplistic and the physical mechanisms leading to filamentary propagation are still under intense investigations by many researchers. To have an overview on almost all the present models for filamentation see Ref. [5] and references therein.

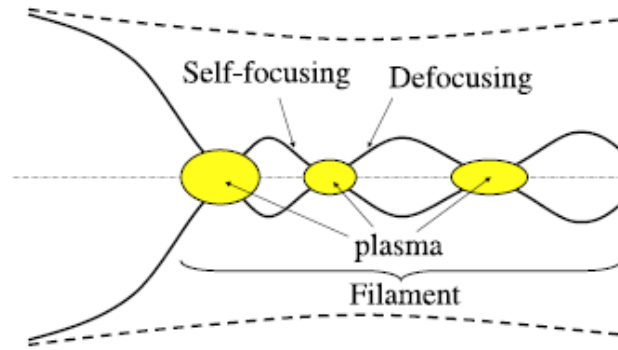


Figure 1.2-1 Schematic representation of focusing-defocusing cycles during filamentary propagation. The solid curves indicate the diameter of the intense core. The filamentation length is the distance covered by these cycles. The dashed line indicates the root mean square radius of the full beam (from [5]).

Recently based on measurements of higher order optical Kerr indices by Loriot *et al.* [32] a new model for filamentation has been proposed [32-34], wherein filamentation in gases is considered to be a result of counterbalancing the self-focusing by the higher-order Kerr effect which, according to their claim, has indices of alternate sign and thus the ionization and plasma contributions are considerably limited. The validity of this model is still under discussion (see for example [35]), since the results found by Loriot *et al.* [32] have not been reproduced by other researchers yet [35-40].

The first observation of filamentary propagation, with average diameter of $\sim 100 \mu\text{m}$, over long propagation distances in air (few meters) was reported by [41]. Shortly after, filamentation of femtosecond laser pulses over much longer propagation distances, up to hundreds of meters and even few km, in air were reported [42, 43].

Moreover, filamentation was also studied in liquids (see for instance, [44]) and transparent solids [45, 46]. Transparent solids have a nonlinear refractive index about three orders of magnitude higher than gases. Consequently, the critical power for self-focusing is in the range of MW comparing to GW range for gases. Therefore, very small energies, of the order of μJ , with ultrashort laser pulses will reach the critical power of self-focusing. Interestingly, the peak intensity in the filament is almost the same as in gases. Typical diameter of filaments in transparent solids can be from a few microns to a few tens of microns and typical length of filaments may change from few hundreds of microns to a few millimeters [45]. The peak electron density in solids reaches typically 10^{18} - 10^{20} cm^{-3} , which is three orders of magnitude

larger than that reached in air but still corresponds to low-density plasma. Furthermore, GVD is more significant in solids than gases and thus plays an important role in filamentation.

1.2.1 Model equation for filamentation

In order to better understand the physics of filamentation of ultrashort laser pulses in different transparent media and create a generic model for this nonlinear propagation regime, several propagation codes have been developed based on various unidirectional propagation equations (see for instance [5, 47-49]). The first numerical simulation in this field started with a minimal model in the form of a nonlinear Schrödinger equation (NLSE) describing the pulse propagation, including only the essential physical parameters. Additional physical effects were added at later stages.

The NLSE, which is analogous to the paraxial wave equation in the nonlinear regime for the envelope of a linearly polarized laser field, in the simplified model that can be obtained directly from the Maxwell equations and adding the associated terms of Kerr self-focusing and plasma defocusing as [5]:

$$\frac{\partial \mathcal{E}}{\partial z} = \frac{i}{2k_0} \Delta_{\perp} \mathcal{E} + ik_0 n_2 |\mathcal{E}|^2 \mathcal{E} - i \frac{k_0}{2n_0} \frac{\rho}{\rho_c} \mathcal{E} \quad (1-2-1)$$

where the first term in the RHS stands for diffraction in the transverse plane ($\Delta_{\perp} \equiv \partial^2 / \partial x^2 + \partial^2 / \partial y^2$). The second term accounts for optical Kerr effect and the last term for plasma defocusing; ρ denotes the plasma density and $\rho_c = \epsilon_0 m_e \omega_0^2 / e^2$ is the critical plasma density above which the plasma becomes opaque. Thus, in this model equation, only the main physical effects are taken into account to be responsible for the self-channeling model of ultrashort laser pulses in air. This equation must be solved simultaneously with the rate equation of the electron density created by photoionization:

$$\frac{\partial \rho}{\partial t} = \sigma_K I^k (\rho_{\text{at}} - \rho) \quad (1.2-2)$$

where it is assumed that the photoionization takes place in the multiphoton regime and $I = |\mathcal{E}|^2$. The quantity σ_K denotes the multiphoton ionization coefficient linked to multiphoton ionization rate $W_{\text{MPI}} = \sigma_K I^K$ involving K photons, where $K \equiv \langle U_i / \hbar\omega_0 + 1 \rangle$, U_i denotes the ionization potential and ρ_{at} denotes the density of neutral atoms.

In this model equation, however, many physical effects that have significant role on the filamentary propagation are neglected, among those are group velocity dispersion, multiphoton absorption, avalanche and contribution of the delayed Kerr effect [50, 51] or Raman effect, to name a few. Therefore, Eq. (1-2-1) can be written in a more generalized form as [5]:

$$\frac{\partial \mathcal{E}}{\partial z} = \frac{i}{2k} \Delta_{\perp} \mathcal{E} - i \frac{k''}{2} \frac{\partial^2 \mathcal{E}}{\partial t^2} + N(|\mathcal{E}|^2, \rho) \mathcal{E} \quad (1.2-3)$$

$$N(|\mathcal{E}|^2, \rho) = N_{\text{Kerr}}(|\mathcal{E}|^2) + N_{\text{Plasma}}(\rho) + N_{\text{MPA}}(|\mathcal{E}|^2) \quad (1.2-4)$$

$$N_{\text{Kerr}}(|\mathcal{E}|^2) = ik_0 n_2 \left[(1 - \alpha) |\mathcal{E}|^2 + \alpha \int_{-\infty}^t \mathcal{R}(t - \tau) |\mathcal{E}|^2 d\tau \right] \quad (1.2-5)$$

$$N_{\text{Plasma}}(\rho) = -\frac{\sigma}{2} (1 + i\omega_0 \tau_c) \rho \quad (1.2-6)$$

$$N_{\text{MPA}}(|\mathcal{E}|^2) = -\frac{\beta_K}{2} |\mathcal{E}|^{2K-2} \left[1 - \frac{\rho}{\rho_{\text{at}}} \right] \quad (1.2-7)$$

coupled with the rate equation of the free electron density

$$\frac{\partial \rho}{\partial t} = \sigma_K |\mathcal{E}|^{2K} (\rho_{\text{at}} - \rho) + \frac{\sigma}{U_i} \rho |\mathcal{E}|^2 - a\rho^2 \quad (1.2-8)$$

The second term on the RHS of (1.2-3) accounts for GVD with coefficient $k'' \equiv \partial^2 k / \partial \omega^2|_{\omega_0}$ and the last term accounts for nonlinearity induced by nonlinear Kerr effect, plasma and multiphoton

absorption MPA. The Kerr term (Eq. (1.2-5)) is split into an instantaneous component due to the electronic response in the polarization and a delayed component, of fraction α , due to stimulated molecular Raman scattering [50]. The function $\mathcal{R}(t)$ denotes the molecular response [50]. The plasma term Eq. (1.2-7) accounts for plasma absorption (real part) and plasma defocusing (imaginary part). The cross-section σ of inverse Bremsstrahlung follows the Drude model and is given by

$$\sigma = \frac{k_0}{n_0 \rho_c} \frac{\omega_0 \tau_c}{1 + \omega_0^2 \tau_c^2} \quad (1.2-9)$$

where τ_c is the electron collision time. In air, $\tau_c = 350$ fs and $\sigma = 5.1 \times 10^{-18} \text{cm}^2$ [52]. Therefore, $\tau_c \gg \omega_0^{-1}$ and in this limit, the defocusing term can be expressed as a function of the critical plasma density as Eq. (1-2-1) $\sigma \omega_0 \tau_c \rho \simeq k_0 \rho / n_0 \rho_c$. The MPA term in Eq. (1.2-7) accounts for energy absorption due to multiphoton absorption; the coefficient $\beta_K = K \hbar \omega_0 \rho_{\text{at}} \sigma_K$ is related to the multiphoton ionization coefficient.

Equation (1.2-8) describes the generation of the plasma by multiphoton ionization with rate of $\sigma_K |\mathcal{E}|^{2K}$ and avalanche with rate $(\sigma / U_i) |\mathcal{E}|^2$. It should be mentioned that for gases and pulse durations less than a few hundreds of femtoseconds, the avalanche ionization can be neglected. The last term on the RHS of Eq.(1.2-8), accounts for plasma recombination mechanisms (electron capture by ion).

1.2.2 Main attributes of light filaments

- **Robustness**

Light filaments can reconstruct themselves even if their central part is blocked [53-55]. This property of light filaments, which is called self-healing [54] or self-reconstruction [55] is because of the energy reservoir around the filaments [56]. Figure 1.2-2 shows numerical and experimental results demonstrating robustness of the light filaments in water. It can be seen that when the filament is blocked, the energy reservoir refills the blocked area and heals the filament.

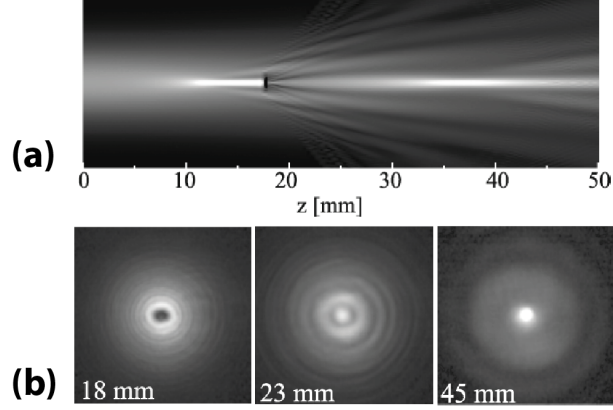


Figure 1.2-2 (a) Numerical result of filament propagation with the core blocked at $z = 18$ cm, and (b) experimental results of self-healing of a filaments in water (from [55]).

The robustness of filaments can be utilized to transfer optical energies in scattering or turbulent media such as foggy or rainy atmosphere [57].

- **Intensity clamping**

A universal feature of light filaments is that the intensity in light filaments is dynamically self-regulated. This effect is referred as intensity clamping. A rough estimation of this clamping intensity can be performed by assuming that the dynamic self-regulation is achieved between Kerr self-focusing and plasma defocusing [5, 41, 58]:

$$n_2 I = \frac{\rho(I)}{2\rho_c} \quad (5.3-10)$$

In air, by using the rough estimate $\rho(I) \sim \sigma_K I^K \rho_{at} t_p$ [5], where ρ_{at} and t_p denote density of neutral atoms and pulse duration, respectively, yields:

$$I \sim \left(\frac{2n_2\rho_c}{\sigma_K t_p \rho_{at}} \right)^{K-1} \quad (5.3-11)$$

For a pulse duration of 100 fs at 800 nm, the clamping intensity is 1.8×10^{13} W/cm².

- **Long range propagation**

As mentioned earlier in this chapter, the filamentation range is very long comparing to the Rayleigh range of the corresponding Gaussian beam. For instance, filamentation length in air ranges from a fraction of meter to hundreds of meters [42] to even kilometers range [59]. During filamentation of ultrashort laser pulses at frequencies far from the resonance absorption of air molecules, the energy losses are minimized since the intensity clamping occurs in just below or very close to the ionization threshold and also the short pulse duration restricts beam attenuation due to occurrence of inverse Bremsstrahlung and avalanche ionization.

- **Spectral broadening**

The spectral broadening, also known as *continuum generation* or *supercontinuum generation* is one of the phenomena accompanying filamentation of optical pulses. It is the result of combined effects of self-phase modulation, self-steepening [60, 61] and ionization of the medium. The spectral broadening depends on the strong reorganization of the temporal shape of the pulse caused by the mentioned effects. An initial pulse centered in the infrared at 800 nm partially converts into a continuum covering the entire visible part of the spectrum when propagating in air. Spectral broadening of a femtosecond laser beam with $\lambda_0 = 800$ nm, $\tau_{\text{FWHM}} = 70$ fs, $P_{\text{in}} = 3$ TW, after filamentation and propagation over 10 m is shown in Figure 1.2-3. The spectral broadening, has been observed up to $5\mu\text{m}$ in the IR [62], with very low intensities. The conversion efficiency from the fundamental to white light depends on the focusing geometry and varies from a few tens of percent for an initially collimated beam to a fraction of the initial energy, for initially focused beam.

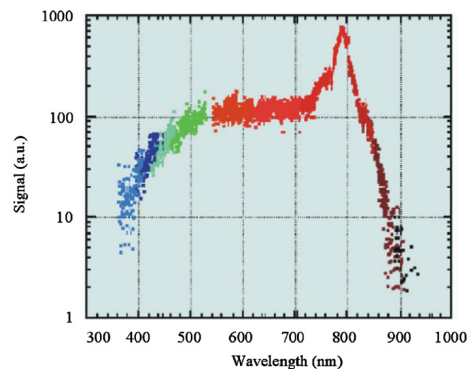


Figure 1.2-3 Spectrum of fs laser beam after propagation over a distance of 10 m in air (from [5]).

- **Conical emission**

The white light generated through filamentation generally consist of a central white part surrounded by a rainbow-like conical emission as shown in Figure 1.2-4. The order of these rings is inverse of typical diffraction with bluer frequencies appearing on the outside rings. This phenomenon is a signature of filamentation. Several mechanisms such as Cerenkov radiation [63, 64], self-phase modulation [65], four-wave mixing [66], X-waves [24, 67] have been proposed to explain this phenomenon but it is not entirely understood yet.

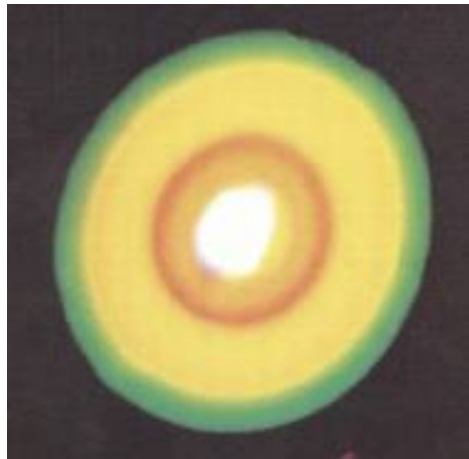


Figure 1.2-4 Photograph of conical emission after 30 m of filamentary propagation in air. The diameter of green ring is ~ 10 cm (from [63]).

- **Pulse self-compression**

Due to different mechanisms that contribute in reshaping optical pulses during nonlinear propagation, filamentation of femtosecond pulses may lead to generation of few cycle optical pulses. For example Couairon *et al.* [68], have shown both numerically and theoretically, that filamentation of 25 fs laser pulses in a gas cell can generate pulses as short as 5 fs.

- **Emission of THz radiation**

Plasma strings generated through filamentation in air emit, besides the wide spectrum covering all visible range, also THz radiation. This phenomenon has attracted a lot of interest because it provides a simple way for the generation strong field THz pulses. A remote coherent THz and sub-THz source is desired for applications such as medical applications and security detection systems.

Coherent sub-THz radiation from filamentation in air was reported by Tzortzakis *et al.* [69]. Intense studies have been performed to enhance and optimize THz emission from filamentation in air (see for instance [70-73]).

- **Multiple filamentation**

When the power of an optical beam is much higher than the critical power for self-focusing, the modulational instability breaks up the beam into a large number of filaments in such a way that each filament carries a power close to the critical [74, 75] (as shown in Figure 1.2-5). The spatial distribution of multiple light filaments that arise from small fluctuations in the initial beam profile intensity is stochastic and they randomly distribute in a transverse plane. Different approaches have been used to control the pattern of multiple filamentation, using, for instance, amplitude masks [76], introducing ellipticity on the input beam [77], inserting a mesh into the beam [78] and applying high astigmatism by tilting the focusing lens [79].

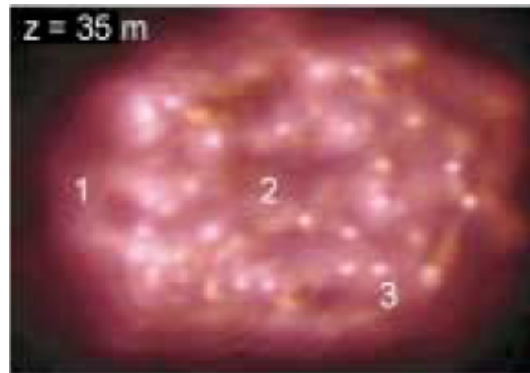


Figure 1.2-5 Multiple filamentation of $700 P_{cr}$ beam (from [75]).

1.2.3 Applications of filamentation

- **White light LIDAR**

Owing to white light generation in the spectral range from UV to IR and long propagation distance, more than 20 km, white light filaments have been used for remote ranging and nonlinear light detection [80]. The light detection and ranging (LIDAR) method, based on atmospheric backscatter signals from actively emitted light pulses has been widely used for atmospheric analysis, such as pollution detection, etc. Classical monochromatic LIDAR can generally detect one substance at a time. In contrast, white-light LIDAR based on white light

emission from long filaments can be used for simultaneous remote analysis of multicomponent gases, composition analysis of aerosols, and detection of atmospheric super-saturation. The schematic of a white-light LIDAR is shown in Figure 1.2-6(a).

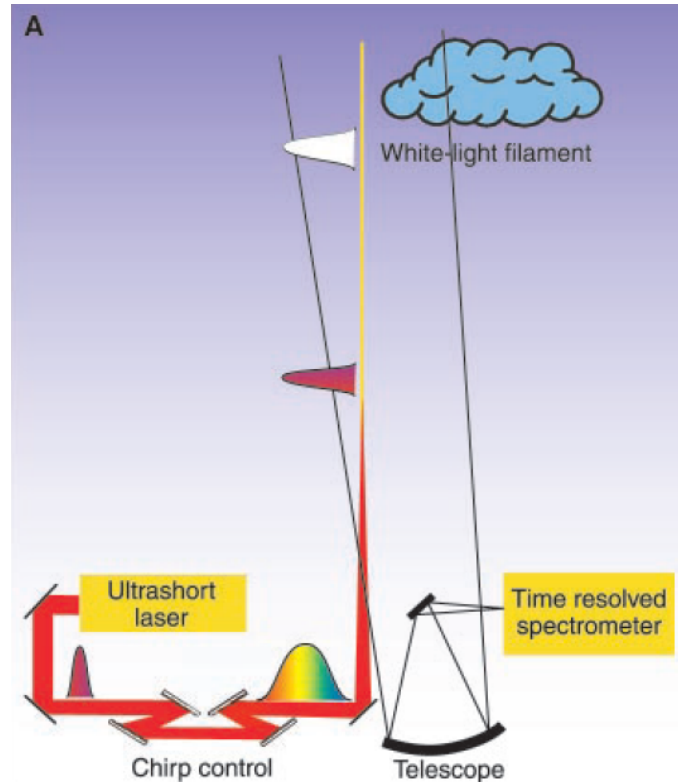


Figure 1.2-6 Schematic of a white-light LIDAR (from [80])

- **Remote LIBS**

For many applications involving material analysis, a proper method should be non-sampling, non-invasive, and *in situ*, and more preferably it should perform a remote analysis. Laser induced breakdown spectroscopy (LIBS) is a fast and accurate method for obtaining qualitative and often quantitative information on the elemental composition of materials. It has been successfully used for the analysis of pigments in paintings, polychromes, pottery, glass, and metal objects.

Filamentation has been implemented in LIBS configurations for remote analyzing of different samples [81-83]. One of the advantages of using filamentation for LIBS analysis is that the laser intensity and beam diameter are self-regulated and therefore complicated optical systems such as those needed for nanosecond remote LIBS are not required. Therefore, the technique can be easily used in a scanning mode and provide rapid mapping of large monuments.

Schematic of a remote LIBS setup utilizing femtosecond UV laser filaments by Tzortzakis *et al.* is shown in Figure 1.2-7.

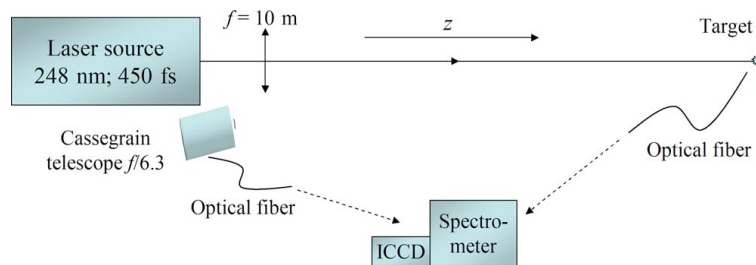


Figure 1.2-7 Experimental setup for local and remote LIBS using femtosecond UV laser filaments (from [83]).

- **Electric discharge triggering and guiding**

Owing to plasma formation over long distances during the filamentation of ultrashort laser pulses, filamentation can be used for guiding and triggering of high-voltage electric discharges [84-86]. Some researchers have even tried to use filamentation for triggering and guiding of lighting (see for instance [87]).

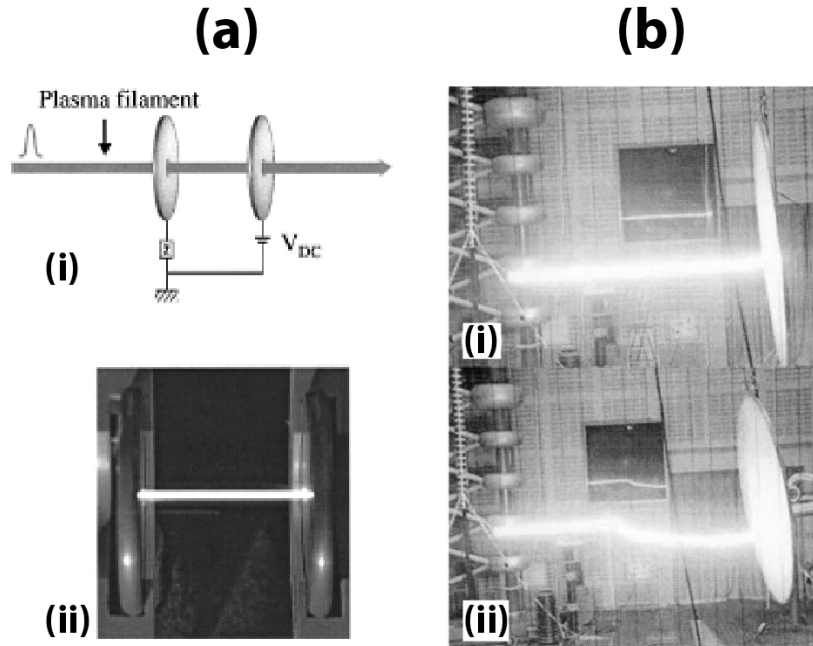


Figure 1.2-8 (a): (i) Experimental configuration of the discharge circuit using a filament, (ii) photograph of a guided discharge between two electrodes; (from [84]). (b): Photographs of a guided discharge (i), and a partially guided discharge (ii); (from [85]).

- **Micro-, Nano-machining in solids**

Filamentation and in general nonlinear propagation of fs laser has been used for micro-,nano-machining in solids. The advantage of this regime of micro-machining in solids is that the nonlinear nature of the absorption confines any induced changes to the focal region and this confinement combined with sample translation or beam scanning, provides the possibility of direct fabrication of complex structures in three dimensions [88]. Figure 1.2-9 shows examples of micromachining in bulk transparent media. Part (a) of this figure shows a microfluidic channel created by micromachining and etching of focal area in bulk fused silica [88] and part (b) shows a periodic structure with a period of $10\ \mu\text{m}$ and the diffraction pattern resulted by illuminating this structure, which is created by direct writing of the structure in the bulk of PMMA [89].

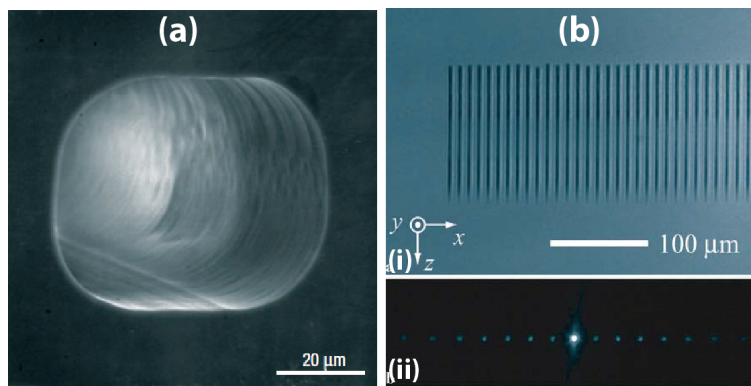


Figure 1.2-9 (a) SEM image of microfluidic channel fabricated by HF-etching fs-micromachined area inside fused silica (from [88]). (b) Image of fabricated periodic structure with period of $10\ \mu\text{m}$ in bulk PMMA and diffraction pattern by illuminated the fabricated structure (from [89]).

Furthermore, nonlinear propagation of fs pulses in transparent solids may lead to interesting features such as nanograting formation in fused silica [90, 91] or void formation in PMMA. These phenomena are discussed in detail in chapter 3.

- **Creation of plasma photonics devices**

Plasma strings created using ultrashort laser pulses can be used to create plasma photonic devices. Plasma mirrors have been introduced and used for improving temporal contrast of intense ultrashort laser pulses [92, 93]. Recently we have demonstrated that filamentation induced plasmas from two perpendicularly crossing beams can form a volume plasma gratings in

air [94]. Figure 1.2-10 shows the diffraction pattern of the white light created by one of the grating-forming beams, diffracted by the formed plasma grating.

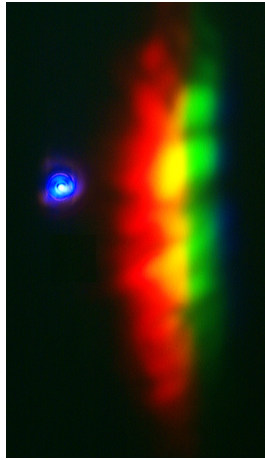


Figure 1.2-10 Diffraction of one of the white light created by one of the grating forming filaments, diffracted by the formed plasma grating. The blue spot is the projection of the second beam.

1.3 Thesis outline

The field of nonlinear propagation and filamentation of femtosecond laser pulses, though not new is still full of unanswered questions in both the understanding of all the involved physical mechanisms as well as in the optimization of various applications.

The role of excited plasma in filamentation is still under debate and there are not many precise diagnostic methods to study the role of plasma in filamentation. Furthermore, though filamentation has been utilized in many applications for micromanipulation of solids, the physics of the interaction and subsequent interesting effects such as nanograting formation in the bulk of fused silica or excitation/relaxation and damage formation in transparent polymers by femtosecond laser pulses has not been well understood yet. Moreover, although it was well known that the filamentation in gases is accompanied with third-harmonic generation, the physics of this phenomenon was not well established.

As filamentation results from the competition of self-action effects, the attributes of the light filaments are self-regulated and cannot be controlled easily. On the other hand, for many applications, an efficient control on the characteristics of filaments such as peak intensity, generated electron density, waist, etc. is needed. So far, controlling the attributes of filamentation was performed by modifying the spatial and temporal characteristics of the initial laser pulse.

The work in this thesis was performed from August 2007 to November 2011, and was focused in investigations of unanswered questions in the filamentation field. The specific topics and problems addressed will be presented in the following chapters.

In chapter 2, diagnostic methods for studying filamentation are investigated and two techniques for measuring electron plasma densities in light filaments are presented in detail. Pump-probe in-line holographic microscopy technique as a powerful and accurate method for retrieving very small perturbations on the wavefront of the probe beam, caused by the filamentation of the pump beam is presented. Plasma conductivity technique, as a simple method for measuring plasma densities in gases and an easy approach to calibrate this method are presented.

Chapter 3 of the thesis is dedicated to filamentation in transparent solids and soft matter. More specifically in this chapter, we present our measurement of the electron plasma densities in fused silica under the conditions, which lead to nanograting formation in the bulk of fused silica glass. Moreover, the dynamics of nonlinear propagation and filamentation of femtosecond laser pulses in the bulk of PMMA, over a wide temporal range will be discussed. Based on our measurements, it is shown that in this medium filamentation is followed by fast excitation of electrons and excited states, which decay quickly and lead to material modification that in turn leads to a pressure wave formation and creation of voids at latter times.

In chapter 4, which covers a few aspects of filamentation in gaseous media, third-harmonic generation and plasma grating formation in air are discussed. It is shown that by introducing a plasma string in the path of a light filament, the third-harmonic generation efficiency can be significantly enhanced. This enhancement is attributed to enhanced third-order nonlinearity of plasma and furthermore a physical model for third-harmonic generation in plasmas is presented. Moreover, it is shown that two intersecting filaments can form a plasma grating in air and the attributes of the grating are characterized.

In chapter 5, filamentation tailoring is studied. Two main approaches are explored. It is shown that the filamentation tailoring can be achieved by introducing a periodic refractive index lattice in the medium or by modifying the input beam characteristics. The results of filamentation tailoring using quasi-periodic plasma lattice are presented and furthermore, it is shown that by using non-diffracting Bessel beams and utilizing a linear technique, the filament attributes can be tuned. The remaining part of this chapter is dedicated to Airy beams. The linear propagation

characteristics of Airy beams are overviewed and an easy approach to generate tunable Airy beams is presented. It is shown that by combining an Airy pulse in time with two-dimensional Airy beam in space, Airy³ light bullets can be generated, which are robust and resist spreading in all spatiotemporal dimensions. Moreover, propagation of Airy beams in different nonlinear regimes is studied.

CHAPTER 2

Development of Diagnostic Tools for Studying Filamentation

2.1 Introduction

As mentioned in the previous chapter, laser generated plasma is playing a significant role in the formation of light filaments, their properties, and their applications. Thus, characterizing the attributes of the filamentation-induced plasma strings is of great importance for understanding the fundamentals of filamentation and accompanied physical effects, manipulation, and control of propagation and optimization and efficient design of the applications.

Due to the very high intensities (10^{13} - 10^{14} W/cm²) in the optical filaments, no physical probe can be placed directly in the propagation path, as it will be permanently damaged. Different techniques have been used to characterize the filamentary propagation and plasma string formation and its attributes.

In this chapter, after an overview of the most widely used techniques, in-line holographic microscopy (i-HOM) is presented in details. It will be shown that i-HOM is one of the most powerful methods to study filamentation. Also, a simple calibration method is presented for the plasma conductivity technique that provides a possibility for quantitative measurements of plasma electron densities in plasma strings, avoiding the complications of the analytical approaches.

2.2 Overview of present methods

In general, all these approaches can be grouped in two categories. The first one includes analytical methods such as interferometric techniques and holographic methods (which will be discussed in the following section) that are capable of spatiotemporally resolving the plasma density distribution. These methods, although accurate, are quite complex in their implementation and cannot be practically used to measure the plasma distribution over an extended filamentation length, which may reach many meters. Moreover, they usually have a

resolving limit that does not allow the study of low-density plasma strings. The second category involves spatiotemporally averaging methods such as plasma conductivity and plasma emission that are much simpler and straightforward in their implementation but difficult and tricky to calibrate for quantitative measurements of the plasma density.

Due to the very small refractive index changes induced by the plasma ($\Delta n \sim 10^{-3}$) as well as the small thickness of plasma strings (few μm to $\sim 100 \mu\text{m}$), the accumulated phase change on a traversing probe beam can be in the order of a few mrad. Therefore, interferometric techniques are commonly used in the laser-plasma interactions with electron densities higher than 10^{17} cm^{-3} . Moreover, techniques like diffractometry and shadowgraphy which use a single intensity profile to reconstruct the amplitude and phase of the perturbed probe wavefront have serious limitations due to the emergence of an artifact well known in holography as twin image. [95, 96]. This artifact deteriorates the quality of the reconstructed wavefront and can lead to ambiguous results. Their deteriorating action is more profound when studying plasma in solids, where both the real and the imaginary parts of the refractive index are perturbed, and in dense plasmas in gases. In an abstract mathematical approach, the twin image problem arises from the fact that in diffractometry (and similar techniques such as shadowgraphy), only the amplitude of the diffracted probe wave and not its phase so the inverse problem is ambiguously posed.

2.2.1 Interferometric Techniques

Perhaps the most widely used interferometric technique in the laser-matter interaction is the spectral interferometry, which is also known as Fourier-domain interferometry (FDI). This method is a linear optical technique for retrieving the phase and the amplitude of an unknown electric field in the femtosecond time domain [97-99]. This technique is widely used in laser-matter interaction experiments, including laser-induced damage [100, 101], laser wakefield particle acceleration [102] etc.

In spectral interferometry, the perturbed laser pulse, which has to be characterized, interferes with a reference pulse in a spectrometer, resulting in spectral fringes of a period that is inversely proportional to the optical path difference between the two pulses and of a contrast that is proportional to the perturbation amplitude. Several schemes have been proposed for spectral interferometry in order to facilitate its application and enhance its sensitivity. Initial schemes were working in multi-shot mode [98] while by using a chirped

probe pulse [97, 103] or a supercontinuum broad pulse [104], the technique can be used in single-shot mode as well.

As an example, the experimental layout of the single-shot spectral interferometry with a chirped probe pulse is shown in Figure 2.2-1. A chirped probe pulse synchronized with the pump pulse is affected by the presence of the pump pulse-induced modification in the focal volume. After passing through an interferometer, the probe beam is imaged using a spectrograph.

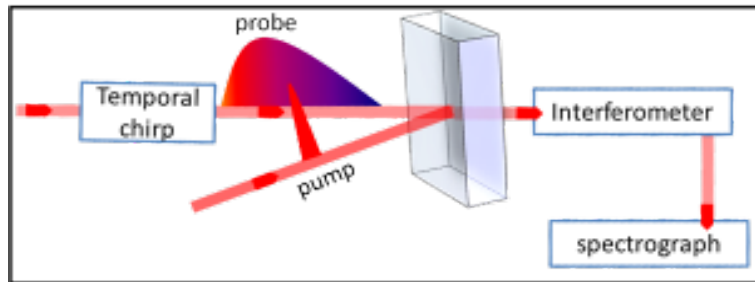


Figure 2.2-1 Experimental layout of single-shot chirped-probe pulse spectral interferometry.

Thus, the phase and amplitude changes imprinted on the wavefront of the probe beam can be spatiotemporally extracted from the contrast and shifts of the interference fringes by comparing the fringe pattern before and after the pump pulse [103]. Once, laser-induced complex refractive index is found it can be correlated to the electron plasma density by using a simple Drude model [5].

2.2.2 Shadowgraphy, diffractometry and holography

The principle of time-resolved optical shadowgraphy and diffractometry is shown in Figure 2.2-2. The laser pulse is split in two parts; one of them creates a filament and the other pulse is used as a probe beam [84, 105]. The probe beam traverses the filament and hence faces a cylindrical phase object. The perturbation caused by the phase object leads to the formation of a set of dark and bright fringes in the far field of the probe beam (Figure 2.2-2). The amplitude and the distribution of the fringes depend on the magnitude and the spatial distribution of changes in the refractive index. By considering the plasma string as a weak diverging lens the refractive index change and the plasma electron density can be estimated. The two methods (shadowgraphy and diffractometry) differentiate on the approach used to estimate the refractive index changes from this fringe pattern. In shadowgraphy [106, 107] a geometric optics approach, using

refraction of rays from the plasma and ignoring wave effects, is used to estimate the changes in the refraction index. On the other hand, in diffractometry, a more accurate wave analysis is followed, and the observed pattern is considered as the far field diffraction pattern of the probe. Although the two techniques have similar accuracy for large phase objects (width $>200 \lambda$), diffractometry is more accurate for smaller object sizes (width $< 100 \lambda$).

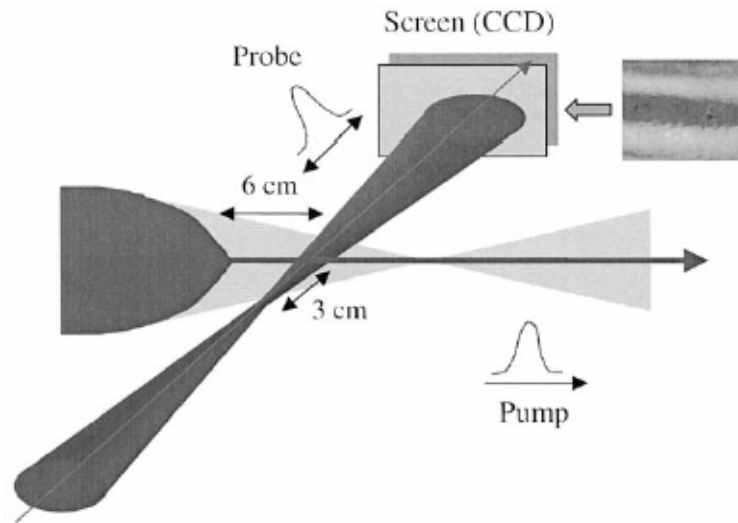


Figure 2.2-2 Experimental scheme for the time-resolved diffractometry. The modified image of the probe beam crossing the filament is recorded at various delays. Also shown is the central dark fringe in the probe far-field image for zero time delay. From [105].

On the other hand, several groups have used similar techniques to diffractometry to create a single diffraction pattern of the probe beam caused by the plasma string [108-113]. These methods are called “holographic techniques”. In these methods the phase change imposed on the probe beam wavefront, caused by the plasma string, is extracted from a single diffraction pattern (hologram) recorded in the Fresnel diffraction range.

2.2.3 Non-optical techniques: Plasma conductivity technique

Plasma conductivity technique has been widely used to study the filamentation of ultrashort laser pulses [84, 114-119]. In the common experimental implementation of this technique, plasma conductivity can be used to reveal the length of plasma strings by measuring the relative electron plasma densities over the filaments [115-117].

In a typical configuration, shown in Figure 2.2-3, a plasma string, created through filamentation, is set up to pass through two rod-shaped electrodes on which a high voltage is applied. The electrodes are connected to an oscilloscope with a known resistance and the whole circuit works in the linear regime.

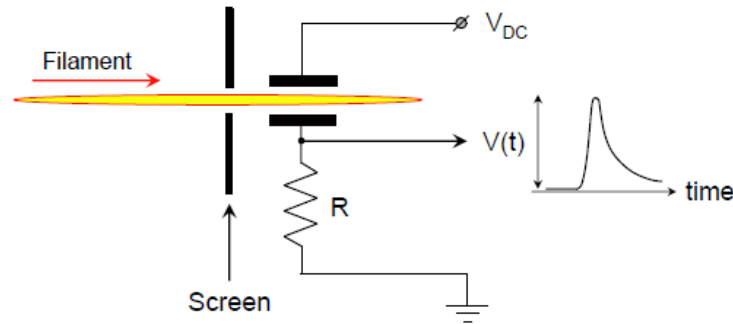


Figure 2.2-3 Experimental scheme of plasma conductivity technique. From [120].

Other techniques that have been used to study filamentation-induced plasma strings include the acoustic wave, fluorescence, and radio frequency generated by the plasma (see [121] and references therein).

2.3 In-line holographic microscopy

In order to adequately address the above-mentioned problems, we have recently developed an accurate and powerful pump-probe in-line holographic microscopy technique [122, 123]. The technique is capable of measuring small transient changes (down to $\sim 10^{-4}$) in both the imaginary and real part of the refractive index of micro-sized volumes. It is based on the use of a bi-telecentric microscope system that allows the accurate capturing of in-line holographic images of the perturbed probe beam. The amplitude and phase of the perturbed probe beam are then accurately retrieved by an iterative wavefront propagation algorithm. The 3D distribution of the real and the imaginary parts of the refractive index perturbation are then revealed using Abel inversion.

In this section, the in-line holographic (i-HOM) is comprehensively studied including a detailed theoretical and experimental analysis. After introducing the principle of the technique, experimental implementation and some of the experimental result are demonstrated, and finally capabilities of the technique to study multiple-filaments (multiple filamentation) are investigated.

2.3.1 Principles of in-line holographic microscopy

The aim of the i-HOM technique is to accurately retrieve the amplitude and phase changes imprinted on the wavefront of a probe beam after the interaction with a pump affected area. As mentioned in the introduction, due to the high intensity of the pump beam, several nonlinear phenomena take place in the focal area, including the optical Kerr effect, multiphoton absorption, ionization, and plasma generation. In general, these effects lead to the perturbation of the refractive index $\Delta\tilde{n} = \Delta n + i\Delta\kappa$, in the real (Δn) and/or the imaginary part ($\Delta\kappa$). Thus, as the probe wavefront propagates through the pump-affected area, the transient changes in the refractive index act as diffracting structures. Figure 2.3-1 shows typical holographic diffraction images (simulated) of a propagating plane probe wavefront after the interaction with a refractive (or absorbing) cylindrical structure. It is clear that in all cases the amplitude of the probe wave is affected by the presence of the structure and that the wavefront is evolving as it propagates. The phase of the probe wavefront follows a similar behavior, so after a short propagation distance the probe wave is perturbed both in amplitude and in phase even in cases where only the real, or only the imaginary part, of the refractive index are perturbed. This complex evolution of the perturbed probe wavefront is a well-known effect of the Fresnel diffraction process and can be exploited to retrieve both its amplitude and phase, only from intensity measurements.

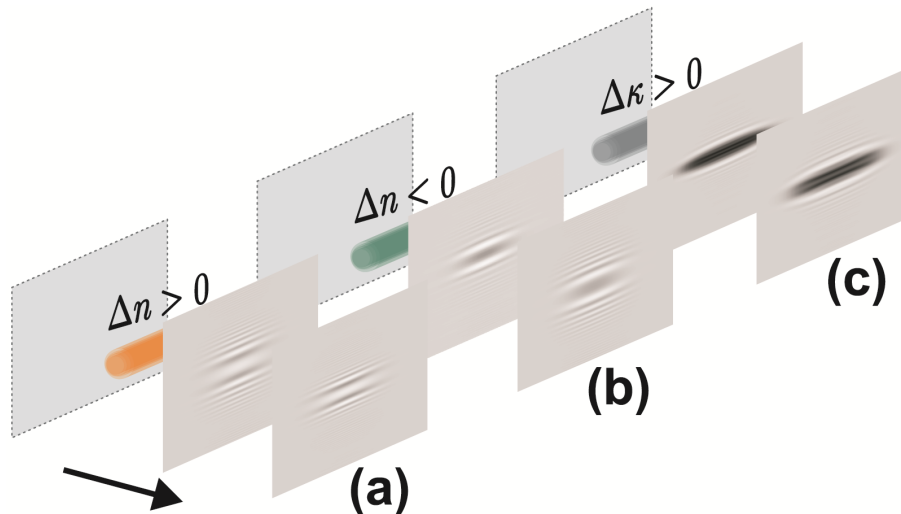


Figure 2.3-1 Typical holographic diffraction images for a probe perturbed by a cylindrical structure with (a) $\Delta n > 0$, ($\Delta\kappa = 0$); (b) $\Delta n < 0$, ($\Delta\kappa = 0$), and (c) $\Delta\kappa \neq 0$, ($\Delta n = 0$).

A very effective way of analyzing the propagation of wavefronts is the concept of the angular spectrum [95, 122, 123]. The various Fourier components of the complex light field $U(x, y; z)$ can be identified as a sum of plane waves traveling in different directions, i.e. different \mathbf{k} vectors, often referred to as angular spectrum. Thus, the field distribution at any other plane can be calculated by adding the contribution of these plane waves taking into account the phase shift they acquire during the propagation up to that point. Therefore, the complex light field at any point can be written as:

$$U(x, y; z) = \iint P_{z_0}(l_x, l_y) e^{i2\pi(z-z_0)\sqrt{1-l_x^2-l_y^2}} e^{i2\pi(xl_x+yl_y)} dl_x dl_y \quad (2.3-1)$$

where x, y, z are the spatial coordinates measured in the probe beam wavelength units (λ); l_x, l_y are the direction cosines of each plane wave and $P_{z_0}(l_x, l_y)$ is the angular spectrum of the complex field distribution at $z = z_0$, and it is given by:

$$P_{z_0}(l_x, l_y) = \iint U(x, y; z_0) e^{-i2\pi(l_x x + l_y y)} dx dy \quad (2.3-2)$$

That is a two-dimensional Fourier transformation of the complex field distribution at $z = z_0$. If both the amplitude and the phase distribution of the light field at a specific position along the propagation are known, the complex light field at any other propagation distance can be numerically calculated using Eqs. (2.3-1) and (2.3-2). However, optical detectors such as CCD cameras are capable of recording only the intensity, and thus the amplitude of the light field. The unknown phase, although not directly measurable, drastically affects the intensity of the light field as the wave propagates. This intensity variation can then be used to retrieve the unknown phase of the wavefront. Therefore, instead of using a single holographic diffraction image one could combine several holographic diffraction images along the wave propagation in order to retrieve the phase along with the amplitude [122-124].

More specifically, a CCD camera located at a plane position z , records the intensity $I(x, y; z)$ and thus the amplitude $|U(x, y; z)| = \sqrt{I(x, y; z)}$ of the diffracted light field. The recorded diffracted light field intensity $I(x, y; z)$ is actually an in-line Gabor hologram [125].

Although one can numerically back propagate a plane wave through this hologram [109], the original wavefront cannot in general be retrieved due to the appearance of a conjugate twin image [95]. This twin image appears in the wavefront reconstruction as an undesirable, conjugate replica of the original object located symmetrically to the hologram. As we have already discussed, it originates from the fact that only the amplitude of the propagating wavefront is measured. We follow an iterative approach in order to overcome this problem and determine both the phase and amplitude of the diffracted light field. A graphical representation of this approach is depicted in Figure 2.3-2.

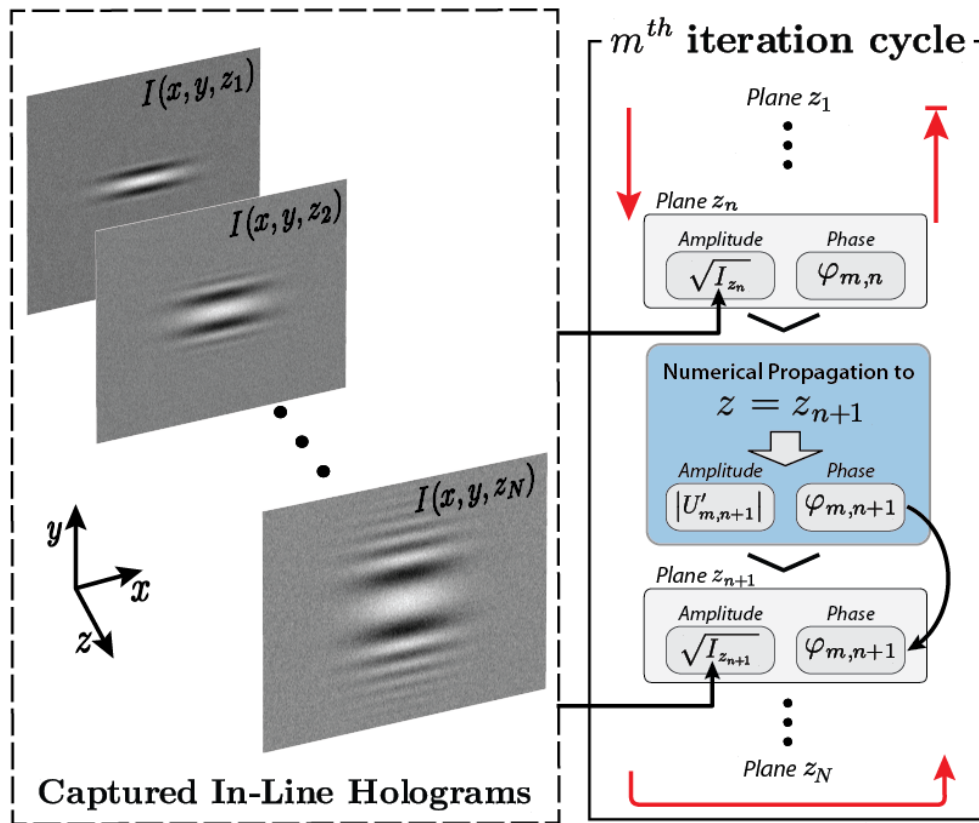


Figure 2.3-2 Schematic representation of the wavefront reconstruction algorithm (see text).

We start by recording a series of in-line holograms $I(x, y; z_i)$, at several positions z_i ($i = 1, 2 \dots N$) along the propagation direction. Starting from a plane at position z_1 , the light field is set as $U(x, y, z_1) = \sqrt{I(x, y; z_1)} \exp[i\varphi_{1,1}(x, y)]$, where $I(x, y; z_1)$ is the recorded intensity pattern (in-line hologram) at the plane located at z_1 and $\varphi_{1,1}(x, y)$ is the initial seed phase

distribution (the first subscript stands for the iteration number while the second one indicates the plane number).

The initial phase distribution can be simply set to a constant value (plane wave) or, to accelerate the convergence of the iterative process, to a distribution closer to the final one, such as the one predicted from the holographic reconstruction of the retrieved in-line holograms. By using Eq. (2.3-1) and Eq. (2.3-2), the complex light field $U'_{1,2}(x, y; z_2)$ at the second plane located at z_2 is numerically estimated. At this point, by combining the experimentally measured intensity $I(x, y; z_2)$ with the numerically estimated phase $\varphi_{1,2}(x, y) = \arg[U'_{1,2}(x, y; z_2)]$ we set a new estimation of the complex light field $U_{1,2}(x, y; z_2) = \sqrt{I(x, y; z_2)} \exp[i\varphi_{1,2}(x, y)]$. We repeat this numerical procedure up to the last plane at position z_N and then we back propagate towards the first plane at position z_1 and this completes the first iteration cycle. The iterations are repeated M times until the calculated complex amplitude $U'_{M,i}(x, y; z_i)$, can adequately predict the experimentally measured intensity $I(x, y; z_i)$. The level of convergence is determined by the merit function:

$$C_m = \sum_{i=1}^N \frac{\iint (|U'_{m,i}(x, y; z_i)| - \sqrt{I(x, y; z_i)})^2 dx dy}{\iint I(x, y; z_i) dx dy} \quad (2.3-3)$$

To explore the capabilities of the wavefront retrieval iterative algorithm, we have first tested its accuracy on simulated sets of in-line holograms. To facilitate the computational effort in these numerical experiments the sets are composed of one-dimensional wavefronts. This wavefront distortion corresponds to the perturbation that would be induced on a plane wave by the presence of a purely refractive object with refractive index distribution $n = n_0 + \Delta n \exp[-4 \cdot \ln 2 \cdot (y/d)^2]$, where n_0 is the refractive index of the surrounding medium, Δn is the refractive index modulation ($\Delta n = -1.5 \times 10^{-2}$) and d is the diameter of the object at FWHM ($d = 10 \mu\text{m}$). The values are chosen so that they correspond to a typical situation of a laser generated plasma string in air. In order to create the input in-line holograms of the iterative retrieval algorithm, the distorted wavefront was numerically calculated at 6

propagation distances $z_{1-6} = 0, 0.1, 0.2, 0.4, 0.8$ and 2 mm and fed into the algorithm. Input in-line holograms are shown in Figure 2.3-3(a). Simulated and retrieved amplitude and phase changes at $z = 0$ and $z = 2$ mm are shown in Figure 2.3-3(b-e). The loose constrain ($C=10^{-3}$, Eq. (2.2-3)), for this simulation was reached after ~ 310 iterations. It is seen that the retrieved wavefront perfectly matches the simulated ones.

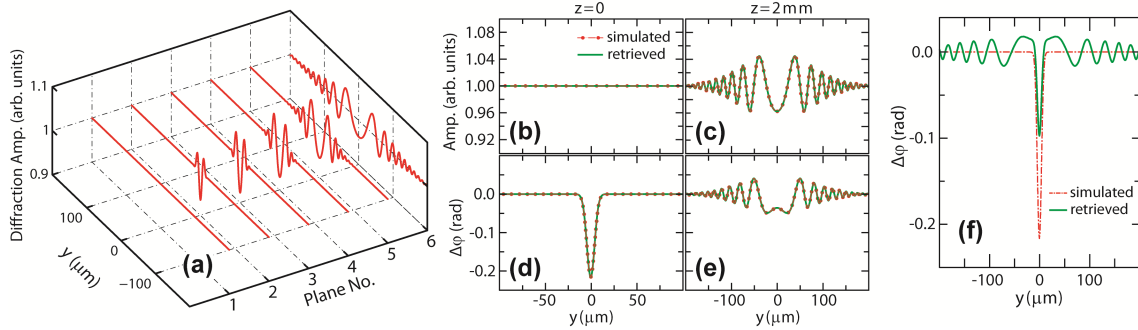


Figure 2.3-3 (a) Simulated input amplitude distributions (in-line holograms) corresponding to the phase object shown in (b) and (d); (b-e) simulated (initial) and retrieved phase and amplitude distributions by using i-HOM technique at two different propagation distances $z = 0$ and $z = 2$ mm. (f) Simulated (initial) and retrieved phase change by using only one diffraction pattern at $z = 2$ mm.

This is a clear demonstration of the ability of this iterative approach to accurately retrieve the phase distribution of an unknown wavefront. Furthermore, for comparison purposes, the phase change corresponding to the same simulated object, retrieved by a single plane diffractometry, using only one diffraction pattern at $z = 2$ mm, is shown in Figure 2.3-3(f); it is obvious that in this case, the retrieved wavefront is significantly distorted due to the twin-image problem.

As a second step, we studied the robustness of the phase retrieval algorithm under the effect of noise. This is typical situation in real experimental images where the background noise cannot be entirely diminished. In this case we followed a similar numerical approach as the former situation ($\Delta n = -1.5 \cdot 10^{-2}$, and $d = 10 \mu\text{m}$) but now in the presence of noise in the in-line holograms. The noise was implemented as a random variation of the calculated in-line hologram amplitude. The noise level was $\sim 2\%$, comparable to the levels usually encountered in experimental images. Figure 2.3-4(a) shows the simulated in-line holograms at different propagation distances $z_{1-6} = 0, 0.1, 0.2, 0.4, 0.8,$ and 2 mm. We have to note here that as in a

typical experiment the noise amplitude does not depend on the propagation distance and thus the signal to noise ratio varies along the propagation. In our simulations since the diffraction amplitude (signal) is very small on the first plane, the signal to noise ratio is close to zero, while for the other planes this ratio varies from minimum (~ 6.5) on the second plane, to maximum (~ 8.8) on the fourth plane.

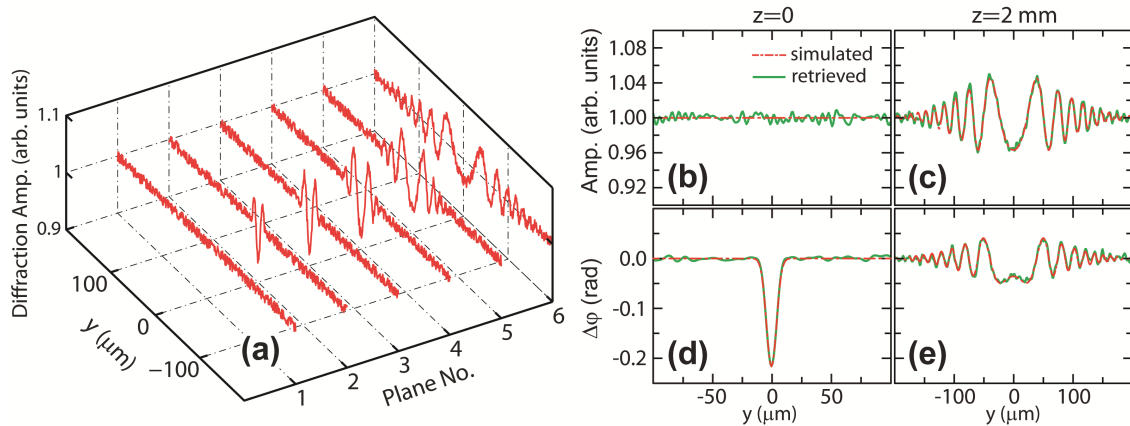


Figure 2.3-4 (a) Simulated input amplitude distributions (in-line holograms) for various propagation distances with the addition of 2% random noise, (b-e) simulated (initial) and retrieved phase and amplitude distributions at two different propagation distances $z = 0$ and $z = 2$ mm.

The simulated and retrieved phase distributions are shown in Figure 2.3-4(b-e). It is clear that the iterative algorithm is still capable of accurately retrieving the amplitude and phase of the wavefront. The process though was now more computationally demanding since the convergence was reached after ~ 475 iterations. This effect is more profound at lower values of signal to noise ratio where convergence is reached after a higher number of iterations. Furthermore, the noise spectral distribution can affect the phase retrieval accuracy and required computational effort.

2.3.2 Experimental Implementation

As demonstrated in the previous section using, instead of one, a number of in-line holographic images it is possible to accurately retrieve the phase distribution of a perturbed wavefront. To implement this method experimentally one has to be able to capture in-line holograms along the propagation of the probe beam. The useful regime lies from just after the interaction area up to the lower boundary of the far-field Fraunhofer diffraction region since from thereon the wavefront experiences a self-similar expansion with no variation in the intensity distribution. A

useful quantitative criterion is the Fresnel number defined as $F \approx d^2 / z$, where d is the diameter of the diffracting object and z is the propagation distance both measured in wavelength units (λ). Under quite loose constraints we can assume that the lower boundary of the Fraunhofer diffraction region is at $F \cong 0.1$. Taking into account that typical sizes of diffracting objects under study (i.e. plasma strings) range from 10 μm to 100 μm the useful measurement region is restricted to 0.8 mm and 80 mm respectively (for $\lambda = 800$ nm). In-line holograms retrieved beyond this region can still be used in the iterative algorithm but in combination with in-line holograms recorded inside this region.

The first and straightforward solution of the direct projection of the in-line holograms onto the sensor of a CCD camera has several restrictions. The working distance, defined by the useful range depends on the size of the object under study, and sometimes is so small that it is very difficult to access it, for example in a bulk medium like glass. Furthermore, the typical CCD pixel size is in some cases comparable to the object size deteriorating the retrieval quality while the finite dimension of the CCD sensor sets a limit on the numerical aperture.

Furthermore, the sensor has to be displaced over a considerable distance along the z -axis in order to acquire a sufficient number of holograms. To resolve these issues the in-line holographic images must be recorded remotely. A typical microscope imaging system, although overcomes the numerical aperture limitations, has some serious experimental complications. Using the concept of the angular spectrum, an imaging system will remotely access the holographic planes only if the angular spectrum is preserved during the imaging process. Thus, in order to preserve the angular spectrum the imaging system should simply fulfill the following condition: a plane wave entering it should exit as a plane wave [95]. Unfortunately, in conventional optical microscope systems the angular spectrum is not preserved. As shown in Figure 2.3-5(a), the plane waves $P_{z_0}(l_x, l_y)$ of the angular spectrum entering the microscope system are in general transformed into spherical waves in the image area and the angular spectrum is disturbed. In this case Eqs. (2.3-1) and (2.3-2) cannot be directly used to analyze and reconstruct the original wavefront. In other words, the image remotely recorded on the CCD sensor will not be a scaled replica of the original in-line hologram. Likewise, the magnification in such an optical system depends on the position of the imaging plane. On the other hand, a bi-telecentric optical system preserves the angular spectrum as shown in Figure 2.3-5(b) and thus the plane

waves entering the system exit as plane waves. An optical system is bi-telecentric when its entrance and exit pupils are located at infinity. Typically, any telescopic system (such as a $4-f$ system) fulfills this condition. This results in an image that is a magnified replica of the original in-line hologram while the magnification factor is constant across the whole image zone.

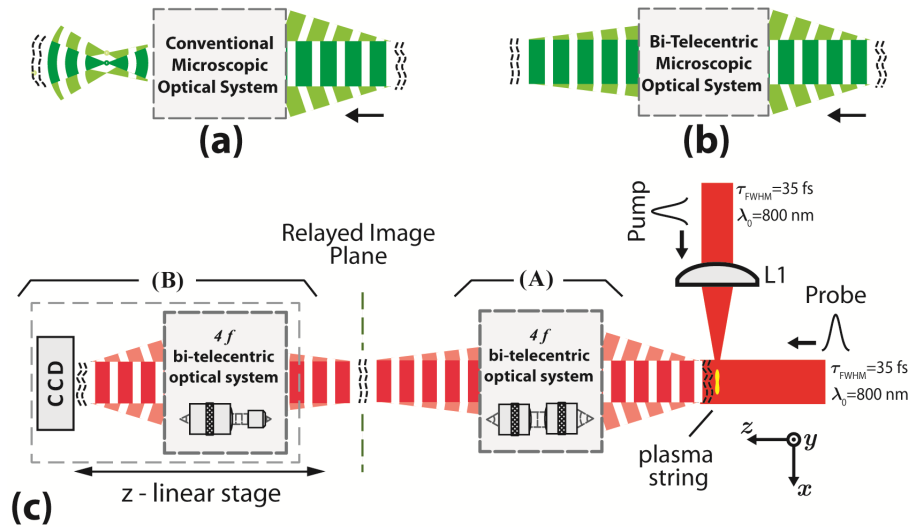


Figure 2.3-5 (a) Imaging in a typical microscope system. Plane waves are transformed to spherical waves. (b) Imaging using a bi-telecentric optical system; Plane waves are still plane after exiting the system. (c) Experimental setup of the pump-probe in-line holographic microscopy utilizing a cascade of bi-telecentric optical system.

We follow a bi-telecentric microscopic method [122] to preserve the angular spectrum while overcoming the above-mentioned limitations (numerical aperture, working distance, resolution, etc.). As shown in Figure 2.3-5(c), the experimental setup is composed of a cascade of two $4-f$ systems. The first one acts as a relaying system (part A, in Fig. Figure 2.3-5(c)) and is consisted of a pair of high-quality photographic lenses. This first bi-telecentric system provides a sufficiently long working distance ($\sim 50 \text{ mm}$). The second $4-f$ system (part B in Figure 2.3-5(c)) is also bi-telecentric and consists of a microscopic objective lens and a high quality zoom photographic lens. The second subsystem can freely move along the z -axis, while the magnification is independent of the propagation distance z . In this way, the angular spectrum is preserved and the outcome is a spatially magnified image of a conjugate plane in the object area. In this case, Eq. (2.3-1) can be rewritten as [122, 123]:

$$U(x, y; \Delta z) = \iint_{NA} P_{z_o}(l_x, l_y) e^{i2\pi\Delta z\sqrt{1-l_x^2-l_y^2}} e^{i2\pi(l_x x + l_y y)} dl_x dl_y \quad (2.3-4)$$

with

$$x = \frac{1}{M_{tot}} x', \quad y = \frac{1}{M_{tot}} y', \quad l_x = M_{tot} l'_x, \quad l_y = M_{tot} l'_y, \quad \Delta z = \frac{(z' - z'_o)}{(M_1)^2}$$

where x, y, z are the spatial coordinates in the object region; x', y', z' are the spatial coordinates in the image region (CCD) measured in the probe beam wavelength (λ) units, l'_x and l'_y are direction cosines as they are transformed by the imaging system, NA refers to the numerical aperture of the optical system and practically limits the collected angular spectrum, $M_{tot.}$ is the total transverse magnification of the imaging system and M_1 is the transverse magnification of the first 4- f system. It can be clearly seen that Eq. (2.3-4) is very similar to Eq. (2.3-1) except that a displacement $\Delta z'$ is equivalent to a smaller displacement $\Delta z = \Delta z' / M_1^2$ in the object region. This can be beneficial from the experimental point of view since it provides a higher accuracy in determining the spacing between in-line holographic planes. In summary, this bi-telecentric microscopic system provides the possibility of having wide view high-resolution images ($\sim 1.5\mu\text{m}$) of any holographic plane in the object area.

The experimental setup is composed of a standard pump-probe setup and the in-line holographic microscope system. The pulsed laser beam (35 fs at $\lambda=800$ nm) is split in two arms in a pump-probe setup as shown in Figure 2.3-5(c). The pump beam is focused by a converging lens (L1: $f=300$ mm, 0.042 NA) and the collimated probe beam is traversing the focal region of the pump beam at 90° . The focal region (filamentation region) of the pump beam is imaged with the in-line holographic microscopic system. In this case, the total transverse magnification and the magnification of the subsystem A were $M_{tot.} = 1.64$ and $M_1 = 1.42$, respectively. A linear CCD camera (12 bit, 1224×968 pixels) is used to remotely record the in-line holograms (part B in Figure 2.3-5(c)). The holograms at different planes are captured by moving subsystem B in Figure 2.3-5(c) along the z -axis. The experimental system is fully computer automated in such a way that single-shot probe images can be recorded for various delays or for a finite number of

accumulated pump laser pulses (of interest when studying propagation in transparent solids where accumulation effects can be important). The noise level in the captured in-line holograms is reduced by subtracting the beam-free background and pump-induced emissions from the focal region, where filamentation occurs.

2.3.3 Experimental results

In order to study the filamentation of ultrashort laser pulses, a pump beam with pulse energy $E_p=0.45\text{mJ}$, which corresponds to $P=3.9\times P_{cr}$ (for $\lambda=800\text{ nm}$, $P_{cr}=3.3\text{ GW}$ [74]), was focused using an $f = 300\text{ mm}$ lens (0.042 NA) and created a single $\sim 1370\text{ }\mu\text{m}$ long filament in air. The filament length was ~ 9 times longer than the corresponding Rayleigh length ($146\text{ }\mu\text{m}$). Since the low-density plasma string has a long life-time, a few hundreds of picoseconds [105], the delay between the pump and the probe pulses was set at 6 ps , to have a net plasma contribution in the observed index changes. In-line holograms were recorded in four plane positions along the propagation direction of the probe beam, located at $z = 0, 3, 6$ and 9 mm . The position $z = 0$ corresponds to the location of the filament, as identified by imaging the corresponding low intensity plasma emission. Typical images of remotely captured in-line holograms are shown in Figure 2.3-6(a). Due to the elongated shape of plasma filaments in air, the diffraction pattern is practically uniform for a considerable length along the pump propagation (x -axis, Figure 2.3-6(a)). This enabled us to reduce the phase retrieval problem to 1-D by using averaged traces of the diffraction intensity over $\sim 420\text{ }\mu\text{m}$ wide slices along the x -axis.

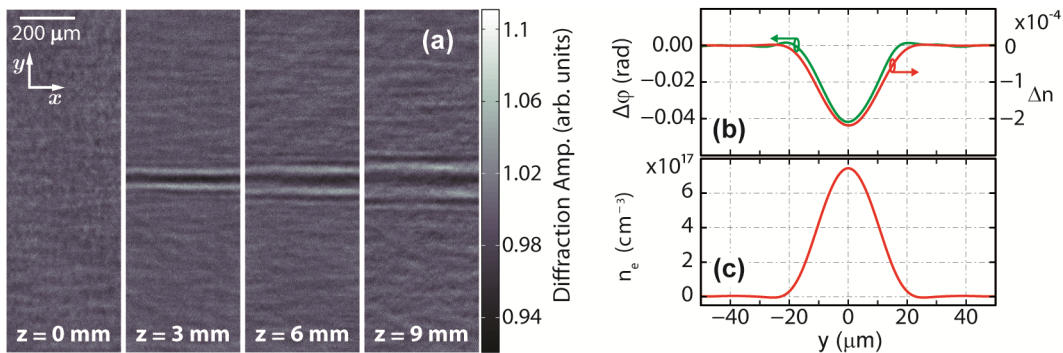


Figure 2.3-6 (a) Experimental in-line holograms remotely captured along the propagation of the probe beam; (b) retrieved phase and corresponding refractive index change (Abel transform), and respective electron density distribution in the plasma string.

This of course is not prerequisite for the iterative phase retrieval algorithm but simply reduces dramatically the computational effort and slightly increases the signal to noise ratio. In the general case that the diffraction pattern is not uniform, a full two-dimensional analysis has to be performed, as we will show below. The loose constrain for the iterative retrieval algorithm was set to $C = 10^{-3}$ (Eq. (2.3-3)) while convergence was succeeded after ~ 1000 iterations. The retrieved phase distribution of the perturbed probe beam is shown in Figure 2.3-6(b) while the corresponding amplitude distribution (not shown) is flat. The refractive index distribution, shown in Figure 2.3-6(b) that caused this perturbation is recovered by using Abel inversion [122, 126]. Likewise, the change in the refractive index can in turn be correlated to the plasma density distribution using a simple Drude model [5] (see also Section 1.1). In this case, the free electron density is analogous to the refractive index distribution: $n_e = -2n_{cr} \cdot \Delta n$ where $n_{cr} = 1.7 \times 10^{21} \text{ cm}^{-3}$ is the critical plasma density in air, for 800 nm probe beam. The corresponding electron density distribution is shown in Figure 2.3-6(c). These results are indicative of the power of the i-HOM technique. Through a series of diffraction images, the refractive index distribution, and the plasma density distribution of a $\sim 22 \text{ }\mu\text{m}$ wide plasma string in air, with plasma density approximately 10^{17} cm^{-3} , is measured. The peak refractive index change is as low as -2×10^{-4} and it is clearly visible from Figure 2.3-6(b) that the signal to noise ratio is very high.

To clearly demonstrate the capability of the high sensitivity and spatiotemporal resolution capabilities of the i-HOM technique we performed time resolved experiments. In this case the pump beam with energy of $40 \text{ }\mu\text{J}$, which corresponds to $P \cong 0.35 \times P_{cr}$, was focused in air using a lens with $f = 100 \text{ mm}$ (0.06 NA) and created a single $\sim 300 \text{ }\mu\text{m}$ long filament in air. The filament length was ~ 4 times longer the corresponding Rayleigh length ($71 \text{ }\mu\text{m}$). The remotely captured in-line holograms as a function of the probe delay are shown in Figure 2.3-7(a). For each delay, six in-line holograms were captured and the phase and amplitude of the perturbed probe wavefront were retrieved using the iterative retrieval algorithm. The corresponding distribution of the refractive index perturbation is shown in Figure 2.3-7(b) and was retrieved by applying Abel inversion [126] to the wavefront phase. In the filament area, the high intensity of the propagating pulse ignites multiphoton ionization and leads to the generation of plasma that decreases the refractive index. This refractive index drop correlated with the propagating pump

as well as the remaining plasma trail is clearly distinguishable in Figure 2.3-7(b). The refractive index values correspond to peak plasma densities of $2.4 \times 10^{18} \text{ cm}^{-3}$.

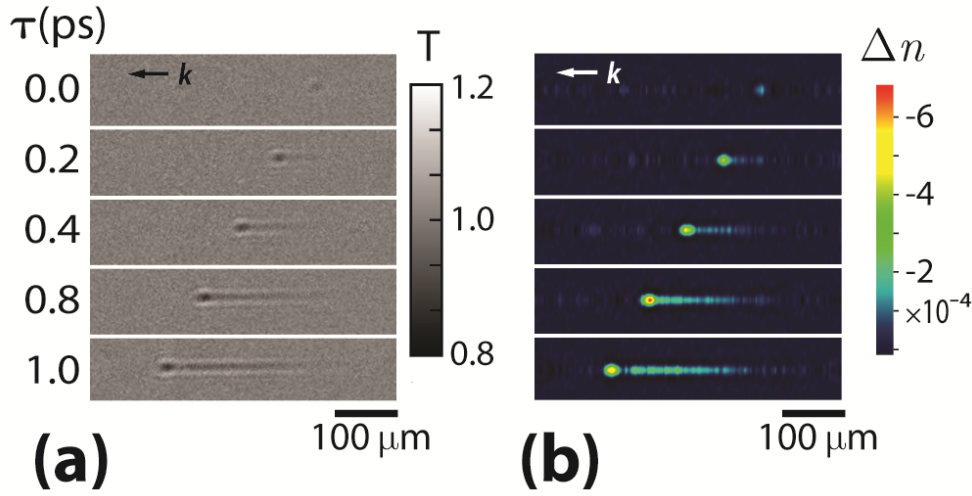


Figure 2.3-7 (a) Experimental in-line holograms of a propagating filament for various pump-probe delays (k denotes the pump wavevector) (b) retrieved refractive index distribution.

The efficiency and the computational load of the iterative reconstruction algorithm depend on the number of in-line holograms used. For this six in-line holograms of a typical short filament in air were recorded. Then, for a constrain constant $C \leq 0.1$, the reconstruction algorithm performance was evaluated using different numbers of input in-line holograms. Figure 2.3-8(a) shows the retrieved phase ($-\Delta\varphi$) as a function of the number of the input in-line holograms. It can be clearly seen that due to the effect of noise, the phase information can be barely retrieved with only two in-line holograms, but the effect of noise is significantly suppressed as we increase the number of in-line holograms. In Figure 2.3-8(b), the number of iterations needed to reach the convergence (under the specified constrain) is shown as a function of the number of in-line holograms. Similarly, more input in-line holograms result in faster convergence of the algorithm.

2.3.4 Investigation of multiple filaments using in-line holographic microscopy

So far we have applied i-HOM to study single filaments, however, for higher laser pulse powers ($> 10 \times P_{cr}$), multiple filamentation occurs. In this regime, modulational instabilities result in the

generation of several light filaments and corresponding plasma strings with a random transverse distribution [74, 75, 127].

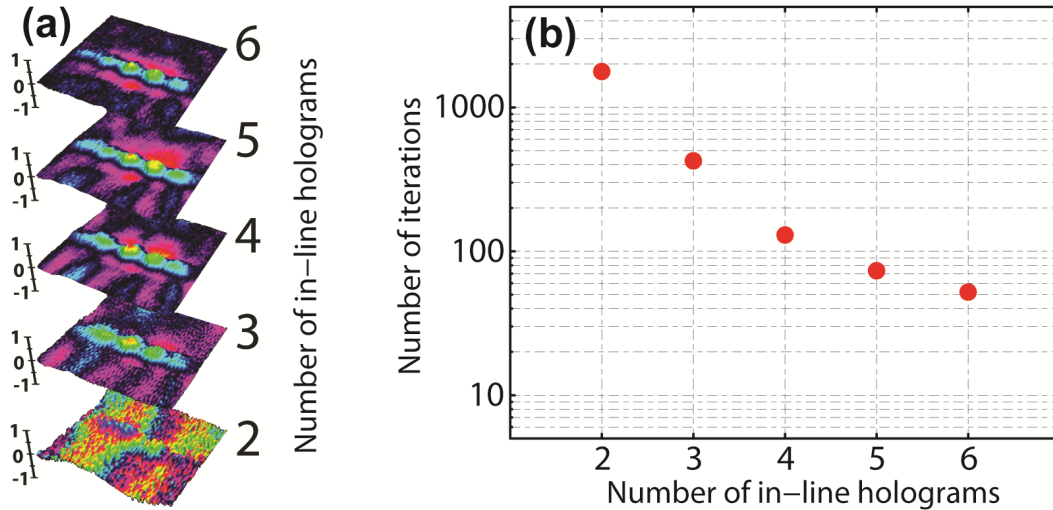


Figure 2.3-8 (a) Retrieved phase information as a function of the number of input in-line holograms. (b) Number of iterations to reach convergence (under the same constrain) versus the number of input in-line holograms.

The stochastic behavior of multiple filamentation is not desirable for some applications wherein a precise localization or shot-to-shot stability of filaments is needed. Different approaches have been used to have control on multiple filamentation. Such methods include, amplitude masks [76], input beam ellipticity [77], introducing a mesh into the beam [78], and applying high astigmatism by tilting the focusing lens [79]. In any case, characterization of organized multiple filamentary structures can be useful for several application as well as optimization of multiple filamentation tailoring.

To examine the potential of i-HOM to characterize complex objects, we studied, using both simulations and experiments, double filamentary structures. In our simulations, two phase objects located on the same plane were representing the double filamentary structures with a refractive index distribution given by:

$$n = n_0 + \frac{1}{2} \Delta n \left[e^{-4 \ln 2 \left(\frac{y-h/2}{d} \right)^2} + e^{-4 \ln 2 \left(\frac{y+h/2}{d} \right)^2} \right] \quad (2.3-5)$$

where n_0 is the refractive index of the surrounding medium, Δn is the refractive index modulation ($\Delta n = -1 \times 10^{-3}$), h is the distance between two objects and d is the diameter of each object ($d = 10 \mu\text{m}$ (FWHM)). Using these values we numerically propagated the known wavefront at six propagation distances $z_{1-6} = 0, 0.1, 0.2, 0.4, 0.8,$ and 1 mm and retrieved the corresponding phase and amplitude. The analysis was repeated for several separation distances, between the two phase objects; $h = 10, 15$ and $20 \mu\text{m}$. The corresponding simulated and retrieved phase change distributions are shown in Figure 2.3-9(a-c), respectively.

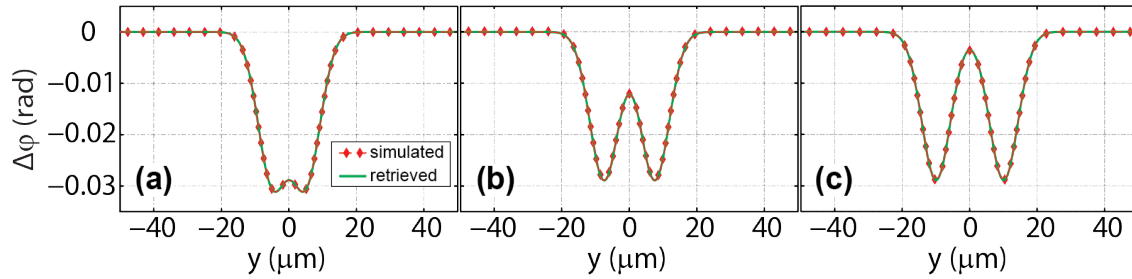


Figure 2.3-9 (a) The simulated and retrieved phase changes, corresponding to two refractive structures, located on the same plane along z -axis and separated by 10 (a), 15 (b) and $20 \mu\text{m}$ (c) along y -axis.

It is clearly seen that the wavefront reconstruction algorithm is capable of distinguishing two different weak phase objects, no matter what the separation distance between them is. However, from the experimental point of view, distinguishing multiple filamentary structures is expected to have a limit because of the stochastic behavior of the multiple filamentation [74].

Experimentally, in order to create a double filamentary structure, the pump beam was split in two parts by using two joint mirrors mounted very close together and with a very small angle. The total pump beam energy was set to 1 mJ and this energy was approximately equally divided between the two parts of the beam, so that each part would create only one filament. The double pump beam was focused with an $f = 300$ mm lens. Using this simple scheme, a double filamentary structure was created with the possibility of controlling the separation between them both along z - and y -axis. First, two filaments were adjusted to lie on the same z position, with different separations along the y -axis. For each separation along y , in-line holograms were remotely captured at $z = 0, 0.5, 1, 1.5, 2,$ and 2.5 mm and then fed into the original wavefront reconstruction algorithm. Typical in-line holograms corresponding to two separation distances of $145 \mu\text{m}$ and $72 \mu\text{m}$ between the filaments are shown in Figure 2.3-10(a-b). Figure 2.3-10(c-d)

show the corresponding retrieved phase distributions. The retrieved amplitude (not shown here) is flat; indicating again that diffracting objects in this case are purely phase objects. The separation distance between the filaments as measured by the phase distribution profiles in Figure 2.3-10(c-d) agree well with independent measurements of burn spot profiles on photographic paper places perpendicularly to the propagation direction of the filaments and exposed to multiple laser shots.

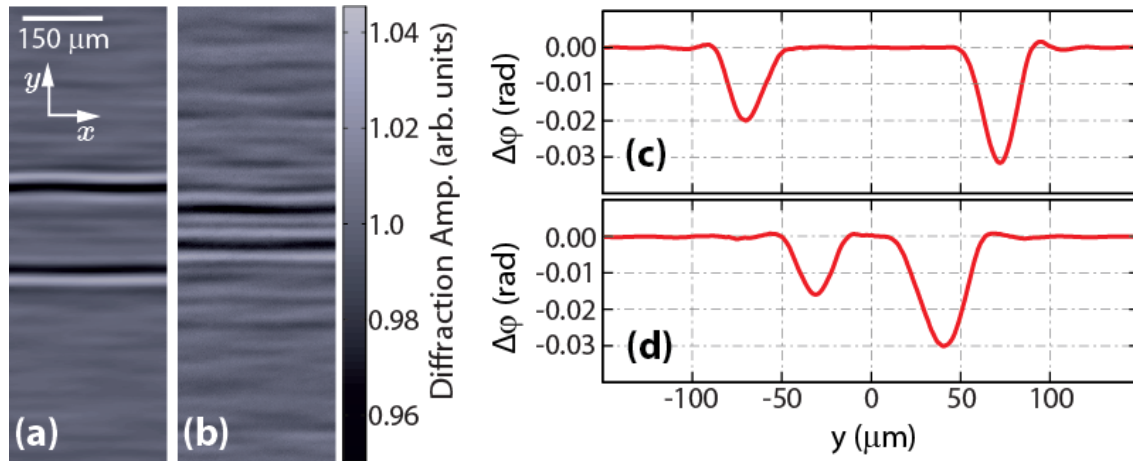


Figure 2.3-10 (a) In-line holograms recorded at $z=1.5$ mm, corresponding to two filaments located on the same plane along the propagation direction of the probe beam, z , separated by ~ 145 μm (a) and ~ 72 μm (b), along the y -axis. (c)-(d) Retrieved phase change profiles corresponding to (a) and (b), respectively.

Furthermore, as it was expected, resolvability of two filaments is practically limited to a separation distance in which the filaments start to dynamically interact between them. Since the interaction between filaments results in complex propagation modes, not reproducible from shot-to-shot, the recorded in-line holograms will be averaged out and the result of the reconstruction algorithm will not be accurate. For the present experimental condition, the minimum separation distance between filaments was ~ 70 μm since below this distance the filaments start to interact.

Finally, we studied a more complicated three-dimensional arrangement by locating the double filamentary structures at two different planes. More specifically in our experiment, the two filaments were separated by ~ 0.5 mm along the propagation direction of the probe beam as shown in Figure 2.3-11.

In-line holograms were captured at the same positions as in the previous experiment and were fed into the wavefront retrieval algorithm.

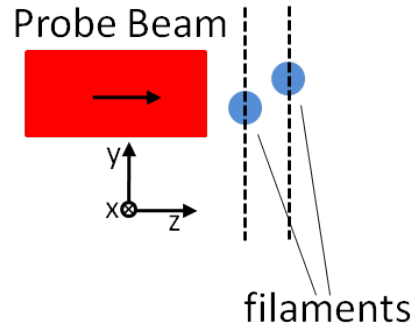


Figure 2.3-11 (a) Two filaments separated along the propagation direction of the probe beam.

To distinguish the two independent plasma strings the retrieved wavefront was numerically propagated from $z = -4$ mm to $z = 4$ mm with a step size of $40 \mu\text{m}$. The phase distribution as a function of the propagation distance is shown in Figure 2.3-12(a). It is clear that phase distribution exhibits a focusing behavior as a function of the propagation distance, z . This is an expected behavior for phase objects and can be used like normal focusing in amplitude objects, to locate their positions along the probe propagation axis. For the filaments (i) and (ii) in Figure 2.3-12(a), normalized phase change distribution along z -axis is shown in Figure 2.3-12(b). These profiles are independently created for each structure by averaging the phase change over six microns around the maximum phase change position in the transverse dimension, y . It can be clearly seen that the maximum phase change positions for each filament is located at a different z position separated by ~ 0.46 mm, which is in good agreement with the distances measured by the burned spot measurements.

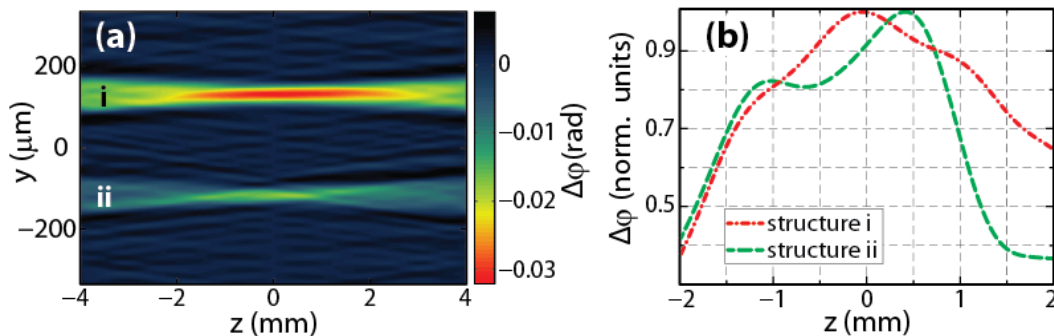


Figure 2.3-12 (a) Phase distribution of the numerically propagated wavefront as a function of the propagation distance z and (b) normalized phase change as a function of propagation distance. The peaks indicated the position of the filaments along the z -axis.

Therefore, the wavefront reconstruction algorithm can indeed distinguish multiple filaments separated along the propagation direction of the probe beam when they are separated enough to avoid interaction between them.

Thus, both by simulations and experiments, the power of the i-HOM method in retrieving very small refractive index changes ($\Delta n \sim 10^{-4}$) caused by the filamentation-induced plasma strings is demonstrated. This estimation does not reflect the ultimate sensitivity of this technique. As it is clear from the simulations, the limit in the sensitivity of the technique is in fact set by the amount of noise, perceived as random intensity variations in the in-line holograms. The effect of noise on the reconstruction algorithm and the role of number of planes on the convergence efficiency were studied as well. Factors that affect the noise level in the reconstruction include the number of in-line holograms used and the actual object shape. In the case of elongated objects (i.e. filaments), the noise can be further reduced by applying 1D averaging and in this case we have shown that we can increase the sensitivity to $\Delta n \sim 10^{-5}$ in the refractive index changes. It is shown that the i-HOM technique can be used to characterize plasma filaments in many different complex spatial configurations with a temporal resolution limited by the probe pulse duration. The full object is revealed using Abel inversion, while the electron density distribution in the plasma string can be calculated using a simple Drude model [Chapter 1].

Nevertheless, this method, though very accurate and powerful, is quite complex in its implementation and cannot be practically used to measure the plasma distribution over an extended filamentation length, which may reach many meters. Therefore, for measuring plasma densities in long plasma filaments, another technique must be used. However, simple techniques such as plasma conductivity technique or plasma emission measurement are only capable of revealing relative plasma density and to have quantitative measurement of electron plasma densities in filaments they must be calibrated, which is not trivial. A simple and at the same time quantitative technique for measuring electron densities would prove very useful for the large scientific community working in this field.

2.4 Calibrated plasma conductivity technique

In this section, after introducing the plasma conductivity technique (PCo) in a specific configuration that is perhaps the easiest to implement, a physical model is presented for calibration of this technique and enrich the PCo technique with the capability of quantitative

electron density measurements [119]. The validity of our approach is confirmed by comparing the calibrated electrical conductivity measurements with the results of the in-line holographic microscopy (i-HOM) which was presented in the previous section.

2.4.1 Experimental setup and physical model

The output of an amplified Ti:Sapphire laser delivering 35 fs laser pulses at a central wavelength of 800 nm with pulse energies up to 30 mJ operating at 50 Hz repetition rate (beam waist of 12.5 mm) was used to create plasma filaments in different focusing geometries. The schematic of the experimental setup is shown in Figure 2.4-1. The laser generated plasma strings were positioned in the area in-between two identical, 1 mm in diameter, metallic cylindrical rods (electrodes) separated by 3 mm. The electrodes were connected to a DC high voltage (1.4 kV) source. Undesired direct illumination of the electrodes by the laser beam was blocked using a Teflon aperture placed in front of them. The emergence of laser-generated plasma between the electrodes in the presence of the external DC electric field leads to a transient current flow in the circuit.

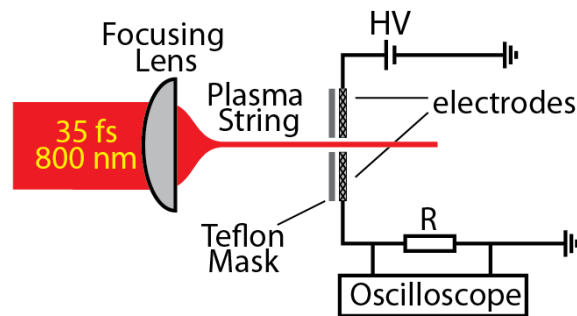


Figure 2.4-1 PCo experimental setup schematic.

This transient current is measured as a voltage drop across a resistance ($R = 8 \text{ k}\Omega$) using a probe connected to an oscilloscope (see Figure 2.4-1). The applied high voltage was chosen in such a way to ensure the linear operation of the circuit, i.e. linear increase of the signal with increased applied voltage. The impedance and capacitance of the oscilloscope were $1 \text{ M}\Omega$ and 16 pF , respectively. It can be easily found that the response time of such a circuit is in the order of $0.1 \text{ }\mu\text{s}$, much longer than the sub-nanosecond lifetime of femtosecond laser generated plasmas in air [105]. A typical signal of such a circuit in the presence of a plasma string is shown in Figure 2.4-2(a).

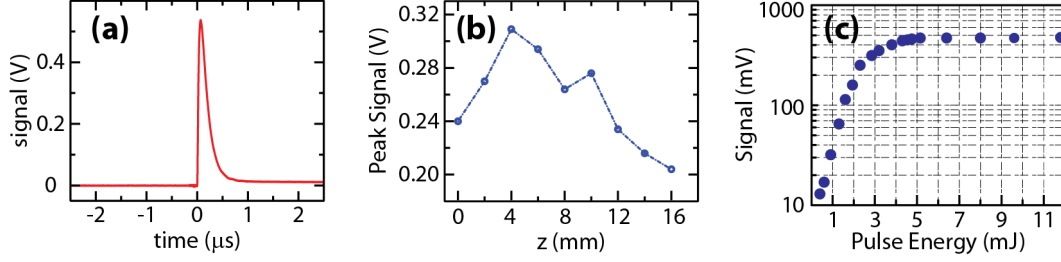


Figure 2.4-2 (a) Typical signal of plasma conductivity (PCo) technique recorded by an oscilloscope, (b) peak signal of PCo along a plasma string created by a focusing the laser pulses by an $f=500$ mm lens, and (c) peak plasma (PCo) signal at the position of maximum plasma fluorescence for different pulse energies ($f=100$ mm).

As already mentioned, without applying any calibration the PCo technique can be used to measure plasma string lengths simply by translating the electrodes along the plasma string. As an example the peak signal of conductivity technique as a function of propagation distance, starting from a point where the plasma fluorescence was visible is shown in Figure 2.4-2(b). In this experiment, an $f=500$ mm lens was used to create the plasma string. Moreover, a typical measured peak signal versus laser pulse energy for the case of a lens with focal length of $f=100$ mm ($\#F \approx 4$) is shown in Figure 2.4-2(c).

A simple physical model will help us understand the mechanism that leads to the transient perturbation and to derive a quantitative relation between the plasma density and the measured current. It is well known that under the action of a strong electrostatic field a charge separation is created between electrons and ions in the plasma, as it is shown in Figure 2.4-3. For each electron-ion pair the induced dipole moment is $\mathbf{p} = q \cdot dz$ where q is the electron charge and dz is the electron-ion separation. Thus, the total induced polarization \mathbf{P} in the plasma volume is

$$\mathbf{P} = \langle n_e \rangle \mathbf{p} = \langle n_e \rangle q \cdot dz \quad (2.4-1)$$

where $\langle n_e \rangle$ is the spatially averaged plasma density. This induced polarization will generate an electric field that will affect the total electric field between the electrodes and under a rather general approach can be approximated as:

$$\mathbf{E}' \propto \mathbf{P} \cdot V_p \Rightarrow \mathbf{E}' \propto \langle n_e \rangle r_p^2 l_p \quad (2.4-2)$$

where V_p is the plasma volume, r_p is the plasma radius and l_p is the plasma length. The electric field generated by this dipole perturbs the total electric field and consequently leads to a voltage drop between the electrodes.

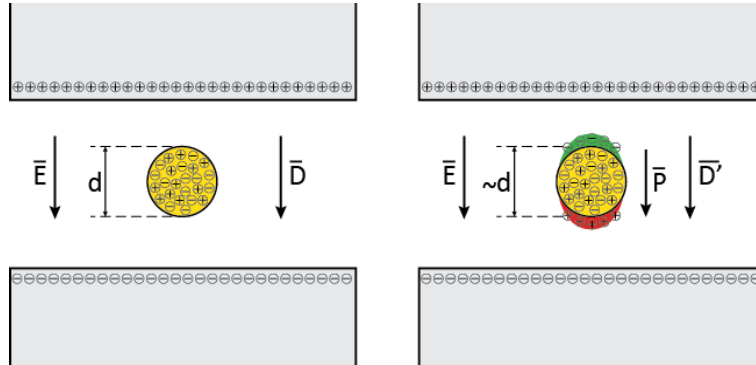


Figure 2.4-3 (a) Schematic of the microscopic model representing the role of plasma dimensions on the conductivity signal; before (left) and after (right) the charge separation due to the external electric field.

Charge trapping in the plasma through recombination eventually stops the process. In response to this perturbation and in order to keep the voltage constant, the HV generator provides extra charges to the electrodes that counter balance the perturbation. This charge flow towards the electrodes creates a transient current I_R that is probed as the voltage drop across the resistance R . Taking into account the response time of the high voltage circuit, this transient current is proportional to the temporal convolution of the plasma induced transient perturbation and the impulse response of the measuring circuit. Numerical simulations, using the plasma decay rates in air and the slow response time of such electrical circuits, show [115] that in the electron density regime up to 10^{17} cm^{-3} there is a linear correlation between the peak electron density and the peak current. However, since the perturbation is related to the induced polarization under the applied HV, its temporal evolution process is even more complex and as we will see in the following our experimental measurements confirm that the proportionality holds, within the experimental error, for even higher electron densities. Under this perspective, the transient current flow through the resistance, and consequently the measured voltage change ΔV is proportional to the initial perturbation:

$$\Delta V = I_R \cdot R \propto \langle n_e \rangle r_p^2 l_p R \quad (2.4-3)$$

The proportionality in Eq. (2.4-3) inhibits the direct estimation of the average electron density of a laser generated plasma string by a single measurement. On the other hand, this technique can be calibrated to provide absolute electron density values if one could use a reference measurement, where both electron density and plasma dimensions are known. Let us assume that a reference voltage change (signal) due to the presence of a plasma string with known dimensions and known electron density is $\Delta V^{ref} \propto \langle n_e^{ref} \rangle (r_p^{ref})^2 l_p^{ref}$. Likewise, the signal from a different plasma string with known dimensions but unknown electron density can be written as $\Delta V \propto \langle n_e \rangle r_p^2 l_p$. Therefore, from the ratio of the two measured signals $\Delta V / \Delta V^{ref}$, the unknown electron density $\langle n_e \rangle$ can be estimated as:

$$\langle n_e \rangle = \left(r_p^{ref} / r_p \right)^2 \left(l_p^{ref} / l_p \right) \left(\Delta V / \Delta V^{ref} \right) \langle n_e^{ref} \rangle \quad (2.4-4)$$

This formula shows that the average electron density of an arbitrary plasma string can be measured if the electron density of a reference plasma string is known. Furthermore, the spatial dimensions of the plasma and more particularly their ratio to the dimensions of the reference plasma should be used as a geometric correction factor to the measured signal ratio. Using this technique the plasma distribution for plasma string lengths shorter than the diameter of the electrodes (<1 mm in our case) cannot be revealed. On the other hand, in extended plasma strings such as those created through filamentation, the longitudinal distribution of the electron density can be measured by translating the electrodes along the propagation direction. The longitudinal spatial resolution is then determined by the diameter of the electrodes. The temporal evolution of the plasma density is practically lost in such a measurement since the measured signal is proportional to the peak value of the plasma density in time.

2.4.2 Experimental results and discussion

Experimentally, plasma filaments were created using the 35 fs laser beam at different input pulse energies and focusing it in air using plano-convex lenses of various focal lengths. In all cases, the electrodes were placed equidistantly from the plasma string at a longitudinal position where the signal was maximized. A typical measured peak signal versus laser pulse energy is shown in Figure 2.4-2(c). The signal increases rapidly as a function of the input energy for energies up to

~2 mJ. This strong, nearly exponential, increase is the result of the increase of the plasma string average electron density and its thickness (see Eq. (2.4-3)). At higher input energies saturation is observed due to intensity clamping in the filament [128].

As already mentioned above, the average electron density of an arbitrary plasma string can be measured from such a signal if the electron density of a “reference” plasma string, along with the spatial dimensions of both plasma strings are known. Also, the reference plasma string should be generated under similar laser pulse durations as we will discuss in the following. A very simple method to measure the plasma dimensions is to image its fluorescence emission. Plasma string fluorescence images were recorded on a transverse plane using a linear CCD camera. Since we are interested in the relative string dimensions a conventional photographic camera could be also used for this purpose. Figure 2.4-4(a) presents the fluorescence images of the plasma strings corresponding to the measurements shown in Figure 2.4-2(c).

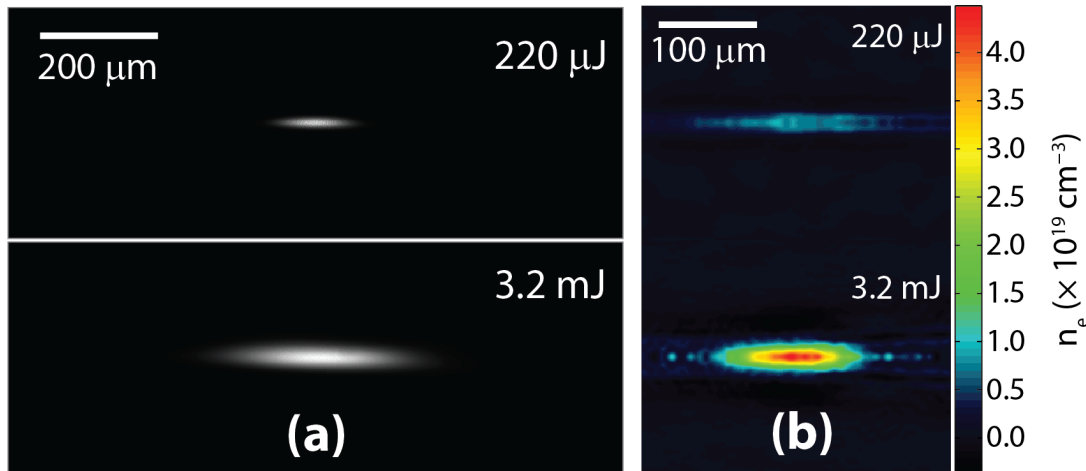


Figure 2.4-4 (a) Transverse CCD images of plasma fluorescence for different laser pulse energies, and (b) corresponding retrieved spatial distribution of the electron density using i-HOM.

Now, having a simple method for measuring the plasma string dimensions, we only need a reference measurement of electron density. For this purpose, we used the i-HOM technique, which is capable of retrieving the 3D distribution of electron density of micrometer sized laser generated plasma strings with a temporal resolution comparable to the pulse duration and is described in detail in the previous section. The 3D distribution of the real and imaginary parts of the refractive index perturbation (caused by the presence of the plasma string) are obtained using

Abel inversion. The electron density n_e in the plasma string is estimated using a simple Drude model $n_e = -2n_{cr}\Delta n$, where $n_{cr} = 1.7 \times 10^{21} \text{ cm}^{-3}$ is the critical plasma density in air for the 800 nm probe pulse. Figure 2.4-4(b) shows the i-HOM retrieved spatial distribution of the electron density for two cases of Figure 2.4-4(a) just after the passage of the pump pulse (maximum electron density).

In Figure 2.4-5 are shown the results of the i-HOM together with the corresponding calibrated PCo measurements for filaments created with a 100 mm ($\#F \approx 4$) focusing lens with different energies. As a reference for the calibration, we have chosen the i-HOM measurement at 3.2 mJ averaged over 1 mm along the propagation direction, since this is the minimal longitudinal spatial resolution of our PCo technique, defined by the diameter of the electrodes.

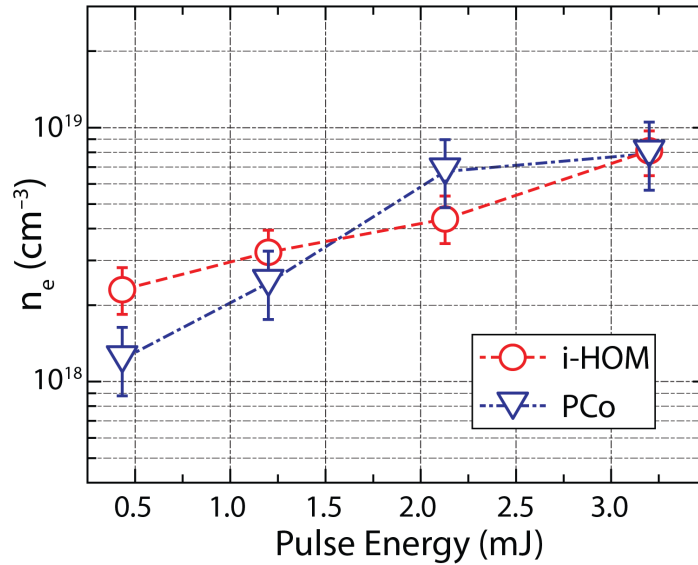


Figure 2.4-5 (a) i-HOM and calibrated PCo-measured electron densities versus input pulse energy for plasma strings created by an $f=100$ mm lens.

In order to confirm that the calibration method does not depend on the focusing geometry we have repeated the same experiments with a 300 mm focusing lens ($\#F \approx 12$). In Figure 2.4-6 are shown the results from the i-HOM together with the calibrated PCo measurements using two different reference measurements, one using the 100 mm lens and the other using the 300 mm lens (both at 3.2 mJ).

The results are clear and indicate that the calibration method is not sensitive to the reference choice or the focusing geometry, resulting in accurate estimations of the average

electron densities of plasma strings. Furthermore, beyond the much simpler implementation, the calibrated PCo technique can be used to study plasma strings with electron densities below the sensitivity threshold of i-HOM (where plasma densities $> 10^{17} \text{ cm}^{-3}$ are needed).

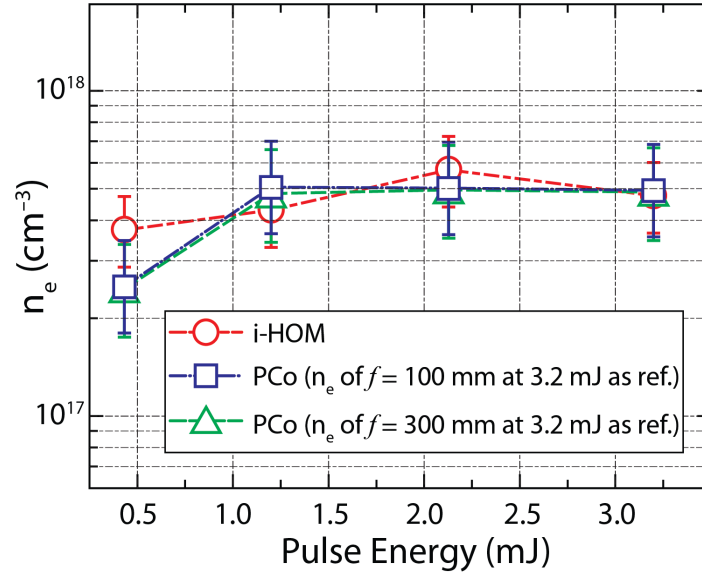


Figure 2.4-6 i-HOM- and calibrated PCo-measured electron densities versus pulse energy for plasma strings created by an $f=300$ mm; two different reference electron densities are used for the calibration of the PCo: electron density measured at 3.2 mJ in a plasma string created by an $f=100$ mm and the same created by an $f=300$ mm (see text).

The validity of the calibration is also verified for different pulse durations. As mentioned earlier, it is well known that the contribution of different ionization mechanisms in plasma formation depend on the pulse duration. For long pulse durations, contribution of the avalanche ionization becomes more significant than the tunnel and the multiphoton ionization and therefore the generated plasma densities in this regime are expected to be higher. Another set of experiments was performed in order to study the effect of the laser pulse duration on the plasma density. For our calibration, a plasma string generated by focusing 3.2 mJ, 35 fs, 800 nm pulses using an $f=100$ mm lens ($\#F \approx 4$) was used as a reference.

The pulse duration was then changed by adding chirp on the pulses, through adjustment of the distance between the two gratings in the compressor of our laser system. The pulse duration was measured using a single shot autocorrelator. The measured electron densities as a function of the pulse energies for pulse durations ranging from 35 fs to 200 fs are shown in Figure 2.4-7.

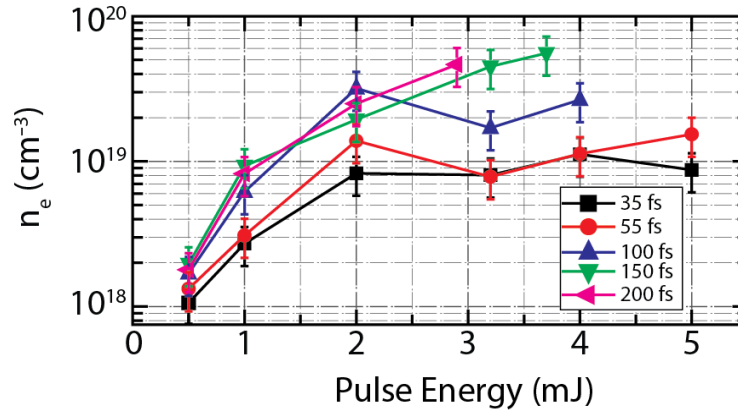


Figure 2.4-7 Estimated electron density from calibrated PCo measurement in plasma strings using different laser pulse durations and energies ($f=100$ mm).

As expected; the generated plasma electron densities are higher for longer pulse durations due to the increased avalanche contribution. We note that the technique can be used for even longer pulse durations but one should perform a specific calibration using a reference with similar pulse duration.

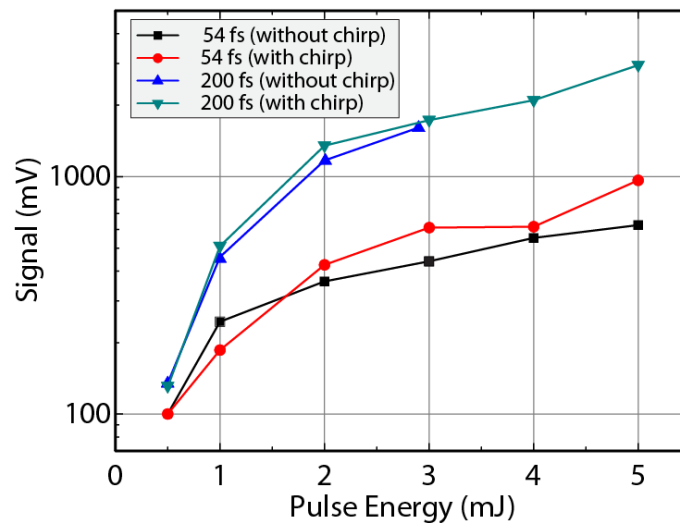


Figure 2.4-8 Comparing plasma conductivity signals of plasma strings as a function of energy for filamentation of transform limited pulses and chirped pulses.

Finally, in order to investigate the possible role of chirp on the generation of plasma we performed an experiment in which the PCo signal was measured for several pulse energies for two different pulse durations, achieved, in either by adding chirp on the spectrum of the initial pulse, or by narrowing the spectrum of the initial pulse via placing a spatial aperture between the

two gratings in the pulse compressor. The results are presented in Figure 2.4-8 and clearly shows that the signal is almost identical for the two cases.

2.5 Conclusion

In the beginning of this chapter, most of the present methods for characterization of filamentation-induced plasmas have been briefly overviewed. The capabilities of the i-HOM technique as one of the most powerful techniques for this purpose have been discussed both through simulation and experimental results. It has been shown that the perturbation in the probe beam wavefront through diffraction from narrow-waist (few tens of microns) low-density plasma strings that would result in small refractive index changes of the order of 10^{-4} can be accurately retrieved by this technique. The capabilities of the i-HOM technique for studying multiple filaments have been also presented both numerically and experimentally. The technique can resolve the wavefront perturbations caused by multiple filaments with any spatial arrangement but avoiding the interaction between filaments.

Furthermore, a simple method for calibration of the PCo technique, which had been so far used for relative measurement of plasma densities in plasma strings, is presented. Based on a simple physical model it has been shown that this technique can be calibrated to obtain accurate and quantitative measurement of electron densities in gaseous media. The calibration needs a reference measurement of electron density along with the dimensions of the reference plasma string and the one in question. The reference electron density was given by the i-HOM technique and for the dimension measurements we used simple spatial imaging of the plasma strings. The agreement between the measured electron densities from the i-HOM technique and the ones obtained from the calibrated PCo technique is very good allowing for simple and at the same time accurate measurements of electron densities in gases.

Filamentation in Transparent Solids

3.1 Introduction

Filamentation and in general nonlinear propagation of intense ultrashort laser pulses in transparent solids is not only valuable for applications, but also for fundamental physics and material science, owing to the contribution of complicated physical and chemical mechanisms that open new frontiers both in nonlinear optics and material science.

One of the features of nonlinear propagation of ultrashort laser pulses with moderate energies in fused silica is the formation of sub-wavelength self-organized nanogratings. In the second section of this chapter, we present the existing theoretical models suggested to explain the generation of nanogratings. Since these models strongly depend on the electron density of the generated plasma, which had never been measured before, we provide our accurate measurements of electron density in such structures, and based on our measurements we investigate the validity and consistency of the present models.

In addition, filamentation in soft transparent solids like polymers, though it has been utilized for micromachining applications, the physics of filamentation in such materials have not been explored. In the third section, filamentation in PMMA is investigated. PMMA is one of the widely used polymers and its laser processing has found extensive scientific interest and technological applications. The nonlinear propagation in this material and the consequent complicated dynamics are investigated in detail.

3.2 Formation of self-organized nanogratings in the bulk of fused silica

It is now well established that tight focusing of ultrafast laser pulses leads to the formation of permanent modifications in the bulk of transparent materials [129]. Under proper selection of the irradiation conditions, anisotropic refraction-index changes, localized in the focal volume, are induced [130]. Hnatovsky *et al.* [131] have experimentally distinguished three regimes of nonlinear propagation of tightly focused ultrashort laser pulses as a function of the optical pulse

duration and pulse energy, as shown in Figure 3.2-1. As it can be seen, in a specific range of pulse duration and pulse energy, nonlinear propagation leads to nanograting formation that macroscopically results in local birefringence.

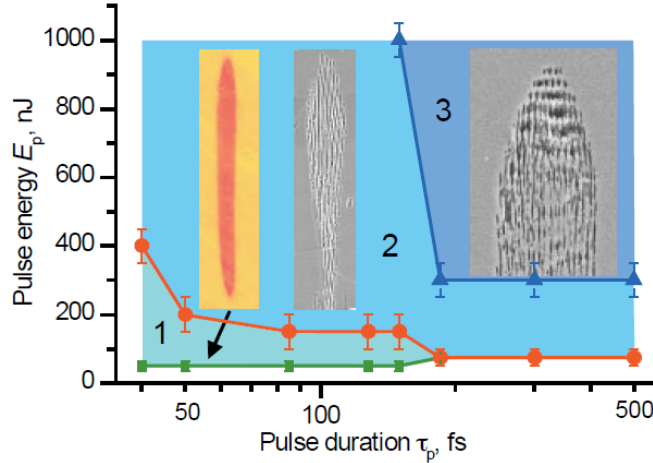


Figure 3.2-1 Different regimes of fs laser induced-modifications in the bulk of fused silica. Regime 1: smooth modification; regime 2: nano-grating formation embedded into smooth modification, and regime 3: complex morphology comprising of disrupted regions, nanogratings, and smooth modifications. From [132].

The physical interpretation of the appearance of localized birefringence in an amorphous material is attributed to the formation of self-organized, periodic refractive-index modulation in the focal volume (nanogratings) [132-134]. This modulation takes the form of arrayed planes of modified material, in such a way that the planes are normal to the writing laser polarization direction while their spacing is about half of the laser wavelength λ .

Self-organized nanogratings are, in fact, modified nano-planes oriented perpendicular to the incident wave polarization. A microscope image of birefringence caused by the formation of nanogratings from a side view is shown in Figure 3.2-2(a) while a low-magnification and high-magnification scanning electron microscope (SEM) image of the nanogratings from side views are shown in Figure 3.2-2(b-c), respectively. In the schemes, illustrating the view of these images, E , S , and k denote the polarization of the light field, scanning direction, and propagation direction of the beam, respectively.

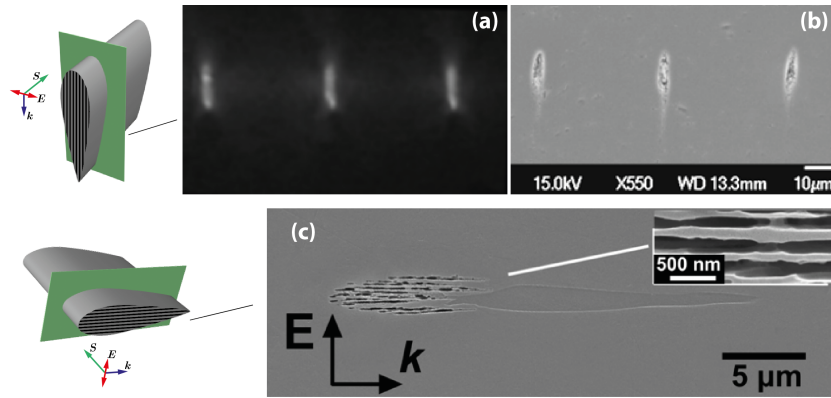


Figure 3.2-2 Side views of modified region. (a) Microscope image of the birefringence from the modified region, (b) low-magnification, and (c) high-magnification SEM image of nanogratings from a side view. In the schemes, E , S , and k denote the polarization, scanning and propagation directions of the incident beam, respectively.

Top view images of the nanogratings are shown in Figure 3.2-3. A nanograting formed by irradiating a single spot by several laser pulses is shown in Figure 3.2-3(a). It can be seen that the nano-planes are oriented perpendicular to the polarization direction of the optical beam. Moreover, the SEM images of the nanogratings generated by scanning the optical beam over the fused silica sample are shown in Figure 3.2-3. The polarization dependency of the structure orientation can be obviously seen.

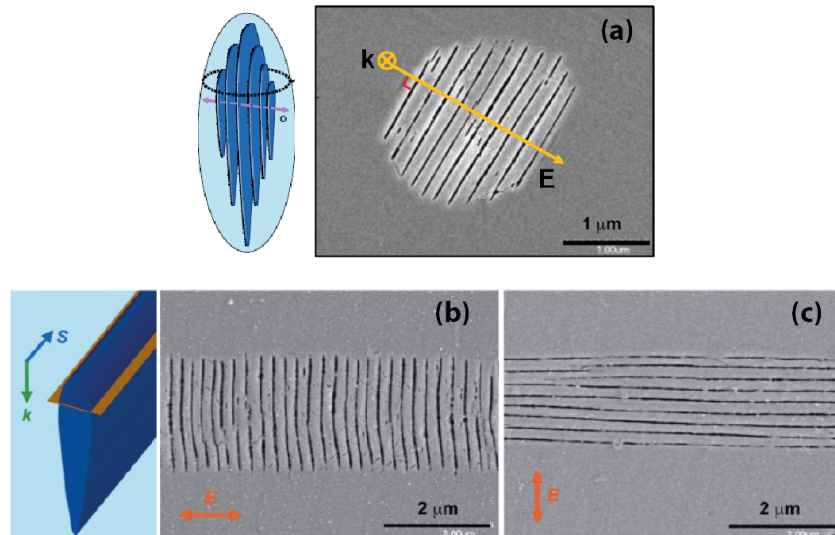


Figure 3.2-3 Top view SEM images of nanogratings formed in by irradiating a single spot in the bulk of fused silica (a), and by scanning the beam along a path ((b) and (c)). From [132].

The physical interpretation of the formation of self-organized nano-gratings is still under debate. Up to now, two theoretical models have been proposed [90, 91] to explain this phenomenon. As we will show later, in both models, the density of the electrons excited by the ultrafast laser pulse plays a crucial role.

The first model suggests that longitudinal bulk electron plasma density waves can be excited via inverse bremsstrahlung absorption of the incident light beam by the generated free electrons [90]. The electric fields of these longitudinal waves are parallel to the direction of propagation. The periodic self-organization is attributed to the coupling between plasma waves and the electric field of the incident light wave as shown in Figure 1.1-1(a). They propose that the initial coupling is produced by inhomogeneities induced by electrons moving in the plane of the light polarization [135]. The interference pattern between plasma wave and the electric field of incident irradiation that leads to the formation of the periodic structure increases the coupling and in turn results in modulation of the electron plasma local density and the structural changes in glass. The coupling, although initiated by the inhomogeneities in the electron density, exponentially increases if the periodic modulation of the plasma density occurs in a direction that fulfills the momentum conservation.

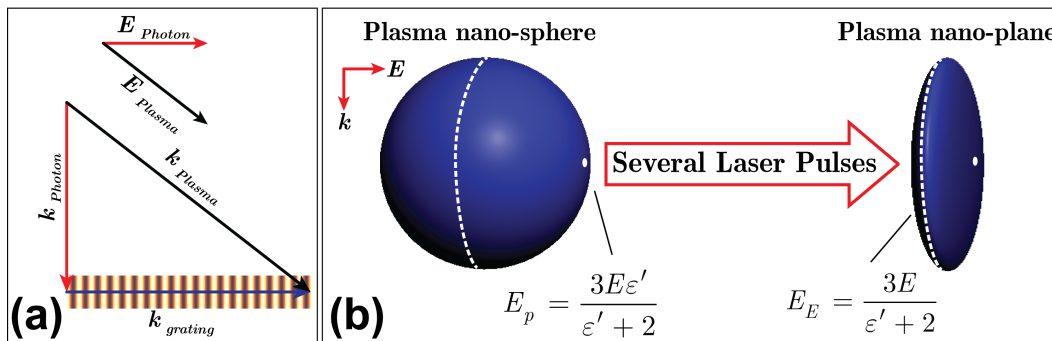


Figure 3.2-4 Two models for the nanograting formation in the bulk of fused silica. (a) Coupling between plasma waves and electric field of the incident beam [90], and (b) conversion from plasma nano-spheres to plasma nano-planes due to electric field enhancement after multiple laser shots [91].

Taking into account the conditions for energy and momentum conservation along with the dispersion relation for the electron plasma waves, the grating period can be analytically calculated as a function of the electron temperature and density. In order to correctly predict the

observed spacing, the model implies quite high electron temperatures ($T_e \sim 10^7$ K \sim 800 eV) and electron densities near the critical density $\rho_{cr} = 1.75 \times 10^{21}$ cm⁻³.

The second model proposes that the ionization is inhomogeneous and leads to the formation of slightly underdense plasma hotspots or plasma nano-spheres [91]. According to this model, the asymmetric field enhancement in directions perpendicular and parallel to the linearly polarized electric field of the light pulse results in the transformation of the plasma nano-spheres to plasma nano-planes oriented perpendicular to the beam polarization. Memory effects of previous nonlinear ionization [136, 137], such as formation of defects, provide the necessary feedback mechanism for the nano-planes to grow between successive pulses. The model attributes the experimentally observed ordering of the nano-planes to mode selection effects. In this sense, the observed spacing is correlated to the minimum spacing required for planar metallic waveguides to support modes having field maxima at the metal dielectric interface. Moreover, based on this model an efficient local field enhancement requires very high electron densities close to the critical value.

Recently it has been experimentally demonstrated that the excited electron plasma density is directly correlated to the permanent refractive index modification in fused silica [138, 139]. Considering that, the electron plasma density plays a significant role in both of the present theoretical models and since there had been no experimental evidence of reaching such high electron densities in the tight focusing regime with moderate pulse energies, we quantitatively explored spatio-temporal dynamics of refractive index and associated electron densities in this regime using in-line holographic microscopy [122, 123] [Chapter 2].

In our experiments, linearly polarized IR (800 nm), 35 fs laser pulses were focused inside the bulk of fused silica using a microscope objective (NA=0.4). After the irradiation, we observed, using polarization optical microscopy, the appearance of form birefringence in the irradiated areas. The birefringence microscope images of the irradiated area are shown in Figure 3.2-2. The formation of nanogratings in the irradiated area was confirmed using SEM, preceded by etching of the irradiated region in the sample. SEM images of the nanogratings are shown in Figure 3.2-2(b-c). The field polarization dependency of the nanogratings was also observed for various linear polarizations of the optical beam.

Under the conditions that led to the formation of nanogratings, we used the i-HOM technique [Chapter2] to investigate the spatiotemporal dynamics in the interaction region. The spatial distribution of the perturbed imaginary part of the refractive index ($\Delta\kappa$) for various delays, is shown in Figure 3.2-5(a). In this case the pump beam with linear polarization and pulse energy of 1 μJ (35 fs, 800 nm) was focused with a microscope objective (NA=0.4) in the bulk of fused silica. The results shown in Figure 3.2-5(a) were obtained by using a fresh sample and a single shot at each time delay. $\Delta\kappa$ increases due to the electron plasma produced by the pulse as it propagates. In our case, 6 photons are required to excite one electron from the valence to the conduction band. The refractive index changes $\Delta\kappa$ reaches values in the order of 7×10^{-4} as the pulse reaches its intensity peak and then decreases as the electrons are trapped.

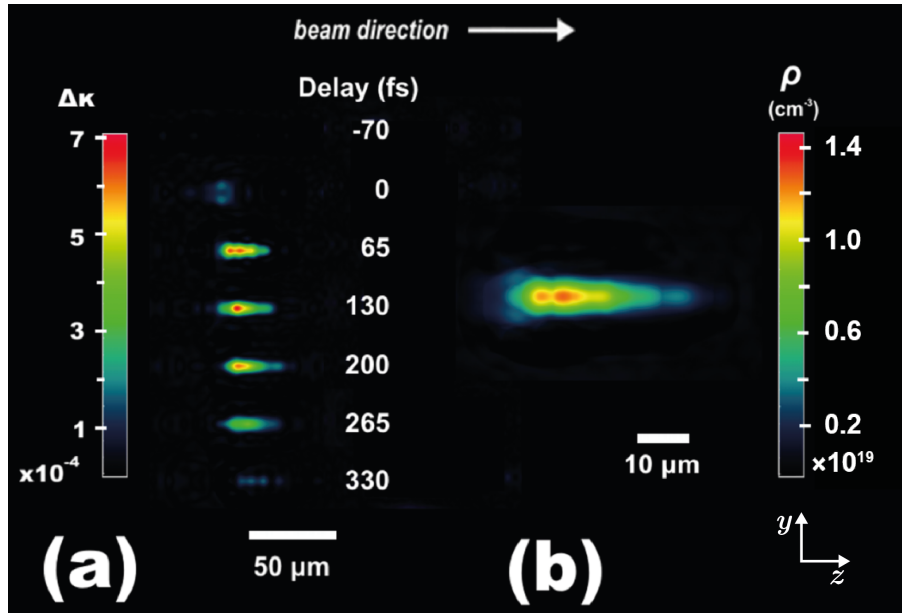


Figure 3.2-5 (a) Spatial distribution of the imaginary part of the refractive index at central longitudinal section for various delays. (b) Spatial distribution of maximal electron density of the plasma string.

From the complex refractive index changes $\Delta\tilde{n} = \Delta n + i\Delta\kappa$, the corresponding electron density values can be estimated using a simple Drude model as [5][Chapter 1].

$$\Delta\tilde{n} \simeq \left(-1 + i \frac{1}{\omega\tau_c} \right) \frac{\rho}{2\rho_{\text{cr}}} \quad (5.3-1)$$

where ρ the electron density, ρ_{cr} is the critical electron density, ω is the incident laser angular frequency and τ_c is the electron collision time. A critical parameter of the Drude model, the electron collision time, τ_c is estimated from our measurement of the real and the imaginary part of the refractive index as

$$\tau_c = -\frac{\lambda_0}{2\pi c} \frac{\Delta n}{\Delta \kappa} \quad (5.3-2)$$

According to the Drude model, the ratio $\Delta n / \Delta \kappa$ is constant and can be used to obtain the collision time. This ratio is plotted for various delays in Figure 3.2-6 and the collision time in fused silica is measured as $\tau_c = (1.6 \pm 0.2)$ fs.

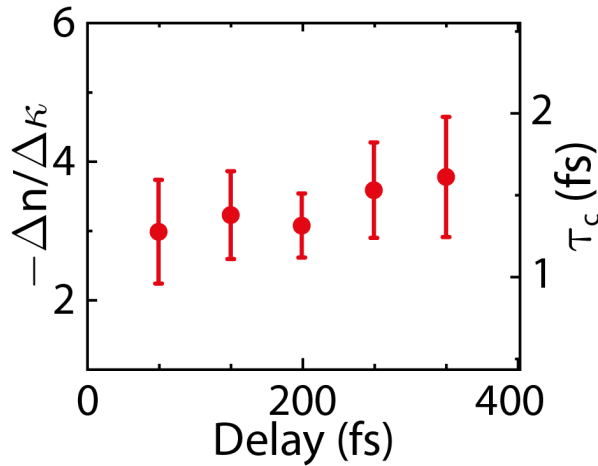


Figure 3.2-6 Ratio of changes in the real part to the imaginary part of the complex refractive index, with inverse sign, for various delays. These results are used for estimation of the collision time in fused silica using the Drude model.

The maximal, in time values of the electron density achieved along the propagation is shown in Figure 3.2-5(b). Our measurement show that the peak electron density is $(1.4 \pm 0.3) \times 10^{19} \text{ cm}^{-3}$ while the mean value in the focal region is $\sim 0.9 \times 10^{19} \text{ cm}^{-3}$. These values are ~ 2 orders of magnitude smaller than what has been considered, but was never measured, in existing theoretical models [90, 91]. The limitation of the electron density to values much smaller than the critical plasma density is a well-known effect of the filamentation process and is related to the dynamic regulation of the peak intensity. This regulation, often referred as intensity

clamping, is a result of the dynamic balance between Kerr self-focusing and ionization induced defocusing, leading to the well-known trapping of the beam to a filamentary structure (see for instance [140]). The spatial distributions of the plasma string are in excellent agreement with the spatial dimensions of the permanent structural changes shown in Figure 3.2-2.

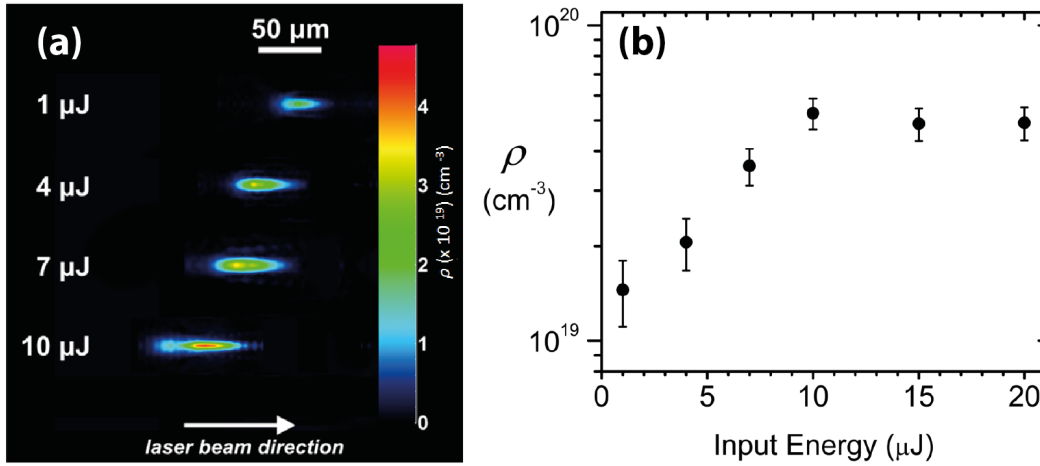


Figure 3.2-7 (a) Electron density distribution in the focal region for various pump pulse energies. (b) Peak electron density as a function of pulse energy.

In order to confirm that nonlinear propagation effects are dominating in this interaction regime we repeated the pump-probe experiments for various input pump energies. The electron density distribution in the focal region for various pulse energies is shown in Figure 3.2-7(a) and the maximal electron density values for input energies ranging from 1 μJ up to 20 μJ are shown in Figure 3.2-7(b). As the input energy is increased, the focus shifted towards the laser source and the focal volume is elongated, as one would expect from nonlinear propagation effects. More interestingly, although the input energy is increased by 20× the electron density saturates at $\sim 5 \times 10^{19} \text{ cm}^{-3}$, because of the above-mentioned dynamically balanced propagation. Our measurements show that for a wide range of input energies the electron density is limited due to the nonlinear propagation effects and stays always ~ 2 orders of magnitude below the critical plasma density. Furthermore, by using the same pump-probe technique we have observed that (not shown here) after the accumulative irradiation by a large number of pulses (≥ 5000 shots), irradiated volume exhibits form birefringence (the macroscopic evidence of nano-plane formation) coincides with the area that the electron density was maximum, as shown in Figure 3.2-8.

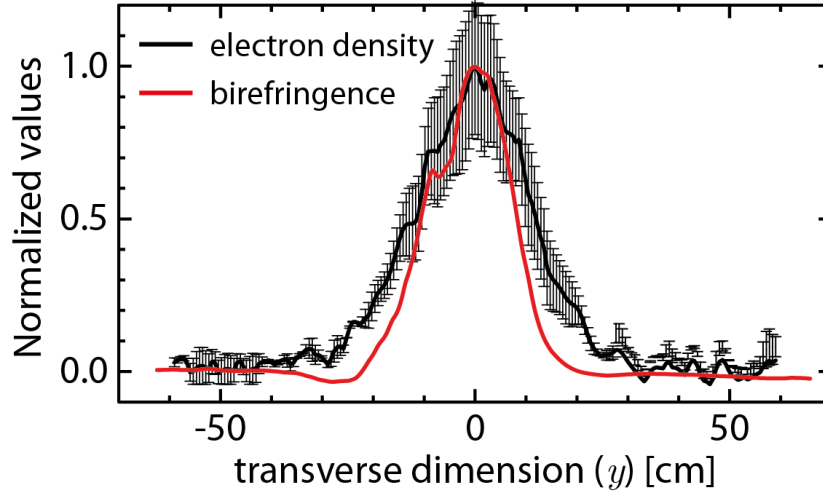


Figure 3.2-8 Measurement of the induced birefringence in comparison with the electron density distribution.

Clearly, these measurements of the electron density are questioning the validity of the existing models. Indeed, both models are seriously compromised when one considers plasma density values, which are ~ 2 -orders of magnitude below the critical density. Introducing the measured plasma densities in the model proposed by Shimotsuma *et al.* [90] requires even higher electron temperatures, reaching to $\sim 2 \times 10^4$ eV, to have the correct periodicity. In any case, such high electron temperatures are clearly unrealistic since the electron temperature is expected to be restricted by electron-ion collisions in the order of the band gap (~ 10 eV) [91]. Also, the model introduced by Bhardwaj *et al.* [91] holds no longer since the asymmetric local field enhancement that is necessary to transform the plasma nano-spheres to plasma nano-planes is very low. The measured plasma density is lower than the 1% of the critical density while the local field enhancement factor is asymptotically reducing to one [137] as the electron density reduces even below 10% of the critical density.

Thus, since both models fail, further investigations are needed for explaining the creation of the nanogratings.

3.3 Dynamics of filamentation in polymers

The interaction of intense fs laser pulses with a variety of solids such as semiconductors and dielectrics has been now demonstrated to involve generally electron plasma generation via multiphoton ionization and subsequent impact/avalanche process. The studies have illustrated

subtle aspects about plasma generation and decay. In particular, for otherwise chemically similar substrates, such as MgO and Al₂O₃, the *free* electrons survive for tens of picoseconds [31], whereas for NaCl, KBr and SiO₂, lifetime are two orders of magnitude smaller. Different dependences on the excitation densities are also observed e.g., in SiO₂ the trapping time is independent of the excitation densities, whereas in NaCl the time decreases with increasing excitation energy. These differences have been tentatively ascribed to the different nature of *trapping* sites in these systems [31].

Plasma formation similarly underlines the processes in the interaction of intense femtosecond laser pulses with molecular systems, as by now demonstrated for H₂O and for biological substrates such as cells (cellular nanosurgery) and tissues (dermatology, ophthalmology) [141]. Plasma formation has been shown to control the UV ablation of polymers with sub-nanosecond pulses, at least at high intensities ($\sim 10^{12}$ - 10^{13} W/cm²). Femtosecond induced filamentation has been exploited for the micro-processing [89].

Despite the importance of the issue, the experimental studies of plasma formation/dynamics in molecular systems have been limited to water. Mazur and co-workers have relied on optical techniques for monitoring the processes in the optical breakdown of H₂O (defined by the critical free-electron density $\rho_{cr} = 10^{21}$ cm⁻³) at 800 nm [142]. They observed that from 200 fs to 20 ps, the electron plasma produced by the laser pulse does not expand, and attributed this delay to the electron-ion energy transfer time. From 30 ps to 200 ps, the ion/electron system expands out of the focal region together, presumably because it is very hot. When the kinetic energy of the plasma has been “consumed”, a pressure wave continues to propagate outward at about 800 ps. After ~ 10 ns, the electron-ion plasma recombines, and much of the ionization energy is converted to heat, leaving a gas filled bubble which expands as a cavitation bubble. However, as the authors noted, the plasma expansion observed on the 30-200 ps is difficult to account for. Furthermore, the study was performed at 10 times above the critical breakdown. On the other hand, at lower irradiances corresponding to the generation of $\rho_e = 2.1 \times 10^{18}$ cm⁻³, a much faster (~ 300 fs) decay of the free electrons was observed. Transient absorption indicates that they decay into solvated electrons, as indicated by their characteristic absorption spectrum. [143].

On the other hand, largely on theoretical considerations, Vogel and co-workers have suggested that femtosecond-induced plasma can result in various processes with far-reaching consequences for the development/optimization of femtosecond laser material processing techniques and relevant applications. They have argued that plasmas with densities from 10^{13} to 10^{19} cm^{-3} that are produced below the breakdown threshold, though not dense enough to result in optical breakdown, may result in material damage via electron-initiated chemical processes [141]. Recently, some indirect/circumstantial evidence in support of these considerations has been advanced in the areas of femtosecond nonlinear spectroscopy and of cellular nanosurgery. Optical breakdown and induced nano-cavitation is indicated to be the underlying mechanism for cell surgery for amplified Ti:Sapphire laser irradiation, while surgery attained with oscillators is indicated to be mediated by free-electron-induced chemical decomposition. However, the nature and dynamics of these chemical processes is still a subject of intense studies.

In this work, we examine filamentation and plasma dynamics in poly(methylmethacrylate) (PMMA). PMMA is the most widely used polymer and its laser processing has found extensive scientific interest and technological applications. In addition, it is considered to be a basic model of tissues and as such, it has been studied in relationship with photorefractive keratectomy [144, 145]. The experiments were performed at relatively low excitation energies, typically used in laser processing of PMMA, far from the optical breakdown regime.

Experimentally, our study relies on the i-HOM technique [122, 123][Chapter 2] for the measurement of the transient and permanent changes in the optical properties of the PMMA due to the laser excitation. For the experiments an amplified Ti:Sapphire laser system is used producing 35 fs pulses at 800 nm. The laser beam is split in two parts in a pump-probe scheme as shown in Figure 3.3-1(a). The pump beam with pulse energy of $0.5 \mu\text{J}$ is focused in the PMMA bulk via a 0.4 NA microscope objective. The collimated probe beam crosses perpendicularly the pump focal region at various delays, and thus the refractive index perturbations change the amplitude and phase of the probe beam. The probe beam is then imaged using an in-line holographic microscopic system that is capable of remotely retrieving high-resolution holographic images of the diffraction of the probe beam along its propagation. By combining a number of these holographic images and applying a numerical iteration process [122, 123][Chapter 2], both the phase and the amplitude of the probe wavefront are retrieved. Then by

using an Abel inversion algorithm the volume distribution of the perturbation of refractive index is retrieved.

Figure 3.3-1(b) shows snapshots of the holographic images recorded at various delays up to ~ 3.5 ns. The diffraction of the probe beam in the pump focal region at early times ($t < 1$ ps) indicates the spatiotemporal overlap of the pump and probe beams and is correlated to a fast excitation and trapping process. At later times ($t > 100$ ps) the probe beam is strongly diffracted by a transiently modified focal region while a formation of an expanding pressure wave is visible. The qualitative information that is retrieved from the diffraction images, although indicative of the interesting dynamics, cannot provide a clear quantitative insight of the physical process that take place. This insight is provided by the retrieved volume distribution of the refractive index change Δn (real part) and $\Delta\kappa$ (imaginary part) as a function of the delay.

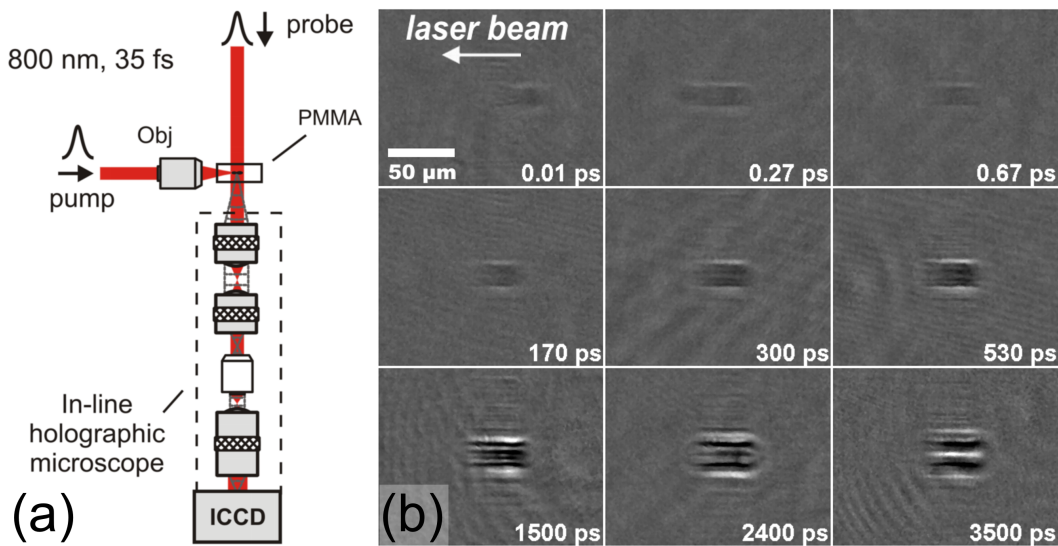


Figure 3.3-1 (a) Pump-probe setup, (b) Transmission images of the probe beam as it traverses the pump-irradiated volume at various delays.

Since different physical processes occur at different timescales we firstly focus our attention at early times ($t < 1$ ps). As shown in Figure 3.3-2(a), $\Delta\kappa$ is rapidly increasing as the pump propagates in the focal area. Initially, filamentary propagation results from the balance between the Kerr self-focusing effect and defocusing due to the plasma generated by multiphoton ionization. For our sample, which was commercial grade PMMA, the gap energy was 3 eV. Thus, in this case, multiphoton ionization involves two photons of our pump beam (800 nm). During filamentary propagation, the laser beam maintains a near-constant beam waist

over many Rayleigh lengths (in our case the Rayleigh length is $\sim 3.5 \mu\text{m}$, see the lower part of Figure 3.3-2(a)). Using the Drude model, we can estimate the excited plasma electron density distribution from the measured refractive index perturbation. The dynamics of free carrier density is shown in Figure 3.3-2(c). As it can be seen, the peak electron density is attained at $\sim 133 \text{ fs}$ and decays with a decay constant of $\tau_d = 217 \pm 35 \text{ fs}$.

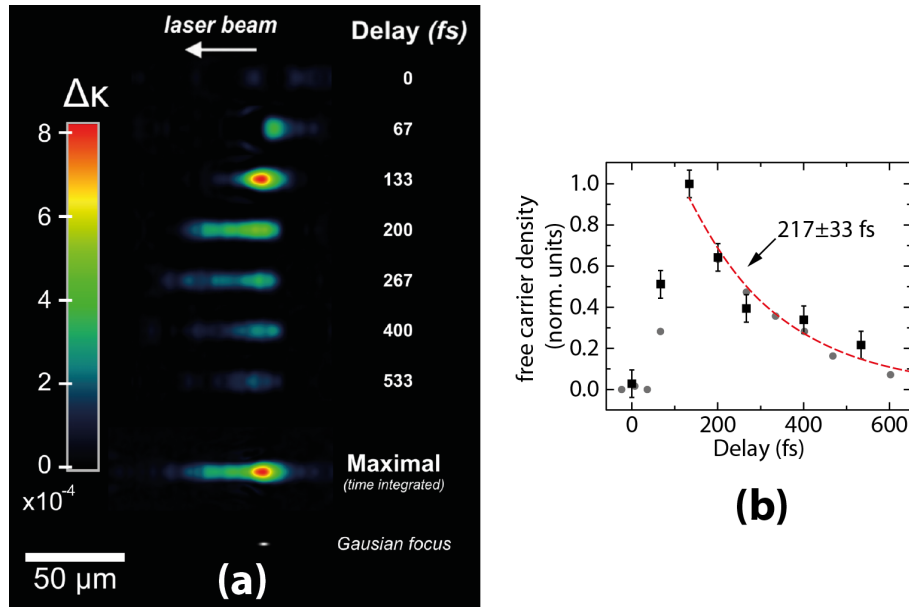


Figure 3.3-2 (a) Spatiotemporal distribution and evolution of the imaginary part of the refractive index induced during the nonlinear propagation of ultrafast laser pulses in PMMA for short delays; at the bottom is shown the maximal (in time) electron density in the focal area. (b) Spatial distribution of the estimated maximal free carrier density. (c) Temporal evolution of the free carrier density (Norm units).

Following this rapid decay, the absorptivity of the probe beam does not drop to zero but remains in low values up to a delay of $\sim 200 \text{ ps}$ as shown in Figure 3.3-3(a). Interestingly, the probe beam absorption is increasing up to $\sim 1 \text{ ns}$ and then decays to zero at $\sim 2 \text{ ns}$. At this delay, as shown in Figure 3.3-3(b), an acoustic pressure wave with a velocity of $\sim 1 \text{ Mach}$ (2.94 km/s) is observed to expand from the focal area.

To better understand the material changes that are taking place for delays higher than 200 ps we have retrieved the volume distribution of the refractive index changes both in the Δn (real part) and $\Delta \kappa$ (imaginary part) for various delays. As shown in Figure 3.3-4(a) the refractive

index perturbation is initially mainly absorbing ($\Delta\kappa > \Delta n$) that transforms to a strong refractive change ($\Delta n \gg \Delta\kappa$) as the delay is increased.

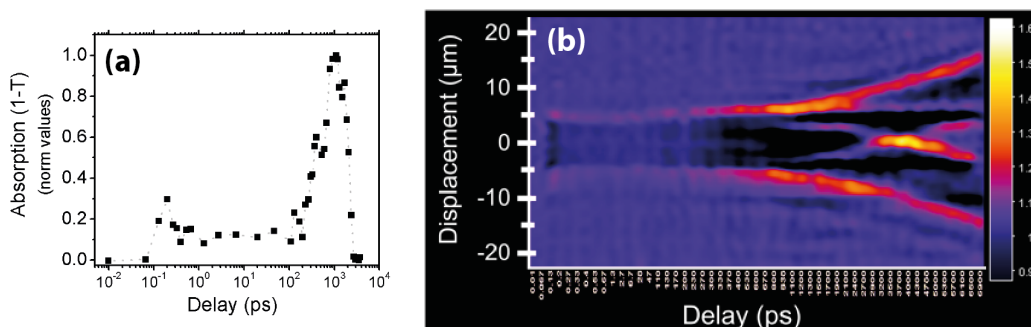


Figure 3.3-3 Temporal evolution of mean absorption (normalized values) in the center of the focal volume. (b) Diffraction pattern as a function of time. The emergence of an expanding acoustic wave is clearly visible at ~ 1 ns (velocity: 2.94 km/sec or ~ 1.03 Mach).

A graphic representation of the process that takes place is given in Figure 3.3-4(b), taking into account that the refractive index perturbations shown in Figure 3.3-4(a) represent central sections of the cylindrically symmetric distributions. Firstly, we observe that at delay of 446 ps the focal volume is mainly absorbing with $\Delta\kappa \cong 2 \times 10^{-3}$. At later delays (2.4 ns) the absorbing area has taken the form of a cylinder with the central part of the focal volume showing a decrease of the real part of the refractive index, indicative of a material rarefaction. At even longer delays (4.3 ns) the focal volume is strongly refractive, while a slight increase of the refractive index in the periphery (shown in purple in Figure 3.3-4(a)), coincides with the position of the outward expanding compressive acoustic wave. The permanent modification of the material is depicted as a lowering of the refractive index in the focal volume that located at the position of the peak of the excited electron density distribution. This agrees with the void formation similar to the one previously reported [146-148].

There is a wealth of information in the above results that shed light in many questions about electron plasma formation in organics/molecular solids. The first major result is the ultrafast excitation and trapping that takes place at time scales < 1 ps. In contrast, simple models of electron-ion recombination suggests times of almost an order of magnitude (20-40 ps) for an electron plasma of 10^{19} cm^{-3} densities to decay. For silica, this fast decay has been explained in terms of electron trapping by excitons that in turn decay to electronic defects. However, in the

case of polymers etc., this concept is hardly sustainable. These systems have been traditionally described in terms of free volume. However, at least for very short time scales, behavior of the liberated electrons in PMMA should be similar to the solvation of free electrons in H₂O [149-151]. Accordingly, free volumes in the polymer do act as “localized” defects, where the electron is stabilized by the high polarity of the chromophores of PMMA (forming a contact ion pair). The time constant for hydration of free electrons in water is about 300 fs [152, 153]. Of course, the electrons remain “hot” and dissipate their energy on a few ps time scale.

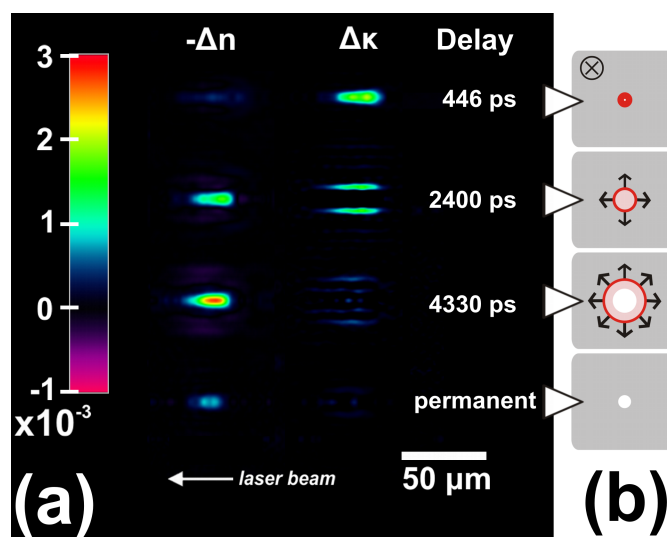


Figure 3.3-4 Spatiotemporal distribution of the refractive index changes (real and imaginary parts) for long delays (>200 ps). (b) Graphical representation of a transverse section of the focal volume (the pump beam propagation is perpendicular to the figure).

The second range that can be clearly defined concerns the time up to 200 ps. What is remarkable in this time range is the very small refractive index and the small absorptivity changes that are observed. It is clear that shock wave is not developed as soon as the electrons transfer their energy to the ions, as generally assumed. The observation that the pressure wave develops only at >200 ps leaves no doubt that it is driven by an expanding gas of high pressure produced in the intermediate period. The pressure required to drive such a wave in PMMA is estimated to be 0.1-0.5 GPa, requiring temperatures >300 K.

For $t < 200$ ps, decomposition of the polymer occurs. However, the nature of the decomposition appears to be quite novel. First, it is surprising that Δn shows negligible changes in the 5-200 ps period. Since the variation of the refractive index of PMMA with temperature

($dn / dT = -1.1 \times 10^{-4} / ^\circ\text{C}$) is almost exclusively due to the variation of density, in the present case, the small change Δn suggests small changes in the density of the material. On the other hand, decomposition species formed via side group elimination should result in an increase of the refractive index from 1.49 to 1.5-1.51. More surprising is the observation that in the 2-200 ps, there is no well-defined gradual evolution of the optical parameters as for example would be the case for a stepwise and random decomposition of the polymer. Such a fast decomposition is incompatible with thermal process, since it is well established that thermal decomposition of PMMA at least at temperatures >300 K occurs on much longer time scales (>10 ns) and continues up to about hundreds of μs or even ms. We can estimate the temperature in the focal volume by the action of a single pulse independently by two approaches. A rough theoretical estimation is that the temperature rise is given by $\Delta T_{\text{max}} = (\rho_e U_i) / (\rho_m C_p)$, where ρ_e is the electron density, U_i the ionization energy, C_p is the heat capacity and ρ_m is the mass density of the medium. Using this approach, and the measured values for ρ_e we get that $\Delta T < 10$ K. On the other hand, the maximal value of the measured refractive index changes Δn , as shown in Figure 3.3-4(a) is $\Delta n_{\text{max}} \cong -3 \times 10^{-3}$. Using this value, we can have an independent estimation of the peak temperature $\Delta T_{\text{max}} = \Delta n_{\text{max}} / (dn / dT) \cong 27$ K. In both cases, we get a temperature increase that is in the order of a few tens of degrees.

All the above considerations strongly preclude the possibility that decomposition proceeds thermally. Excitation to dissociative electronic states would be a plausible explanation for the observed fast decomposition. On the other hand, such fast decomposition is more consistent with electron-initiated processes. PMMA scavenges electrons rather efficiently, resulting in matrix radical anions. There is ample information about such processes from conventional studies based on 2-photon excitation of dopants, radiolytic and γ -irradiation studies. From these studies, it is known that the PMMA radicals are unstable and start depolymerizing according to the following scheme:



where P represents the chain of PMMA. It is reasonable to consider that similar electron-mediated depolymerization processes are induced in the femtosecond UV irradiation, though of

course, the details will differ, as a result of differences in the electron energy distributions, densities and time scales. Given the very high number of electrons trapped, we can presume that such depolymerization events are initiated “simultaneously” at several sites along the polymer chains. The time scale for electron-induced depolymerization is not known, but we can envisage that for picosecond time scales, we have breakage of the chain and slow release of monomer. Thus, no major change in the refractive index is expected; in addition, since absorption of PMMA and of its fragments and of its monomers MMA at 800 nm is minimal, small absorptivity changes are expected.

The final stage includes well-studied processes such as the expansion of a compressive acoustic wave with the parallel development of a rarefaction wave towards the center of the irradiated area. Using the measured values of the refractive index changes, shown in Figure 3.3-4 and Figure 3.3-5, we can follow this process in detail and estimate the peak pressure associated with the compressive and the rarefaction wave.

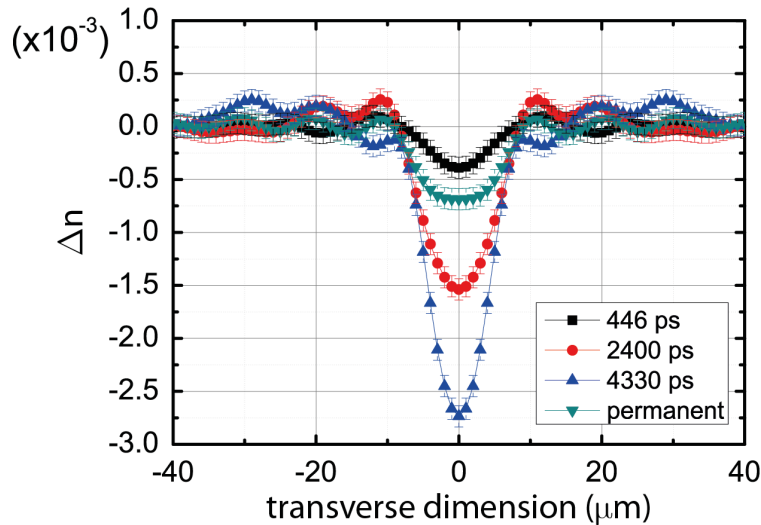


Figure 3.3-5 Refractive index change distribution profiles along the transverse dimension, perpendicular to the pump beam propagation direction, for various long pump-probe delays.

The peak value for the refractive index increase is $\Delta n_{\max} = (2.7 \pm 0.1) \times 10^{-4}$. From this value, we can estimate the peak pressure of the compressive wave using the piezo-optic coefficient π_{PMMA} of PMMA:

$$\begin{aligned}
 |\Delta B_{\max}| &\equiv \left| \frac{2\Delta n_{\max}}{n_o^3} \right| = \pi_{\text{PMMA}} \cdot \sigma_{\max} \\
 \sigma_{\max} &= \frac{2\Delta n_{\max}}{n_o^3} \frac{1}{\pi_{\text{PMMA}}} \cong \frac{2 \cdot (2.7 \pm 1) \cdot 10^{-4}}{1.489^3} \frac{1}{26 \cdot 10^{-12} \text{Pa}^{-1}} \cong (6 \pm 2) \text{ MPa}
 \end{aligned} \tag{3.3-1}$$

Taking now into account that the rarefaction wave is “focused” in the center of the cylindrical structure we can use the peak value for the refractive index decrease in the center $\Delta n_{\max} = -(2.8 \pm 0.1) \times 10^{-3}$ (at 4.3 ns) to estimate the peak tensile stress in the center:

$$\sigma_{\max} = -\frac{2\Delta n_{\max}}{n_o^3} \frac{1}{\pi_{\text{PMMA}}} \cong \frac{2 \cdot (2.8 \pm 0.1) \cdot 10^{-3}}{1.489^3} \frac{1}{26 \cdot 10^{-12} \text{Pa}^{-1}} \cong (63 \pm 3) \text{ MPa} \tag{3.3-2}$$

This value is well within the range of PMMA tensile strength (48-76 MPa). Therefore the formation of permanent cavity under these conditions can be attributed to the emergence of the rarefaction wave.

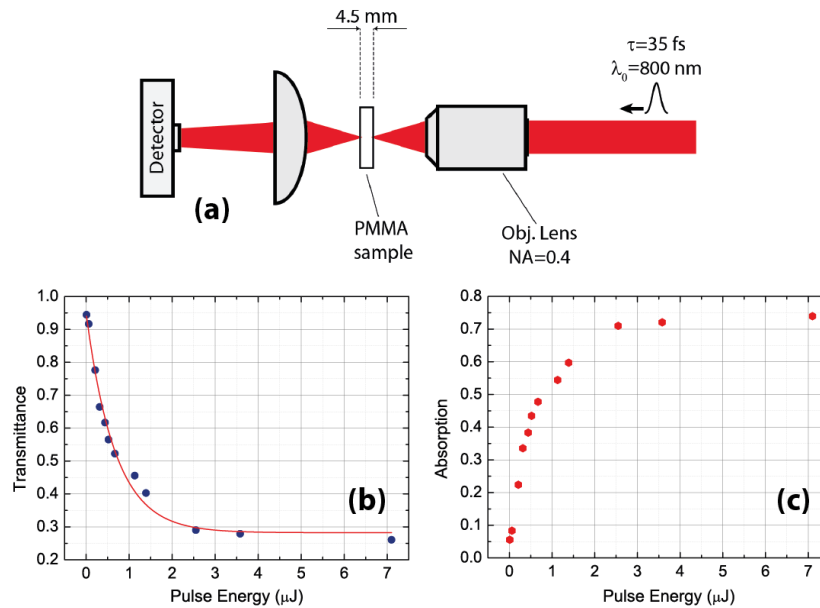


Figure 3.3-6 (a) Experimental setup for measuring transmission of PMMA as a function of pulses energy, and (b)-(c) transmission and absorption of the PMMA sample as a function of input pulse energy. Solid curve is an exponential fit with a decay constant of $0.67 \mu\text{J}^{-1}$.

For better clarification of the physical mechanisms involved in the dynamics of filamentation in PMMA, we conducted another set of experiments to investigate the temporal evolution of the modified region. Using the experimental scheme depicted in Figure 3.3-6(a) we investigate the transmission (and absorption $A=1-T$) of the PMMA sample as a function of pulse energy. The results are shown in Figure 3.3-6(b)-(c). The solid curve in Figure 3.3-6(b) is an exponential fit, with a decay constant of $0.67 \mu\text{J}^{-1}$. Based on the measurements it is revealed that in the pulse energy of $0.5 \mu\text{J}$, nearly 57% of the laser pulse energy is nonlinearly absorbed.

The temporal dynamics of the modified region as a function of pulse energy was further investigated by analyzing the diffraction images of the modified region using the experimental scheme shown in Figure 3.3-7(a). The pump beam focused with a microscope objective of $\text{NA}=0.4$, with different pulse energies in the bulk of PMMA results in modifications in the focal volume and therefore the probe beam reaching the focal volume at several delay times after the pump beam is diffracted from the modified region. The diffraction pattern of the probe beam was then recorded using a CCD camera and an imaging lens, for various delays beyond 1 ns.

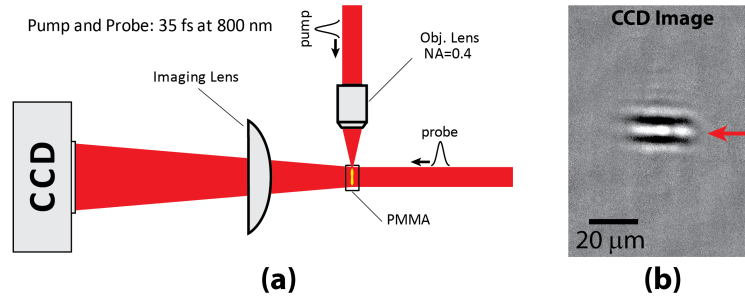


Figure 3.3-7 (a) Experimental scheme for recording diffraction images of probe beam from the pump beam-induced modifications in the focal region in the bulk of PMMA. (b) Typically acquired diffraction image using.

Figure 3.3-8(a) shows a typical picture of the dynamics of the modified region created by stitching $\sim 7\text{-}\mu\text{m}$ -wide slices of the diffraction images. In addition, in Figure 3.3-8(b) is shown a typical plot of the temporal evolution of the radius of the modified region measured from the stitched slices. Three different expansion regimes of the modified region are distinguishable. The first region starts from 1 ns to ~ 3 ns, the second region is quick expanding region from ~ 3 ns to ~ 5 ns, and the third region from ~ 5 ns to ~ 7 ns.

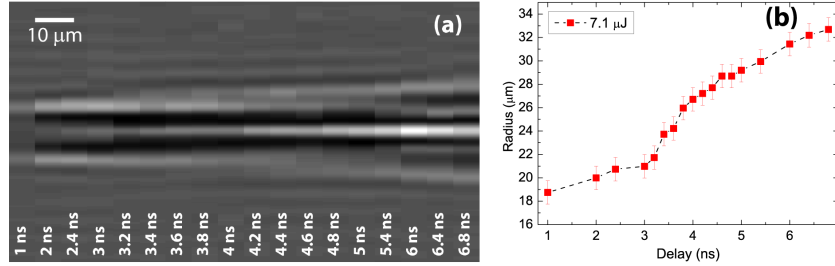


Figure 3.3-8 (a) A montage of $\sim 7\text{-}\mu\text{m}$ -wide horizontal slices from the central part of the CCD images shown in Figure 3.3-7(b), corresponding to different pump-probe delays, and (b) measured radius of the modified region at different delays for the indicated input pulse energy.

The three regimes of the expansion rate of the modified region were analyzed for several input pulse energies. In Figure 3.3-9 are shown expansion speeds of at the first expansion region before 3 ns (a) and the third expansion region after 5 ns (b). It can be obviously seen that the expansion speeds at this two regions do not change dramatically. The average speed at the first region is $\sim 0.824 \mu\text{m/ns}$, three times smaller than the speed of sound $2.94 \mu\text{m/ns}$ in PMMA. However, at the third region the average expansion speed is $\sim 2.35 \mu\text{m/ns}$, slightly smaller than the acoustic wave propagation speed.

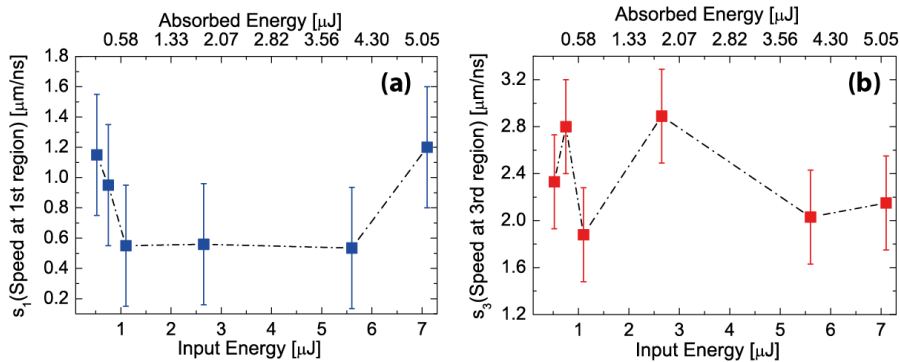


Figure 3.3-9 Expansion speeds of the modified volume as a function of input pulse energy and absorbed energy at (a) first expansion region before 3 ns, and (b) third expansion region after 5 ns.

On the other hand, at the second expansion region, the expansion speed drastically depends on the input pulse energy. The expansion speeds at this region are shown in Figure 3.3-10 as a function of input pulse energy (a) and as a function of absorbed energy in (b). The dashed straight lines in these figures indicate the acoustic wave speed of $\sim 2.94 \mu\text{m/ns}$ (1 Mach). The solid curves show the power function fits as $s_2 = c_1 x^{c_2}$. The c_1 and c_2 fit parameters for Figure

3.3-10(a) and Figure 3.3-10(b) are (0.3862, 0.2591) and (4.482 and 0.20), respectively. For the cylindrical geometry, the scaling of the shock wave velocity with the absorbed energy has the form of $v = E^{0.25}$ [154]. The difference between the reported value of 0.25 and our measured value of 0.2 can be attributed to the fact that in our experiment, the object has shape of longitudinally elongated sphere.

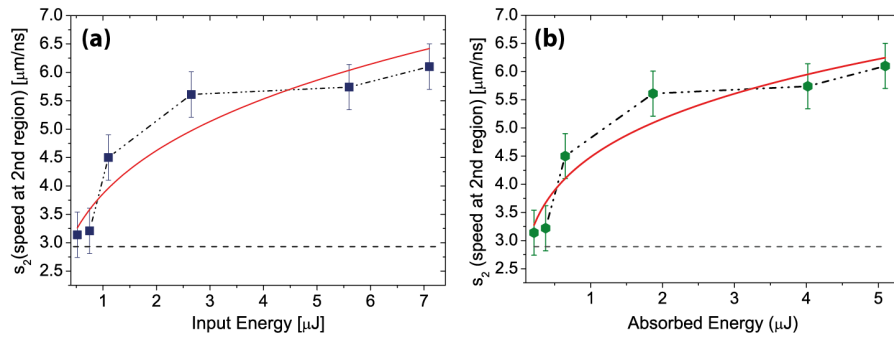


Figure 3.3-10 Expansion speed at the second region (~ 3 ns ~ 5 ns) as a function of (a) input energy, and (b) absorbed energy. The dashed straight lines indicate 1 Mach and the solid curves are the fits (see text).

Interestingly, as shown in Figure 3.3-11(a) the pressure wave start-up time is almost constant as a function of input pulse energy, starting on average at ~ 3.15 ns. The length of structure as a function of input pulse energy is shown in Figure 3.3-11(b). It can be seen that the change in the length of structure as a function of input energy is considerable. Moreover, the expansion speed in the second region as a function of absorbed energy per unit length is shown in Figure 3.3-11(c).

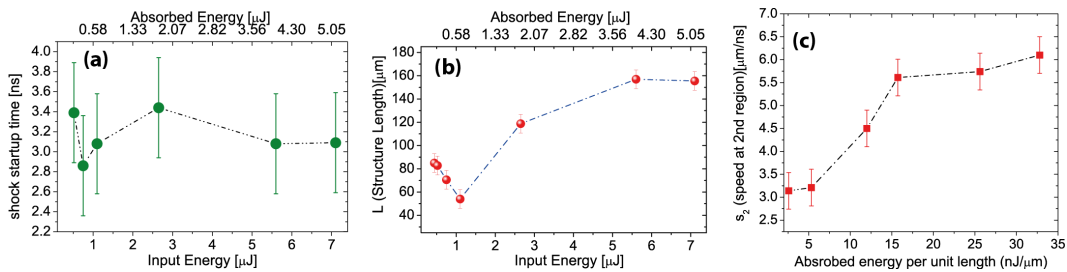


Figure 3.3-11 (a) Shock startup time as a function of input pulse energy, (b) the length of the modified region (structure) as a function of input pulse energy, (c) speed at the second region as a function of absorbed energy per unit length.

In conclusion, using the i-HOM technique we have examined the dynamics of filamentation in poly(methyl methacrylate) polymer with a high temporal and spatial resolution. Electron decay is found to be very fast ~ 220 fs. At the attained peak electron densities ($\sim 1.5 \times 10^{19} \text{ cm}^{-3}$), there is no evidence that the final void formation is due to the expansion of a “hot” electron/ion cloud. Instead, a chemical decomposition initiated by the dissociative attachment of electrons results in the development of a strong acoustic wave and the formation of void starting at ~ 200 ps.

3.4 Conclusion

In summary, we have shown that under certain fs excitation conditions, self-organized nanostructures are formed in the bulk of fused silica glass. Under these conditions, we have accurately measured the electron plasma density and its dynamics both in space and time, using the i-HOM technique. We have demonstrated that even for pulse energies much higher than the ones that lead to nanograting formation, the electron density is at least 2 orders of magnitude less than the values assumed in the two present theoretical models. Since, both models are strongly correlated to very high electron densities (close the critical electron density), it is been shown that these models cannot correctly explain the phenomenon.

Moreover, we have investigated the nonlinear propagation dynamics of ultrashort laser pulses in PMMA. We have found that the electrons decay very fast (within ~ 220 fs). At the reached peak free carrier densities ($\sim 1.5 \times 10^{19} \text{ cm}^{-3}$), there is no evidence that the final void formation is because of the expansion of a hot electron/ion cloud. Instead a chemical decomposition initiated by the dissociative attachment of electrons results in the development of a strong acoustic wave and the formation of void starting at ~ 200 ps.

CHAPTER 4

Filamentation in Gases

4.1 Introduction

In gaseous media, filamentation leads to some interesting effects that are more pronounced in these media than transparent solids or liquids. In particular, third harmonic (TH) generation has drawn considerable attention in the last decade. Moreover, laser-generated plasma in gases (more specifically, air) can be used as robust optical medium in plasma photonic devices. Such devices can handle energies much beyond the damage threshold of most of commonly used optics.

In this chapter, starting from filamentation-induced TH generation, it is shown that when a filament crosses a plasma slab, the conversion efficiency from the fundamental wavelength to its third harmonic can be increased by at least two orders of magnitude. The physical mechanism behind this enhancement is investigated and it is shown that effective plasma-enhanced third order susceptibility is causing the enhancement while the other factors such as neutral air-plasma interface are not playing a significant role in this phenomenon. Moreover, it is shown that by crossing two filaments we can create a simple plasma photonic device, i.e. a plasma grating and the attributes of such a grating are studied in detail.

4.2 Enhancement of filamentation-induced third-harmonic (TH) generation

One of the most interesting nonlinear phenomena that can occur during the filamentation is harmonic generation. In particular, third-harmonic (TH) generation has drawn considerable interest in the last decade with air being the most popular medium for harmonic generation [155-161]. An attractive feature of TH generation using filamentation of high intensity IR femtosecond laser pulses is that ultrashort pulses can be generated in UV wavelength range [155]. So far, in air, TH conversion efficiency up to 0.2% has been reported [156, 158, 159]. Besides air, generation of third harmonic wave through filamentation has been observed in noble gases [157, 162-164], methane [165] and various liquids [166].

4.2.1 TH generation from a single filament

It has been shown both numerically [167-169] and experimentally [160, 161, 167] that TH generation during IR femtosecond laser pulse filamentation in air results in both on-axis and off-axis (conical emission) TH components. Axial TH emission starts at pump powers below the critical power for self-focusing in air and it grows as the pump energy is increased despite the fact that the phase-matching condition between the fundamental and TH waves on the propagation axis cannot be satisfied. To explain this, it has been proposed a quasi-phase-matching due to a nonlinear phase-locking mechanism between the fundamental and TH pulses in the filament [159, 167]. On the other hand, generation of off-axis TH component due to phase matching between the fundamental and TH waves starts at pump powers around the critical power. In the far field, the off-axis component appears as a ring whose diameter corresponds to a phase-matching cone half-angle of about 6 mrad [159, 167]. At pump powers above the critical power for self-focusing, most of the TH energy is concentrated in the ring pattern. The TH beam profile and its evolution as a function of energy are shown in Figure 4.2-1 [167].

4.2.2 Enhancement of TH generation with a plasma slab

We show here that when a plasma string is placed perpendicularly into the path of a filament the typical ring structure of the TH wave produced by the IR light filament reshapes to a Bessel-like far-field distribution and a significant (more than two orders of magnitude) enhancement of TH pulse energy occurs [170, 171].

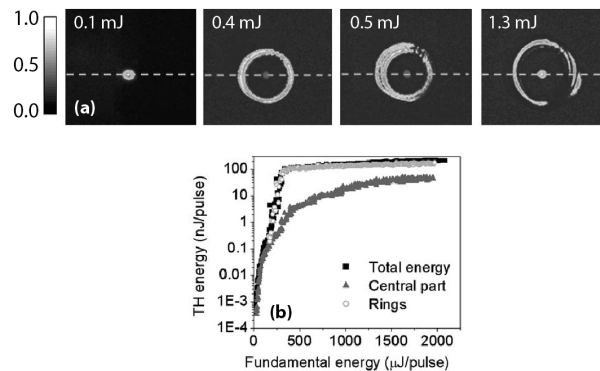


Figure 4.2-1 (a) TH images taken by an ICCD camera at different pump energies using 100 cm focal length lens, and (b) Experimental measurements of total energy of the TH generated in air as a function of the fundamental energy and the TH energy contained in the rings structure and central spot using the same lens. Both from [167].

- **Experimental setup**

The experiments were conducted using a Ti:Sapphire chirped-pulse amplification laser system supplying 35 fs (FWHM) transform limited near-infrared pulses at central wavelength of 800 nm and capable of producing pulses with energies up to 30 mJ at 50 Hz repetition rate. The experimental setup is shown in Figure 4.2-2(a). First, the fundamental laser beam was split into two arms, Pump and Signal, using a beam splitter. Laser pulses in the Signal arm with energies up to 3 mJ were focused using a 40 cm-focal-length lens L2, and created a light filament in air with a length about 2 cm. The signal beam was cropped using a circular iris 7 mm in diameter in order to obtain a long filament by lowering the numerical aperture. Pulses in the pump arm with energies up to 5 mJ were focused perpendicular to the Signal beam (Figure 4.2-2(b)) with another lens L1 (focal length 10 cm) to produce a dense plasma channel in air which was indicated by the appearance of an approximately 2 mm-long spark. The position of lens L1 was adjusted to allow the light filament in the Signal arm to cross the central part of the spark. Similarly, to optimize the energy and spatial profile of the generated TH wave, we varied the position of the Pump plasma string along the filament by changing the position of L2 and the delay between the pulses in the two arms was adjusted with a delay line.

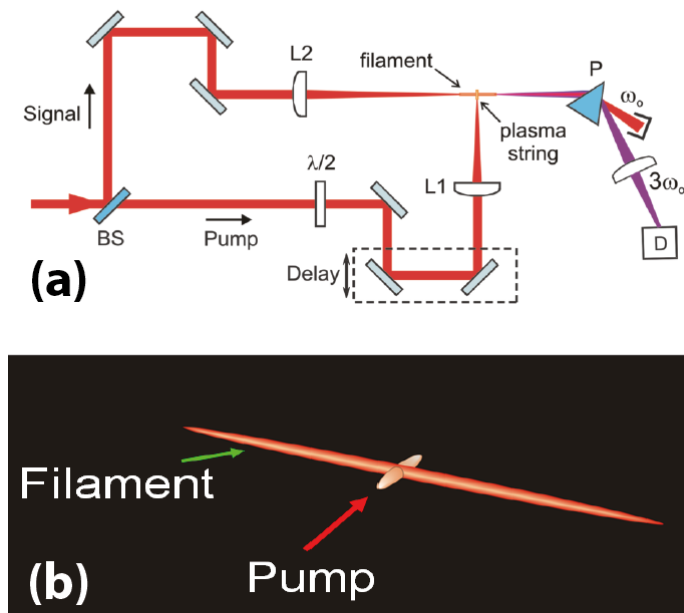


Figure 4.2-2 (a) Schematic of the experimental setup; here: BS, beamsplitter; L1, L2, lenses; P, prism; D, photodetector. (b) Scheme of the spatial arrangement of the plasma slab (Pump beam) and the filament (Signal beam).

After the filament, the far field spatial pattern of the TH and fundamental waves in the Signal arm were visualized using a paper screen where the images of the produced fluorescence were captured with a photographic camera. In addition, for more accurate measurement of the far-field intensity distribution of the generated third harmonic, the Signal beam was projected onto a 12-bit UV sensitive linear charge-coupled device (CCD) camera, preceded by appropriate interference filters at 266 nm in order to isolate the TH beam. For the TH energy measurements, a fused silica prism P was used as a dispersive element to separate the TH from the fundamental, and total TH energy was measured with a calibrated photodetector D as shown in Figure 4.2-2(a).

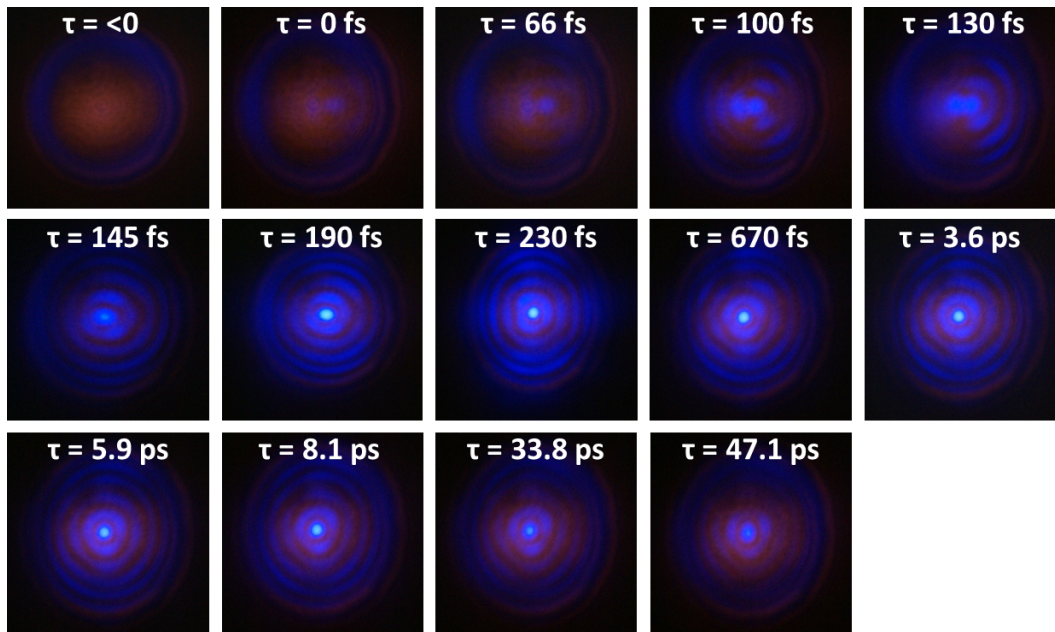


Figure 4.2-3 Spatial distribution of the fundamental and TH beams at several delays between Signal and Pump pulses. Negative delay means that the pump pulse reaches the crossing point after the Signal pulse.

- **Experimental results**

First, fluorescence images produced by the TH and fundamental beams on the screen, placed at a distance 1.4 m beyond the filament position, at several values of the relative delay τ between pulses of the two beams were recorded as shown in Figure 4.2-3. The Pump and Signal pulse energies were 0.5 mJ and 0.6 mJ, respectively. Figure 4.2-4 shows spatial distribution of the TH (blue ring) and of the fundamental beam (red spot) for negative values of τ corresponding to the situation where the Signal pulse arrived at the crossing point well before the Pump pulse. We

defined a zero delay point as a delay at which the effect of the Pump pulse on the Signal pulse propagation dynamics becomes noticeable. As one would expect, TH generation is not affected by the presence of the Pump for negative τ , and its far-field profile exhibits a characteristic ring pattern [161, 167].

When τ becomes positive (Signal pulse arrives to the crossing point after the Pump pulse), the plasma string generated by the Pump pulse in the Signal beam path changes dramatically the TH generation dynamics, transforming the TH far-field profile into a bright central spot surrounded by rings (Bessel-like shape) as shown in Figure 4.2-3 and Figure 4.2-4(b).

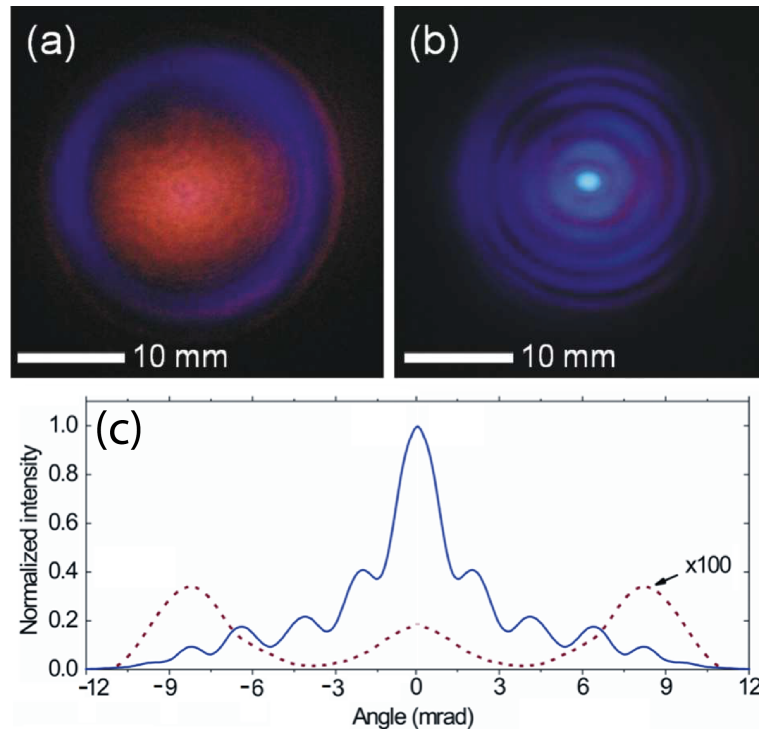


Figure 4.2-4 Far-field images of the TH (blue ring) and of the fundamental (red central spot) beams taken with a digital camera on a paper screen placed at 1.4 m from the filament for (a) negative τ , and (b) $\tau = 200$ fs. In (a), the fundamental beam spot is partially shadowed by the TH ring. (c) TH intensity profiles, versus divergence angle, measured with a linear CCD, dashed and solid curves for (a) and (b), respectively.

It is worth mentioning that in Figure 4.2-4(b) the camera exposure time was reduced by 50 times, comparing to Figure 4.2-4(a) and still resulted in saturation of the TH central spot indicating a very strong increase of the TH intensity. At small positive delays up to 150 fs, TH beam profile was asymmetric, and it acquired radial symmetry at $\tau = 200$ fs, which corresponds to the overlap of intensity maxima of the two pulses at the center of the Signal filament (200 fs is

equivalent to 60 μm of propagation in air, and the laser filament diameter is approximately twice this distance [5]). As shown in Figure 4.2-3, for longer delays up to 47 ps – the maximum range of our delay line – TH distribution remained symmetric while its energy monotonically decreased with an increase of the delay. In order to achieve the highest TH generation efficiency the position of the plasma slab was changed along the Signal filament (e.g. where the slab crosses the filament) and as it is shown in Figure 4.2-5 maximum conversion efficiency was observed when the Pump plasma string crossed the central part of the Signal filament where the light intensity was highest.

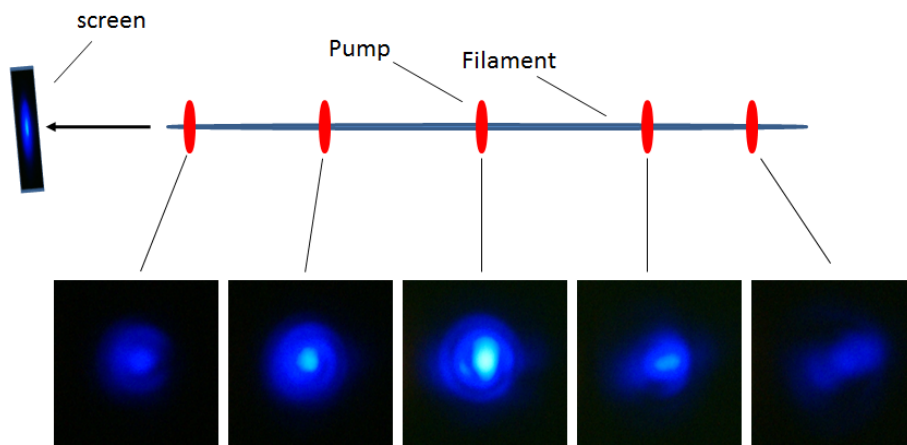


Figure 4.2-5 Conversion efficiency and spatial distribution of the TH beam at several positions for the pump slab along the Signal filament.

In both Figure 4.2-4 (a) and (b), the polarization of TH emission in both cases was linear and parallel to the polarization of the Signal beam. Clearly, the centro-symmetric shape of the TH cannot be explained considering only the Pump cylindrical plasma string and would suggest that the Signal filament beam profile plays an important role. By Fourier transforming the far-field Bessel-like TH pattern, one can retrieve its near-field profile, which consists of a central spot surrounded by a single ring as shown in Figure 4.2-6. This kind of profile is known to exist in filamentation produced by circularly apertured Gaussian beams (see for example [172]). For further confirmation of this scenario, we repeated the experiments without using the iris aperture on the Signal arm, which resulted in a simple Gaussian filament mode. The TH obtained in the latter case showed only an on-axis component without any surrounding rings.

To find the far-field divergence and relative intensities of the generated third-harmonic beams, we recorded their intensity distributions at various distances from the filament using a linear CCD. Dashed and solid curves in Figure 4.2-4(c) represent the one-dimensional azimuthally averaged TH intensity profiles versus divergence angle, which correspond to Figure 4.2-4(a) and (b), respectively. It is clear that the insertion of the Pump plasma string dramatically reshapes the intensity distribution in a way that the axial emission now dominates. The divergence of the high-intensity central lobe (~ 1 mrad half-angle) is 8 times smaller than that of the TH ring of Figure 4.2-4(a) (~ 8 mrad half-angle).

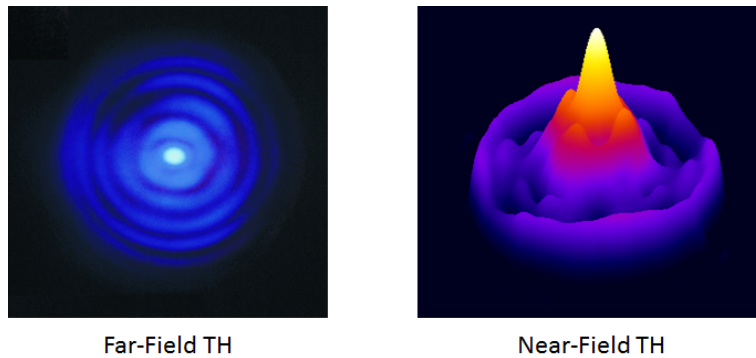


Figure 4.2-6 Far-field and near field of the TH beam. The near-field profile is simply achieved by a two-dimensional Fourier transformation of the far-field profile.

The total energy of the generated TH wave as a function of the delay τ is presented in Figure 4.2-7. Here, plots for two different Pump pulse energies, 0.5 mJ and 2 mJ, are shown. For each energy, TH signal was recorded first for collinearly polarized Pump and Signal waves (open triangles and open circles for 0.5 mJ and 2 mJ Pump, respectively), and then for cross-polarized beams (solid triangles and solid circles for 0.5 mJ and 2 mJ Pump, respectively). Regardless of the Pump energy, similar behavior was observed. TH signal grew fast with an increase of the delay reaching, a maximum at $\tau \approx 250$ fs, and stabilized at $\tau \approx 500$ fs. At longer delays (see inset in Figure 4.2-7), the TH energy exhibited a slow monotonic decay, well described by a $(1 + \beta t)^{-1}$ function with decay constant $\beta \approx 0.02 \text{ ps}^{-1}$ which is in good agreement with that measured by Tzortzakis *et al.* in Ref. [105] for free-electron density decay in a femtosecond laser induced plasma channel in air. This is a strong indication that TH generation efficiency is correlated to free-electron density in the Pump plasma string.

It is clear that Kerr and other intensity related contributions to the TH signal are limited to the delays comparable with ~ 500 fs needed for the Pump pulse to cross the Signal filament core. This is confirmed by the fact that TH maxima in Figure 4.2-7 are well pronounced for co-polarized beams whereas for cross-polarized geometry they are barely visible. Such difference is attributed to higher intensities produced due to interference of the two pulses in the co-polarized case. On the other hand, for $\tau > 500$ fs, the enhancement of the TH signal occurs solely due to the presence of the plasma string generated by the Pump pulse, and compared to the negative- τ case, it represents approximately 50- and 70-fold increase in TH energy for 0.5 mJ and 2 mJ Pump, respectively.

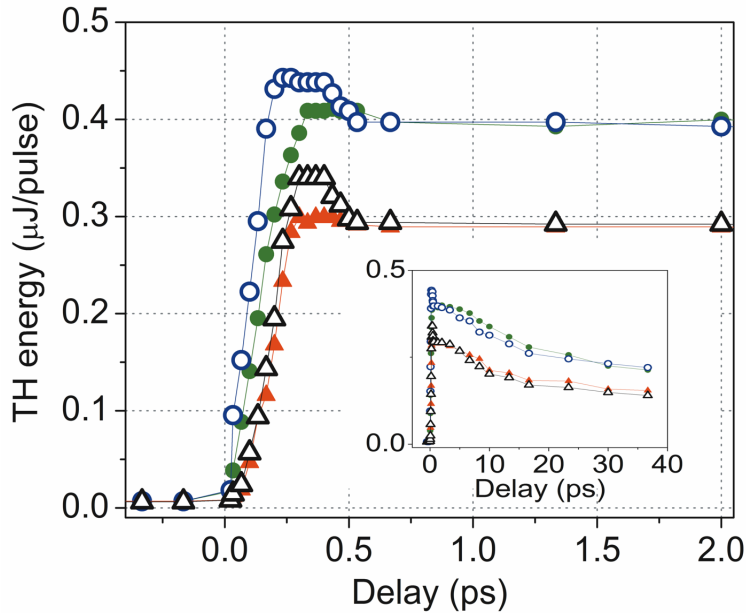


Figure 4.2-7 TH energy as a function of the delay between the Pump and Signal pulses. Two lower curves: Pump energy 0.5 mJ, open and solid triangles for co-polarized and cross-polarized beams, respectively. Two upper curves: Pump energy 2 mJ, open and solid circles for co-polarized and crossed-polarized beams, respectively. Inset: the same plot with the delay scale extended to 40 ps.

The dependence of the TH signal on the Pump energy is shown in Figure 4.2-8(a) for three different Signal pulse energies: 0.15, 0.7, and 1.5 mJ. The delay τ was set at 1 ps to make sure that any Kerr contribution to the generated TH is avoided. Figure 4.2-8(a) shows that regardless of the Signal energy, TH energy reached saturation at the same (approximately 1 mJ) Pump energy. This behavior is correlated with the appearance of saturation in the plasma string electron density to the gas density $\sim 2.5 \times 10^{19} \text{ cm}^{-3}$ confirmed by independent electrical

conductivity (PCo) [117, 119] and in-line holographic microscopy (i-HOM) [122, 123] that are discussed in detail in Chapter 2.

Since the increase of Pump energy beyond 1 mJ/pulse resulted in saturation of TH energy, we wanted to find optimal conditions in terms of TH generation efficiency. For that purpose, we measured TH energy as a function of Signal pulse energy for a constant Pump of 2 mJ/pulse, and conducted similar measurements in the absence of the Pump beam. The corresponding experimental results, along with the TH enhancement factor calculated as a ratio of the TH signal in the presence of Pump to that without Pump beam, are presented in Figure 4.2-8(b). They show that for Signal energies up to 0.6 mJ/pulse we have about two-orders of magnitude enhancement of TH energy while for 2.5 mJ/pulse it is increased by mere 50%. Hence, TH generation in the presence of the Pump plasma string has a particular advantage at low Signal pulse energies up to 0.6 mJ/pulse enabling us to obtain both the much higher energy and the better-collimated TH beam.

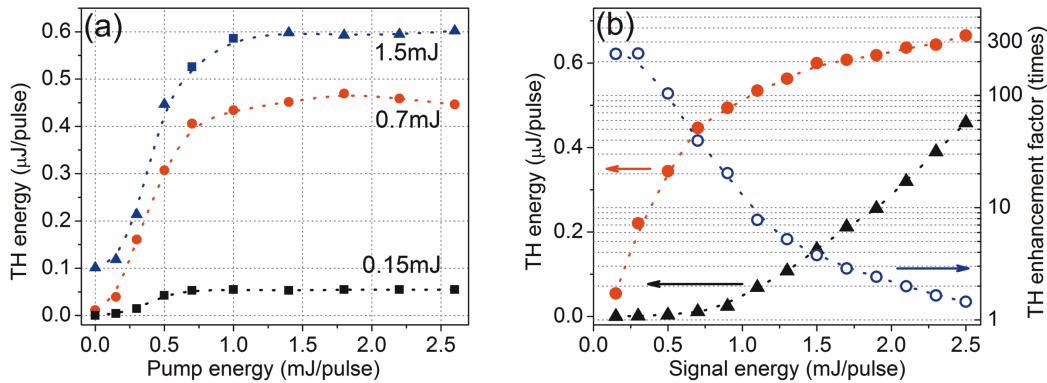


Figure 4.2-8 (a) Measured dependence of TH signal on Pump energy for Signal pulse energy 0.15 mJ (squares), 0.7 mJ (circles), and 1.5 mJ (triangles). (b) TH energy versus Signal pulse energy in the absence of Pump (triangles) and at Pump energy 2 mJ/pulse (circles). The ratio of these two curves represents the TH enhancement factor shown with open circles in (b).

The correlation of the TH emission with plasma attributes such as saturation and decay rate is a strong indication that plasma presence is responsible for the significant enhancement of TH conversion efficiency. Although further exploration is needed to establish a clear view on the physics behind the observed effect, we can propose several candidate mechanisms that could lead to this interesting behavior. It is clear that the presence of a thin (<100 μm) plasma string perpendicular to the filament propagation leads to a significant and abrupt change of the optical

properties of the medium. As it was recently shown by numerical simulations [169], the TH generation arises from the total material polarization response, i.e. this process can be viewed as a first order scattering process of the incident field from the refractive index changes induced by the intense propagating pulse. Thus, the TH beam is practically decoupled from the core filament after being generated by the nonlinear processes. Likewise, the enhanced TH generation in our case can be the result of an effective increase of the nonlinearity that is induced either by the nonlinear properties of plasma [173] or by an interface effect [174]. More specifically, the plasma can be viewed as a nonlinear medium [173] at the intensity levels achieved in the filament core ($\sim 10^{13}$ W/cm²) if we take into account the interaction of the strong laser field with electrons under the perturbation of a strongly nonlinear ionic potential. This model predicts an effective enhancement of the TH generation efficiency, which is proportional to the square of plasma density. On the other hand, a significant enhancement of the generated TH has been reported [174] when an ultrafast laser beam is focused on interfaces. The effective nonlinear coefficient for the case of an air/glass interface [174] is by at least 3 orders of magnitude higher than that of bulk glass or air. This enhancement was attributed to either an interface enhanced susceptibility affected by the field gradient [174] or to a competition [175] between the group and phase velocity mismatch that is sensitive only to interfaces.

4.2.3 Enhancement of TH emission from a filament screened by an obstacle

While performing the above-mentioned experiments by considering the Pump plasma slab as an obstacle that partially blocks the Signal filament, we concluded that any other obstacle with similar diameter to the Pump plasma should result in similar results. In order to confirm this scenario, we inserted a piece of 90 μm thick copper wire in the path of the filament, a two orders of magnitude enhancement and also redistribution of the TH beam was observed and similar results were obtained by replacing the wire with a 120- μm -thick optical fiber. In Figure 4.2-9 are shown the fundamental and TH beam profiles resulted by placing the optical fiber and the wire, captured on a piece of yellow paper. Interestingly, the enhancement and reshaping occurred after a few seconds until the obstacles were ablated and even cut by the filament. Moreover, like the former experiment, the maximum enhancement in the TH conversion efficiency was obtained when the obstacles were placed at the center of the Signal filament.

This observation though not reported by us, was confirmed both through simulations [176] and experiment [177]. In their work, this enhancement is attributed to the diffraction of the TH emission on the fiber and the reconstruction of two-colored filament (fundamental and TH) that redistributes the energy.

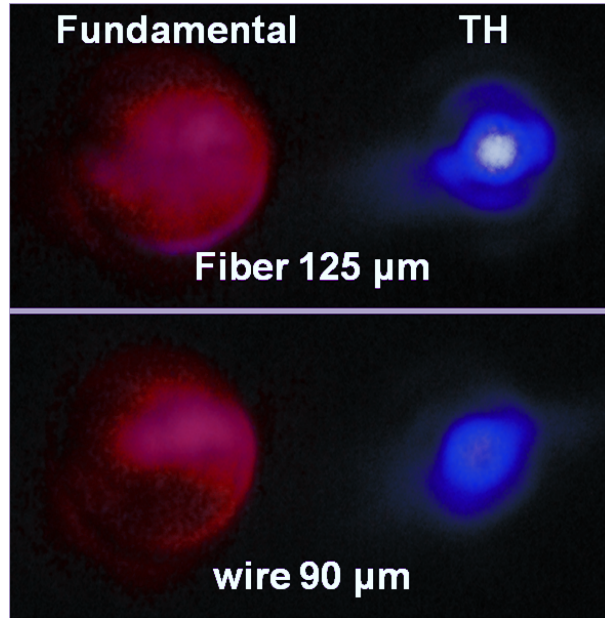


Figure 4.2-9 Reshaping and enhancement of TH by introducing a piece of 125 μm -thick optical fiber (top) and a 90 μm -thick copper wire in the middle of the Signal filament. The images of the separated fundamental and TH beams are captured on piece of paper by a photographic camera.

4.2.4 Physical mechanism of TH generation enhancement in the presence of the Pump plasma slab

Although strong correlation of THG efficiency with plasma density saturation and with its decay rate indicated the plasma presence was responsible for the observed effects [170], the underlying physical mechanism was not clearly understood. We contemplated two completely different approaches that could, in principle, explain the observed enhancement of THG efficiency. The enhancement of the TH generation could emerge from a bulk effect, that is an increase of the nonlinear coefficient correlated with the presence of plasma as suggested in [173, 178], or through a neutral air-plasma interface effect similar to that observed by Tsang at air-dielectric interfaces [174].

To reveal the physical mechanism of THG efficiency enhancement in the presence of the plasma string, we conducted a series of experiments and theoretically investigated possible scenarios. We show that the bulk plasma-enhanced nonlinear susceptibility, and not the air-plasma interface effect, is responsible for the observed TH enhancement. Furthermore, we propose a phenomenological model and derive a simple expression for the TH intensity that quantifies the dependence of the TH signal on the plasma density. Using this model, which also takes into account phase matching between the fundamental and the harmonic waves in the plasma volume, we discuss the limitations of the technique in producing energetic pulses at third-harmonic frequency in a low-density plasma.

- **Experimental results and discussion**

The experiments were conducted using a Ti:Sapphire chirped pulse amplification laser system supplying 35-fs, 800-nm IR pulses with energies up to 30 mJ at a 50-Hz repetition rate. The schematic is shown in Figure 4.2-10. First, the fundamental laser beam was split in two arms, Pump and Filament, using a beamsplitter. Laser pulses in the Filament arm with 0.5-mJ energy were focused using a 100-cm-focal-length lens L1 creating a light filament in air with a length of about 5 cm. The filament interacted with the plasma string generated by pulses in the Pump arm that were focused perpendicularly to the Filament beam with a combination of a spherical (L2, focal length 10 cm) and a plano-convex cylindrical (CL, focal length $\infty/10$ cm) lens. This astigmatic arrangement leads to the generation of two orthogonally oriented plasma channels in the sagittal and meridional foci. By changing the distance between L2 and CL we were able to vary the length of the horizontally oriented plasma string in the meridional focus, while its spatial overlap with the filament was achieved by moving the two lenses as a whole along the Pump beam path. The delay between the pulses in the Filament and the Pump arms was adjusted with an optical delay line. After the filament, a fused silica prism P was used to angularly separate the TH and fundamental waves. Finally, the TH energy was measured using a calibrated photodetector (D) which was preceded by an interface filter at 266 nm.

In order to study the nature of the physical mechanism responsible for the harmonic emission enhancement, we first need to distinguish between the two different mechanisms that could, in principle, explain the observed effect, namely the bulk plasma properties and the neutral air-plasma interface.

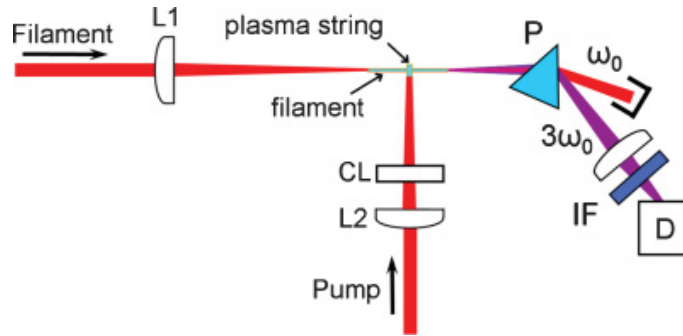


Figure 4.2-10 Experimental setup: L1, L2, lenses; CL, plano-convex cylindrical lens (cylindrical axis is parallel to the plane of the figure); P, prism; IF, interface filter at 266 nm; D, calibrated photodetector.

More specifically, the presence of charged species (free electrons and ions) can effectively increase the third-order susceptibility of the medium [173, 178]. Thus, the enhancement of TH generation in this case would be the result of a bulk effect in the plasma volume. On the other hand, since the refractive index of a medium changes in the presence of plasma, then by introducing the Pump plasma string we create an interface between the two media with different refractive indices (under our experimental conditions, this difference in air can be as high as 7×10^{-3} [119, 122, 123]). Therefore, at such an interface, the inversion symmetry of the bulk along the Filament beam propagation direction is broken, resulting in a field gradient that could be responsible for the enhancement of TH emission (see for example Ref. [174]).

In the case of bulk nature of the effect, one would expect the harmonic emission to grow with the plasma thickness (assuming all other parameters are the same), while this would have no effect in the case of the interface model, as the number of interfaces remains the same. Therefore, in order to clarify the origin of the physical mechanism that drives the enhancement of the harmonic wave, we conducted TH generation experiments with various thickness of the Pump plasma string. Using the astigmatic two-lens arrangement, described above, we created three plasma strings in the Pump arm with different thicknesses of 0.4, 0.7, and 1 mm, respectively. To guarantee the same mean plasma density ($\sim 5 \times 10^{17} \text{ cm}^{-3}$) inside all three plasma strings, the Pump pulse energy was set at 2.5, 5, 8 mJ, respectively. The total measured TH energy as a function of the delay τ between the Pump and Filament pulses for all three cases is shown in Figure 4.2-11(a). For better understanding these results, a simple schematic of the relative position of the Pump and Filament pulses at different delays is shown in Figure 4.2-11(b). We define a zero delay point as the delay at which the plasma, produced by the Pump

pulse, starts to affect the Filament pulse propagation and, consequently, the energy of the harmonic emission. With further increase of the delay, the filament pulse will interact with the remaining portion of the Pump plasma channel.

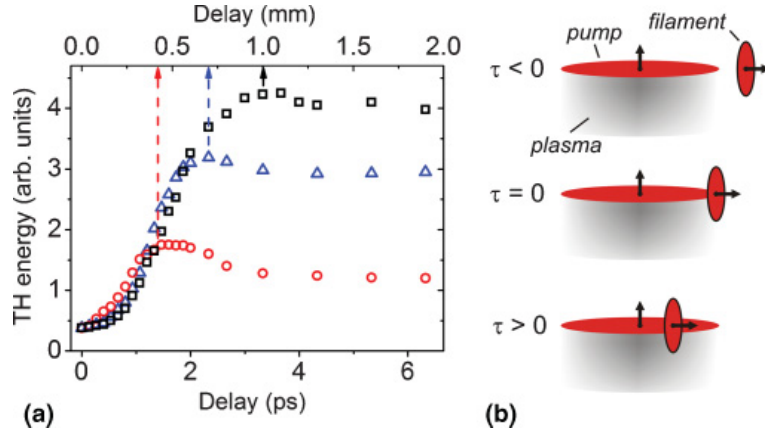


Figure 4.2-11 (a) TH energy as a function of the delay between the Pump and Filament pulses for Pump plasma channel thickness of 0.4 mm (circles), 0.7 mm (triangles), and 1mm (squares). The locations of the harmonic signal maxima are indicated by vertical arrows. (b) Schematic of the relative position of the Pump and Filament pulses at different timing in the experimental geometry.

Finally, the maximum interaction length will be achieved when the delay (expressed in millimeters of light propagation in air) becomes equal to the Pump plasma string thickness. Therefore, the delays that correspond to the maxima of the TH energy in Figure 4.2-11(a) are equal to the respective plasma string thicknesses, namely 0.4, 0.7, and 1 mm. The results of Figure 4.2-11(a) are a clear indication of the bulk nature of the effect since the maximum TH energy monotonically grows with the plasma thickness. Additionally, the concept of TH enhancement through an interface effect fails to predict our experimental results because in this case the TH energy should depend on the number of interfaces, which in all three cases is constant (two interfaces). The observed subsequent drop in the harmonic emission in Figure 4.2-11(a) at higher delays is due to the plasma density decay in the Pump channel, as was also observed in Ref. [170].

- **Theoretical model**

Since we have proven that the effect of interface in our case is not important during TH generation in a plasma channel, we focus on the concept of the enhanced bulk third-order optical susceptibility due to the presence of free-electron-ion plasma. Using this assumption and

according to the well-known formula [179, 180], the third-harmonic intensity for the case of a Gaussian beam focused in the middle of a plasma medium can be written as

$$I_{3\omega}(\Delta k, L) = \frac{(3\omega)^2}{16 \cdot n_{3\omega} n_{\omega}^3 c^4 \varepsilon_0^2} \left| \chi_{pl}^{(3)} \right| I_{\omega}^3 \left| \int_{-L/2}^{L/2} \frac{\exp(i\Delta k z)}{(1 + iz/z_R)^2} dz \right|^2 \quad (4.2-1)$$

where $\chi_{pl}^{(3)}$ is the plasma-enhanced third-order susceptibility, I_{ω} is the fundamental intensity, $\Delta k = 3k_{\omega} - k_{3\omega}$ is the total wavevector mismatch between the fundamental and TH waves, L is the plasma thickness, z_R is the Rayleigh length, and n_{ω} , $n_{3\omega}$ are the refractive indices at the fundamental and TH frequency, respectively. Equation (4.2-1) takes into account the generation of the third-harmonic wave in the bulk of an ionized medium due to effective third-order susceptibility, as well as the effect of the phase mismatch between the fundamental and harmonic waves due to chromatic dispersion. Although Eq. (4.2-1) is written for continuous-wave beams, it still holds for ultrashort laser pulses under our experimental conditions, since the maximum calculated walk-off between the fundamental and TH pulses caused by the group velocity dispersion in a thin plasma layer or ionized air does not exceed 1 fs. In a quasiplanar limit for the fundamental wave phase front ($L \ll Z_R$), which was also the case in our experiments, Eq. (4.2-1) can be simplified to

$$I_{3\omega}(\rho_e, L) \propto \left| \chi_0^{pl(3)} \right|^2 \rho_e^2 \frac{\sin^2(\Delta k L / 2)}{(\Delta k / 2)^2} \quad (4.2-2)$$

where we replaced $\chi_{pl}^{(3)}$ with $(\chi_0^{pl(3)} \rho_e)$ where $\chi_0^{pl(3)}$ is the specific effective third-order optical susceptibility, and ρ_e is the plasma density (representing the density of the effective nonlinear medium).

It is worth noticing that the wave-vector mismatch Δk in Eq.(4.2-2) is itself a function of plasma density. The absolute value of the total wavevector mismatch as a function of the plasma density, calculated using the Sellmeier, for atmospheric density air [181] and the Drude model for plasma [122], is plotted in Figure 4.2-12(a). Clearly, since there is always nonzero Δk , on-

axis third harmonic generation in plasma is not phase-matched. Let us now analyze how the harmonic intensity given by Eq. (4.2-2) depends on the plasma density ρ_e . As can be seen in Figure 4.2-12(a), for densities up to 10^{16} cm⁻³ the wavevector mismatch is nearly constant (~ 5.3 cm⁻¹) because the major contribution to it comes from the linear dispersion of air. Therefore, in the low plasma density limit, Eq.(4.2-2) can be written as $I_{3\omega} \propto \rho_e^2$, $\rho_e \leq 10^{16}$ cm⁻³. On the other hand, at densities in excess of 5×10^{17} cm⁻³, Δk is dominated by the plasma-induced refractive index changes and is linearly proportional to the plasma density. Hence, in the high plasma density limit, Eq. (4.2-2) becomes: $I_{3\omega} \propto \sin^2(\text{const} \times \rho_e L)$, $\rho_e > 5 \times 10^{17}$ cm⁻³.

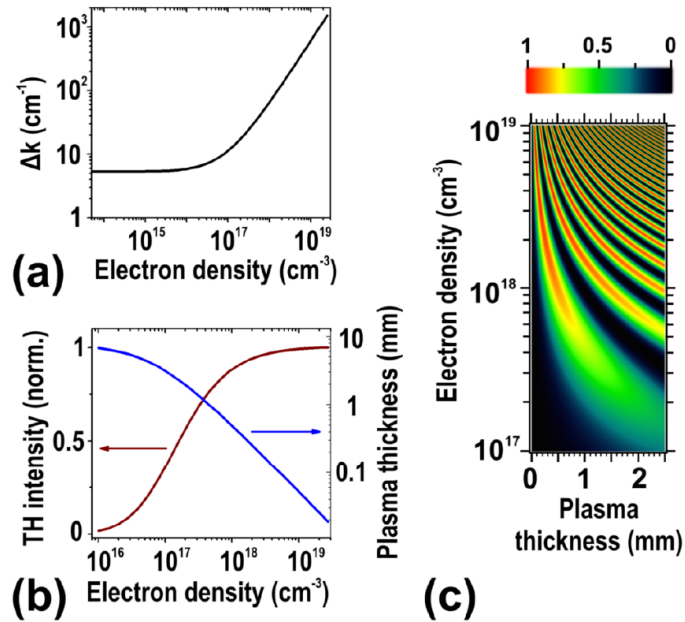


Figure 4.2-12 (a) Total wave-vector mismatch Δk between 800 and 267 nm wavelengths as a function of plasma density. (b) Maximum TH intensity in normalized units (left vertical scale) and minimum plasma thickness L needed to reach it (right vertical scale) versus electron density. (c) False color two-dimensional map of TH intensity versus plasma density and plasma thickness (normalized units).

Equation (4.2-2) predicts oscillations of the harmonic intensity as the plasma density ρ_e or plasma thickness L are increased while the oscillation amplitude is no longer dependent on ρ_e . Figure 4.2-12(c) shows the two-dimensional map of TH intensity versus plasma density and its thickness, calculated using Eq. (4.2-2). In addition, the maximum harmonic intensity versus minimum plasma thickness needed to reach it, are plotted in Figure 4.2-12(b) as a function of

plasma density. Clearly, to generate stronger harmonic signal, it is advantageous to use higher density (and respectively, thinner) plasma string. In any case, the TH signal will finally saturate because of the already discussed independence of the amplitude of TH intensity oscillations on ρ_e at high plasma densities. This limits the efficiency of the TH generation achievable with the described technique. To further increase the efficiency, other techniques should be used (e.g. quasi-phase-matched plasma structure such as an optically performed period plasma waveguide [182] or plasma with density ripple [183]).

To verify the proposed phenomenological approach, we measured first the TH signal as a function of Pump pulse energy. As in the previous work (Sec. 0 and also [170]), a thin (<100 μm) plasma string was produced in the Pump arm using a single 10 cm-focal length spherical lens. Since the theoretical harmonic intensity of Eq. (4.2-2) is given in terms of plasma density, the next important step was to find the correlation of plasma density and the thickness of the produced plasma channel with the Pump pulse energy. This was done using independently in-line holography [122, 123] and plasma conductivity techniques [119]. Our measurements showed that as the pump pulse energy varied from 0.15 to 1.5 mJ, the peak plasma density ρ_e and the effective thickness L varied in a range $7 \times 10^{18} \text{cm}^{-3}$ to $1.55 \times 10^{19} \text{cm}^{-3}$, and 8 to 38 μm , respectively. In Figure 4.2-13, we compare the normalized theoretical and experimentally measured TH intensities plotted as a function of plasma density. The theoretical points were calculated by substituting the experimentally measured values of the plasma string density and thickness into Eq. (4.2-2). The agreement between the theoretical predictions and the experimental values is excellent.

Despite the significant number of theoretical studies in the literature on third-harmonic generation in plasmas, most of them consider fully ionized plasmas and/or relativistic regime (laser intensities above 10^{18}W/cm^2). A consistent quantum-mechanical analysis of THG in low-density gaseous plasma under conditions close to those in our experiments is missing. However, the successful prediction of the behavior of the TH intensity by the simple phenomenological model of the enhanced third-order susceptibility enables us to go one step further and give a rough estimate of the $\chi_{pl}^{(3)}$ value.

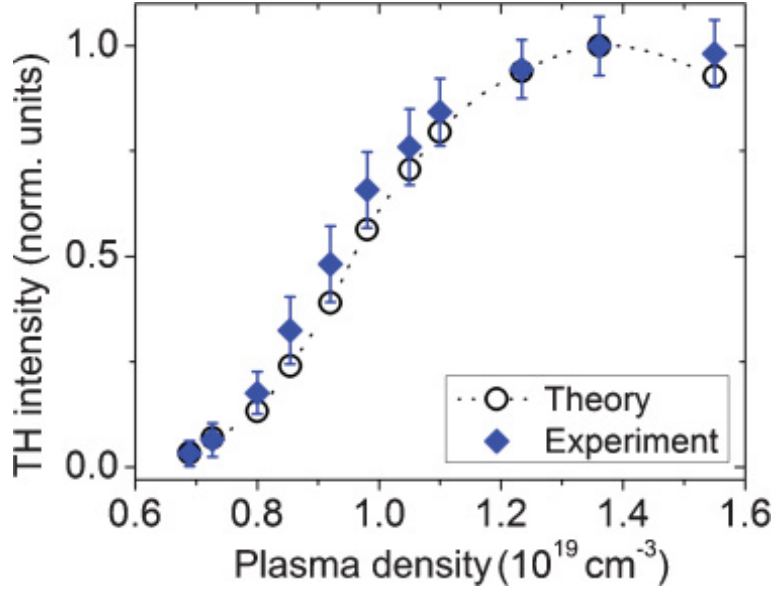


Figure 4.2-13 Theoretical (circles) and experimentally measured (diamonds) normalized TH intensity as a function of the plasma density in the Pump channel.

This can be done using Eq. (4.2-1) and the results of our work in Section 0 [170], where approximately 250 times enhancement of TH intensity was achieved upon intersecting the filament by a thin ($L \sim 30 \mu\text{m}$), dense ($\rho_e \sim 2 \times 10^{19} \text{ cm}^{-3}$) plasma channel. We estimate that during the filamented pulse propagation in air under our experimental conditions, the peak fundamental intensity I_ω reached $(5 \pm 2) \times 10^{13} \text{ W/cm}^2$ [5]. The value of the peak harmonic intensity $I_{3\omega} \sim (1.2 \pm 0.6) \times 10^{12} \text{ W/cm}^2$ was found using the measured TH pulse energy $0.6 \mu\text{J}$, the estimated harmonic pulse duration $(30 \pm 3) \text{ fs}$, and the TH beam near-field diameter of $(50 \pm 10) \mu\text{m}$. By substituting these numbers into Eq. (4.2-1), we estimate $\chi_{pl}^{(3)}$ to be approximately equal to $(1.8 \pm 0.75) \times 10^{-23} \text{ m}^2/\text{V}^2$. This number is more than one order of magnitude higher than the third-order nonlinear susceptibility of air $\chi_{\text{air}}^{(3)} \sim 1.1 \times 10^{-25} \text{ m}^2/\text{V}^2$ (corresponds to the Kerr nonlinear coefficient of atmospheric pressure air $n_2 \sim 3.2 \times 10^{-19} \text{ cm}^2/\text{W}$ [184]).

Thus, we have shown that the enhancement of third-harmonic wave generated within femtosecond IR filament in air when it crosses a thin plasma string, created by another advancing focused laser pulse, is a bulk process that does not rely on the properties of the produced neutral air-plasma interfaces. Despite the complex dynamics arising from a variety of linear and

nonlinear effects involved, the more than two-order-of-magnitude increase of third-harmonic generation efficiency in a presence of the relatively low density ($\rho_e < 2 \times 10^{19} \text{ cm}^{-3}$) plasma string can be satisfactorily described by an effective, plasma-enhanced third-order optical susceptibility. Using this simple phenomenological approach, we are able to accurately describe the functional dependence of the THG enhancement on the plasma density. More recently, Rodriguez *et al.* [185] have proposed to characterize laser-induced air plasmas by THG. To describe the enhancement of the third harmonic generation in plasma, they have also considered the enhancement of third-order susceptibility by the plasma. In a similar approach to ours, they have also found an effective third-order susceptibility, for electron densities similar to our experiments, that is in very good agreement with our findings. Our results suggest the use of free-electron-ion plasma as a nonlinear medium for efficient wave-mixing process such as generation of energetic XUV pulses. Also this finding could eventually explain the strong THz emission from filaments in air [186] and maybe the observation of Kerr saturation [32, 35].

4.3 Plasma Diffraction Gratings

In the present section, it is demonstrated that in a proper configuration, the filamentation-induced plasma strings can form plasma photonic devices. The creation of volume plasma gratings in air by temporally overlapped high intensity IR femtosecond laser pulses is demonstrated experimentally. Through diffraction of various probe beams, the plasma grating properties are recovered including its thickness and refractive index modulation, as well as its decay dynamics. The diffraction properties of these plasma photonic devices suggest that they can be used in applications involving high intensity lasers, such as filamentation, where no physical objects can be placed in the path of the laser beams.

- **Plasma photonic devices**

Over the past two decades, nonlinear effects in plasma and high intensity laser-plasma interactions have been a subject of considerable interest in the scientific community. Many exciting novel phenomena have been predicted, with some of them now having important practical applications. For instance, the so-called *plasma mirror* is nowadays widely used for improving the temporal contrast of intense ultrashort laser pulses [93, 187] as depicted in Figure 4.3-1. CPA generated temporal profiles usually have a prepulse and a wider pedestal, which its

presence can be detrimental for many of the applications for which high intensity lasers are being developed. As illustrated in Figure 4.3-1, upon the reflection from the first plasma mirror most of the low-intensity component is attenuated and upon the reflection from the second plasma mirror results in further cleaning of the pulse and 10^4 times improvement in the pulse contrast [188]. Other applications of plasma mirrors such as ultrafast gating of femtosecond pulses [189] and generation of few-optical-cycle pulses in the midinfrared [190] have also been demonstrated.

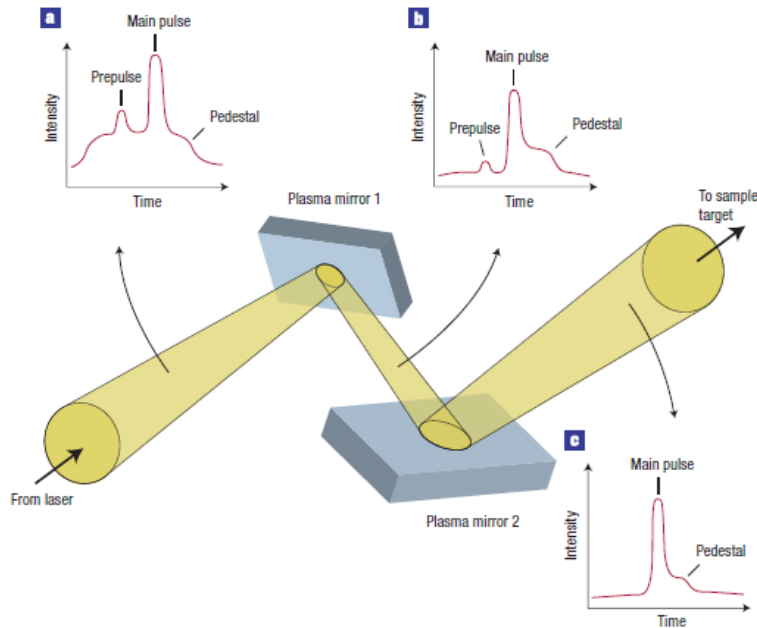


Figure 4.3-1 Laser pulse cleaning by a double plasma mirror (a) CPA generated temporal profile, which usually has a prepulse and a wider pedestal. (b) The same pulse after reflection from the first plasma mirror. (c) Reflecting this off a second plasma mirror cleans the pulse still further. From [188].

Considerably less attention has been paid to another category of potential photonic devices, plasma diffraction gratings. A decade ago, the possibility of inducing a grating-like electron density distribution at the surface of uniform plasma by two intersecting laser beams has been explored theoretically [191]. More recently, the formation of volume electron and ion density grating induced by two counter-propagating/intersecting high-intensity laser pulses inside the bulk underdense plasma has been also investigated theoretically [192, 193]. In all these studies, either surface or bulk plasma density variations have been formed in pre-existing uniform plasma. Moreover, the research activity in this area has remained purely theoretical.

Here we report on the experimental demonstration of the formation of a volume-plasma-density-grating in air by temporally overlapping high-intensity IR femtosecond laser pulses of two intersecting focused laser beams. Unlike earlier theoretical studies [192, 193], in which pre-existing uniform plasma with rather high initial electron densities up to $0.3\rho_c$ was assumed (where ρ_c is the critical electron density; $\rho_c = 1.7 \times 10^{21} \text{ cm}^{-3}$ in air for 800 nm); plasma density modulation in our experiment is created in ambient air and follows the sinusoidal intensity distribution produced by two interfering laser pulses.

Contrary to conventional optical elements exhibiting specific, and usually low, damage threshold, plasma gratings could be considered prospective candidates for a variety of high-intensity laser applications, e.g., pulse stretching, chirped pulse compression, phase-matched relativistic harmonic generation, etc., [193-195]. In addition, the possibility of creation of more sophisticated three-dimensional (3D) plasma photonic lattices would open new ways in controlling the propagation of high-intensity ultrafast laser beams and laser filaments. Actually, laser filaments are ideal candidates for using plasma photonic lattices to optimize and control their properties [196].

4.3.1 Experimental setup and theoretical background

The schematic of the experimental setup is shown in Figure 4.3-2. The output of the laser (35 fs at central wavelength of 800 nm with pulse energies up to 30 mJ, operating at 50 Hz repetition rate) was split into two arms. Pulses in the Beam 1 and Beam 2 arms with energies 0.7 mJ each were focused in a perpendicular geometry with lenses L1 and L2 (focal length 10 cm and 40 cm, respectively), each one producing a few millimeters-long dense plasma channel in air. To study the diffraction properties of the grating created at the intersection of these two beams, we used a third probe arm, as shown in Figure 4.3-2. In different experiments, either a second-order nonlinear Beta-Barium Borate crystal (BBO) to produce the second harmonic (SH) of the fundamental wave or a fused silica plate to generate a broad supercontinuum (SC) was inserted into the probe arm. The timing between different pulses was adjusted using standard optical delay lines. All beams in the experiments were polarized linearly, perpendicular to the plane of Figure 4.3-2. Furthermore, no diffraction effects were observed when Beam 1 and Beam 2 were orthogonally polarized.

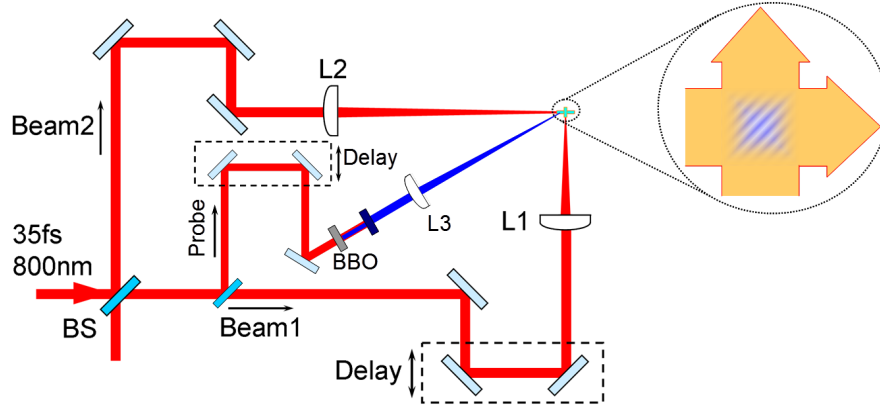


Figure 4.3-2 Schematic of the experimental setup to create and study plasma diffraction gratings in the air. L1, L2, and L3 lenses; BS, beam splitter.

4.3.2 Experimental results and discussion

It is clear that when the high-intensity Beam 1 and Beam 2 pulses are temporally overlapped, the total intensity is spatially modulated due to their interference. This intensity pattern leads to respective, spatially modulated, refractive index changes through nonlinear effects such as the optical Kerr effect and nonlinear ionization. The refractive index modulation can be written as $\Delta n = \Delta n_{\text{Kerr}} + \Delta n_{\text{Plasma}}$, where $\Delta n_{\text{Kerr}} = n_2 I_{\text{tot}}$ is the Kerr contribution, n_2 is the nonlinear Kerr coefficient and I_{tot} is the total intensity and where $\Delta n_{\text{Plasma}} = -\rho_e / (2\rho_c)$ is the plasma contribution, ρ_e is the plasma density, and ρ_c is the critical plasma density. While the optical Kerr effect acts only when the pulses are temporally overlapping, the generated plasma results in refractive index changes that persist until the electrons are trapped back by the ions. Thus, a volume index grating (also called volume Bragg or volume holographic grating), persisting for a few tens of picoseconds, should then be formed due to the interference of the two beams. For our orthogonal beams configuration in air, the grating period would be $\Lambda = \lambda_0 / \sqrt{2} \approx 566$ nm, and its refractive index planes would be oriented along the bisector of the angle formed by two beams as shown in Figure 4.3-3. The coupled wave analysis of Kogelnik [197] was used to describe the diffraction properties of these gratings. According to this analysis, when a volume grating with a period of Λ is formed in air (i.e. the grating background index is close to unity), a monochromatic wave at wavelength λ will be efficiently diffracted if its angle of incidence onto

the grating $\theta_i(\lambda)$ and the diffraction angle $\theta_d(\lambda)$ with respect to the normal to the grating wavevector G satisfy the Bragg's condition:

$$\theta_i(\lambda) = \theta_d(\lambda) = \sin^{-1}(\lambda / 2\Lambda) \quad (4.3-1)$$

- **Characterizing the plasma diffraction grating**

A series of experiments were performed to characterize these volume-plasma-density-gratings and to demonstrate that they can be used as ordinary volume gratings. To measure the grating period we increased Beam 1 energy to 1.5 mJ/pulse to generate SC in this arm, as shown in Figure 4.3-4(a). Even though SC is generated simultaneously with the grating formation, a small fraction of it still experiences diffraction. A schematic of this SC diffraction process is shown in Figure 4.3-4(b), where the incident and diffracted SC waves are shown together with the relevant beams' and grating wavevectors. A photograph of the diffracted SC taken with a digital camera on a paper screen placed perpendicularly into the Beam 2 path is shown in Figure 4.3-4(c).

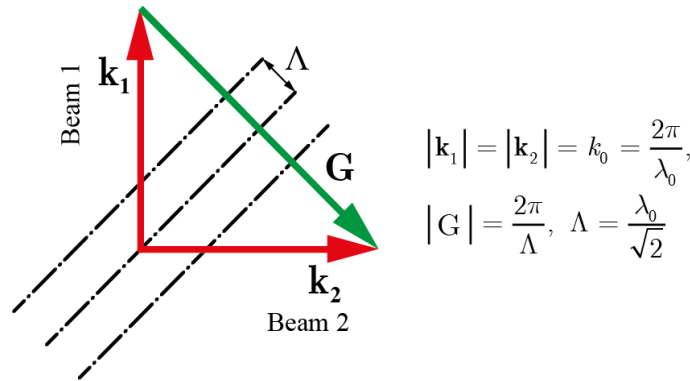


Figure 4.3-3 Wavevectors of Beam 1 and Beam 2 and the plasma diffraction grating. The dashed-dotted lines represent the refractive index planes.

In order to explain the observed rainbow-like appearance of the SC diffraction pattern, we have performed numerical simulations of the diffraction of a similar to experiment, wide-angular spectrum, SC beam by volume gratings with various thicknesses, based on the coupled wave analysis of hologram gratings [197]. The simulated diffracted intensities are presented in Figure 4.3-5. They show that the extent of the diffraction pattern in the vertical direction is highly dependent on the grating thickness because, as the latter increases, the grating is transformed

from a thin to thick one. In the latter case, the Bragg conditions apply and diffraction is observed only in directions where $k_1 = k_2 + G$.

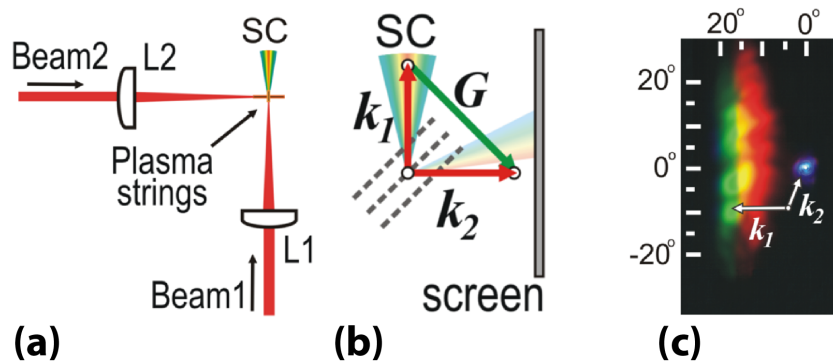


Figure 4.3-4 (a) Experimental setup, (b) wavevectors of the Beam 1 and Beam 2 and grating vector and, (c) diffracted SC of the Beam 1 from the grating (Beam 2 is the white-bluish spot).

The good qualitative agreement between experimental and simulated pattern (apart from the modulation of the experimental one caused by the inhomogeneities of the incident SC profile) allows us to infer an effective grating thickness of $<8 \mu\text{m}$, which is quite smaller than that of a fully formed grating measured in the experiments that will be described in the following.

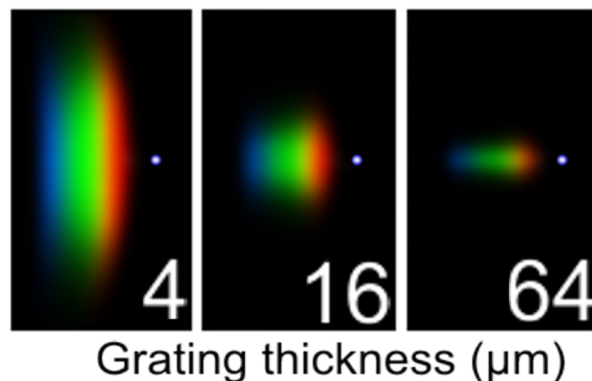


Figure 4.3-5 Simulated intensity patterns of the diffracted SC for different values of the grating thickness. In all pictures, Beam 2 appears as a bright white-bluish spot.

This difference can be easily understood as the diffraction of the SC takes place during the overlap of the two grating forming IR pulses, thus the SC experiences an effectively smaller grating thickness. On the other hand, in the horizontal direction the various SC wavelengths are

diffracted at their respective Bragg angles. By scanning the fiber tip of a spectrometer (Ocean Optics HR4000CG) in the plane of the screen along the horizontal line that passes through Beam 2 spot, we measured the diffraction angles for wavelengths ranging from 500 to 770 nm. The results are shown in Figure 4.3-6. Using Bragg's condition (Eq. (4.3-1)), grating period is $\Lambda = (566 \pm 5)$ nm, as expected from theory. We should note here that this self-SC diffraction is a nice and simple technique for synchronizing in time intense ultrashort pulses, without the need of using nonlinear crystals (e.g., BBO) and delicate sum/frequency processes, while it can be easily used for a wide variety of beam crossing angles.

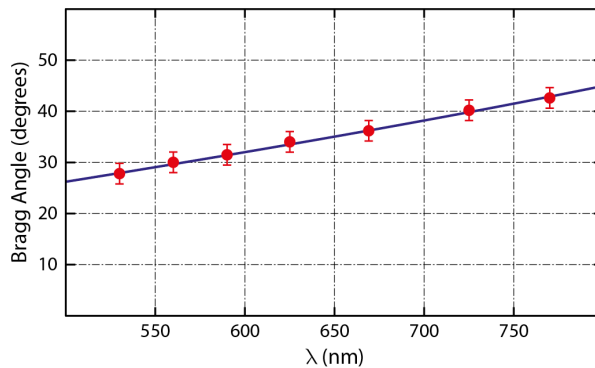


Figure 4.3-6 Measured diffraction angle of various SC components from the plasma grating (red solid circles) and theoretical fit used to calculate the period of the plasma grating (solid curve).

In the following, to retrieve the other plasma grating properties, i.e., its thickness and refractive index modulation, we studied diffraction of additional probe pulses using the setup shown in Figure 4.3-8(a). As the Bragg's condition should be fulfilled, a volume grating possesses spectral selectivity properties, and therefore, diffraction efficiency of polychromatic beam is determined by the convolution of the diffraction efficiency of a monochromatic wave with the spectrum of the polychromatic beam [198]. To obtain an incident probe beam with a broad spectrum, we inserted a fused silica plate into the probe beam arm (as shown in Figure 4.3-8(a)) and generated a SC ranging from approximately 400 to 970 nm, shown with a dashed-dotted curve in Figure 4.3-8(b). This SC beam was then weakly focused onto the grating at a Bragg angle for 543 nm wavelength ($\theta_{\text{Bragg}} \approx 28.7^\circ$), where the latter was chosen because the obtained SC spectrum is essentially flat within ~ 100 nm range centered on that wavelength.

Under these conditions, the measured diffracted probe spectrum, shown with a solid curve in Figure 4.3-8(b), should follow the grating spectral selectivity curve given by [198]:

$$\eta(\Delta\lambda) = \frac{\sin^2 \left\{ \left(\pi d_{\text{eff}} / F_{\pi/2} \right) \left[\left(\Delta n / \lambda_0 \right)^2 + \left(f^2 \Delta\lambda / (2n_{\text{av}}) \right)^2 \right]^{1/2} \right\}}{1 + \left(f^2 \lambda_0 \Delta\lambda / (2n_{\text{av}} \Delta n) \right)^2} \quad (4.3-2)$$

where Δn is refractive index modulation amplitude of the grating, d_{eff} is its' effective thickness (since we consider a constant δn in the grating), λ_0 is the central incident wavelength, $f = 1 / \Lambda$ is the spatial frequency of the grating planes, n_{av} is average refractive index of the grating and surrounding medium and $F_{\pi/2}$ is the inclination factor for the normal transmitting grating and it is given by [198]:

$$F_{\pi/2} = \left[1 - \left(\frac{\lambda_0 f}{2n_{\text{av}}} \right)^2 \right]^{1/2} \quad (4.3-3)$$

As an example, normalized spectral selectivity curves for $\Delta n = 1.5 \times 10^{-3}$, $n_{\text{av}} = 1$, $\Lambda = 566 \text{ nm}$ ($f \simeq 1.77 \times 10^6 \text{ m}^{-1}$) at $\lambda_0 = 540 \text{ nm}$ for various plasma grating thicknesses are shown in Figure 4.3-7.

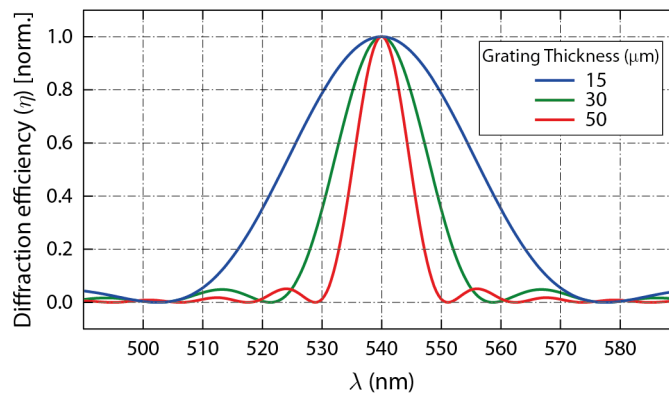


Figure 4.3-7 Spectral selectivity curves (diffraction efficiency vs wavelength) for a plasma grating with $\Delta n = 1.5 \times 10^{-3}$, $n_{\text{av}} = 1$, $\Lambda = 566 \text{ nm}$ at $\lambda_0 = 540 \text{ nm}$ for various grating thicknesses.

This figure clearly shows that for thicker gratings the bandwidths of the diffracted waves are considerably narrower. By fitting this spectrum with the calculated spectral selectivity curve, an effective (assuming constant refractive index modulation Δn of the grating planes) grating thickness $d_{\text{eff}} \approx 30 \mu\text{m}$ was found. This value is in good agreement with the width of free-electron density cross-sectional distributions of plasma channels created by Beam 1 and Beam 2, which we measured independently using in-line holography [122, 123] [Chapter 2].

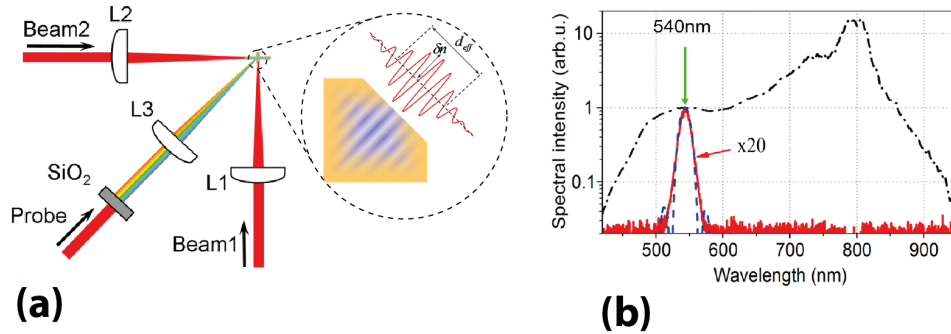


Figure 4.3-8 (a) Schematic of the experimental setup to form the plasma diffraction grating and find its dimensions. (b) Incident SC on the plasma grating at incidence angle of $\theta_i = 28.7^\circ$ (dashed-dotted curve), diffracted spectrum (red solid curve) and spectral selectivity curve for $\lambda_0 = 540 \text{ nm}$ for which the Bragg condition is held.

To measure Δn , we replaced the fused silica plate in the probe arm with a nonlinear β -BBO crystal where the SH of the fundamental wavelength was generated. After filtering out the fundamental wavelength using a band-pass filter, the SH pulses were again weakly focused onto the grating at the respective Bragg angle ($\theta_{\text{Bragg}} \approx 20.7^\circ$). It should be noted that the energy of the focused SH beam was low enough to be treated as a probe beam (as was the case for the SC in the previous experiment). Based on the maximum measured SH diffraction efficiency, which was 7.2%, and on the already known value of d_{eff} , the amplitude of the sinusoidal refractive index modulation can be obtained $\Delta n = (1.2 \pm 0.5) \times 10^{-3}$ (at 400 nm). Using a simple Drude model, we also estimate that the respective peak plasma electron density ρ_e is close to the maximum electron density of $2.5 \times 10^{19} \text{ cm}^{-3}$ that can be achieved in air considering single electron ionization per atom.

- **Temporal behavior of the grating**

In order to clearly prove the existence of a plasma density grating, we studied the dependence of the signal on the delay of the SH probe pulse with respect to the grating forming pulses. The corresponding results are shown in Figure 4.3-9. Here, negative delays correspond to the case when the incident SH pulse arrives at the Beam 1/Beam 2 crossing-point before the grating is formed, and therefore is not diffracted. The diffracted signal was observed for delays up to a few tens of picoseconds, a direct proof that we are dealing with a plasma density grating and not with a Kerr one. The decay rate for delays longer than 10 ps is consistent with the reported in the Ref. [105] plasma decay rate of $\beta = 2.2 \times 10^{-7} \text{ cm}^3/\text{s}$, taking into account that, according to Kogelnik [197], the diffraction efficiency η of such volume gratings is proportional to a square of its refractive index modulation: $\eta \propto \Delta n^2$. This dependency can be also revealed using Eq. (4.3-2), by setting $\Delta\lambda = 0$ and Taylor expanding the *sin* function.

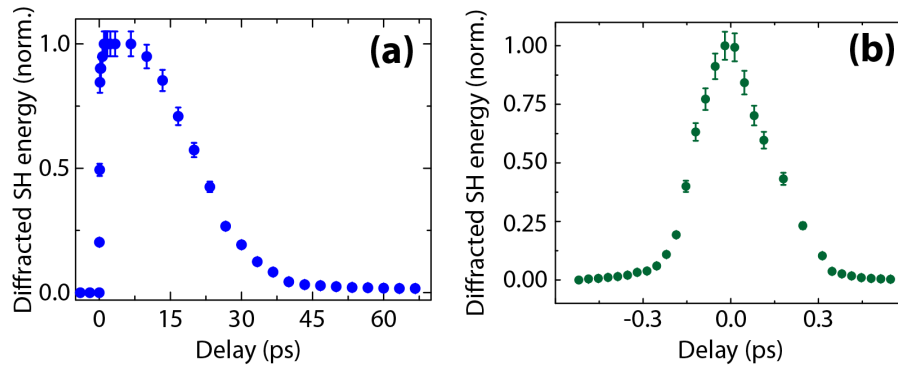


Figure 4.3-9 (a) Diffracted SH signal as a function of the delay of SH probe pulse with respect to the Beam 1/ Beam 2 pulses. (b) Diffracted SH signal vs the delay between Beam 1 and Beam 2 pulses at a fixed SH pulse delay of 1 ps.

Therefore, after 40 ps, assuming that the grating thickness d_{eff} does not change significantly with time, the plasma grating still retains $\sim 20\%$ of its maximum modulation. It is worth noticing that there is no significant decrease in the diffracted signal for delays up to ~ 10 ps, an interesting property that needs further investigation. At this point, we can only exclude a plasma density saturation mechanism as the plateau in the diffracted SH energy persisted even when Beam 1 and Beam 2 energies were reduced seven times, down to 0.1 mJ/pulse. The results of a similar experiment, where we varied the delay between Beam 1 and Beam 2 pulses keeping SH delay fixed at 1 ps, are presented in Figure 4.3-9(b) and show that the diffracted signal

exhibits fast rise and fall as the pulses of the grating forming beams are scanned through one another.

Moreover, we studied SH diffraction as a function of Beam 2 pulse energy (Beam 1 energy was kept constant at 0.7 mJ/pulse), the obtained experimental results are shown in Figure 4.3-10 with red dots, were fitted using a simple theoretical model. By combining the Kogelnik's analysis with the Drude model, we calculated the diffraction efficiency as $\eta \propto \rho_e^2$, where the peak plasma density ρ_e can be easily estimated considering eight-photon ionization process (for O₂). Although quite simple, this model successfully predicts the diffractive behavior of these volume plasma gratings, see the continuous curve in Figure 4.3-10. The diffraction efficiency saturates when the total intensity is high enough to fully ionize the medium. Interestingly, our measurements show that the periodic grating-like plasma density modulation is still produced when Beam 2 pulse energy is decreased to submicrojoule values, i.e., three orders of magnitude below that of Beam 1.

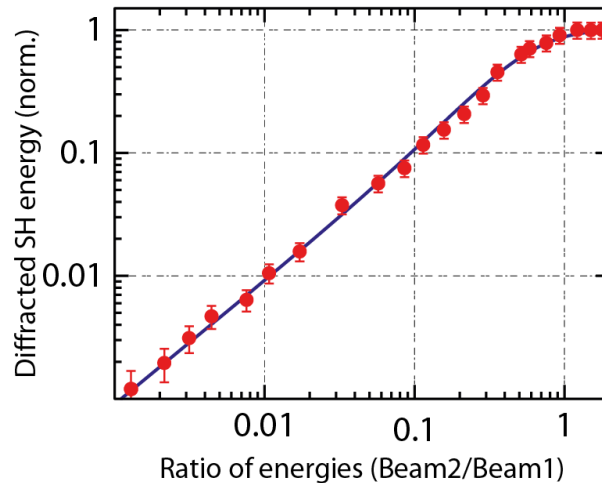


Figure 4.3-10 Normalized diffraction efficiency of the SH wave as a function of the ratio of the Beam 2 energy to the Beam 1 energy: Experimental data (dots) and theoretical fit (solid curve) assuming an eight-photon ionization process.

- **Diffraction of light filaments with the plasma grating**

Furthermore, we investigated the possibility of diffracting a light filament at the fundamental wavelength of 800 nm with the plasma Bragg grating. The plasma grating was formed by two laser pulses at the fundamental wavelength crossing at an angle of 40°, which resulted in a

grating period of $\Lambda = 1.17 \mu\text{m}$. The grating forming pulses with the pulse energies of 1.7 mJ apertured by an iris with a diameter of 2 cm were focused using 100 mm lenses and the filament beam with the pulse energy ranging from 20 to 700 μJ , apertured with an iris with a diameter of 7 mm was focused by a 150 mm lens.

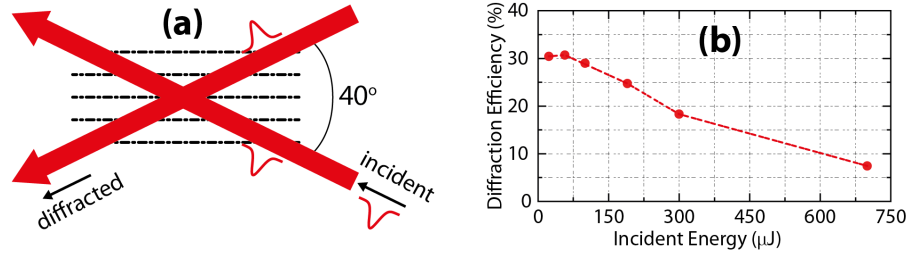


Figure 4.3-11 (a) Schematic of the experimental setup for diffraction of a light filament, and (b) diffraction efficiency versus the filament beam energy.

The effective thickness of the grating was considered to be $d_{\text{eff}} \approx 30 \mu\text{m}$ and refractive index modulation at 800 nm was considered to be $\delta n \sim 4 \times 10^{-3}$. The crossing angle between the two pump beams which create the plasma grating was chosen in a way that the spectral selectivity of the grating (given by Eq. (4.3-2)) is wide enough to cover the spectral bandwidth of the beam. This leads to maximum diffraction efficiency of $\sim 32\%$ at the incidence angle of 20° . Thus, the filament arm should be in the direction of one of the grating forming beams. To achieve this, the filament beam was delayed with respect to the grating forming beams by 1 ps. Figure 4.3-11(a) depicts the experimental setup and in Figure 4.3-11(b) the diffraction efficiency of the light filament is shown as function of the filament pulse energy. It can be seen that for small pulse energies in the filament beam, the maximum diffraction efficiency is achieved while by increasing the energy, the diffraction efficiency is reduced. The reduction is expected to be a result of attenuation of the refractive index modulation of the grating due to the additional plasma by the filament itself.

4.4 Conclusion

In conclusion, we have demonstrated that by introducing a plasma string in the path of a light filament a significant enhancement (by two-orders of magnitude) in the third harmonic generation occurs with an evident dramatic reshaping of TH far-field profile with a significant fraction of its total energy contained in the high-intensity axial component. The measured

dependence of TH energy on the relative delay between the two intersecting pulses has clearly demonstrated that the observed behavior is attributed to the interaction of the filament with plasma produced by the other pulse.

We have proven that the enhancement is a result of a bulk effect and does not rely on the properties of the produced plasma/air interfaces. Furthermore, despite the complex dynamics arising from a variety of linear and nonlinear effects involved, the more than two orders of magnitude increase of THG efficiency in the plasma string can be satisfactorily described by an effective, plasma enhanced third-order optical susceptibility. Through this simple phenomenological approach, we have accurately described the functional dependence of the THG enhancement on the plasma density.

On the other hand, we have shown that two crossing filaments can form a plasma Bragg grating. For orthogonal configuration of the two intersecting beams, the period 566 nm of the created plasma density modulation was found to be equal to the separation of the intensity interface fringes produced by the two pulses. By studying the diffraction efficiency and spectral characteristics of different probe beams, the effective grating thickness, $d_{\text{eff}} \approx 30 \mu\text{m}$, and its refractive index modulation at 400 nm, $\Delta n \approx 1.2 \times 10^{-3}$, were extracted. The measured grating decay characteristics within ~ 100 ps range confirm the plasma origin of the created refractive index modulation. Furthermore, the diffraction of a light filament by the plasma grating has been explored and revealed that when the intensity of the light filament is high enough to create additional plasma, the redistribution of the plasma reduces the diffraction efficiency of the grating.

Filamentation Tailoring and Exotic Optical Beams

5.1 Introduction

For many applications, such as a single-cycle pulse generation for attosecond drivers [199, 200], electric discharge triggering and guiding [84], remote sensing [80], intense THz generation [73, 186, 201], and many other [5], tuning of the light filament attributes and accompanying physical effects is of crucial importance.

Filamentation tailoring denotes the selective optimization of specific filament attributes. Its importance is fundamental in view of the numerous applications of filaments that are promising but have remained compromised up to now by poor control over the filamentation process. For instance, it has recently been shown that the THz emission from two-color filaments strongly depends on the uniformity of the plasma string and its length [71]. In another example, one could consider the use of long filaments at intensities just below ionization for generating higher harmonics and attosecond pulses.

However, as filamentation results from the competition between self-action effects, its attributes are not easily controllable, and control is further hindered by the high intensities in filaments (exceeding 10^{13} W/cm² in air) that exclude optical elements from being introduced in their path. Thus, the majority of efforts, to date, were limited to the control of the spatial and temporal characteristics of the initial laser pulses [5]. Example of these approaches include the use of amplitude and phase masks or the introduction of aberrations on the initial beam wavefront [76, 79]. More recently, impulsive alignment of molecular gases has been shown to also strongly affect the propagation of ultrashort laser pulses [202-204].

In the solitonic propagation regime wherein the Kerr self-focusing is mainly balanced with the linear diffraction, without ionization and nonlinear losses, it has been shown that the two dimensional spatial solitons, which are unstable [6, 205], can be stabilized by introducing a proper periodic lattice and their attributes, such as intensity and waist, can be controlled [206-

212]. Inspired by these theoretical and experimental studies in the solitonic propagation regime, it has been recently shown, through a numerical simulations, that likewise the attributes of intense laser filaments can be significantly controlled by introducing a periodic lattice [196].

On the other hand, filamentation of diffraction-free beams such as Bessel [115-117, 120, 213, 214] and Airy beams [27, 204, 215-218] has attracted considerable attention since, as it will be discussed later in this chapter, by tuning the parameters of these beams, filamentation attributes can be controlled. Moreover, due to their very interesting features such as self-healing, non-diffracting, acceleration, etc., diffraction free beams are very promising for many applications.

In this chapter, filamentation tailoring through the above two approaches (i.e., by introducing a periodic lattice and using non-diffracting beams) is investigated. It is shown that indeed we can control the length, and waist, and hence intensity, of the optical filaments by introducing a quasi-periodic plasma lattice, while similar control can be also achieved when introducing non-diffracting optical beams, like Bessel and Airy beams.

5.2 Filamentation tailoring by a plasma lattice

Spatial laser solitons in one dimension have been extensively studied in the past. In this case, self-focusing induced by the optical Kerr effect is balanced by diffraction or other linear propagation phenomena. These pulses propagate in a lossless regime because the intensity is never high enough to allow nonlinear losses, like multiphoton ionization. However, solitonic solutions of the nonlinear Schrödinger equation are known to be unstable in two-spatial dimensions [6, 205], leading to diffraction or wave collapse of the initial beam. Nevertheless, it was shown that in the presence of a periodic waveguide lattice, the beam is localized in the high-index areas, leading to the formation of discrete solitons [219, 220]. It has been demonstrated both theoretically and experimentally that such solitons can be stabilized in the presence of a periodic lattice [206, 207, 209, 210, 221]. Interestingly, it has been demonstrated that the attributes of solitons can be tailored by using discrete waveguide arrays (see [212] and references therein). In the presence of a periodic potential, self-focusing balances the linear diffraction induced by the waveguide array and by tuning the array parameter and total input power, the soliton attributes such as the peak intensity and width, can be controlled.

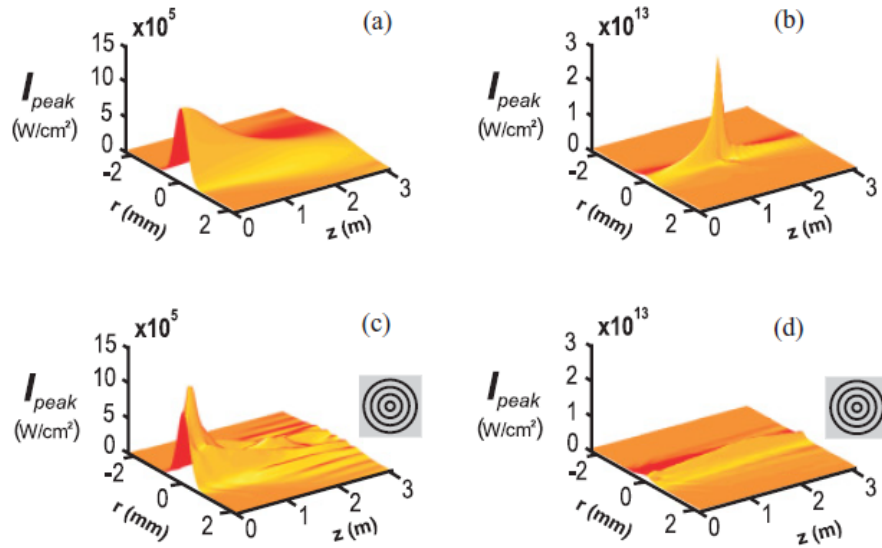


Figure 5.2-1 Comparison of peak intensities $I_{\text{peak}}(r, z)$ for propagation (a,b) and (c,d) in a cylindrical lattice. Left column: linear propagation regime ($P_{\text{in}} = 10^{-6} P_{\text{cr}}$). Right column: nonlinear propagation and filamentation regime ($P_{\text{in}} = 1.25 P_{\text{cr}}$). Lattice parameters: $\Lambda = 350 \mu\text{m}$, $w = 100 \mu\text{m}$, and $\Delta n_0 = -3.3 \times 10^{-7}$. Insets are graphic representations of the cylindrical lattice. Darker rings show lower refractive index. From [196].

In principle, a similar approach could be used for tailoring laser filaments, despite their much higher peak intensities and hence the number of nonlinear effects involved in filamentation compared to the solitonic propagation. Recently, Panagiotopoulos *et al.* [196] demonstrated numerically that the properties of intense femtosecond laser filaments such as their peak intensity, diameter, length and plasma string uniformity can be effectively tailored using periodic lattices. They have numerically studied filamentation tailoring in several periodic lattices, such as square and cylindrical lattices. A case of a cylindrical lattice composed of cylinders of finite width w , spacing (period) Λ , and smaller refractive index, Δn_0 , than the surrounding medium is in Figure 5.2-1. It can be clearly seen that in the linear regime (Figure 5.2-1(c)) the lattice causes discrete diffraction and further spreading of the beam whereas in the filamentation regime the presence of the lattice significantly moderates (Figure 5.2-1(d)) the peak intensity of the filament shown in Figure 5.2-1(b).

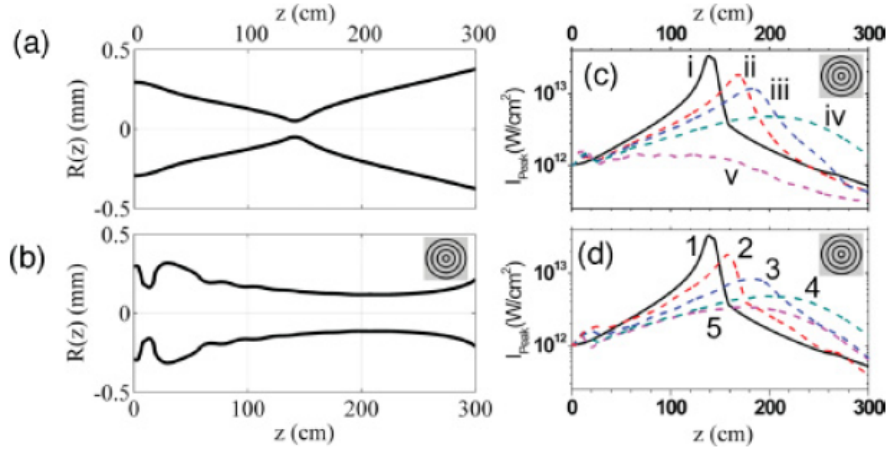


Figure 5.2-2 Beam width as a function of the propagation distance z , without lattice (a), and with lattice (b). Peak intensity I_{peak} as a function of the propagation distance z for (c) lattice strengths Δn_0 of 0 (curve i), -2×10^{-7} (curve ii), -2.5×10^{-7} (curve iii), -3.3×10^{-7} (curve iv), and -5.0×10^{-7} (curve v) and (d) lattice periodicities Λ of ∞ (curve 1), $450 \mu\text{m}$ (curve 2), $400 \mu\text{m}$ (curve 3), $350 \mu\text{m}$ (curve 4), and $300 \mu\text{m}$ (curve 5). From [196].

In Figure 5.2-2(a) is shown the width of the beam along the propagation axis in the filamentation regime, without the lattice. It can be seen the width of $100 \mu\text{m}$ is held for $\sim 25 \text{ cm}$. On the other hand, in the presence of the lattice (Figure 5.2-2(b)), for a propagation distance of $\sim 180 \text{ cm}$ the beam waist is almost constant to about $270 \mu\text{m}$. In this case, the beam waist depends on the lattice period, allowing a control on its size and consequently the peak intensity. Figure 5.2-2(c) shows the peak intensity as a function of the propagation distance for various depths Δn_0 of the effective refractive index modulation for a constant period of $\Lambda = 350 \mu\text{m}$. The modulation depth was varied from 0 (curve i), corresponding the absence of the lattice, to -5.0×10^{-7} (curve v). As the modulation becomes deeper the peak intensity drops, and its distribution is widened and shifted toward the longer propagation distances. Moreover, the effect of lattice periodicity Λ , on the peak intensity as a function of propagation distance is shown in Figure 5.2-2(d), for a constant modulation depth of $\Delta n_0 = -3.3 \times 10^{-7}$. The period Λ is varied from infinity (curve 1), corresponding to the absence of the lattice, down to $300 \mu\text{m}$ (curve 5). As the lattice period gets smaller, the peak intensity drops, and its distribution is widened and shifted toward longer propagation distances.

In this section, a direct experimental evidence of effective control of the filament properties using a periodic lattice of refractive index is provided. The propagation medium is

water, and the lattice is a transient plasma structure generated by two intense co-propagating non-diffracting Bessel beams. The complex intensity pattern created by the interference of two Bessel beams leads, through multiphoton ionization, to a local 2D periodic plasma lattice. With numerical simulations, we confirm that the observed tunability is not a result of linear guiding but of an enforced balance between the nonlinear propagation effects and linear diffraction from the refractive index modulation induced by the plasma lattice.

- **Experimental Setup**

The schematic of the experimental setup is shown in Figure 5.2-3(a). The output of a Ti:Sapphire amplified laser system delivering 35 fs (FWHM) pulses at central wavelength of 800 nm operating at 50 Hz repetition rate, with a linear polarization was split into two arms, the pump and the probe. The pump pulses (up to 1mJ) were used for the generation of a plasma lattice. Using a half-plate, their polarization was rotated by 90° and spatial phase was modulated by reflective-type phase-only spatial light modulator (SLM, Hamamatsu LCOS). After passing through the beam-splitter BS2, the phase modulated pump beam was collinearly recombined with the delayed probe beam. The two beams were directed into a variable length tank filled with distilled, de-ionized water. The probe beam used to generate a light filament was independently focused inside the water tank using a 200 mm focal-length lens. The relative timing between pump and probe pulses was adjusted using an optical delay line. The probe beam used to generate a light filament was independently focused inside the water tank using a 200 mm focal-length lens. The relative timing between pump and probe pulses was adjusted using an optical delay line.

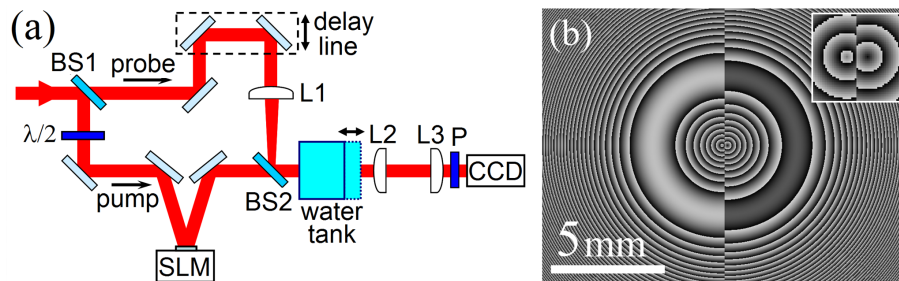


Figure 5.2-3 (a) Schematic of the experimental setup: BS1, BS2, beam-splitters; L1, L2, L3, lenses; P, polarizer, (b) Gray-scale image of the phase mask (black and white colors denote 0 and 2π phase, respectively). A zoomed view of the central part of the mask is shown in the inset.

The imaging part of the setup, comprised of a two-lens (L2, L3) with magnification of 5.7 and a charge-coupled device (CCD) camera, was used to capture the pump and probe intensity distributions in water at the exit window of the water tank. Since the polarizations of the pump

and probe were crossed, their intensities could be recorded independently using a polarizer P placed in front of the CCD.

Let us now explain in more detail the way we create the desired lattice of refractive index in water. It is important that the lattice length be sufficiently long, much longer than the normal filament [196]. Therefore, to create such long transient structures we used non-diffracting Bessel beams [21] which can be realized by focusing Gaussian beams with a conical lens or an axicon [222]. By combining two co-propagating Bessel beams that are π -phase shifted with respect to each other, we succeeded to generate a quasi-periodic modulation of intensity and thus of the corresponding refractive index. In our experiments, each Bessel beam was generated by using a combination of radially symmetric linear and quadratic phase corresponding to an axicon combined with a spatial lens, which is necessary for their spatial separation and the extension of the Bessel zone. In our case, the required phase is given by

$$\varphi(r) = -\frac{2\pi}{\lambda} \left(\tan(\gamma)r + \frac{r^2}{2f} \right) \quad (5.2-1)$$

where r is the radius, λ is the wavelength, γ is the Bessel cone angle, and f is the focal length of the lens. The phase mask used is shown in Figure 5.2-3(b). The left and right π -phase shifted halves of the image each correspond to the wrapped (modulo 2π) phase of a Bessel beam of 0.25° cone angle combined with a negative lens ($f = -700$ mm).

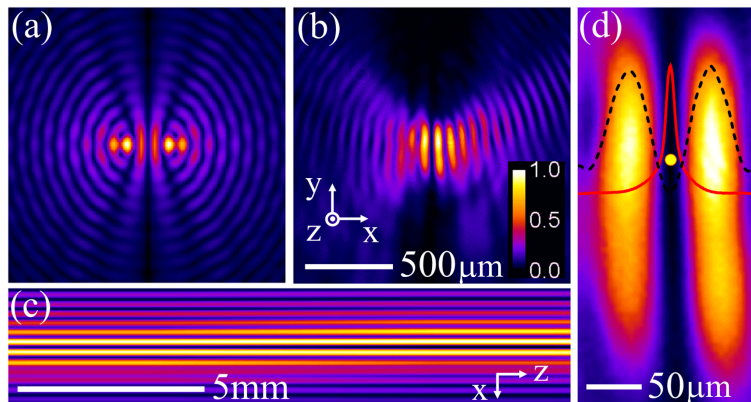


Figure 5.2-4 The simulated (a) and measured (b) double Bessel distribution of the pump beam. (c) xz -plane cut of the pump intensity. (d) Magnified image of the two brightest pump fringes with a yellow spot indicating the launching position of the filament.

The centers of the two phase patterns are separated by 250 μm as shown in the inset of Figure 5.2-3(a). The resulting simulated intensity distribution that is created at a propagation distance of 100 cm from the SLM is depicted in Figure 5.2-4(a) while Figure 5.2-4(b) shows the experimentally recorded intensity of the pump beam at the same distance. There is a fairly good qualitative agreement between simulation and experiment. The vertical extension of the spots in the experimental intensity profiles is due to an astigmatic distortion in the initial beam and needs a complicated optical design to have a round and symmetric spots. However, even this profile was sufficient for the purpose of this experiment. The most important aspect is that the intensity profile remains practically invariant along the propagation axis. As clearly shown in Figure 5.2-4(c), the mean period changes by less than 1.5% within 15 mm of propagation. The high intensity of the pump beam leads to electron excitation and plasma formation that in turn perturbs the refractive index [122, 223]. In this way, the intensity and plasma distribution acts as a template for the generation of an elongated transient refractive index modulation. Because of the multiphoton nature of the ionization process, the refractive index changes are proportional to a power of the intensity distribution $\Delta n \propto I^k$ ($k = 5$ for water at 800 nm).

- **Results and discussion**

In the experiment the probe pulse energy was set at 2 μJ , slightly above the experimental threshold for filamentation and the created light filament was launched parallel and exactly in-between the central pump intensity fringes as shown by a yellow spot in Figure 5.2-4(d). The red solid and black dashed curves in this figure represent the one-dimensional (1D) intensity profiles, along the x -direction, of the filament and of the pump beam, respectively. For comparison, in the linear regime the measured waist of the probe beam was 40 μm . Clearly, in such an arrangement at an appropriately adjusted pump-probe delay, the reduced refractive index change due to the plasma generated by the pump effectively results in the formation of a ~ 75 μm -wide slab-type quasi-2D lattice for the probe beam propagation.

The laser system compressor was tuned to compensate for the normal group-velocity dispersion of water and optics upstream to obtain the shortest pulses, and hence the highest pump intensities, at a propagation distance of 7 cm in water. In addition, the position of L1 was adjusted to initiate probe beam filamentation at the same z -plane.

The xz -cuts of the recorded filament intensity in the absence of the lattice (top) and with the lattice (bottom) at 80 fs relative delay between the pump and the probe are shown in **Figure 5.2-5(a)**. These filament profiles were obtained by stitching the respective filament xy intensity distributions captured at various z -planes over 6.6 mm of propagation with a 0.2 mm step (at each step the length of the variable water cell was increased).

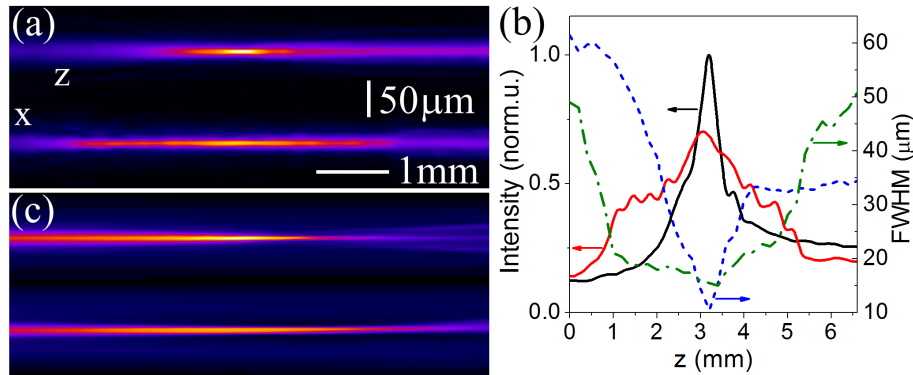


Figure 5.2-5 (a) Experimental xz -plane intensity distribution of the filament without the lattice (top), and in the presence (bottom) of the plasma lattice. (b) 1D filament peak intensity without (black solid) and with (red solid) lattice. Blue dashed and green dashed-dotted curves represent the respective widths of the filaments. (c) The simulated intensity of the filament without (top) and in the presence (bottom) of the lattice.

Note that the action of the lattice drastically changes the filamentary propagation, resulting in filament elongation and peak intensity depression, similar to the numerical predictions of [196]. Our measurements indicate that at a relative delay of 80 fs, the refractive index modulation is due to the presence of the pump-excited plasma. To better visualize the difference between these two filamentation regimes, in Figure 5.2-5(b) we plot the respective filament peak intensities and beam widths (FWHM). As can be seen, the propagation inside the plasma structure induced by the pump pulses results in ~ 4 times elongation of the filament length (FWHM) while its peak intensity is decreased by $\sim 40\%$. Moreover, a nearly constant filament waist of $\sim 20 \mu\text{m}$ is sustained over more than 3 mm of propagation, which is in striking contrast with the typical filament behavior whose minimum waist of $10 \mu\text{m}$ is doubled within less than half a millimeter. These results are clear demonstration of filamentation tailoring [196] where the competition of nonlinear effects with the linear diffraction induced by the lattice results in a new regime of filamentary propagation.

To confirm that the observed changes in the filaments propagation is not just the result of linear guiding inside the plasma-induced positive index slab waveguide we conducted numerical simulations using a three dimensional (2D+1: 3 spatial coordinates with frozen time) propagation code. Details about the model used can be found in [196]. The refractive index changes due to the free-electron plasma generated in the trail of the pump pulse were modeled based on a five-photon ionization process in water at 800 nm wavelength and the Drude model for plasma defocusing and absorption [122] using the pump intensity distribution of Figure 5.2-4(a). The peak power of the probe pulse was set at $2 \times P_{\text{cr}}$ where $P_{\text{cr}} \approx 3.8$ MW is the critical power for self-focusing in water ($n_2 \approx 1.9 \times 10^{16}$ cm²/W at 800 nm). The simulated xz -plane intensity profiles of the probe filament are shown in Figure 5.2-5(c) where the upper and the lower images represent propagation without and with the lattice, respectively. In excellent agreement with the experiment, similar changes in the filament attributes -its elongation, better uniformity, and peak intensity depression- are clearly identified. In addition, we performed simulations with only linear effects (not shown). In this case, coupling of the probe beam into the neighboring waveguides of the lattice led to the spreading of energy towards the outer waveguides thus confirming that the observed changes in the filamentary propagation in the high-intensity regime are not the result of linear guiding.

Thus, we have experimentally demonstrated that femtosecond laser filamentation can be tailored by using periodic lattice of refractive index. The major filament attributes, such as its length and diameter were effectively controlled. Numerical simulations confirm that the observed changes in the filamentary propagation are not the result of linear guiding but of a new enforced balance between the nonlinear propagation effects and linear diffraction caused by the refractive index modulation of the lattice. Our results suggest that more sophisticated structures both transient (e.g. laser generated plasma, molecular alignment [224] and permanent (e.g. laser written waveguides in solids) can open the way for extensive and effective control of the filamentation process.

5.3 Filamentation tailoring using exotic beams

As it has been already mentioned, one of the approaches for filamentation tailoring and gaining control on the attributes of filaments is to tune the optical beam parameters prior to

filamentation. Such methods include the use of amplitude masks [76], the introduction of ellipticity in the input beam [77] and others [78, 79]. On the other hand, owing to their special features, exotic beams such as Bessel and Airy beams can also be used to create and control optical filaments. The most striking feature of these beams is their non-diffracting nature that can be utilized in filamentation tailoring via adjusting beam parameters. Moreover, the self-healing and acceleration in these beams can be also used to control filaments. In this section, generation, linear propagation, nonlinear propagation, and filamentation of two classes of non-diffracting beams, namely Bessel and Airy beams, are discussed.

5.3.1 Filamentation of Bessel beams

Interestingly, filamentary-like propagation is also achievable even in the linear propagation regime, by using Bessel beams. Bessel beams can be considered as the superposition of infinite plane waves whose wavevector lies on a cone or as a superposition of two Hankel beams [225]. As this conical wave propagates, due to interference effects, an intense central core, surrounded by lower intensity rings is formed in the propagation direction, as it is shown in Figure 5.3-1(a). In the nonlinear regime, the high intensity core of the Bessel beam will lead to the generation of free electrons through multiphoton ionization.

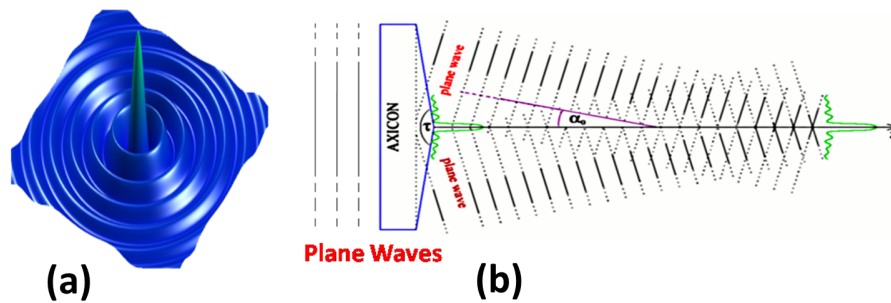


Figure 5.3-1 (a) Spatial intensity distribution in the Bessel beam, (b) Generation of Bessel beam by an axicon.

Bessel beams are commonly used using axicons [222, 226], while more complex optical systems such as holographic elements [227] and lensacones [228] can be also used for this purpose. An axicon is an optical element with one side flat and the other side conical. As the beam propagates through the axicon and exits from the conical side, the flat wavefront is

transformed to conical one as depicted in Figure 5.3-1(b). The total length of the Bessel zone depends on the input beam diameter and the conical angle of the axicon.

Filamentation dynamics in various media using pulsed Bessel beams has already been studied [214]. More recently, ultrafast IR (800 nm) Bessel beams have been used to generate long plasma strings in air [115, 116]. In these works, the reported simulated electron density values were in the range of 10^{16} cm^{-3} . Furthermore, the plasma density was not uniform exhibiting either oscillations, due to the use of narrow beams and blunt-tip axicon [115] or significant variation over the propagation distance [120]. Also, it was reported [120] that by adding temporal chirp in the pulse, the plasma string position and length could be relatively extended but in the expense of peak electron density.

Here, we demonstrate the creation of tunable in length, uniform plasma strings with high electron densities ($\sim 10^{18} \text{ cm}^{-3}$) in air using UV short pulse Bessel beams. The use of UV radiation makes the ionization process very efficient and along with the optimization process achieved by tuning the Bessel beam angle, and hence the Bessel zone, makes it a perfect candidate for the generation of very long and uniform plasma strings in air. The string length tunability is achieved without sacrificing the plasma uniformity, while the impact on the peak electron densities is also very small.

- **Experimental Setup**

A hybrid feedback distributed dye/KrF excimer laser, delivering 0.5 ps (or 5ps), 248 nm pulses was used in our study. The output of laser beam profile was top-hat with spatial dimensions $50 \times 50 \text{ mm}^2$. The central part of the laser beam was selected by means of an iris and was directed towards the optical system that transformed the beam to conical. The optical system was either a simple fused silica axicon, with a base angle of $\gamma = 5^\circ$ (170° apex angle) or a system composed by the same axicon preceded by a fused silica plano-concave lens of $f = -200 \text{ mm}$ focal length, placed 3 cm from the axicon. In the experiments both available laser pulse modes, 0.5 ps and 5 ps, were used.

The calibrated plasma conductivity technique (PCo) [Chapter 2] [119] was used to measure the electron density in the filaments created by the UV Bessel beam. The measurement system consisted of two steel electrodes ($\sim 1 \text{ mm}$ diameter) separated by 3 mm distance. Undesired

direct illumination of the electrodes by the laser beam was blocked using a Teflon aperture placed in front of electrodes. The plasma string passed between the two electrodes while a DC high voltage (1.4 kV) was applied on them.

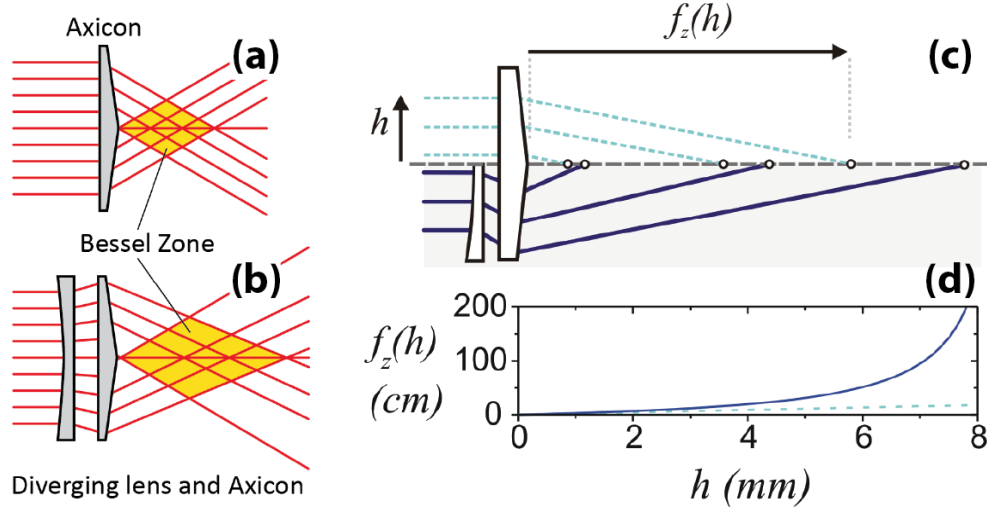


Figure 5.3-2 Schematic representation of the Bessel zone of a single axicon (a) and an axicon preceded by a negative spherical lens (b). (c) Ray tracing comparison of the Bessel zones of an axicon (dashed lines) and the system of axicon-negative lens (solid line), and (d) Bessel zone vs the incident beam height for an axicon (dashed curve) and the system of axicon negative lens (solid curve).

The laser generated plasma redistributed in the presence of the applied external electric field (~ 4.7 kV/cm) and screened out [229] the external field, generating a potential drop across the electrodes that caused a current to flow through the 8 k Ω probe resistance. The voltage drop across the resistance was measured using a standard oscilloscope. When this detection setup is operated in the ohmic regime (current is linearly proportional to the applied high voltage) the measured electric signal depends linearly on the mean, over the plasma channel diameter, excited electron density ($\langle \rho_e \rangle$). The correlation of the electric conductivity measurements to plasma density estimations was done by comparison with a precise, but more complex, holographic method [119, 122, 123][Chapter 2].

As mentioned above, an axicon was used to generate the Bessel beam. From a ray-tracing point of view, an axicon focuses all the rays that lie on a cylinder of radius h to an axial focus at a distance $f_z(h)$ from the axicon apex, as shown in Figure 5.3-2(c). In contrast to a spherical lens the axial focus position depends linearly on the ray height h . For an axicon with small base angle the axial focus position can be written as

$$f_z(h) \cong \frac{h}{(n - n_0)\gamma} \quad (5.3-1)$$

where γ is the base angle of the axicon, n is the refractive index of the axicon and n_0 is the refractive index of the surrounding medium (air). The longitudinal size of the focal region in this case is defined by the base angle of the axicon and the beam diameter. A highly efficient way to expand this region is to place a diverging lens before the axicon. The axial focusing range is expanded while the axial focus position is now a nonlinear function of the ray height h , as shown in Figure 5.3-2(d). In this case, with a good approximation the axial focus position can be written as:

$$f_z(h) \cong \frac{h}{(n - n_0)\gamma + h / f} \quad (5.3-2)$$

where f is the focal distance of the diverging lens. It is clear that after the insertion of the diverging lens the optical system acts as an axicon with an effective base angle of γ_{eff} given by:

$$\gamma_{\text{eff}} \cong \gamma + \frac{h}{f(n - n_0)} \quad (5.3-3)$$

The effective base angle is no longer constant and linearly depends on the ray height. Figure 5.3-2(d) shows the significant extension of the longitudinal focusing range achieved by this approach.

- **Results and discussion**

The electron density distributions of the plasma strings created when using the axicon alone are shown in Figure 5.3-3(a) for both pulse durations. In both cases, a homogeneous plasma channel ~ 150 mm long is created. The estimated electron density values are in the range of $\sim 2.5 \times 10^{18}$ cm^{-3} and $\sim 1 \times 10^{17}$ cm^{-3} for the 0.5 ps and 5 ps pulses, respectively. The difference in the peak electron densities is due to the lower pulse intensity of the longer pulses.

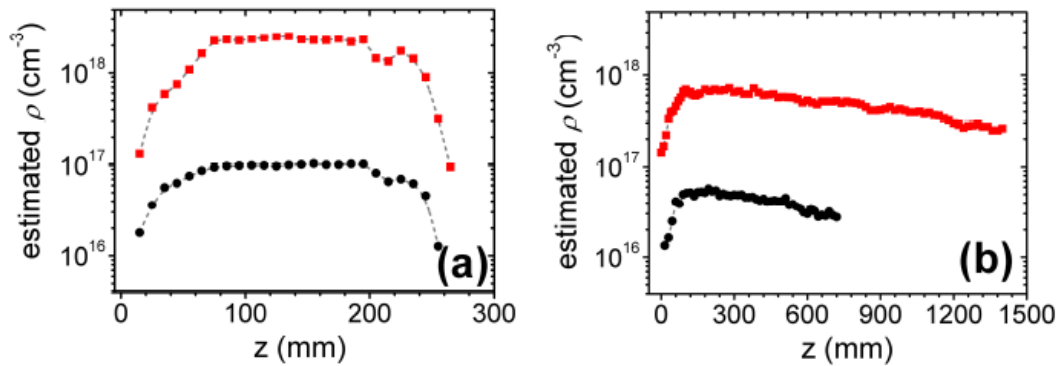


Figure 5.3-3 Electron density ρ versus propagation distance for 248 nm, UV Bessel beams. (Squares) 7.5 mJ, 0.5 ps, (circles) 10.25 mJ, 5 ps, (a) axicon only (base angle $\gamma = 5^\circ$), (b) axicon with diverging lens ($f = -200$ mm).

Although homogeneous, the plasma strings obtained in this way are relatively short in length. To obtain longer plasma strings we introduced the diverging lens as described above. The obtained plasma string electron distributions are shown in Figure 5.3-3(b), for the same input pulse parameters as in Figure 5.3-3(a). One observes a considerable increase in the length of the plasma strings, without any compromise in the plasma uniformity, accompanied by a small reduction of the peak electron density. For the shorter 0.5 ps pulses the plasma string length was extended by a factor of $\sim 10\times$ with a $\sim 3.4\times$ reduction in the peak electron density ($\sim 7.4 \times 10^{17} \text{ cm}^{-3}$). Despite this reduction, the plasma density is still two orders of magnitude higher than previously reported values from relative studies [115, 116]. Likewise, for the 5 ps pulses the plasma string length was increased by factor of $\sim 5\times$, accompanied with a $\sim 2\times$ reduction of the electron density values ($\sim 6 \times 10^{16} \text{ cm}^{-3}$).

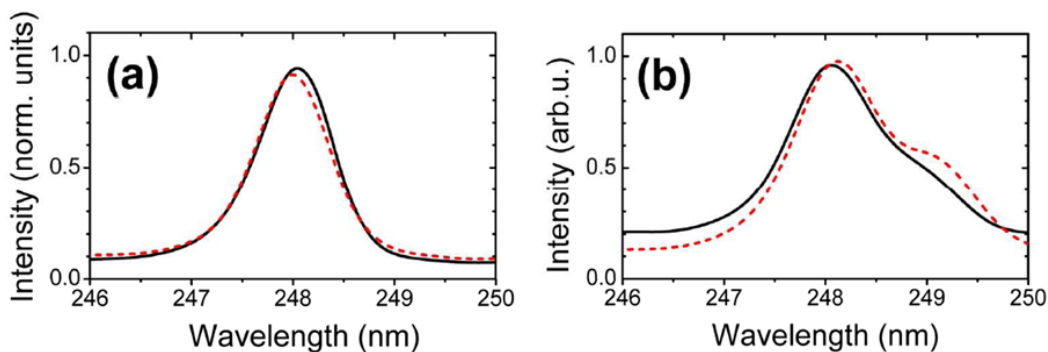


Figure 5.3-4 The measured spectra of the pulse before (solid curve) and after (dashed line) formation of the plasma channel; (a) for 5 ps pulse duration and (b) for 0.5 ps pulse duration.

Beyond the spatially achieved stationarity, we verified that this conically driven filamentary propagation does not involve any temporal effects either. For this, we monitored the UV laser pulse spectrum before and after the formation of the plasma strings. The comparative spectral are shown in Figure 5.3-4 for both pulse durations, showing insignificant spectral evolutions. This is a strong indication that no temporal effects, like pulse splitting, takes place during the pulse propagation and plasma string formation.

In order to further explore this conical filamentation regime numerical simulations of the nonlinear propagation have also been performed, using a complete 3D code that solves the nonlinear Schrödinger equation (NLSE) coupled with a rate equation for the electron density evolution. The numerical model is described in detail in [5] and it takes into account diffraction, plasma defocusing, group velocity dispersion by using the full dispersion relation (Sellmeier-like) for air, and nonlinear effects such as the Kerr effect, and multiphoton absorption. The electron density evolution equation takes into account multiphoton ionization, as well as avalanche ionization and trapping. The effect of the axicon is modeled by the multiplication of the input field with a phase mask $\exp[-i\varphi(h)]$ where the phase is set as:

$$\varphi(h) = \frac{2\pi}{\lambda} \sin[(n-1)\gamma]h \quad (5.3-4)$$

where λ is the wavelength and n , γ are respectively the refractive index and the base angle of the axicon.

Simulations were performed under the same conditions as in the experiment (0.5 ps, 248 nm, axicon base angle $\gamma = 5^\circ$, diverging lens $f = -200$ mm). Furthermore, to clarify the role of nonlinear effects in the propagation we simulated two distinct cases: one for the input energy of 7.5 mJ, as in our experiments, and one for very low, 7.5 nJ input energy (corresponding to a power $7 \times 10^{-5} P_{cr}$) with all the other parameters fixed.

The results of the simulations are shown in Figure 5.3-5. As it can be clearly seen, the on-axis intensity for the low input energy is $\sim 10^6$ times smaller than the on-axis intensity, corresponding to the 10^6 times higher input energy, but follows the same shape as for the high input laser energy.

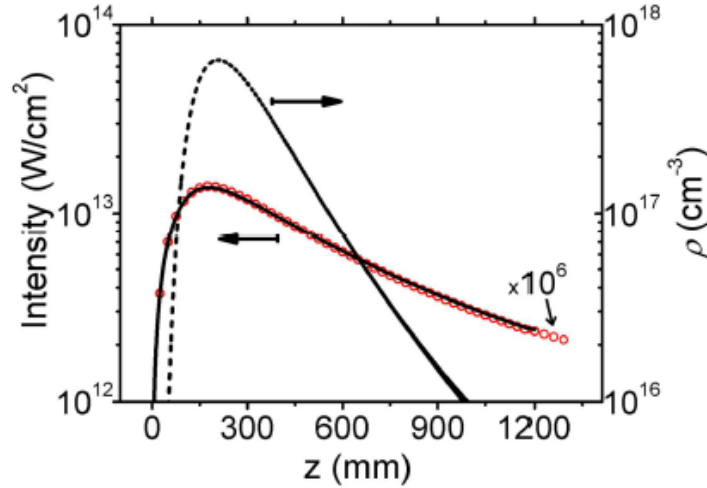


Figure 5.3-5 Simulated on axis intensity and electron density profile for 7.5 mJ, 248 nm, 0.5 ps pulses illuminating an axicon (base angle of $\gamma = 5^\circ$) preceded by a diverging lens ($f = -200$ mm) (solid line)-Intensity (circles) –Intensity values for a 7.5 nJ pulses ($\times 10^6$), (dashed line) – on axis electron density.

This result confirms that the propagation is governed by the linear induced conical wavefront. The on-axis electron density, for the case of the 7.5 mJ input energy is also shown in Figure 5.3-5. The peak electron density value $6.5 \times 10^{17} \text{ cm}^{-3}$ of the simulation agrees with the measured one $7.4 \times 10^{17} \text{ cm}^{-3}$, while the simulated electron density is decaying faster as a function of propagation distance. This discrepancy could be attributed to the fact that the electrodes, results in averaged electron density values $\langle N_e \rangle$, while the simulation results refer to the peak electron densities in the center of the plasma string core. Finally, the numerical results show no temporal evolution of the filamented laser pulses, in agreement with the experimental findings.

Thus, in summary we have demonstrated here that long, uniform and high density plasma strings can be generated in air using conically shaped UV short laser pulses [117]. The combination of axicons with diverging lenses, actively tunes the conical angles and results in a remarkable increase of the plasma string length with no sacrifice in the string uniformity and minimal peak electron density changes. Since the beam propagation is mainly governed by linear effects, the propagation is stationary both in space and in time. These results could be scaled up to higher input energies as the presence of strong nonlinear absorption would result to intensity clamping effects that would further flatten the intensity spatial profile, keeping the plasma density high over long propagation distances. Our approach is an attractive candidate for

filamentation tailoring and can be used in numerous applications like THz pulse generation or lighting control.

5.3.2 Airy beams: generation, linear and nonlinear propagation

Airy beams have recently been introduced into the optical science and since then have attracted enormous attention, owing to their special features including being the only non-spreading solution in 1D and more interestingly their acceleration in time and transverse dimension in space. In this section, the Airy beams are studied in detail from their formation to their linear and nonlinear propagation. Here it is shown that, instead of using expensive fabricated phase masks or spatial light modulators (SLMs) (which also have some other limitations for practical use) we can take advantage of optical aberrations (specifically, comma aberration) to create 1D or 2D Airy beams. Using the advantage of the airy function as unique non-spreading solution in one-dimension, we have shown experimentally realized linear Airy³ light bullets, which are non-spreading in all spatial dimensions and time and investigated their nonlinear propagation. The nonlinear stationarity of the Airy beams with a Gaussian temporal profile is also studied and a regime of stability is theoretically achieved and further confirmed by numerical simulations and experimental results. Propagation of finite energy Airy beams, or in other words, the role of truncation on the propagation of these beams, is also studied. Moreover, through experimental results it is shown that even way beyond the regime of stability in the nonlinear propagation, when the optical power is extremely high, the Airy beams are reconstructed and their profile is very close to their linear profile.

- **Airy function**

Airy functions were first introduced in physics (more specifically, in quantum mechanics) by Berry and Balazs [230] as a unique non-spreading solutions for the Schrödinger equation in one-dimension. More recently, the Airy function is also introduced and realized in the context of optics as Airy beam [23, 231]. This interesting class of non-diffracting beams is unique because these beams lack parity symmetry and tend to accelerate during propagation. Non-diffracting beams/pulses carry infinite energy but even with a finite energy content they can be considered practically non-spreading since their spread in space/time is indeed negligible in comparison to classical wave packets.

Airy function is defined mathematically by the following integral [232]:

$$Ai(x) = \frac{1}{\pi} \int_0^{\infty} \cos\left(\frac{t^3}{3} + xt\right) dt \quad (5.3-5)$$

which is the solution of the homogenous differential equation, called the Airy equation:

$$y'' = xy \quad (5.3-6)$$

The profile of the real part of the air function and its intensity (square of its amplitude) are shown in Figure 5.3-6(a) and Figure 5.3-6(b), respectively.

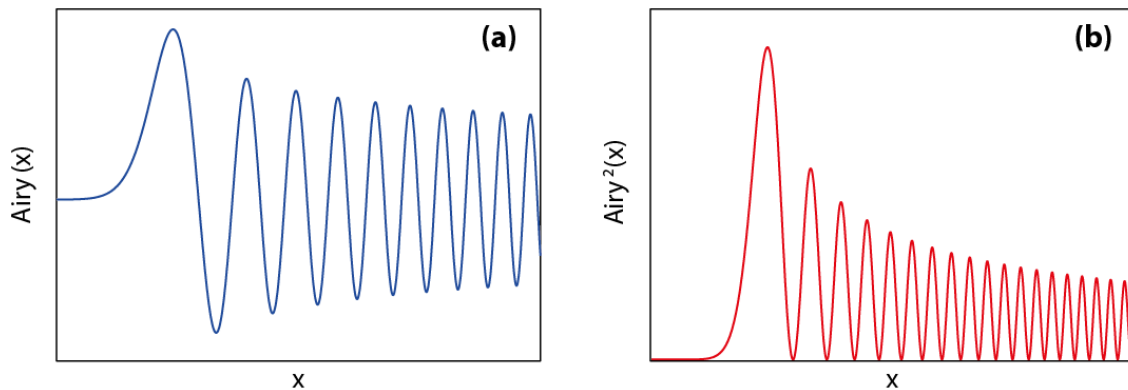


Figure 5.3-6 Profile of Airy function (a) and its intensity (b).

- **Optical Airy beams and their properties**

Perhaps the most known example of 2D diffraction-free optical wave is the so-called Bessel beam, which was first suggested and observed by Durnin [21]. Other kinds of non-diffracting beams in optics have also been realized such as, higher-order Bessel beams Mathieu beams and their higher-order counterparts and waves based on parabolic cylinder functions [22, 233, 234]. These beams, share common characteristics: first, they are all generated from an appropriate conical superposition of plane waves. Even more importantly, all these solutions are known to carry infinite energy but, in practice, because of the lack of space and power, they are always truncated in experimental realization [235]. However, as mentioned earlier, if the truncation aperture size is not that small that it blocks the features of the these beams, the diffraction process is slowed down and for practical use these beams can be considered diffraction-free.

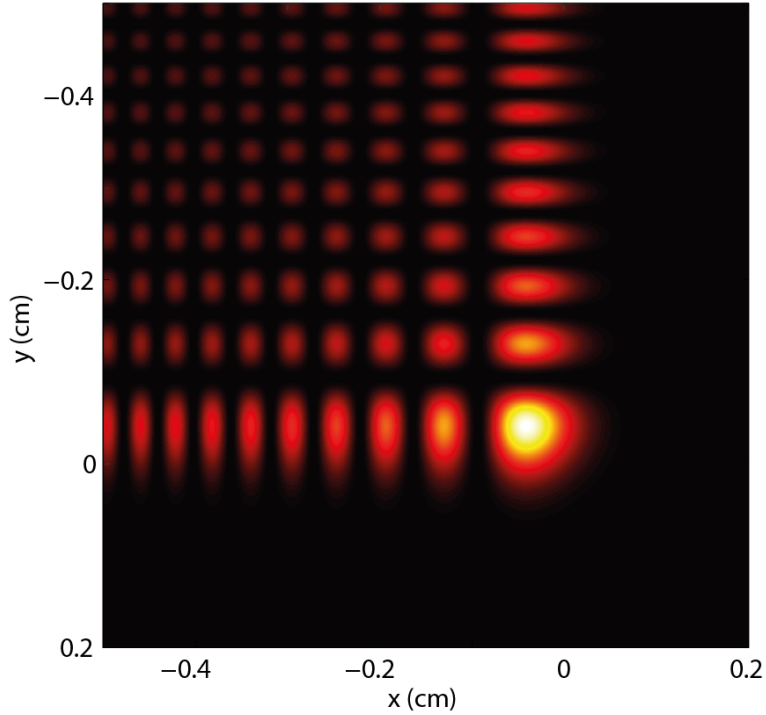


Figure 5.3-7 Intensity profile of 2D Airy beam with $x_0 = y_0 = 300 \mu\text{m}$.

Airy beams were first observed and studied in optics by Siviloglou *et al.* [23, 231]. Perhaps, the most interesting aspect of Airy beams is their transverse acceleration (bending). They resist diffraction while their main intensity maxima or lobes tend to accelerate during propagation along parabolic trajectories. This behavior persists over long propagation distances while the center of gravity of these wavepackets remain constant (in accordance to Ehrenfest's theorem) and eventually diffraction takes over [23, 236]. An intensity profile of a two-dimensional Airy beam described by $I = \text{Ai}^2(x / x_0)\text{Ai}^2(y / y_0)$, with $x_0 = y_0 = 400 \mu\text{m}$ is shown in Figure 5.3-7. As it can be seen, the main intensity lobe is the most intense one and depending on truncation, it may contain most of the energy of the beam.

To investigate the linear propagation of the Airy beams, we start with the normalized 1D paraxial wave equation as:

$$i \frac{\partial E}{\partial v} + \frac{1}{2} \frac{\partial^2 E}{\partial u^2} = 0 \quad (5.3-7)$$

where E is the electric field envelope, $u = x / x_0$ denotes a dimensionless transverse coordinate, x_0 is an arbitrary transverse scale, $v = z / kx_0^2$ is a normalized propagation distance, and $k = 2\pi / \lambda_0$. Equation (5.3-7) admits the following non-spreading Airy solution [23, 230],

$$E(v, u) = \text{Ai}\left(u - (v/2)^2\right) e^{i(uv/2 - v^3/12)} \quad (5.3-8)$$

where Ai stands for the Airy function and as it can be seen at the origin we have: $E(0, u) = \text{Ai}(u)$. It is clear from Eq. (5.3-8) that this wave remains invariant during propagation while it acquires constant acceleration during propagation. The term $v^2 / 4$ in the argument of the Airy function in this equation, describes the *ballistic* trajectory in the Airy beam propagation. Figure 5.3-8 depicts the propagation dynamics of an ideal (untruncated) Airy beam with the $x_0 = 300 \mu\text{m}$ and $\lambda_0 = 800 \text{ nm}$ over a propagation distance of $z = 500 \text{ cm}$. It can be clearly seen that the Airy beam accelerates in the transverse coordinate x (or equivalently u) while propagating along the z -axis (or equivalently v -axis).

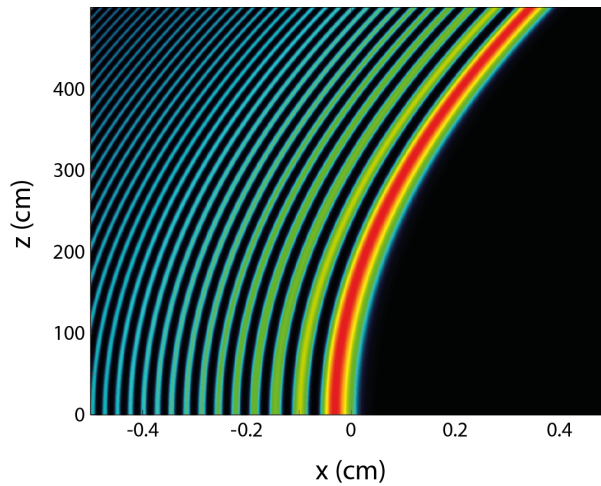


Figure 5.3-8 Propagation dynamics of an ideal (untruncated) Airy beam with $x_0 = 300 \mu\text{m}$ and $\lambda_0 = 800 \text{ nm}$ over a propagation distance of $z = 500 \text{ cm}$.

The acceleration of the Airy beams does not violate the Ehrenfest's theorem [237] which describes the motion of the center of gravity of a wavepacket, since the center of gravity of an Airy beam (without any truncation) cannot be defined because of divergence of its square

integral ($\int \text{Ai}^2(x)dx \rightarrow \infty$) and for the finite energy Airy beams (truncated) the center of gravity propagates on a straight direction [215, 217].

On the other hand, as it has been already mentioned, the truncation of Airy beams is unavoidable in reality for experimental realization because of finite power and space. Recently the propagation dynamics of finite energy Airy beams in the linear regime has been studied both theoretically [231] and experimentally [23]. From the mathematical point of view, the amplitude of exponentially truncated Airy beam at the origin can be written as [231]:

$$E(v = 0, u) = \text{Ai}(u)e^{(au)} \quad (5.3-9)$$

where a is a positive parameter to ensure that the beam contains finite energy. Figure 5.3-9 shows the intensity profiles of an exponentially truncated Airy beam (with $x_0 = 300 \mu\text{m}$) described by Eq. (5.3-9), with different truncation parameter a values. It can be seen that for higher values of truncation parameter a , the Airy profile approaches a Gaussian profile. Typically, $a \ll 1$ so that the resulting wavepacket resembles the Airy profile.

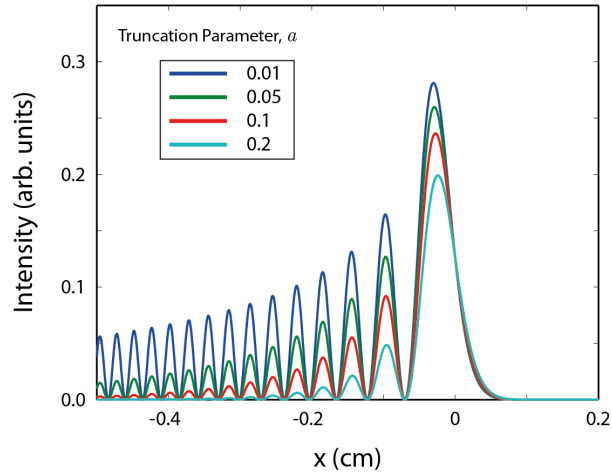


Figure 5.3-9 Intensity profile of an exponentially truncated Airy beam (with $x_0 = 300 \mu\text{m}$) for different values of truncation parameter, a .

By directly integrating equation (5.3-9) one gets [23, 231]:

$$E(v, u) = \text{Ai}\left(u - (v/2)^2 + iav\right) e^{(au - (av^2/2) + i[-(v^3/12) + a^2v/2 + av/2])} \quad (5.3-10)$$

The propagation dynamics of a truncated Airy beam described by Eq. (5.3-10), with $a = 0.05$, $x_0 = 300 \mu\text{m}$ and $\lambda_0 = 800 \text{ nm}$ over a propagation distance of 500 cm is shown in Figure 5.3-10. On the other hand, the Fourier transform of $E(v = 0, u)$, can be easily found as [231]:

$$E_0(k) \propto e^{(-ak^2)} e^{(ik^3/3)} \quad (5.3-11)$$

This equation shows that the angular Fourier spectrum of the truncated Airy beam is Gaussian and involves a cubic phase resulting from the Fourier transform of the Airy function itself. As it will be discussed later in this section, this specific form of the spectrum is important for experimental synthesizing the truncated airy beams.

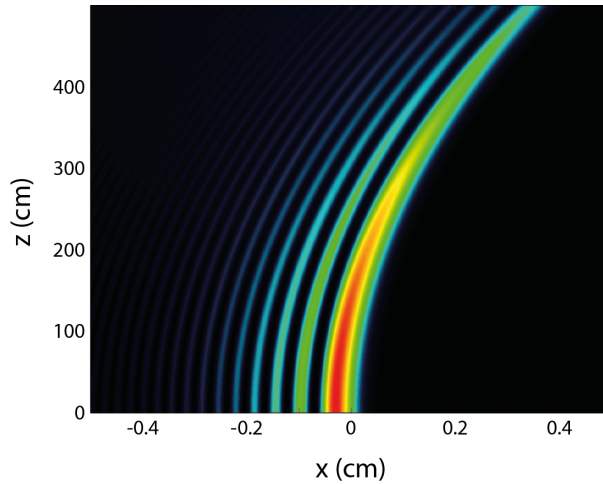


Figure 5.3-10 Propagation dynamics of a truncated Airy beam with $a = 0.05$, $x_0 = 300 \mu\text{m}$, $\lambda_0 = 800 \text{ nm}$ over a propagation distance of $z = 500 \text{ cm}$.

Furthermore, the ballistic dynamics of Airy beams have been studied by Siviloglou *et al.* [238]. Starting from Eq. (5.3-7), if we consider the input field distribution as:

$$E(v = 0, u) = \text{Ai}(u) e^{au} e^{i\eta u} \quad (5.3-12)$$

where the new parameter η is associated with the initial launch angle of this beam. Under these conditions, direct integration of Eq. (5.3-7) results in:

$$A(v, u) = Ai \left[u - (v/2)^2 - \eta v + iav \right] e^{[au - (av^2/2) - a\eta v]} \times e^{i[-v^3/12 + (a^2 - \eta^2 + u)v/2 + \eta u - (\eta v^2/2)]} \quad (5.3-13)$$

From the argument of the Airy function in Eq. (5.3-13) one can conclude that this beam follows a ballistic trajectory in the $u - v$ plane that is described by the parabola $u = \eta v + (v/2)^2$. By placing the physical parameters, the deflection of the beam intensity is found as:

$$x_d = \theta z + \left(z^2 / (4k^2 x_0^3) \right) \quad (5.3-14)$$

where the actual launch angle θ in the $x - z$ coordinates is related to the normalized η parameter through $\theta = \eta / kx_0$. The corresponding kinematical equations describing these ballistics are $d^2x / dz^2 = 1 / (2k^2 x_0^2) = g$, and $dx / dz = gz + \theta$ where g plays here the role of *gravity*. The ballistic dynamics of Airy beam with $a = 0$, $x_0 = 200 \mu\text{m}$, $\lambda_0 = 800 \text{ nm}$, and for different launching angles $\theta = -1.6 \text{ mrad}$, $\theta = -31.4 \text{ mrad}$, $\theta = 31.4 \text{ mrad}$ and $\theta = 1.6 \text{ mrad}$ are shown in Figure 5.3-11, respectively. These launching angles correspond to $\eta = -2.47$, -0.49 , 0.49 , and 2.47 , respectively.

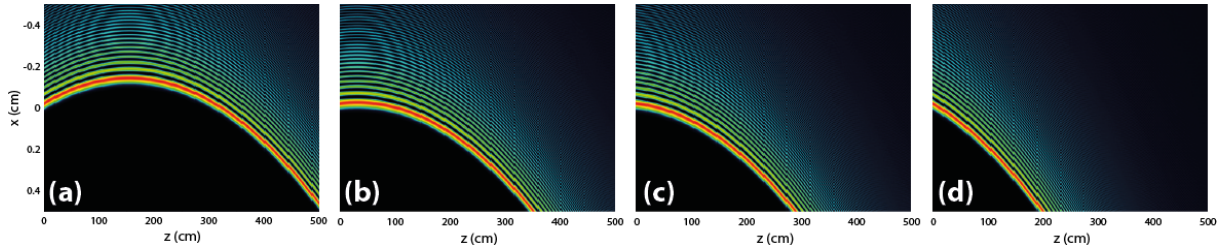


Figure 5.3-11 The ballistic dynamics of an Airy beam with $a = 0$, $x_0 = 200 \mu\text{m}$, $\lambda_0 = 800 \text{ nm}$ and different launching angle (a) $\theta = -1.6 \text{ mrad}$, (b) $\theta = -31.4 \text{ mrad}$, (c) $\theta = 31.4 \text{ mrad}$, and (d) $\theta = 1.16 \text{ mrad}$. These launching angles correspond to $\eta = -2.47$ (a), -0.49 (b), 0.49 (c) and 2.47 (d).

When the launching angle is negative ($\eta < 0$), the beam initially ascend until it turns due to the downwards acceleration at $z_t = -\theta / g = -2k^2 x_0^3 \theta$. At the climax point the maximum

divergence is $x_{d,\max} = -\theta^2 k^2 x_0^3$ [238]. From that point on, the beam will accelerate downwards as shown in Figure 5.3-11. As it can be clearly seen, at any launching angle the Airy beam intensity profile has a ballistic trajectory suggesting that the Airy wavepacket can circumvent an opaque obstacle lying in its straight pass. This characteristic behavior of Airy beam has been used in optical micromanipulation for particle cleaning and sorting [239, 240]. In fact, in this process the particles are being attracted by gradient optical forces towards the main peak of the Airy beam and subsequently propelled along the parabolic paths by the optical radiation pressure. The difference between micromanipulation with Airy beams and other non-diffracting beam such as Bessel beams, is due to the fact that the Airy beam itself, and therefore the trapping potential, freely self-bends during propagation. Moreover, in contrary to Bessel beam, the Airy beam is highly asymmetric and occupies only one-quarter of space.

Another very interesting characteristic of non-diffracting beams and especially Airy beams is their self-healing property. This attribute of the Airy beam was first studied by Broky *et al.* [241] both numerically and experimentally. They showed that this class of waves tends to reform during the propagation in spite of the severity of the imposed perturbations. This property of Airy is interpreted through their internal transverse power flow. Experimentally, they blocked the main lobe of a 2D Airy beam with an opaque rectangular obstacle. In this case, the main lobe energy content was 40% of the whole beam. In order to investigate the self-healing property of the beam, they monitored its propagation at different distances along the propagation direction. The initial intensity distribution of the beam after the obstruction of the main intensity lobe is shown in Figure 5.3-12(a). The Airy beam profile in different propagation distance of $z = 11$ cm $z = 30$ cm are shown in Figure 5.3-12(b-c), respectively.

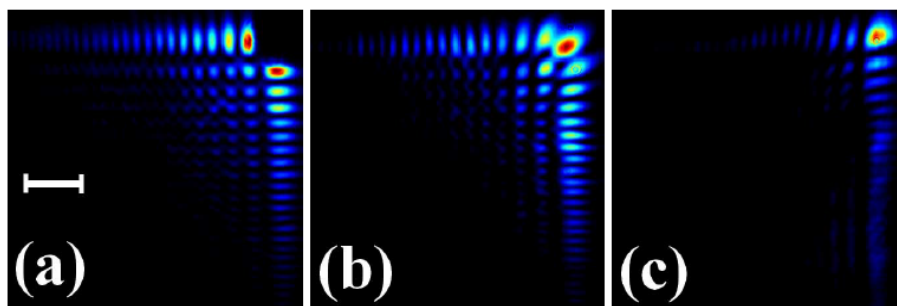


Figure 5.3-12 Self-healing of an Airy beam with the main lobe obstructed. Observed intensity pattern at (a) the input $z = 0$, (b) $z = 11$ cm, and (c) $z = 30$ cm. From Ref. [241].

It should be noted that with their experimental conditions the propagation distance of 30 cm, was nearly 4 times the diffraction lengths of the main lobe, and thus launching only the main lobe would result in 5-fold increase in the beam width over the same propagation distance and the peak intensity value would have dropped to 5% of its initial value. The self-healing characteristic of the Airy beams can be better understood by calculating the Poynting vector. In the paraxial regime, the Poynting vector is given by [241, 242]

$$\vec{S} = \vec{S}_z + \vec{S}_\perp = \frac{1}{2\sqrt{\mu_0 / \epsilon_0}} |E|^2 \hat{z} + \frac{i}{4k\sqrt{\mu_0 / \epsilon_0}} [E\nabla_\perp E^* - E^*\nabla_\perp E] \quad (5.3-15)$$

where \vec{S}_z denotes the longitudinal component and \vec{S}_\perp stands for the transverse component of the Poynting vector. In fact, self-healing is caused by the transverse component. The transverse component of the Poynting vector, which describes the energy flow in the transverse coordinates for Airy beams, is shown in Figure 5.3-13. As it can be seen, the energy flow from the side lobes to the main lobe and thus any obstruction or perturbation in the main lobe will be healed during the propagation.

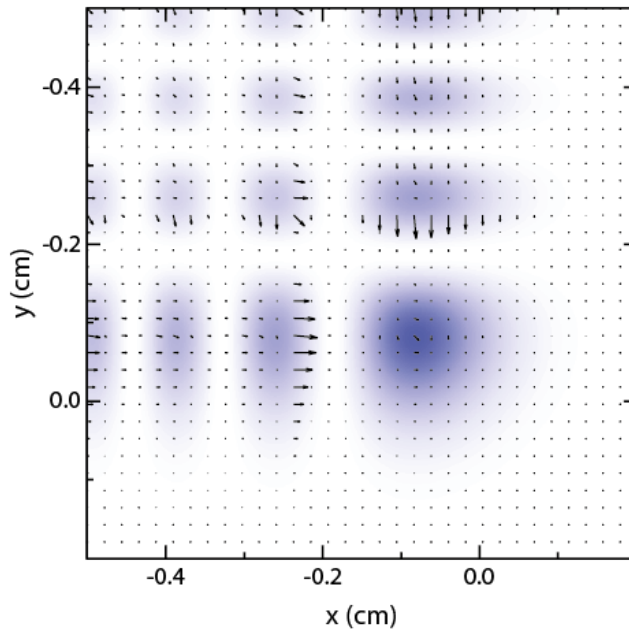


Figure 5.3-13 Transverse energy flow in a 2D Airy beam.

- **Experimental realization of Airy beams**

As already mentioned, the generation of Airy beams relies on the fact the angular Fourier spectrum of an exponentially truncated Airy beam is Gaussian distribution with a cubic phase resulting from the Fourier transform of the Airy function itself (see Eq. (5.3-11)). Therefore, an optical Airy beam can be synthesized by imprinting a cubic phase modulation on a Gaussian beam and then Fourier transforming it by a converging lens [23]. In Figure 5.3-14 are shown the procedure of generating a two-dimensional Airy beam. Figure 5.3-14(a) depicts the input Gaussian pulse, Figure 5.3-14(b) shows the wrapped (modulo 2π) cubic phase imprinted on the input Gaussian beam and Figure 5.3-14(c) shows the obtained two-dimensional Airy beam after Fourier transformation by a spherical lens.

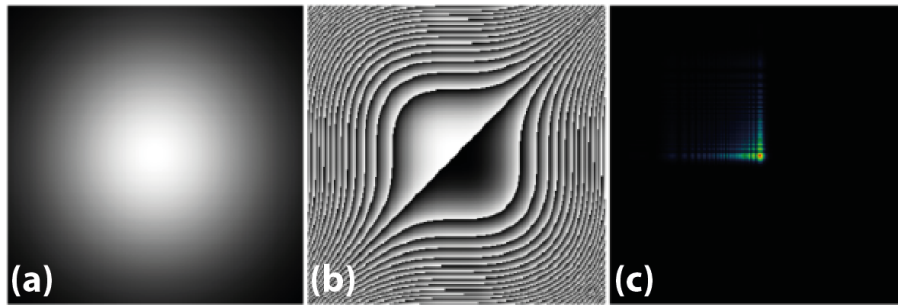


Figure 5.3-14 Experimentally synthesizing an Airy beam: (a) Input Gaussian beam, (b) wrapped (modulo 2π) cubic phase map imprinted and the input Gaussian beam, and (c) obtained Airy beam after Fourier transformation by a spherical lens.

However, applying a cubic phase modulation on an optical beam is not a trivial task. So far, the generation of optical Airy beams has been demonstrated using liquid crystal spatial light modulators (SLMs) [23, 231], specially designed cubic phase masks [215, 216], and three-wave mixing in asymmetric nonlinear photonic crystals [243]. In all these cases, the required cubic phase distribution for the generation of the Airy beams was achieved using complicated, expensive, and technically demanding approaches, which also suffer from other drawbacks such as limitations on the input power and tunability. For example, although SLMs are tunable and easy to use, they are limited to a maximum phase delay of $\sim 2\pi$ and rely on phase wrapping to achieve higher phase modulations, making it difficult to implement strong spatial gradients of the phase and also causes wavefront errors due to the discrete nature of the device. Furthermore, SLMs cannot handle intense beams or beams in the UV range. On the other hand, cubic phase masks can sustain high laser intensities and in principle can be designed for application in the

UV, though they are not tunable since they are designed and fabricated for specific wavelengths. Finally, the use of asymmetric nonlinear photonic crystals for the generation of Airy beams relies on the two-dimensional poling of nonlinear crystals and cannot handle intense or UV beams.

Here we show that optical aberrations can be used to induce cubic phase modulation [204]. The possibility of generating a cubic phase modulation using optical aberrations emerges from the general formulation of the Siedel wave aberrations [244] of a single spherical lens [204, 244]:

$$\varphi^{(4)} = -\frac{1}{4}B\rho^4 - \frac{1}{2}(2C \cos^2 \theta + D)r_0^2\rho^2 + Er_0^3\rho \cos \theta + Fr_0\rho^3 \cos \theta \quad (5.3-16)$$

where B , C , D , E and F are the spherical aberration, astigmatism, field curvature, distortion, and coma aberration coefficients, respectively; r_0 is the object height; ρ is the zonal radius; and θ is the polar angle at the exit pupil of the lens. In Figure 5.3-15(a) the ray-tracing simulation of the aberrations caused by tilting an ordinary spherical lens is shown. In fact, this simple approach can be used to create curved plasma channels. This is demonstrated in Figure 5.3-15(b), where focusing the intense laser beam by a tilted spherical lens with a focal distance of $f = 100$ mm, has resulted in a curved plasma string.

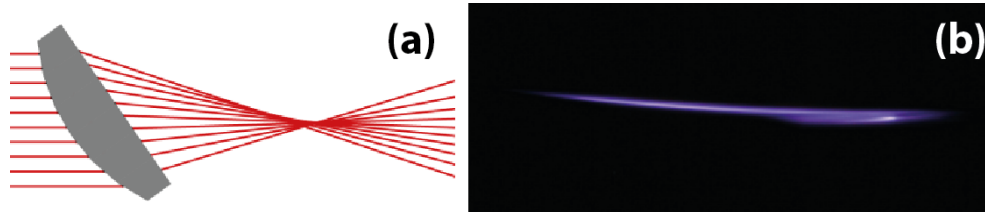


Figure 5.3-15 (a) Ray-tracing simulation of a tilted spherical lens, and (b) CCD image of a curved plasma channel fluorescence by focusing the laser beam with a tilted lens.

Now, let us show how we can use the wave aberration described by Eq. (5.3-16) to imprint a phase modulation on the output wavefront. It is clear that the terms that have cubic dependency on ρ will lead to spatial cubic phase modulation. Only the coma aberration, though it also depends on the planar angle, fulfills this condition with respect to the zonal radius. On the other hand, the required phase modulation for the generation of Airy beams is actually a one-

dimensional process and therefore one-dimensional optical elements should be used. Cylindrical lenses are thus good candidates and in this case. Thus, Eq. (5.3-16) takes the following form:

$$\varphi_{\text{cyl}}^{(4)} = -\frac{1}{4}Bx^4 - \frac{1}{2}(2C + D)x_0^2x^2 + Ex_0^3x + Fx_0x^3 \quad (5.3-17)$$

where x_0 is the objects height and x is the distance, measured from the lens center, along the normal cylindrical axis of the lens. It is now evident that for a cylindrical lens the coma aberration induces a pure spatial cubic phase modulation term that could, in principle, be used for the generation of Airy beams. Unfortunately, when using a single lens, the coma induced cubic term in Eq. (5.3-17) cannot, in general, be isolated from the other terms (quadratic, quartic). However, a two-lens optical system can be tuned in such a way that only a single optical aberration will be dominant within a portion of the output wavefront. This is possible by using combinations of lenses with opposite signs of aberration coefficients so that the undesired optical aberrations can be canceled out. Note that this is a well-known technical approach in the design optical systems for minimizing aberrations [244].

In our case the optical system should transform a plane wavefront to a cubic phase modulated one. Thus, our optical system design criterion is the cancellation of all the aberrations except from the coma. This can be achieved by using a tilted variant of the well-known cylindrical beam expander. The cylindrical beam expander is shown in Figure 5.3-16(a). As shown in Figure 5.3-16(b), when this optical system is not tilted and the optical axis of the system is adjusted to coincide to be on the center of input beam, the total amount of induced spatial phase on the input beam is zero, while in the tilted cylindrical beam expander, shown in Figure 5.3-16(c), by controlling the tilt angles and also spacing between the lenses and displacing the optical elements center with respect to the beam a pure cubic spatial phase can be achieved as it is shown in Figure 5.3-16(d).

In paraxial optics approximation, the collimated input beam remains collimated upon exiting the beam expander since the back and front focal points of the lenses coincide. As shown in Figure 5.3-16(c), we tilt first the diverging cylindrical lens by an angle φ_1 to induce the necessary optical aberrations.

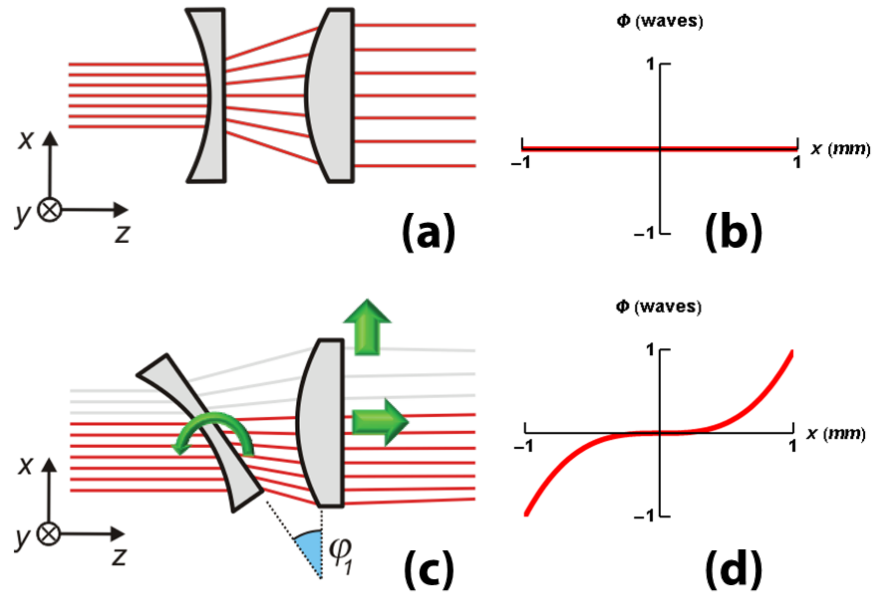


Figure 5.3-16 (a) Ray-tracing simulation of a conventional cylindrical beam expander without tilt, (b) calculated spatial phase imprinted on the input beam using a conventional untitled cylindrical beam expander, (c) tilted cylindrical beam expander; arrows denote the degrees of freedom to control the aberration induced spatial phases and (d) calculated imprinted cubic spatial phase on the input beam using the optimized (for cubic spatial phase only) tilted cylindrical beam expander.

In order to compensate all the undesired aberrations, except the coma, we displace the second converging lens in both the longitudinal and the transverse direction. Using these displacements as the only free parameters, we carried out the whole optimization process by using ray-tracing simulations that provide a quantitative analysis of the output wavefront. We first use a rough longitudinal displacement in a way to maintain the rays nearly collimated at the exit of the system. A few iterative steps of fine-tuning, using small transverse and longitudinal displacements are then used to practically compensate for any unwanted linear, quadratic, and quartic phase distortions. Using this method over a wide range of parameters, such as tilt angle and focal length of the cylindrical lenses, we have successfully tuned the optical system to generate a well-controlled cubic phase variation along the x -axis. It is important to note that compensation is achieved only in the lower portion of the output beam, indicated by red rays in Figure 5.3-16(c) while the upper portion of the output beam, represented by gray rays in the same figure, is dominated by the presence of strong quadratic term. Hence, in order to have the desired net cubic phase, the beam should cover only the lower half of the optical system.

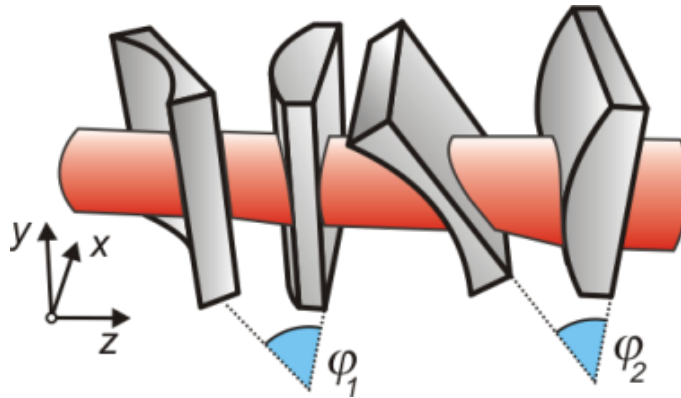


Figure 5.3-17 Configuration for the generation of the 2D cubic phase modulation (along the x and y axes)

The procedure can be easily expanded to two dimensions by adding a second cylindrical telescopic system, after the first one, in a perpendicular orientation, as shown in Figure 5.3-17. In this way, the cubic phase variation along the x -axis is tuned by the first system and the respective phase pattern in the y direction is imposed by the second system.

The capability of such optical systems to generate, in a tunable way, a cubic phase modulation across the wavefront of collimated input beam can be clearly demonstrated with ray-tracing simulations. We have simulated the optical systems using 25-mm-wide BK7 cylindrical lenses of ± 50 mm focal length, illuminated by a collimated beam at 800 nm. Figure 5.3-18(a) shows the phase variation along the x -axis after the single cylindrical telescope for two different tilt angles φ_1 . In both cases, the ray-tracing results are nicely fitted with cubic functions αx^3 for an optical field of ~ 8 mm wide.

These results are obtained by displacing the second converging lens by ~ 14 mm (longitudinally) and 1 mm transversely for 35° tilt angle while the displacements reduce to 8.3 and 0.5 mm, respectively, for the tilt angle of 25° , as measured from the center of the input face of the first diverging lens. The process is completely tunable since the rate constant α of the cubic fit is a monotonic function of the tilt angle φ_1 . Furthermore, the cubic phase rate constant is quite high, approaching values of ~ 0.3 waves/mm³. For the cubic phase modulation in two dimensions, we use the two cylindrical telescopic systems described earlier and shown in Figure 5.3-17 (with the second telescope identical to the first one).

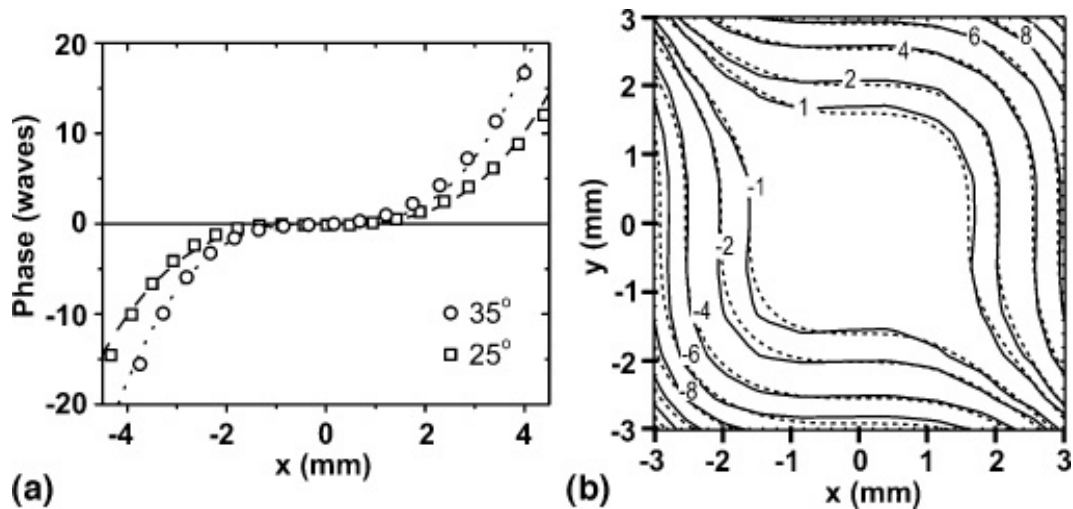


Figure 5.3-18 Simulated phase modulation at the exit of the optical system. (a) 1D phase modulation of the two-lens system and respective cubic fits αx^3 for two tilt angles φ_1 : open squares, simulation results for $\varphi_1=25^\circ$; dashed line, cubic fit with $\alpha=0.16$ waves/mm³; open circles, simulation results for $\varphi_1=35^\circ$; and dotted line, cubic fit with $\alpha=0.27$ waves/mm³. (b) Contour plots of the 2D phase modulation (in waves) for the four-lens system ($\varphi_1 = \varphi_2 = 35^\circ$) and respective cubic phase fit $\alpha(x^3 + y^3)$: solid line, simulation results; dotted lines, contour curves of the 2D cubic fit with $\alpha=0.25$ waves/mm³.

The resulting phase variation in xy -plane for 35° tilt angle is shown in Figure 5.3-18(b). The contour curves of the ray-tracing results are again in very nice agreement with a 2D cubic fit $\alpha(x^3 + y^3)$ for a field of ~ 6 mm wide. Our ray-tracing simulations clearly demonstrate the capability of such tilted cylindrical telescopic systems to induce a cubic phase modulation, in one or two dimensions, on the incident plane wave. In order to demonstrate experimentally the ability of the proposed optical phase systems to generate intense Airy beams, we exploit the fact that such a beam can be generated by first imprinting a cubic phase modulation on a Gaussian beam and then spatially Fourier transforming it using a converging lens [215, 231]. In our experiments, linearly polarized IR (800 nm), 35-fs laser pulses with energy of 1 mJ/pulse were used. The Gaussian-shaped femtosecond laser beam propagated through the optical systems shown in Figure 5.3-16(c) and Figure 5.3-17 to imprint the one-and two-dimensional cubic phases, respectively; all lenses had ∓ 50 mm focal lengths, as in the previous simulations. Subsequently, the beam was spatially Fourier transformed to generate the Airy beams using different converging spherical lenses of focal lengths $f = 100, 200,$ and 500 mm.

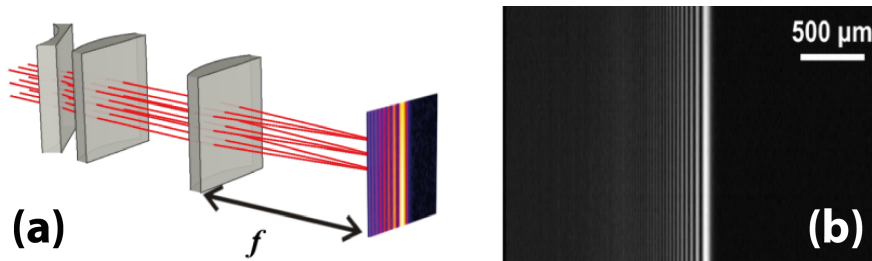


Figure 5.3-19 (a) Experimental setup to generate 1D Airy beams and (b) generated 1D Airy beam. The focal length of the titled cylindrical beam expander, used to induce spatial cubic phase in 1D were ∓ 50 mm and an $f=100$ mm cylindrical lens is used for Fourier transformation.

The generated Airy beams were images using a 12-bit CCD camera. Figure 5.3-19(a) shows the experimental scheme used to create a 1D Airy beam and generated Airy beam is shown in Figure 5.3-19(b). For the 1D Airy beam an $f = 100$ mm cylindrical lens is used for Fourier transformation and the one-dimensional Airy beam is formed at the focal distance of this lens. Figure 5.3-20(a) shows the experimental scheme used for 2D Airy beam generation and the generated 2D Airy beam with an $f = 100$ mm lens used for Fourier transformation is shown in Figure 5.3-20(b).

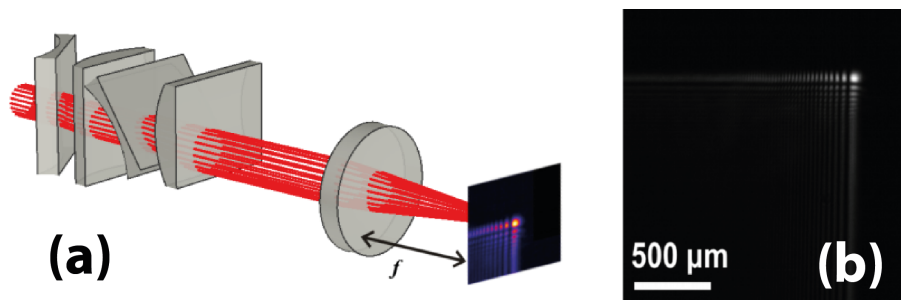


Figure 5.3-20 (a) Experimental setup to generate 2D Airy beams and (b) generated Airy beam beams with two sets of titled cylindrical beam expanders with lenses of focal length of ∓ 50 mm used to induce spatial cubic phase modulation and a spherical lens with $f=100$ mm used for spatial Fourier transformation.

In both one-and two-dimensional generated Airy beams the characteristic multi-lobed pattern of the Airy beam is evident in the images while the highest intensity lobe is $\sim 54 \mu\text{m}$ wide. As already mentioned, another interesting attribute of the Airy beams is their transverse bending. The deflection D is a quadratic function of the propagation distance and can be estimated using the equation $D(\Delta z) = 3.7 \times 10^{-2} (\lambda^2 / W_A^3) \times \Delta z^2$ [215], where λ is the

wavelength, W_A is the full width at half maximum (FWHM) of the highest intensity lobe at the Fourier plane, and Δz is the propagation distance measured from the Fourier plane. Figure 5.3-21 depicts the experimentally measured deflection D along the x -axis of the primary intensity lobe of the generated 2D Airy, for two Fourier transforming lenses as a function of the distance Δz . The smaller size of the high-intensity lobe of the Airy generated by the 100-mm lens ($W_A = 54 \mu\text{m}$) results in much stronger deflection compared to the Airy generated by the 500-mm lens ($W_A = 140 \mu\text{m}$). The experimental points nicely fit to quadratic functions $D(\Delta z) / \Delta z^2 = (150 \pm 1) \times 10^{-4} \text{ mm/cm}^2$ for the 100-mm lens for range of $\sim 12 \text{ cm}$ and $D(\Delta z) / \Delta z^2 = (9.3 \pm 0.2) \times 10^{-4} \text{ mm/cm}^2$ for the 500-mm lens for a range of $\sim 70 \text{ cm}$. In both cases, the measured deflection rate is in good agreement with the theoretically predicted ones of $D_{th}(\Delta z) / \Delta z^2 \simeq 1.44 \times 10^{-4} \text{ mm/cm}^2$ for the 100-mm lens and $D_{th}(\Delta z) / \Delta z^2 \simeq 8.4 \times 10^{-4} \text{ mm/cm}^2$ for the 500-mm lens.

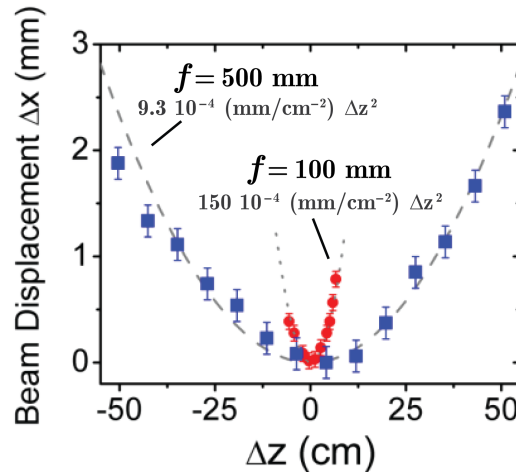


Figure 5.3-21 Transverse acceleration Δ_d of the 2D Airy beam main lobe (along the x -axis) for two Fourier transforming lenses as a function of the distance Δz from their Fourier plane. Circles, experimental points; dotted line, quadratic fit, for the $f = 100 \text{ mm}$ lens; and Squares, experimental points; dashed line, quadratic fit for the $f = 500 \text{ mm}$ lens.

Moreover, nonlinear propagation of Airy beams and filamentation of Airy beams has attracted enormous attention in the past years. Due to their very interesting features such as

transverse acceleration (bending), self-healing, they have been the subject of many studies by various groups. Polynkin *et al.* have experimentally demonstrated that the Airy beams can be used to generate curved plasma channels [215]. The possibility of generating curved plasma channels by 2D Airy beams has been also investigated by analytical calculation of the energy flux towards the main lobe and taking into account the role of Kerr effect by Kasparian *et al.*, [217]. Filamentation and white light generation by Airy beams has been studied experimentally by Polynkin *et al.*, [216] and the effect of Kerr nonlinearity on the propagation of the Airy beams has been theoretically studied by Chen *et al.* [245]. In several publications we have also studied the nonlinear propagation of the Airy beams [27, 204, 218], which will be discussed in the following.

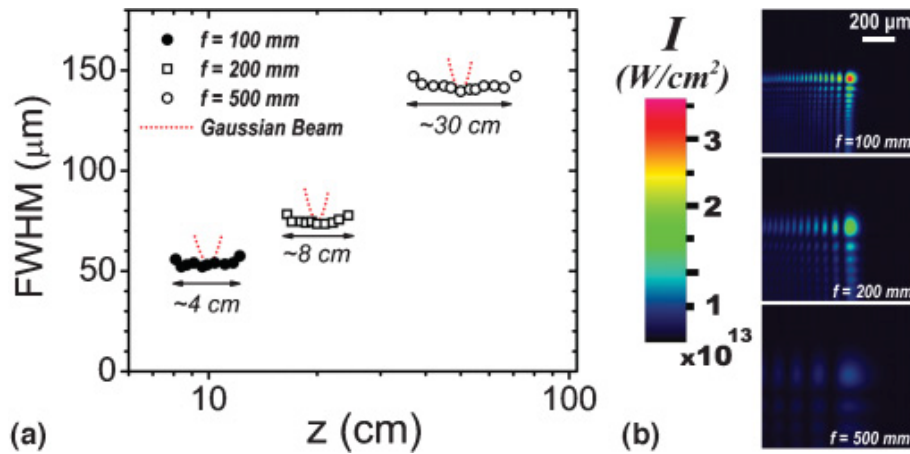


Figure 5.3-22 (a) FWHM of the 2D Airy peak intensity lobe as a function of the propagation distance z for three Fourier transforming lenses with $f = 100$, 200, and 500 mm. The evolution of equivalent Gaussian beam is also presented. (b) Calibrated intensity profiles on the Fourier plane of each of the three Fourier transforming lenses.

We have demonstrated that using our approach to generate the Airy beams we can practically control the main lobe dimensions and intensity, and hence, we gain control on the filaments created by these beams. The ability to tune the size and amplitude of the main lobe intensity, and consequently the corresponding filament, by changing the focal length of the Fourier transforming lens is demonstrated in Figure 5.3-23. Our experimental data show that the FWHM of the main intensity lobe on the Fourier plane is, as expected, a linear function of the focal lens f and can be described by $W_A \cong 32 \mu\text{m} + (0.21 \mu\text{m} / \text{mm})f$. As it is shown in Figure 5.3-23(a), the FWHM of the main lobe remains practically constant over an extended

propagation range. The length of this filamentary-like propagation is roughly $\sim 3.5 z_R$, where z_R is the Rayleigh length of an equivalent Gaussian beam with FWHM equal to W_A . Furthermore, Figure 5.3-23(b) shows the corresponding intensity distribution for the Airy beams. The intensity profiles were obtained using a calibrated linear 12-bit CCD camera. The peak intensity of the Airy filaments is in the range of $3.5 \times 10^{13} \text{ W/cm}^2$ (for $f = 100 \text{ mm}$) to $5 \times 10^{12} \text{ W/cm}^2$ (for $f = 500 \text{ mm}$). From the preceding it becomes clear that tunable Airy beams offer a unique way of tailoring ultrafast intense filaments in both diameter and intensity (for a given medium), something that could not be done easily with any other method known to date.

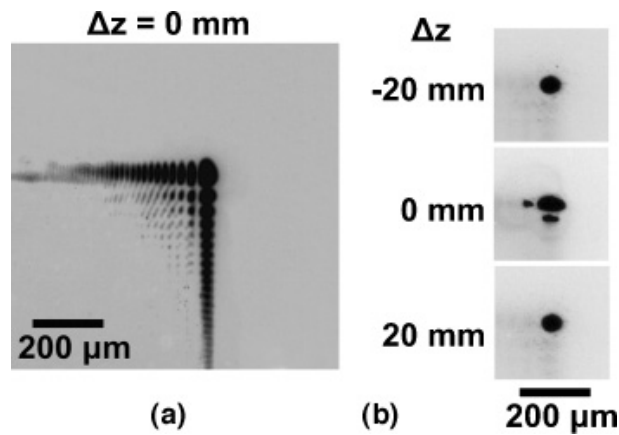


Figure 5.3-23 Microscope images of damage spots generated by Airy beams (35 fs, 1mJ) using an $f = 100 \text{ mm}$ Fourier transforming lens. Δz refers to the distance from the Fourier plane. (a) Single shot-burn spots on Cr of a 2D Airy beam. (b) Microscope images of ablation spots on glass generated from the 2D Airy beam.

A further demonstration of the ability to generate intense Airy filaments is clearly depicted in Figure 5.3-23 where we show microscope images of damage spots (on metals and glass) generated from our Airy beams (input energy 1 mJ, and $f = 100 \text{ mm}$ spherical Fourier transforming lens). In Figure 5.3-23(a) we show the burn spots on metallic (Cr) surface for a 2D Airy beam. The burn spot in Figure 5.3-23(a) follows the intensity distribution of Figure 5.3-23(b). This intense filamentary structure is sustained over an extended propagation region, as illustrated by ablation experiments on glass plates shown in Figure 5.3-23(b). From these images, the filament created on the central lobe is shown to have an almost constant diameter over a region of $\sim 4 \text{ cm}$. In addition, since the input power is high enough, secondary, but shorter, filaments appear around $\Delta z = 0$ on the first two side lobes.

Thus, we have demonstrated the possibility of using optical aberrations to induce a continuous cubic phase modulation on an input beam wavefront. A cascade of two tilted cylindrical telescope systems, with orthogonal orientation with respect to each other, is used to imprint the cubic phase and then a spherical lens is used for spatial Fourier transformation. This procedure is tunable and can be applied to generate intense ultrafast Airy beams and tailored filaments. Furthermore, using cylindrical mirrors instead of cylindrical lenses, the same concept can be used to generate Airy beams, in principle, throughout the electromagnetic spectrum, like UV or even THz radiation.

5.3.3 Airy³ light bullets

Formation of non-spreading wavepackets has been always a major challenge in optics. Since spreading is a general property of electromagnetic wavepackets. Essentially, the spreading is caused by the presence of distinct frequency components, which are superposed to create a wavepacket. In such a case, each component would propagate with different velocities and/or different directions. For instance, the transverse spreading of a laser beam is due to diffraction, or likewise a light pulse spreads in time as they propagate in a material due to the group velocity dispersion. Nonlinearity, in general, increases the disintegration of a wavepacket but under special conditions, it compensates the linear spreading effects. Such a balance between the linear spreading effects and the nonlinear counterbalancing phenomena results in the formation of *solitons* which have been the subject of vast amount of studies in the past decades (see [14] and references therein). Thus optical solitons are localized electromagnetic waves that propagate stably in nonlinear media with dispersion, diffraction or both.

A soliton or *solitary wave* that propagates in a medium with both dispersion and diffraction without a significant spreading in time or space is called *spatiotemporal soliton* or *light bullet*. Thus, light bullets are localized wavepackets that are robust against both diffraction and dispersion. As proposed by Silberberg [13] light bullets are feasible in the context of nonlinear optics where the Kerr nonlinearity may compensate the effect of diffraction and dispersion. The generation of stable 3D (localized in both space and time) light bullets is a very delicate task [14], since it is possible only when the effects of dispersion and diffraction are equalized [13, 14]. Thus, the spatiotemporal solitons may be understood as the result of the simultaneous balance of diffraction and dispersion by the transverse self-focusing and nonlinear phase

modulation in the longitudinal dimensions, respectively (Figure 5.3-24). Furthermore, these light bullets are very sensitive to any modulation or structural instability [6].

On the other hand, in the linear propagation regime, several non-diffracting, non-spreading wavepackets have been demonstrated with the Bessel beam being perhaps the most studied case in the spatial domain [21] (see also Sec. 0 and references therein), while in the spatiotemporal domain the linear light bullets were either X-waves [24] or O-waves [246] for normal and anomalous dispersions, respectively [247].

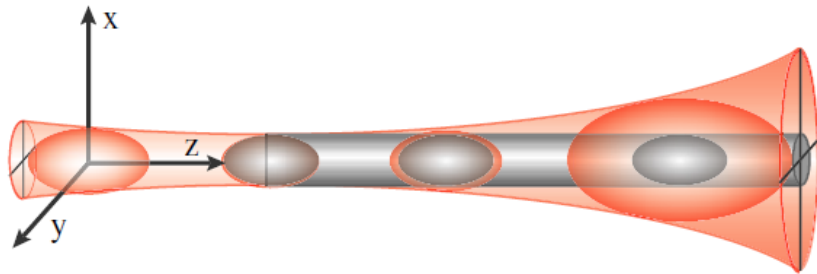


Figure 5.3-24 Formation of nonlinearly generated spatiotemporal soliton due the simultaneous balance of diffraction and dispersion by nonlinear self-focusing. From [14].

On the other hand, if time and space can be disentangled, 3D spatiotemporal light bullets can be obtained in the linear regime [231]. This is possible only by using the Airy function in the temporal domain, since they are the only non-spreading solution in one dimension. Following the theoretical prediction of Siviloglou *et al.* [231], Chong *et al.* [26] have demonstrated the generation of versatile linear light bullets consisting of a Bessel distribution in space and an Airy temporal profile. The schematic of their approach is shown in Figure 5.3-25.

Since the space-time decoupling in the linear propagation regime is possible, a wavepacket comprised of an Airy pulse and a non-diffracting beam such as Bessel, Airy, or Mathieu beams [22] will propagate as a light bullet without the need for equalization of dispersion and diffraction effects. Such versatile linear 3D light bullets open up new exciting possibilities in numerous applications.

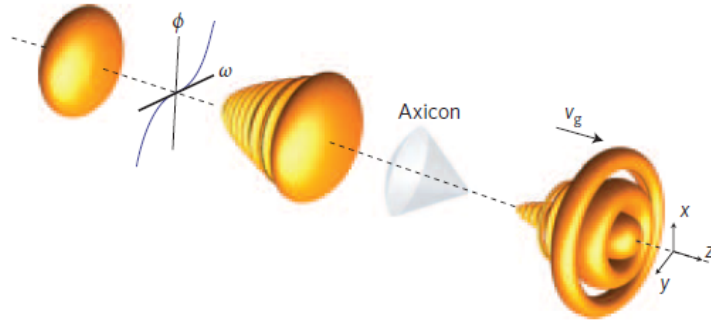


Figure 5.3-25 Iso-intensity plots of Gaussian-Gaussian (initial profile), Airy-Gaussian (after adding a large cubic phase), and Airy-Bessel (after the axicon) wave packets. From [26].

However, for high intensity applications such as filamentation, electric-discharge triggering, and guiding and remote sensing, a question that arises is how the bullet will be affected when its peak intensity is high enough to cause strong nonlinearities. In contrast to the Gaussian wavepackets, these linear light bullets rely on a strong energy redistribution mechanism induced by their specific spatiotemporal profile that redirects energy from the low intensity reservoir to the high intensity peak. This makes the propagation of such wavepackets in the high intensity regime quite interesting, since the linear redistribution mechanism competes in the spatiotemporal domain with nonlinear effects such as the optical Kerr effect, multiphoton or tunnel ionization, and nonlinear losses [5].

We have reported the first experimental realization of Airy^3 light bullets [27]. These light bullets are described by an Airy distribution in all spatial and temporal dimensions. Moreover, in this work we have shown that, going from the linear to the nonlinear regime, the Airy^3 light bullets maintain their robustness, resisting spreading in both space and time. In particular, we show that as the peak power is increased above the critical power for self-focusing P_{cr} , optical filaments, formed inside the main intensity lobes of the bullet, significantly distort the spatial and temporal characteristics of the Airy wavepacket. Despite this, as it propagates, the Airy^3 light bullet gradually recovers in both space and time with only minor energy dissipation at the expense of energy contained in the peripheral low intensity lobes.

Owing to the possibility of space-time decoupling, the spatiotemporal intensity of an Airy^3 wavepacket whose electric field satisfies the linear paraxial wave equation can be written as

$$I(x, y, z) = I_0 \text{Ai}^2\left(\pm \frac{x}{x_0}\right) \text{Ai}^2\left(\pm \frac{y}{y_0}\right) \text{Ai}^2\left(\pm \frac{\tau}{\tau_0} - \frac{(k_0'')^2 z^2}{4\tau_0^4}\right) \quad (5.3-18)$$

where Ai denotes the Airy function, x , y and z are the two transverse and the propagation coordinates, respectively, $\tau = t - (z / v_g)$ is the reduced time with v_g being the group velocity, of wavepacket, x_0, y_0 and τ_0 are the two spatial and temporal scale factors proportional to the spatial and temporal widths of the wavepacket (proportionality coefficient for FWHM of intensity main lobe is 1.66; for example $x_{\text{FWHM}} = 1.66x_0$, where x_{FWHM} is the width (FWHM) of the intensity main lobe along x -axis), respectively, and $k_0'' = \partial^2 k / \partial \omega^2$ is the dispersion coefficient of the medium at the central frequency.

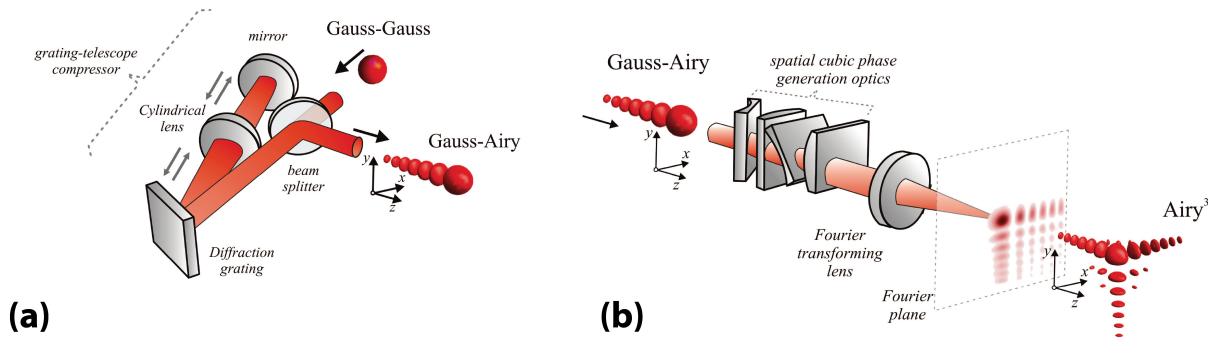


Figure 5.3-26 Graphical representation of an Airy^3 light bullet generation; (a) a spatiotemporal Gaussian pulse (Gaussian in time and Gaussian in transverse dimensions) is transformed to a temporal Airy pulse with a Gaussian spatial distribution by a grating-telescope compressor, (b) The Gauss-Airy spatiotemporal wavepacket is transformed to a spatiotemporal Airy^3 wavepacket by a cascade of two orthogonally-oriented tilted cylindrical telescope systems.

To obtain an Airy temporal profile, we imposed a cubic spectral phase on our initial Gaussian laser pulses by using a grating-telescope compressor [248], similar to the one used by Chong *et al.* [26]. The experimental scheme to create Airy pulse with a spatial Gaussian profile is shown in Figure 5.3-26(a). More specifically, 35 fs Gaussian laser pulses at the central wavelength of 800 nm, were incident on a diffraction grating (groove density 1800 l/mm), the first-order diffraction was collected by an $f=150$ mm cylindrical lens and then sent back on the grating after reflection by a mirror. This system was first simulated using ray-tracing simulations to choose a range of parameters for optimized imprinting of the cubic phase on the

initial pulse and then the grating-telescope compressor parameters (incident angle on the grating, grating-lens and lens-mirror separations) were tuned to imprint $\sim 6 \times 10^5 \text{ fs}^3$ of cubic phase onto the initial laser pulse. Using this arrangement, Airy pulses with main lobe pulse duration $\tau_{\text{Airy}} \simeq 200 \text{ fs}$ (intensity FWHM) were generated. To measure the temporal intensity of the generated Airy pulses, we cross-correlated them with a $\tau_{\text{ref.}} = 35 \text{ fs}$ Gaussian reference pulse using a non-collinear second-order cross-correlation technique [249]. It is important to mention that for the short reference pulse duration ($\tau_{\text{Airy}} \simeq 5.7 \tau_{\text{ref.}}$), this cross-correlation (XC) signal matches very closely the intensity distribution of the pulse being measured.

To create spatial 2D Airy profile, we used a cascade of two tilted cylindrical telescopes each composed of a pair of $f = \mp 50 \text{ mm}$ cylindrical lenses. Details of this approach are described in the previous section as well as in Ref. [204]. The Fourier lens for this experiment was an $f = 500 \text{ mm}$ spherical lens.

The schematic of the experimental setup to create Airy^3 wavepacket from a temporal Airy pulse with spatial Gaussian profile is shown in Figure 5.3-26(b). For our experimental arrangement, the measured FWHM of the main Airy lobe was $\sim 200 \mu\text{m}$ with the primary Airy^3 lobe containing $\sim 3\%$ of the total spatiotemporal energy content of the wavepacket.

In order to confirm the non-spreading behavior of the generated Airy^3 linear wavepackets, we studied their propagation through the bulk of a transparent polymer samples [PMMA: poly(methyl methacrylate)]. According to third-order susceptibility measurements [250], the critical power for self-focusing in PMMA is estimated to be $P_{\text{cr}} \simeq 1.85 \text{ MW}$ (corresponds to $0.36 \mu\text{J}$ at 200 fs). Taking this into account, the total pulse energy for linear propagation was set at 200 nJ , corresponding to $\sim P_{\text{cr}} / 60$ in the primary lobe of the Airy^3 wavepacket. To characterize the extended propagation of such wavepackets, we compared their propagation to a Gaussian wavepacket having the same dimensions both in space and in time as the primary intensity lobe of the Airy^3 wavepacket. The characteristic linear diffraction and dispersion lengths are then defined as L_{R} and L_{D} , respectively, given by:

$$L_R = \frac{\pi n d_0^2}{2 \ln 2 \lambda_0} \quad (5.3-19)$$

$$L_D = \frac{\tau_0^2}{4 \ln 2 \text{GVD}}$$

where λ_0 is the central wavelength, n is the refractive index, GVD is the group velocity dispersion, and d_0 and τ_0 are the intensity FWHM of the main lobe of the Airy³ in space and time, respectively. In our case, $d_0 = 200 \mu\text{m}$ and $\tau_0 = 200 \text{fs}$; thus, the diffraction and dispersion lengths inside the PMMA sample are 16.8 and 26 cm, respectively. In the experiments we used a 20-, 60-, 100-, and 140-cm-long PMMA samples corresponding to $(1.2 L_R, 0.8 L_D)$, $(3.6 L_R, 2.3 L_D)$, $(6 L_R, 3.9 L_D)$, and $(8.3 L_R, 5.4 L_D)$. The Airy³ wavepackets were spatially and temporally characterized after exiting the PMMA samples. Figure 5.3-27 shows the normalized XC traces of the Airy primary peak and the respective normalized spatial profiles (recorded by a 12-bit CCD camera) after different propagation lengths in PMMA.

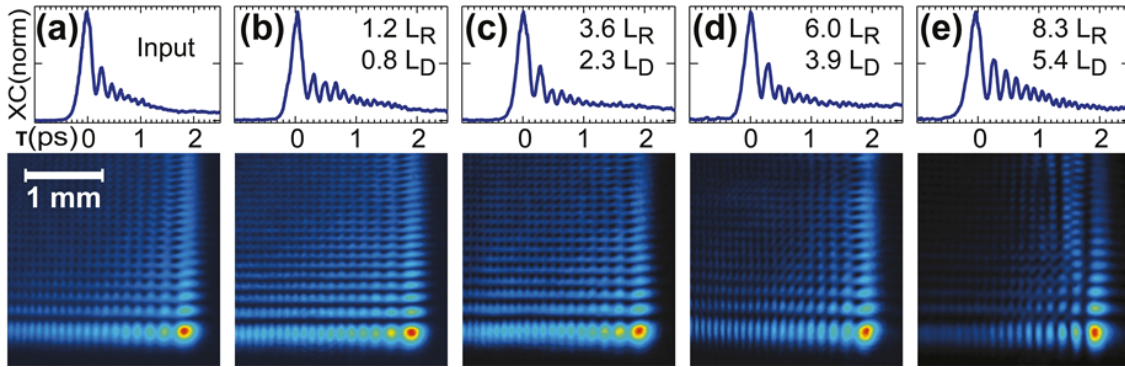


Figure 5.3-27 Normalized spatial and temporal profiles of the Airy³ wavepacket. (a) Initial and (b)-(e) after propagation through $(1.2 L_R, 0.8 L_D)$, $(3.6 L_R, 2.3 L_D)$, $(6 L_R, 3.9 L_D)$ and $(8.3 L_R, 5.4 L_D)$, respectively. L_R and L_D denote the diffraction and dispersion lengths, respectively.

We note that the observed background in the temporal XC traces is mostly due to the quadratic and quantic phase terms which are unavoidable in the folded grating-telescope system shown in Figure 5.3-26(a). In order to explore the effect of quadratic and quantic phase terms on the shape of the generated Airy pulse, recalling that the Fourier transform of the Airy function is a Gaussian distribution with a cubic phase modulation, we add also a quadratic and quantic phase

terms and numerically Fourier transform it into the t space. Now, let us assume that in ω space the Airy-like function is:

$$U(\omega) = \exp\left(-(\omega / \Delta\omega)^2\right) \exp\left[i\left(a\omega^2 + b\omega^3 + c\omega^4\right)\right] \quad (5.3-20)$$

where $\Delta\omega$ denotes the spectral width, and a , b , c are coefficients of the quadratic, cubic and quartic phase modulations, respectively. For the sake of simplicity, we numerically calculate the Fourier transform of the U and plotted its' intensity for a different values of quadratic, cubic and quartic phase coefficients. The results are shown in Figure 5.3-28. The cubic phase coefficient was set to $b = 9000 \text{ fs}^3$, quadratic, and quartic phase coefficients for several situations were set as the following: solid profile: $a = 0, b = 9000 \text{ fs}^3$, and $c = 0$; dashed profile: $a = 1000 \text{ fs}^2$, $b = 9000 \text{ fs}^3$, and $c = 0$; dashed-dotted profile: $a = 2000 \text{ fs}^2$, $b = 9000 \text{ fs}^3$, and $c = 0$; and dotted-profile: $a = 2000 \text{ fs}^2$, $b = 9000 \text{ fs}^3$, and $c = 10000 \text{ fs}^4$. It can be clearly seen that in the presence of quadratic phase terms a background is produced and when a significant amount of quartic phase is added, in addition of increased background, the contrast of secondary peaks is also decreased; a situation similar to the experimental cross-correlation traces shown in Figure 5.3-27.

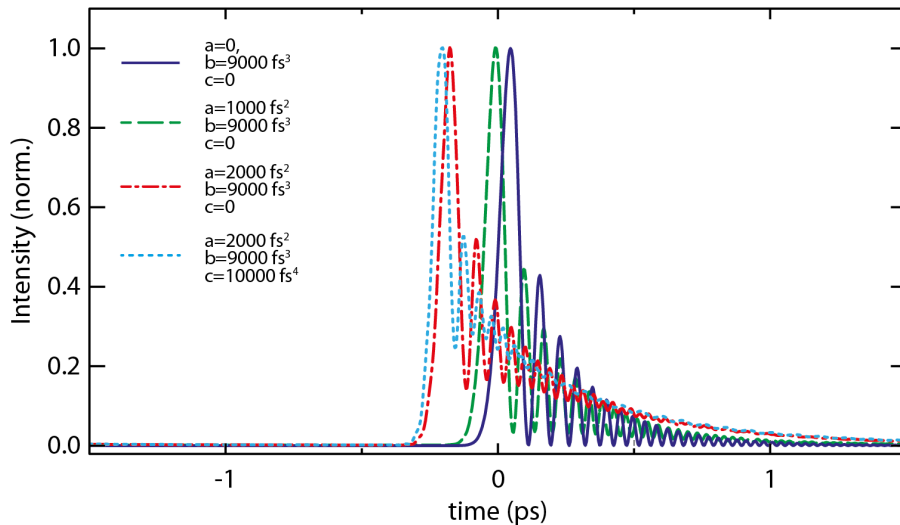


Figure 5.3-28 Effect of quadratic and quartic phase terms on the intensity profile of an Airy pulse. The cubic phase coefficient is set to $b = 9000 \text{ fs}^3$, while the other coefficients were changed as the following: ($a = 0, b = 9000 \text{ fs}^3, c = 0$): Solid curve; ($a = 1000 \text{ fs}^2, b = 9000 \text{ fs}^3, c = 0$): dashed curve; curve; ($a = 2000 \text{ fs}^2, b = 9000 \text{ fs}^3, c = 0$): dashed-dotted curve; ($a = 2000 \text{ fs}^2, b = 9000 \text{ fs}^3, c = 10000 \text{ fs}^4$): dotted curve.

By combining the experimentally measured temporal trace of Figure 5.3-27(e) with the corresponding spatial intensity distributions, we created a 3D intensity iso-surface of the experimentally Airy³ light bullet which is shown in Figure 5.3-29(a). On the other hand, Figure 5.3-29(b) clearly shows that the spatiotemporal dimensions of the main lobe of the Airy³ light bullet remain practically invariant within the measured propagation distance. The variation is about 5% (comparable to our error bar), while, for comparison, a Gaussian pulse with the same spatiotemporal extent as the main lobe of Airy³ light bullet, would have broadened by a factor of 8.4 in space and 5.5 in time over the same propagation distance (140 cm in PMMA). Nonetheless, it is worth mentioning that the slight distortion of the spatial profile in Figure 5.3-27(e) is mainly due to the finite truncation of the experimentally realized Airy beam that is as discussed earlier- known to set a limit on the range of ideal diffractionless propagation.

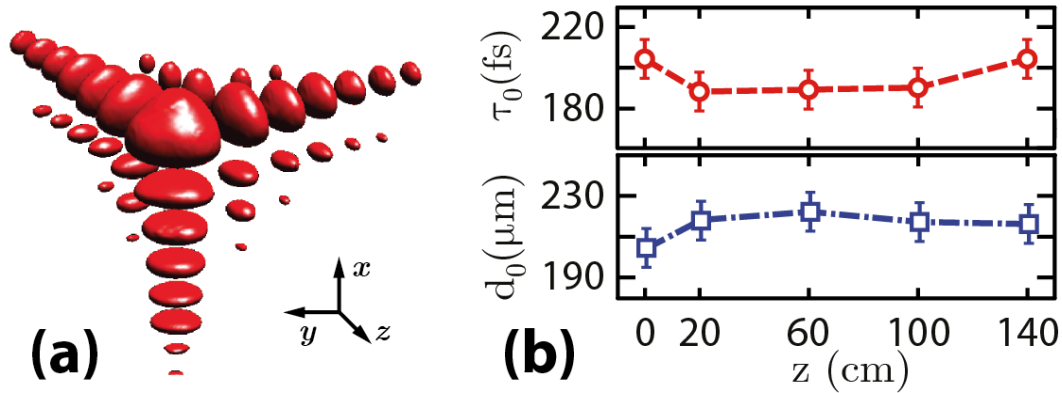


Figure 5.3-29 (a) Intensity iso-surface of the experimentally realized Airy³ light bullet (to assist visualization, the z -axis, time, is stretched by 5 times). (b) Temporal and spatial widths of the main lobe of the Airy³ light bullet vs propagation distance.

Contrary to the linear propagation regime, in the nonlinear regime space-time coupling is unavoidable [14]. Therefore, important questions arise: How intense can an Airy³ light bullet be before the nonlinear propagation effects take over? Would the bullet be destroyed by such effects, or would it recover?

To answer these questions we experimentally studied the nonlinear propagation of Airy³ light bullets in PMMA by monitoring the spatiotemporal profile after propagation through a 2.5-cm-long PMMA sample for different pulse energies. One could expect that as the energy is increased the primary Airy³ peak, as well as the some of the side lobes containing peak powers

above P_{cr} , would be affected by strong nonlinear propagation effects like filamentation. The typical length of a light filament in condensed media ranges from tens of microns to several millimeters while the typical diameter is of the order of $10\ \mu\text{m}$ [5, 45]. Figure 5.3-30(a)-(c) show the spatial profiles of the Airy³ bullet at the exit surface as a function of the total input energy. By comparing to the linear regime, it is clear that as the energy is increased to 0.4 mJ, the spatial Airy profile is distorted and an intense hot spot appears in the main lobe. The transverse dimensions of the hot spot agree well with the typical filament diameter in solid media. As the input energy is further increased (Figure 5.3-30(b)-(c)) similar hot spots emerge in the adjacent secondary lobes in both transverse directions. Furthermore, multiple hot spots appear in the Airy peak leading to deterioration of its spatial profile. The behavior is typical indication of multiple filamentation as the input power exceeds P_{cr} by a considerable amount. This is further supported by strong changes observed in the temporal profiles. The corresponding XC traces of the main spatial lobe are shown in Figure 5.3-30(d) as a function of the input energy. It is clear that with an increase of the input energy the effect of nonlinear propagation becomes progressively more profound, resulting in a severe distortion of the Airy temporal profile. Because of the limitations imposed by the finite size of the XC setup, temporal profiles were measured at distance of 20 cm from the exit face of the sample. Our results show that above a certain input energy (0.4 mJ in our case) strong nonlinear spatiotemporal effects take place during the propagation of intense Airy³ light bullets. Below this threshold, in a regime, which we refer to as weakly nonlinear, the Airy³ propagates practically in a linear fashion.

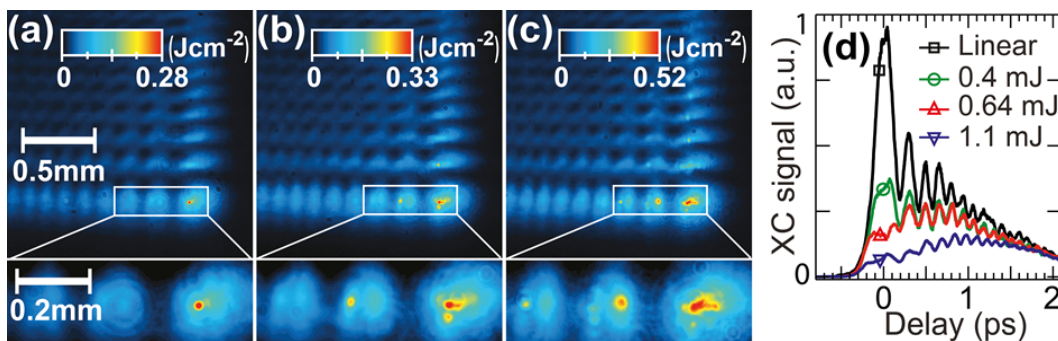


Figure 5.3-30 Spatial profiles, representing the fluence distribution, of the Airy³ light bullet at the exit surface of a 2.5-cm-long PMMA sample for (a) 0.4, (b) 0.64, (c) 1.1 mJ total energies. (d) Respective temporal profiles at a distance of 20 cm from the sample exit.

Although the Airy³ light bullets are distorted by the presence of nonlinear effects, one has to bear in mind that these effects are intensity-dependent and predominantly take place in the primary intensity lobes. For an Airy beam, which is not heavily truncated, the amount of energy contained in these lobes can be a relatively small fraction of the total energy (3% in our case). In this perspective, the nonlinear propagation effects such as multiphoton absorption, ionization, and filamentation, which lead to the deterioration of the primary intensity main lobes both in space and in time can be envisioned as dynamic obstacles to the intense Airy³ light bullet. Thus, since most of the energy is contained in the secondary lobes, which propagate linearly, one should expect the spatiotemporal bullet profile to gradually recover within some propagation distance. This effect should be more profound if the nonlinear effects are abruptly switched off so that the pure action of the linear Airy spatiotemporal energy flux would heal the nonlinearity induced changes of the Airy³ spatiotemporal profile.

In order to check this scenario where the self-healing properties of Airy³ light bullet plays an important role, we exploited the fact that optical nonlinearities of PMMA and air differ by several orders of magnitude. Hence, an Airy³ light bullet exiting the PMMA sample (where the propagation is nonlinear) is equivalent to an abrupt switch from a nonlinear to a linear propagation regime. Figure 5.3-31(a) depicts the spatial profile of the Airy³ bullet with total energy of 0.4 mJ at the exit surface of the PMMA sample. As was already discussed, at this energy a single filament is formed in the main lobe of the Airy beam. The spatial profile of the same beam after additional propagation of 9 cm in air is shown in Figure 5.3-31(b). Clearly 9 cm of propagation is enough to reconstruct the characteristic spatial profile of the Airy light bullet.

Also, although XC traces recorded at an even further distance of 20 cm from the PMMA exit, shown by the red curve in Figure 5.3-31(c), still exhibit the severe distortion of the main temporal peak of the Airy³ light bullet. However, complete temporal self-healing occurs after 80 cm of propagation in air as shown by the black curve in Figure 5.3-31(c). It is worth mentioning here that, since the energy flux rate towards the main lobe of the bullet is not necessarily symmetric in space and time, the respective healing rates differ as well. Therefore, complete spatial and temporal self-healing occurs after different propagation distances in air. Similar behavior was also observed after propagation in long PMMA samples where the Airy³ spatiotemporal profile fully recovered at the exit surface of the sample.

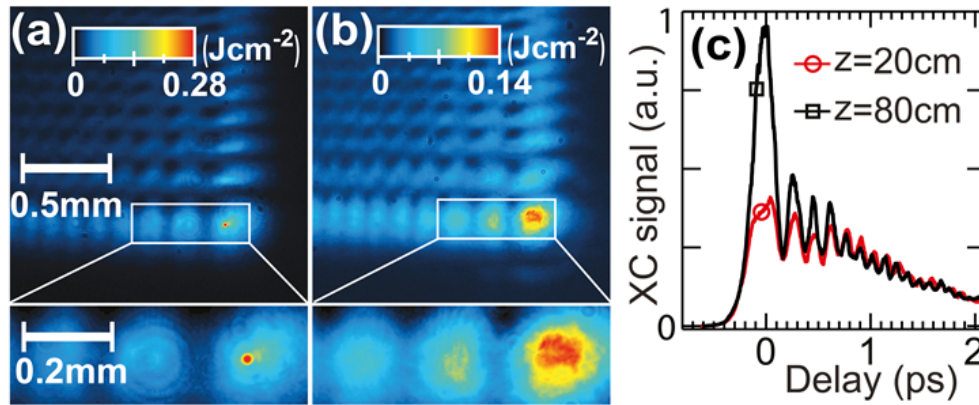


Figure 5.3-31 Spatial profiles, representing the fluence distribution, of the Airy^3 light bullet with total energy of 0.4 mJ (a) at the exit surface of the sample and (b) after $z = 9$ cm of propagation in air. (c) Respective temporal profiles at $z = 20$ cm (\circ) and $z = 80$ cm (\square) after the exit surface of the sample.

Thus, we have demonstrated the formation of Airy^3 light bullets, which represent a novel type of spatiotemporally non-spreading and robust wavepackets capable of simultaneously resisting both dispersion and diffraction. In the high intensity regime, nonlinear effects materialize in the presence of filaments in the primary spatial lobes and distortion of Airy temporal profile. However, if the nonlinear effects are weak enough, the energy reservoir in the secondary lobes heals the distortions and reconstructs the spatiotemporal profile of the Airy^3 light bullet. In addition to non-spreading and robustness properties, temporal and transverse spatial acceleration (bending) of these bullets can be exploited in many applications in different fields such as tomography, microscopy, and long-range signal transmission as well as biological applications. Furthermore, the formation of these bullets paves the way for the experimental realization of 3D light bullet interactions.

- **Stationary nonlinear Airy beams**

As mentioned earlier, by increasing the Airy peak intensity, the main lobe and some of the side lobes which have enough power to trigger the nonlinear effects would undergo filamentation [27], break up and tangential emission [216] or exhibit shrinking and modification of the Airy profile even below the critical threshold power for self-focusing [217, 245]. Recently we have demonstrated the existence of stationary Airy-like solutions in the presence of third-order Kerr nonlinearity of any sign (i.e., focusing or defocusing) and, most importantly, even in the presence of nonlinear losses (NLLs). We perform a detailed analysis that describes the shape and

main features of one-dimensional nonlinear Airy wavepackets, i.e., monochromatic beams that exhibit a curved trajectory. The Kerr nonlinearity is shown to lead to a compression of the Airy lobes (for focusing nonlinearity) and nonlinear losses lead to an imbalance of the incoming energy flux towards the main lobe, which in turn induces a reduction in the contrast of the Airy oscillations. This finding is then verified in numerical simulations and experiments that show the spontaneous emergence of the main features of stationary nonlinear Airy beams.

Analytical description: We consider the propagation of a monochromatic beam of frequency ω_0 in one spatial dimension. The electric field $\mathcal{E}(x, z, t) = E(x, z) \exp(-i\omega t + ik_0 z)$ where $k_0 = \omega_0 n_0 / c$ is the modulus of the wavevector at ω_0 and $n_0 = n(\omega_0)$ is the value of the refractive index at ω_0 . In the presence of nonlinearity, such as the Kerr effect and multiphoton absorption, propagation may be described by the nonlinear Schrödinger equation for the complex envelope of the field:

$$\frac{\partial E}{\partial z} = \frac{i}{2k_0} \frac{\partial^2 E}{\partial x^2} + ik_0 \frac{n_2}{n_0} |E|^2 E - \frac{\beta^{(K)}}{2} |E|^{2K-2} E, \quad (5.3-21)$$

where the nonlinear Kerr modification of the refractive index is $\delta n = n_2 |E|^2$, while K and $\beta^{(k)} \geq 0$ are the order and the coefficient of multiphoton absorption, respectively.

In the case of linear propagation, Eq.(5.3-21) admits the Airy beam solution $E = \text{Ai}(y) \exp[i\phi(y, \zeta)]$, whose intensity profile is invariant in the uniformly accelerated reference system defined by the normalized coordinates $\zeta = z / k_0 w_0^2$, $y = x / w_0 - \zeta^2 / 4$ with $\phi_L(y, \zeta) = y\zeta / 2 + \zeta^3 / 24$ and w_0 a typical length scale so that the acceleration or curvature is given by $1 / 2k_0^2 w_0^3$. We are interested in finding *stationary* nonlinear solutions to Eq.(5.3-21), in the above sense (invariant in the accelerated reference system), with boundary conditions compatible with the shape and properties of Airy beams, whose asymptotic behavior as $y \rightarrow \pm\infty$ reads [251]

$$\text{Ai}(y) \sim |y\pi^2|^{-1/4} \sin(|\rho| + \pi / 4) \quad \text{for } y \rightarrow -\infty \quad (5.3-22)$$

$$\text{Ai}(y) \sim \frac{(y\pi^2)^{1/4}}{2} \exp(-|\rho|) \text{ for } y \rightarrow +\infty \quad (5.3-23)$$

where $\rho = (2/3) \text{sgn}(y)|y|^{3/2}$. We therefore impose the constraints of a weakly localized tail toward $y \rightarrow -\infty$ and exponentially decaying tail toward $y \rightarrow +\infty$. Solutions, hereafter called nonlinear Airy beams (NABs) must also match Airy beams in the absence of nonlinearity. We thus rewrite Eq. (5.3-21) in normalized units in the accelerated reference frame

$$\frac{\partial E}{\partial \zeta} - \frac{1}{2}\zeta \frac{\partial E}{\partial y} = \frac{i}{2} \frac{\partial^2 E}{\partial y^2} + i\gamma |E|^2 E - \alpha |E|^{2K-2} E, \quad (5.3-24)$$

The nonlinear parameters read as $\gamma = k_0^2 n_2 w_0^2 / n_0$ with $\alpha = \beta^{(K)} k_0 w_0^2 / 2$. In order to find the shape of NABs, we consider the complex envelope $E = A(y) \exp[i\phi(y, \zeta)]$ with a ζ -invariant modulus, substitute into Eq.(5.3-24), separate real and imaginary parts, and require that the ζ dependence of the phase be the same as the that of linear Airy beams $\phi(y, \zeta) = \phi_L(y, \zeta) + \psi(y)$. The modulus $A(y)$ and nonlinear phase $\psi(y)$ satisfy

$$A'' - yA - (\psi')^2 A + 2\gamma A^3 = 0, \quad (5.3-25)$$

$$\psi' A^2 = 2\alpha \int_y^{+\infty} A^{2K} dy \equiv N_y, \quad (5.3-26)$$

where the primes stand for d/dy . The LHS of Eq. (5.3-26) represents the net power flux N_y per unit propagation length through a y boundary of a semi-infinite domain $[y, +\infty)$ in the co-accelerating reference frame. Equation (5.3-26) imposes the requirement that the flux compensates for the power N_y lost by nonlinear absorption within this domain. In the linear case, i.e., with no NLLs ($\alpha = 0$), there is no net energy flux ($\psi' = 0$) and phase fronts exhibit the curvature of Airy beams [230]. Nonlinear losses, assumed to be finite (with Airy beams, NLLs

are finite only for $K > 2$), increase from $N_{+\infty} = 0$ at $y \rightarrow +\infty$ to $N_{-\infty} \equiv 2\alpha \int_{-\infty}^{+\infty} A^{2K} dy$ at $y \rightarrow -\infty$, thereby establishing an additional curvature of the phase front in the weakly decaying tail of the beam, since $\psi' \rightarrow N_{-\infty} / A^2$, whereas the exponentially decaying tail has the curvature of the Airy beam. By introducing the variable $B(\rho) = A(y)|\rho|^{1/6}$, Eqs. (5.3-25) and (5.3-26) can be combined into a Newton-like equation governing the tail amplitude in the limit $y, \rho \rightarrow \pm\infty$:

$$\frac{\partial^2 B}{\partial \rho^2} \mp B = \frac{N_{\pm\infty}^2}{B^3} \text{ for } \rho \rightarrow \pm\infty \quad (5.3-27)$$

Equation (5.3-27) admits solutions in the form $B \sim \exp(-\rho)$ and $B^2(\rho) \sim B_{-\infty}^2 [1 + C \sin(2|\rho|)]$ as $\rho \rightarrow \pm\infty$. The latter exhibits oscillations of finite amplitude around the mean value $B_{-\infty}$ and contrast $C \equiv (1 - N_{-\infty}^2 / B_{-\infty}^4)^{1/2}$, decreasing as the amount of total losses increases. In the absence of nonlinear absorption ($N_{-\infty} \rightarrow 0$), it reduces to the asymptotics of Eq. (5.3-22) with maximum contrast $C = 1$. The contrast vanishes for $B_{-\infty}^2 = N_{-\infty}$, showing that no solution exist above a certain threshold of total losses.

In analogy with the physics of nonlinear Bessel beams [25], NABs can be viewed as Airy beams reshaped by nonlinear absorption and the Kerr effect, the former being responsible for the power flux from the weakly decaying tail toward the intense lobes where nonlinear absorption occurs and the latter of a nonlinear phase shift [252]. This is expressed by considering the NAB as an unbalanced superposition of two stationary Hankel beams, each carrying energy in the direction of, or opposite to the main lobe:

$$A(y) e^{i\psi(y)} = \frac{1}{2} \sqrt{\frac{-y}{3}} [a_1 e^{-i\pi/6} H_{1/3}^1(|\rho|) + a_2 e^{i\pi/6} H_{1/3}^2(|\rho|)] \quad (5.3-28)$$

The power fluxes associated with each Hankel component exactly compensate for the balanced for the balanced superposition with $a_1 = a_2 = 1$, which gives the stationary Airy beam

with no net power flux, Unbalancing creates a net flux associated with a lowering of the contrast of the oscillating tail.

We numerically integrated Eqs. (5.3-25) and (5.3-26) from $+\infty$ to $-\infty$ starting from the linear asymptotic solution as a boundary condition in order to retrieve the intensity and phase profiles of the NAB.

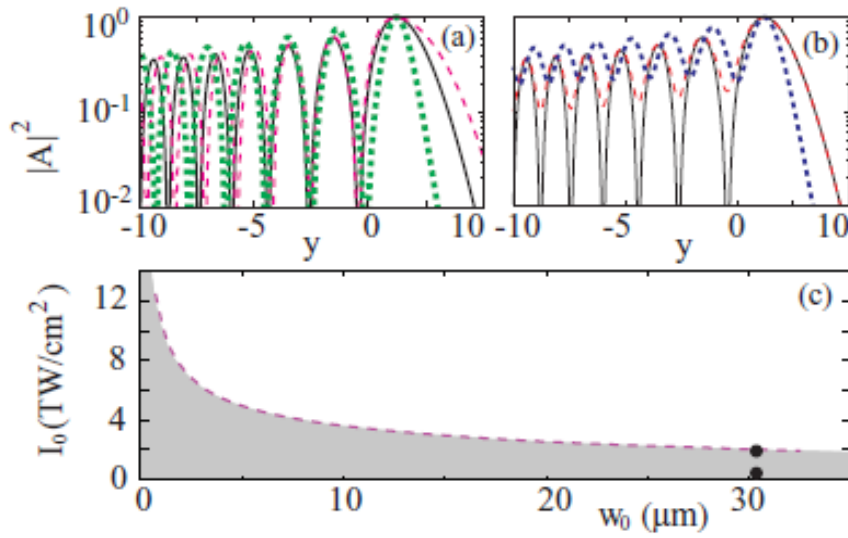


Figure 5.3-32 Nonlinear Airy wave forms for (a) a pure Kerr focusing (green dotted line) and defocusing (red dashed line) nonlinearity with no NLLs; (b) NLLs alone with $K=5$ (red dashed line) and Kerr + NLLs (blue dotted line). (c) Domain of existence (shaded region) of the NAB solution in the case of water at $\lambda_0 = 800$ nm as a function of peak intensity and width of the linear solution. The circles indicate the peak intensities at which numerical simulations were performed (Figure 5.3-33).

Figure 5.3-32(a) shows the normalized intensity profiles in the pure Kerr case, i.e., $\alpha = 0$, for focusing ($\gamma > 0$) and defocusing ($\gamma < 0$) Kerr nonlinearity, respectively. The width of the main lobe is narrower or wider depending on the sign of γ . Since the reference system in which we are considering the solution is always referred to the linear case, the nonlinear solution preserves the same acceleration although the relation between the width of the main lobe and the peak acceleration no longer holds. In Figure 5.3-32(b) for the $K = 5$ case and $\gamma = 0$ (red dashed line), we show the effect of multiple absorption and we observe a reduction of the contrast in the decaying oscillations, which asymptotically goes to C , and this reduction is greater when the total amount of energy lost in absorption (proportional to $N_{-\infty}$) is greater (data not shown).

When we have both Kerr nonlinearity and multiphoton absorption, we observe features characteristic of both regimes (blue dotted line). As in the pure Kerr case, the acceleration of linear Airy beams is preserved. We performed a scan in the parameter space in order to derive the region of existence of these stationary solutions.

Figure 5.3-32(c) shows this domain in the (I_0, w_0) coordinates for water at $\lambda_0 = 800$ nm (we considered $n_2 = 2.6 \times 10^{-16}$ cm²/W, $n_0 = 1.3285$, $K = 5$, and $\beta^{(K)} = 8.3 \times 10^{-50}$ cm⁷/W⁴ [253]), where I_0 is the maximum intensity of the nonlinear profile and w_0 is the width of the corresponding linear solution, which represents the acceleration as $a(w_0) = 1 / (2k_0^2 w_0^3)$.

Nonlinear Airy beam evolution. A relevant question is whether one is actually able to excite or experimentally observe stationary NABs. The ideal beams described above have infinite energy whereas experiments obviously resort to finite-energy realizations that cannot guarantee perfect stationarity. However, as in the linear case in which finite-energy Airy beams still exhibit the main stationary features, e.g., sub-diffractive propagation of the main intensity lobe, over a limited distance, we may expect the nonlinear Airy beam to emerge during propagation in the nonlinear regime. The rationale behind this reasoning is also based on the observation that stationary wave forms have been shown to act as attractor states for the dynamical evolution of laser beams and pulses in the nonlinear regime, e.g., dynamically evolving X waves during ultrashort laser pulse filamentation [67, 254], nonlinear unbalanced Bessel beams during the evolution of high-intensity Bessel beams [25, 255] and the spatial Townes profile during the self-focusing of intense Gaussian pulses [256].

We performed a series of numerical simulations, solving Eq. (5.3-21) for the same material parameters as in Figure 5.3-32 with an input Airy beam defined as in the linear regime, for various increasing input intensities. The Airy beam was generated by applying a third-phase mask to a Gaussian beam (FWHM of 0.5 mm) followed by a f linear propagation so as to obtain Fourier transform in the focal plane of the lens (focal length of $f = 20$ cm). This layout is shown at the top of Figure 5.3-33. In Figure 5.3-33 we show a lineout of the nonlinear profile (dashed red line) obtained by numerical simulations based on Eq. (5.3-21), at $z = 20$ cm from the focusing lens for $I_0 = 2$ TW/cm². The linear Airy profile (solid blue line) is included for comparison. The contraction of the main lobe and the different periodicity of the side lobes is

clearly evident, while the effect of NLLs (i.e. loss of contrast in the side lobe oscillations) is not that evident. We therefore performed additional simulation (black dotted line) at the same peak intensity with an increased nonlinear absorption coefficient $\beta^{(K)}=8.3\times 10^{-45} \text{ cm}^7/\text{W}^4$: the strong reduction in the contrast of the Airy beam oscillations is now clear, indicating the presence of inward flux that is stabilizing the energy loss in the main lobe.

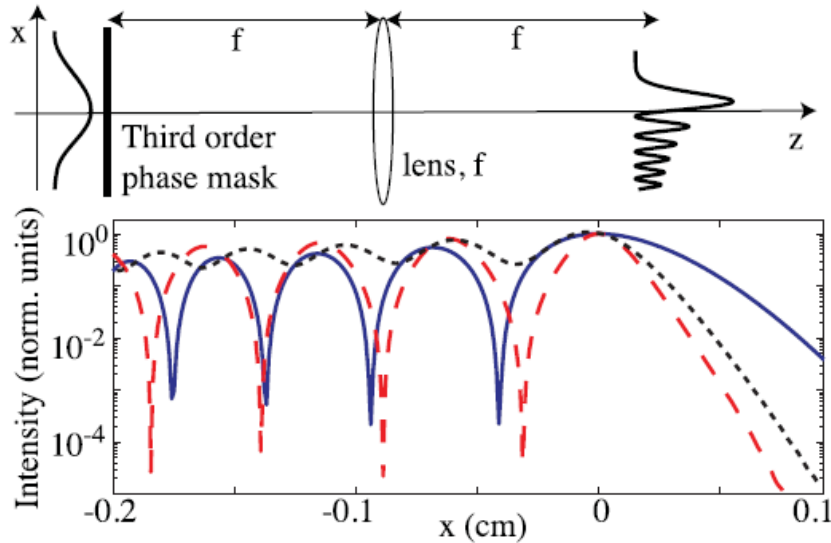


Figure 5.3-33 Numerical results: propagation in water with focal length $f = 20$ cm. Solid blue line, linear Airy profile; dashed red line, nonlinear Airy profile; black dotted line, nonlinear case with artificially increased NLLs. All profiles are shown in the focal plane of the lens $f(z = 20 \text{ cm})$.

Experiments. We conducted two series of experiments by launching one-dimensional Airy beams with increasing input energy into two different nonlinear media: (a) a 2-cm-thick cuvette filled with water and (2) a 2.5-cm-thick sample of polymer polymethyl-methacrylate (PMMA). The experimental setup is shown in Figure 5.3-34(a): a third-order spatial phase, together with a quadratic one corresponding to a cylindrical Fourier lens, is impressed onto a Gaussian-shaped beam delivered by an amplified Ti:Sapphire laser with 35 fs pulse duration, using a spatial light modulator (SLM) (Hamamatsu LCOS). The Airy-shaped beam then propagates through the nonlinear sample and the beam profile at the exit surface is imaged onto a CCD camera. Figure 5.3-34(b) shows the spatial fluence profiles (in logarithmic scale) for three different input energies 25 nJ (linear propagation), 350 μJ , and 530 μJ for an input phase profile such that the linear Airy main lobe FWHM is 159 μm . The main lobe undergoes an evident contraction that

increases with increasing the input energy, in agreement with the prediction summarized in Figure 5.3-32 (a) for the Kerr-dominant NAB. We then repeated the measurements with an increased input phase such that the Airy main lobe has a FWHM of $182\ \mu\text{m}$. Figure 5.3-34(c) shows the results for the same energies in Figure 5.3-34(b). The reduced density of the Airy peaks and the corresponding lower spatial intensity gradients imply that now both self-focusing effects and energy flux within the beam are weaker. We may therefore expect the effects of NLLs to become more evident.

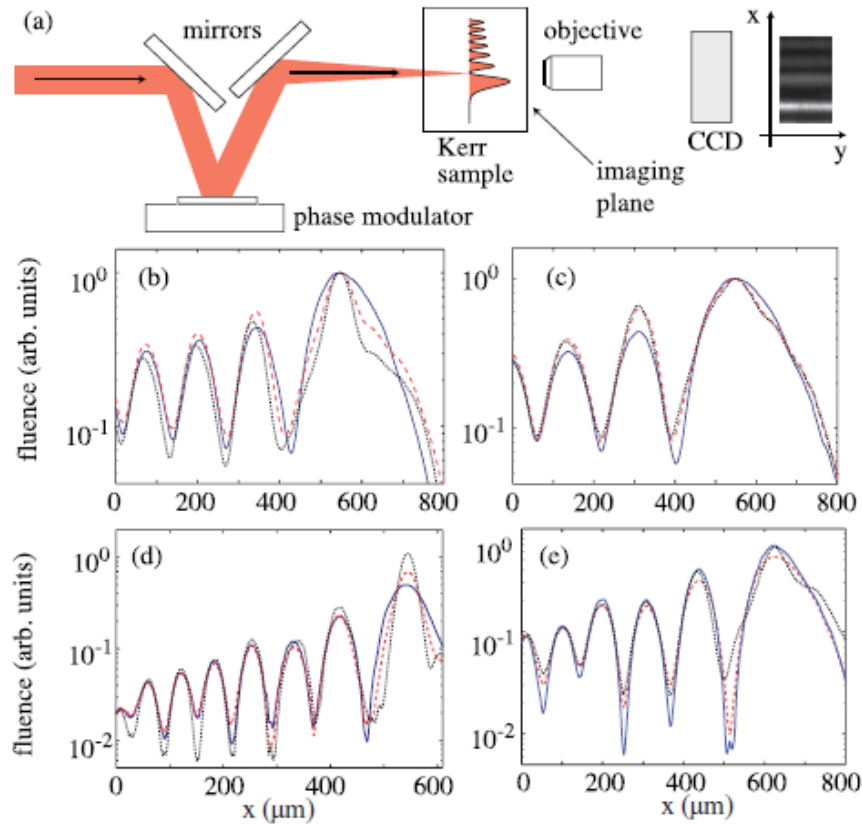


Figure 5.3-34 Experimental results: (a) Schematics of the experimental setup. (b)-(e) Output Airy beam fluence profiles in logarithmic scale. (b) Water at three input energies 25 nJ (solid line), 350 μJ (dashed line), and 530 μJ (dotted line) and for input Airy pulse with a main lobe FWHM of $159\ \mu\text{m}$. (c) Water at same energies as in (b) and main lobe FWHM of $182\ \mu\text{m}$. (d) PMMA at three different input energies of 25 nJ (solid line), 78 μJ (dashed line), and 196 μJ (dotted line) and for an input Airy main lobe FWHM of $78\ \mu\text{m}$. (e) PMMA at same energies as (d) and a main lobe FWHM of $136\ \mu\text{m}$.

Indeed, while Kerr self-focusing effects are nearly absent, the contrast in the secondary Airy lobes decreases in agreement with the expected behavior of the unbalanced Airy beam, as

summarized in Figure 5.3-32(b). These effects are even more pronounced in measurements in performed in PMMA, which is expected to have higher NLLs due to the lower multiphoton absorption photon number, $K = 3$. As for the case of water two different Airy widths were tested, 78 μm (Figure 5.3-34(d)) and 159 μm (Figure 5.3-34(e)), at three different energies 25 nJ, 78 μJ , and 246 μJ , with similar dynamics as in water and with the larger peak leading to increased NLL effects. We observe an increase of minimum intensity values by nearly an order of magnitude with increasing input energy. Although we do not have the same resolution and dynamic range as in the numerics, the experiments clearly show the predicted trends for the stationary NAB.

Based on these results, the existence of a freely accelerating solution in the nonlinear regime that remains stationary even in the presence of nonlinear losses is shown. Clearly, these results may be extended to the original quantum context in which Airy wavepackets were proposed for the first time. NABs could also find practical applications in a similar fashion to stationary Bessel beams where the beam stability above ablation intensities has led to technical improvements in micromachining optical materials [257] or soft tissue laser surgery by using them as razor blades with well-defined curvature. Stationarity is also a critical issue in “analog Hawking” emission experiments [258]: the nonlinear Airy beam may be used to reach huge $\sim 10^{21}$ m/s^2 accelerations and thus investigate related photon emission mechanisms [259].

- **Nonlinear propagation of finite energy Airy beams**

Beyond the stationarity regime, where a truncated 2D airy beam is intense enough to cause strong nonlinearities, we expect the Airy profile to be deteriorated. In order to further investigate this propagation regime, we conducted numerical simulations and experiments to study the role of strong nonlinearities and their effect on the propagation of these beams and also to explore the competition between the linear features of 2D Airy beams with nonlinear effects such as optical Kerr effect, multiphoton absorption and ionization, to name a few.

For the numerical modeling, the propagation is governed by the nonlinear evolution for the envelope E of the beam along z -axis, which extends the linear paraxial equation:

$$\frac{\partial E}{\partial z} = \frac{i}{2k} \Delta_{\perp} E + i \frac{\omega_0}{c} n_2 |E|^2 E - \frac{\beta_K}{2} |E|^{2K-2} E - ik \frac{\rho_{nt}}{2\rho_c} \int_{-\infty}^t \sigma_K |E(t')|^{2K} dt' \quad (5.3-29)$$

where the first term in the RHS stands for the diffraction, the second term accounts for the optical Kerr effect with coefficient $n_2 = 3.2 \times 10^{-19} \text{ cm}^2/\text{W}$ for air, associated with a critical power for self-focusing of $P_{\text{cr}} = 3 \text{ MW}$ at the laser wavelength of 800 nm. The remaining terms describe multiphoton absorption (MPA) with cross-section $\beta_K = 4 \times 10^{-95} \text{ cm}^{13}/\text{W}^7$ and plasma defocusing, with ρ_c being the critical density beyond which the plasma becomes opaque, $\sigma_K = 4 \times 10^{-96} \text{ s}^{-1} \text{ cm}^{16}/\text{W}^8$ the cross section for multiphoton ionization with $K = 8$ photons for air and $\rho_{\text{nt}} = 5 \times 10^{18} \text{ cm}^{-3}$ the density of density of neutral oxygen molecules in air. We note here that the Eq. (5.3-29) is similar to Eq.(5.3-24) with the last term in the latter added to account the plasma defocusing.

The simulation start from an already formed Airy beam whose electric field envelope is given by

$$E(z = 0, x, y) = E_0 \text{Ai}(x / w_0) \text{Ai}(y / w_0) T(x, y) \quad (5.3-30)$$

where T mimics the effects of a circular diaphragm with a radius of r_d which truncates the Airy beam and transforms it into a finite energy Airy beam (FEAB). We assume T to have the following form:

$$T = \begin{cases} 1 & \text{for } r \equiv (x^2 + y^2)^{1/2} < r_d \\ 0 & \text{for } r \equiv (x^2 + y^2)^{1/2} > r_d \end{cases} \quad (5.3-31)$$

By placing the circular aperture at the focal point, we truncate the already formed wide Airy beam to the desired size without influencing the shape of the inner lobes. The position immediately after the circular diaphragm is the initial stage for the simulation. This is analogous to linearly focusing a beam on the entrance face of a sample and investigating the subsequent nonlinear dynamics, or reshaping of a beam before it enters a nonlinear medium.

The corresponding laser pulse is assumed to be Gaussian with FWHM of 35 fs and to remain undistorted. We consider Airy beam truncated by a circular aperture ($r_d = 4.5 \text{ mm}$), with initial peak intensity of $I_0 = 7 \times 10^{12} \text{ W}/\text{cm}^2$ and different width of main lobe $w_0 = 100 \text{ }\mu\text{m}$,

$w_0=200 \mu\text{m}$ and $w_0=300 \mu\text{m}$, corresponding to power contents of the main lobe $P = 2 \text{ GW}$ ($0.66 P_{\text{cr}}$) $P = 8 \text{ GW}$ ($2.6 P_{\text{cr}}$), $P = 18 \text{ GW}$ ($5.8 P_{\text{cr}}$).

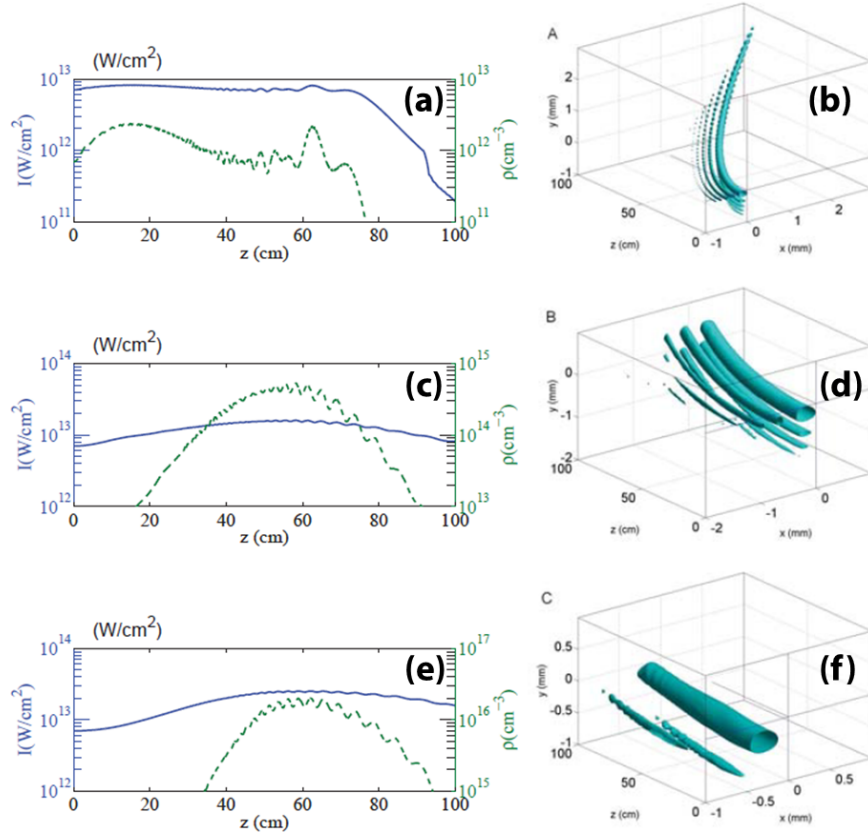


Figure 5.3-35 Simulation results of nonlinear propagation of intense Airy beams with main lobe width of $100 \mu\text{m}$ ((a)-(b)), $200 \mu\text{m}$ ((c)-(d)) and $300 \mu\text{m}$ ((e)-(f)). (a), (c) and (e): Peak intensity (solid blue curve, left-axis), electron density (dashed curve, right axis). (b), (d) and (f): iso-intensity surfaces of the intensity distribution shown the trajectories of the main and secondary lobes of the Airy beam.

The results of simulations are shown in Figure 5.3-35: The left column shows a comparison of the peak intensity and generated plasma density during the nonlinear propagation of three Airy beams with main FWHM of $100 \mu\text{m}$ ((a)-(b)), $200 \mu\text{m}$ ((c)-(d)) and $300 \mu\text{m}$ ((e)-(d)). In these three cases, for each propagation distance, intensities and electron densities reported in Figure 5.3-35 correspond to different positions x, y of the peak of the Airy beam because of their bending. However, the main lobe remains the most intense part of the beam all along the propagation distance and the reported electron densities in this figure are generated by the main lobe. The right column of Figure 5.3-35 shows iso-intensity surfaces for the three cases,

plotted in the x, y, z space (central time slice $t = 0$). It can be readily seen that in these cases, in spite of high intensities and nonlinear effects, the main and the secondary lobes follow a parabolic trajectory that would characterize the linear propagation of the input Airy beam.

For an Airy beam, widening the lobe width while keeping the input peak intensity constant leads to an increase in the power content of the main lobe. Although the critical power for self-focusing is not an absolute reference, as it is evaluated for a Gaussian beam profile, the power of the main lobe exceeds P_{cr} for the FEAB with $w_0 = 200 \mu\text{m}$ and $w_0 = 300 \mu\text{m}$. Thus, the main lobe will tend to self-focus and collapse upon itself these cases. One may expect a collapse arrest by the multiphoton absorption, plasma generation, and plasma defocusing as ultrashort laser pulse filamentation, however, these phenomena are high-order processes that lead to saturation of intensity and arrest of beam collapse. This can be true only to certain extent for the Airy beams since based on our results, no obvious nonlinear focus of the main lobe appears in the range corresponding to the collapse distance estimated from Marburger's formula [5] for Gaussian beams with the same widths and powers as the considered Airy beams i.e., 7.8 and 8.4 cm for the beams with 200 μm containing $2.6 \times P_{cr}$ and 300 μm containing $5.8 \times P_{cr}$. Therefore, any comparison in the nonlinear propagation of Airy beams with Gaussian beams should be made with cautions.

Furthermore, although the intensity profile along propagation distance for the Airy beam with main lobe FWHM of $w_0 = 100 \mu\text{m}$ (Figure 5.3-35(a)) exhibits a plateau over several tens of centimeters similarly to the behavior observed in standard filamentation, the power of this Airy beam is below threshold and its peak intensity stays below 10^{13} W/cm^2 and also lower than for the threshold for a standard filament in air; the electron density of the generated plasma does not exceed a few 10^{12} cm^{-3} . For the Airy beams with wider main lobe of $w_0 = 200 \mu\text{m}$ (Figure 5.3-35(c)) and $w_0 = 300 \mu\text{m}$ (Figure 5.3-35(e)), the peak intensity reaches values up to $2 \times 10^{13} \text{ W/cm}^2$, the electron density exceeds 10^{16} cm^{-3} but no plateau is obtained indicating the absence of saturation process unlike filamentation.

In contrast, the intensity profile is well explained by finite size effects: If the Airy beam were infinitely wide, an energy flux from the tail carrying infinite energy would push the main lobe along the diagonal $x = y$ and could sustain its intensity over extended distances exactly as

in the case of Bessel beams. With finite energy, the profile of the peak intensity of a linearly propagating Airy beam is known to be governed by finite size effects and should decrease as $\exp(-az^2 / k^2w_0^4)$ according to Eq. (5.3-10), i.e., faster for large Airy beam lobes. This is the behavior we also observed in the nonlinear regime (second stage of propagation in Figure 5.3-35(c)-(d) and Figure 5.3-35(e)-(f)), in conjunction with an initial self-focusing stage that prevails at the beginning of the propagation.

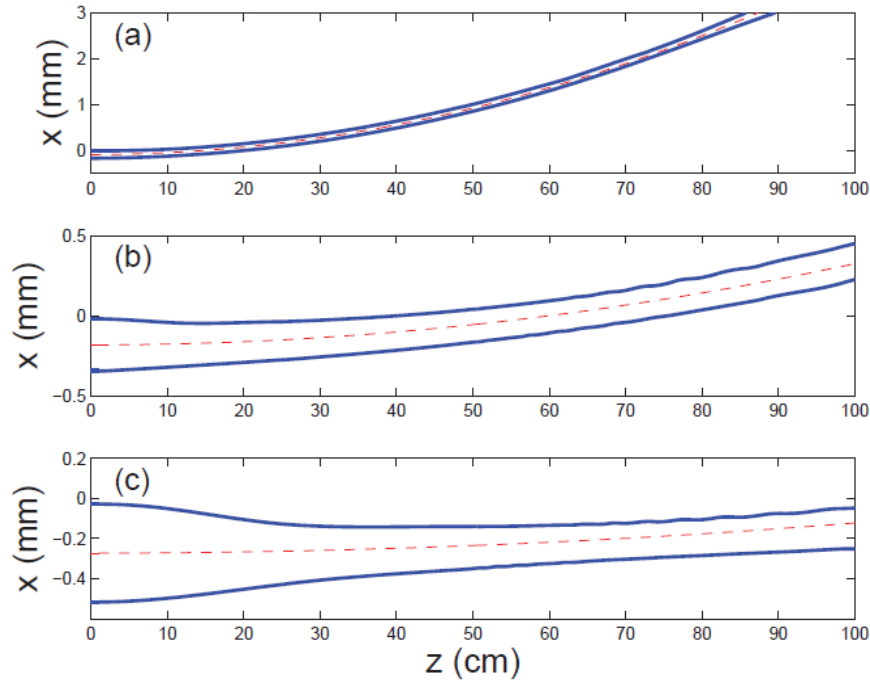


Figure 5.3-36 Projection of the main lobe trajectory and FWHM of the Airy beam along the x -direction for Input Airy beam with $w_0 = 100 \mu\text{m}$ (a), $w_0 = 200 \mu\text{m}$ (b) and $w_0 = 300 \mu\text{m}$ (c). Dashed red curve shows the trajectory of the linear Airy beam with the same characteristics.

Although Airy beams are intense enough to undergo Kerr self-focusing and induce multiphoton absorption, the trajectory of the main lobe obtained in the linear regime is preserved in the three cases shown in Figure 5.3-35. The Airy beam with the smallest lobe width clearly follows a parabolic trajectory that corresponds to the smallest curvature radius. Figure 5.3-36 shows the projection of the trajectory of the Airy main lobe in the x - z plane and its FWHM diameter. The main lobe clearly bends as a linear Airy beam does, following a parabolic trajectory defined by $x_d = z^2 / (4k^2x_0^3)$ (Eq. (5.3-14)) that is shown by the dashed curves Figure

5.3-36. For the wider Airy beams (Figure 5.3-36(b-c)), the nonlinear propagation starts by a Kerr induced self-focusing stage with a decrease of the FWHM diameter from $z = 0$ to $z = 30$ cm. This indicates a competition between Kerr self-focusing and the acceleration of the Airy beam. Thus, when the power content of the main lobe is high enough the bending property of the beam is suppressed by the self-focusing. As it has been discussed already, the power content of the main lobe can be increased by several means. Increasing the width of the main lobe for a certain truncation aperture, will increase the power carried by the main lobe, however, this also leads to the increase of the radius of curvature of parabolic trajectory that results in smaller deflection in a fixed propagation distance. On the other hand, increasing the total energy of the beam, for a fixed truncation also increases the power of the main lobe as well as the other side lobes, however, for intensities close to 10^{13} W/cm² the ionization of air initiates and leads to plasma generation that consequently decreased the intensity of the main lobe due to the plasma defocusing. Clearly, the power content of the main lobe can be increased by reducing the truncation aperture, though this leads to efficient control of on the intensity of main lobe width respect to the side lobes, however, this approach sets a limit on the non-diffracting range of propagation. In order to investigate the effect of acceleration quenching with an Airy beam with reasonable lobe width, over propagation distances shorter than 1 m, we therefore arbitrarily increased the Kerr index coefficient by a factor 10, thus leading to an increase of P / P_{cr} by a factor 10 and an unchanged curvature radius of the FEAB with $w_0 = 200$ μ m and $r_d = 4.5$ mm. This enables us to artificially isolate the self-focusing and separate it's effect from the other nonlinearities, such as multiphoton absorption and plasma defocusing.

The energy fluxes in a 2D Airy beam with $w_0 = 200$ μ m in the nonlinear propagation regime are shown in Figure 5.3-37. The first row shows the transverse energy fluxes of the Airy beam propagating in air (with $n_2 = 3.2 \times 10^{-19}$ cm²/W) at two different propagation distances of $z = 2$ cm and $z = 16$ cm, while the second row depicts the transverse energy fluxes of the Airy beam with artificially increased nonlinear refractive index of $n_2 = 3.2 \times 10^{-18}$ cm²/W at the same propagation distances. It can be obviously seen that in the case of standard nonlinearity (Figure 5.3-37(a)-(b)), the energy flux is towards the main lobe and along the symmetry axis of $x=y$, while in the case of ten-times increased nonlinearity (Figure 5.3-37(a)-(b)), the main lobe

undergoes filamentation and part of the energy flux from the tails of the beam is filling the secondary lobes which in turn undergoes self-focusing and nonlinear losses.

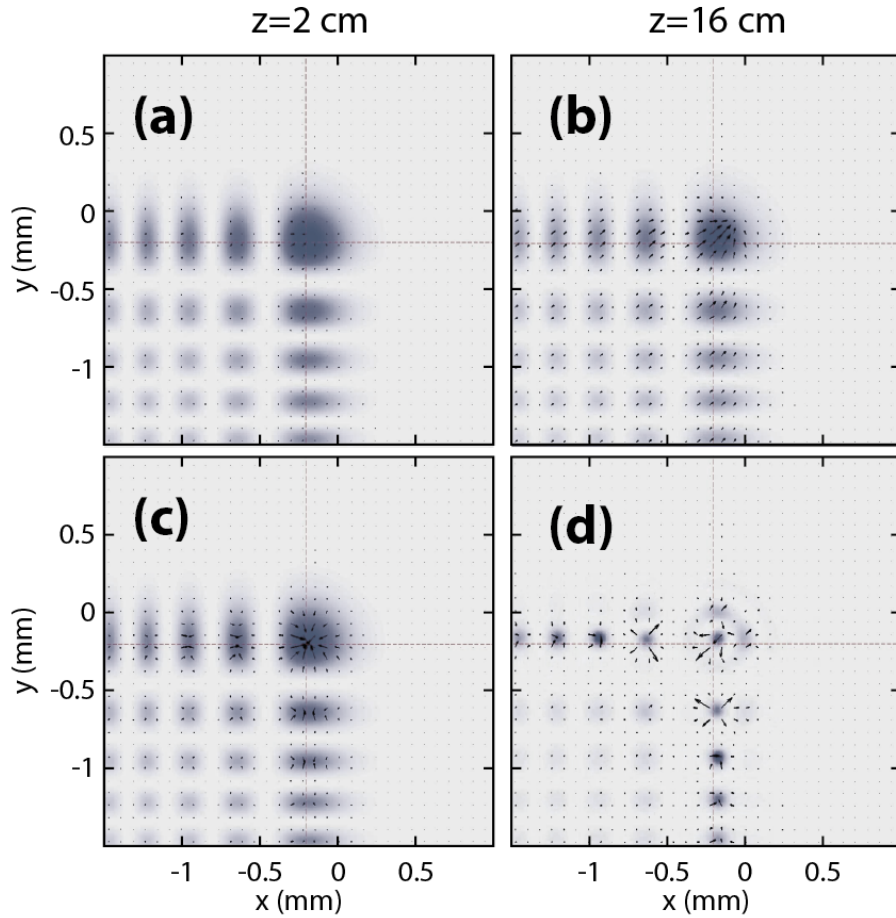


Figure 5.3-37 Transverse energy flux plots at two different propagation distances $z = 2$ cm (first column) and $z = 16$ cm (second column) for a 2D Airy beam with the main lobe FWHM of $200 \mu\text{m}$. (a)-(b) for $n_2 = 3.2 \times 10^{-19} \text{ cm}^2/\text{W}$, and (c)-(d) $n_2 = 3.2 \times 10^{-18} \text{ cm}^2/\text{W}$.

Experimentally, a cascade of two identical tilted cylindrical telescopes were used to impose cubic phase on the initially Gaussian shaped beam of 35 fs laser pulses at $\lambda_0 = 800 \text{ nm}$ and a spherical lens with $f = 500 \text{ mm}$ was used for the Fourier transformation and generation of a 2D Airy beam with main lobe FWHM of $w_0 = 235 \mu\text{m}$. The main lobe of the generated Airy beam had $\sim 7\%$ of the total beam energy. A 12-cm-long water tank was placed $\sim 52 \text{ cm}$ from the Fourier lens. The spatial profile of the Airy beam was monitored at the exit surface of the tank

using a 12-bit CCD camera and an appropriate imaging system. The spatial profiles of the images as function of the main lobe energy content are shown in Figure 5.3-38(a)-(d) as follows (a) 1.6 nJ, (b) 0.5 μ J, (c) 1.3 μ J, and (d) 5.4 μ J. Since the critical power of self-focusing in water is ~ 3.7 MW, these main lobe energies correspond to $0.01 \times P_{cr}$, $3.8 \times P_{cr}$, $9.7 \times P_{cr}$, and $40 \times P_{cr}$, power content of the main lobe, respectively.

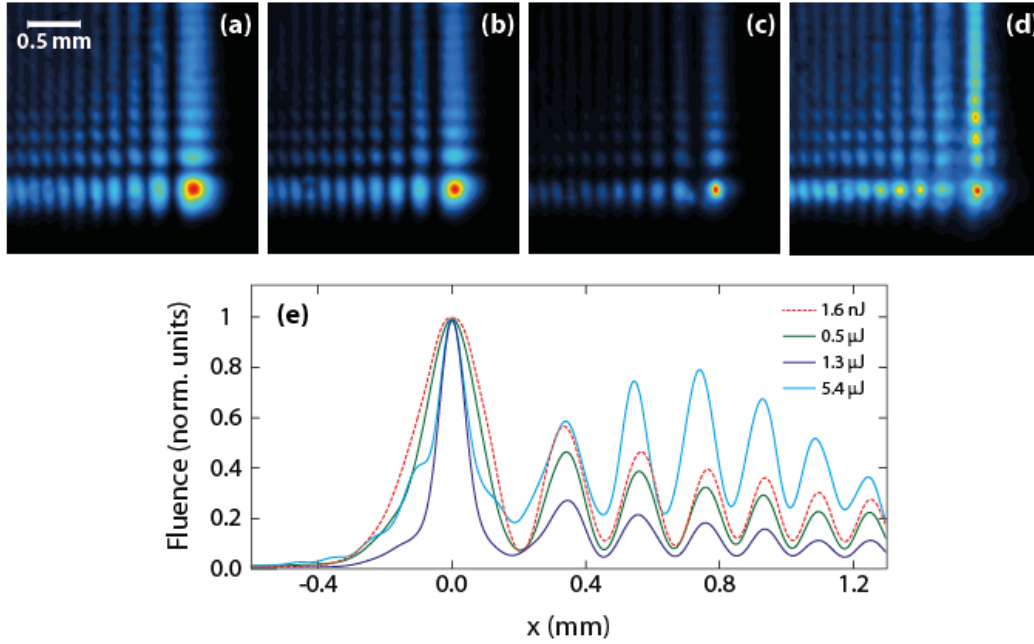


Figure 5.3-38 Normalized fluence distribution of 2D Airy beam with $w_0 = 235$ μ m as a function of main lobe energy content; (a) 1.6 nJ, (b) 0.5 μ J, (c) 1.3 μ J, and (d) 5.4 μ J. (e) Normalized line-outs of the 2D profiles depicted in (a)-(d) along x -axis.

It can be clearly seen that by increasing the whole beam energy, and consequently the energy content of the main lobe up to few times the critical power of a Gaussian beam with similar extent as the main lobe, the main lobe undergoes an evident self-focusing, which can be readily seen also in Figure 5.3-38(d), and further increasing the energy results in self-focusing and consequently the filamentation of other side lobes as well. As a consequence the energy flux towards the main lobe is reduced and eventually the backwards energy flux leads to deterioration of the Airy profile.

More interestingly, we have observed that for smaller main lobe width of $w_0 = 40$ μ m, there is a regime of *highly nonlinear propagation* beyond the stationarity regime and nonlinear

destruction of the characteristic profile, wherein the Airy profile is reconstructed with very high intensities. For this experiment, after the tilted cylindrical telescopic lens a shorter focal length lens of $f = 100$ mm was used for Fourier transformation. The propagation medium was water and the propagation of the intense 2D Airy beam was monitored at the exit surface of a 11 cm-long water tank, which was placed ~ 6 cm after the Fourier transforming lens. The images of the beam profile were captured at the exit surface of the water tank using a 12-bit CCD camera for several input pulse energies. In this case, the main lobe of the Airy beam conveyed 4% of the total pulse energy of the beam. Figure 5.3-39 shows the fluence distribution of the Airy beam for various main lobe energy contents and the corresponding power multiplies of the critical power in water. For high input pulse energies, above few 100 μJ , a clear white light generation and conical emission was observed and in order to avoid the effect of the white light background on the captured CCD images, an interference filter of 20 nm bandwidth centered at 800 nm was placed in front of the camera. It can be clearly seen that by increasing the energy, the beam profile is distorted by the formation of filaments in the main lobes as well intense side lobes but further increasing results in reconstruction of super-intense spots which have exactly the profile of the linear Airy beam.

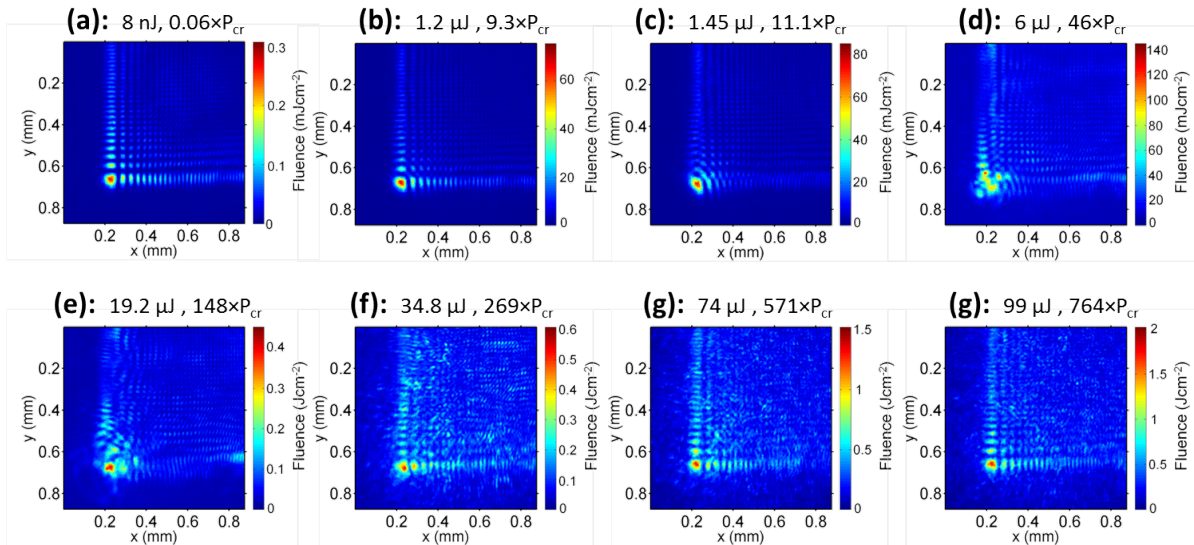


Figure 5.3-39 Reconstruction of 2D Airy beam profile in highly nonlinear regime.

The same behavior was observed for the Bessel beams. In this case, the Beam was created with an axicon of base angle of 1° , preceded by an $f = 10$ cm lens. The Bessel beam profile was

recorded (not shown) at the exit surface of the 11-cm-long water tank for several energies. In the *moderate* nonlinear regime, the Bessel profile was deteriorated by the appearance of filaments and increasing the energy led to multiple filamentation in the central part of the beam as well as the intense surrounding, however, further increasing the input energy resulted in the reformation of the Bessel profile with a very high fluence. It should be mentioned that to avoid the damage in lenses, we were not able to increase the intensities to study the occurrence of this phenomenon in air.

The physics of this very interesting phenomenon it is not clear yet; and because of the extremely high intensities, the numerical simulations do not succeed in reaching this regime. On the other hand, beyond the physical mechanism, this phenomenon can open up new frontiers in physics of extreme nonlinear optics and applications. The possibility of transferring gigantic amount of optical energy to a specific destination, above the filamentation regime, can be tempting for various applications.

5.4 Conclusion

In summary, we have shown that by using periodic or quasi-periodic optical lattice an efficient control on the attributes of the optical filaments can be achieved. Through numerical simulations and experimental results, we have demonstrated that filamentation can be tailored using periodic lattice of refractive index. The main filament properties such as its length and diameter were effectively controlled by introducing a quasi-periodic Bessel-like plasma lattice in water.

As an alternative approach, it has been shown that filamentation tailoring can be also achieved using non-diffracting optical beams such as Bessel and Airy beams. For the Bessel beams, we have demonstrated that long, uniform, and high- density plasma channels can be formed in air by using conically shaped UV short laser pulses. The combination of axicons with diverging lenses, actively tunes the conical angles and results in a considerable increase of the plasma string length. Since the beam propagation in such a configuration is mainly governed by linear effects, the propagation is stationary both in space and in time.

Airy beams has been studied in detail in this chapter, including their inherent properties such as transverse acceleration and self-healing. We have shown that the Airy beams can be produced by taking the advantage of optical aberrations to induce continuous cubic phase modulation on the input beam wavefront. A cascade of two tilted cylindrical telescope systems,

with orthogonal orientation with respect to each other, is used for imprinting the cubic phase and then a spherical lens is used for the spatial Fourier transformation. This procedure is tunable and can be applied to generate intense ultrafast Airy beams and tailored filaments.

We have demonstrated the realization of intense Airy³ light bullets by combining a spatial Airy beam with an Airy pulse in time. These light bullets are a novel type of spatiotemporally non-spreading and robust wavepackets capable of simultaneously resisting both dispersion and diffraction. It has been shown that in the high intensity regime, the appearance of filaments strongly distorts the spatiotemporal profile of the light bullets; however, at latter times, the energy reservoir in the secondary lobes heals the distortions and reconstructs the Airy³ light bullets.

Furthermore, it has been shown that even in the presence of Kerr nonlinearity, and nonlinear losses, 1D Airy beams are stable in a specific regime depending on their intensity and main lobe width. For 2D Airy beams, we have demonstrated that the two regimes of nonlinear propagation can be distinguished by the power content of the Airy main lobe. At moderated powers, Airy beams propagate smoothly without exhibiting an abrupt increase of intensity even if the power carried by the main lobe is several times above the critical power for self-focusing with a transverse acceleration such as the linear propagation. In the high-power regime, if the Kerr effect dominates, multiple lobes will form filaments. This procedure leads to a destruction of the Airy beam profile and thus the acceleration is quenched. Alternatively, when the linear transverse flux dominates, the beam tends to accelerate along the diagonal, even though individual lobe shrinking (due to self-focusing) is still observed.

Finally, in this chapter, we have reported our observation of extremely nonlinear propagation of 2D Airy beams with small main lobe size. We have demonstrated that at very high intensities, well beyond the regime in which the spatial profile is deteriorated by the appearance of multiple filaments in the main lobe and some of the side lobes, the Airy profile is reconstructed. The same behavior has been observed for Bessel beams with similar central core dimensions. The physics of this reconstruction is not well understood yet and it will be the subject of further studies since it is promising for many applications.

References

1. Saleh, B.E.A., *Fundamentals of Photonics*. Second ed. 2007: Wiley.
2. Yariv, A., *Quantum Electronics*. 3rd ed. 1989: Wiley.
3. Fowles, G.R., *Introduction to Optics*, in *Introduction to Optics*. 1989, Dover.
4. Boyd, R.W., *Nonlinear Optics*. 3rd ed. 2007, New York: Elsevier.
5. Couairon, A. and A. Mysyrowicz, *Femtosecond filamentation in transparent media*. *Physics Reports*, 2007. **441**(2-4): p. 47-189.
6. Kelley, P.L., *Self-Focusing of Optical Beams*. *Physical Review Letters*, 1965. **15**(26): p. 1005.
7. Shen, Y.R., *Self-focusing: Experimental*. *Progress in Quantum Electronics*, 1975. **4**(Part 1): p. 1-34.
8. Chiao, R.Y., E. Garmire, and C.H. Townes, *Self-Trapping of Optical Beams*. *Physical Review Letters*, 1964. **13**(15): p. 479.
9. Fibich, G. and A.L. Gaeta, *Critical power for self-focusing in bulk media and in hollow waveguides*. *Opt. Lett.*, 2000. **25**(5): p. 335-337.
10. Marburger, J.H. and E. Dawes, *Dynamical Formation of a Small-Scale Filament*. *Physical Review Letters*, 1968. **21**(Copyright (C) 2009 The American Physical Society): p. 556.
11. Shen, Y.R., *The Principles of Nonlinear Optics*. 2003, Hoboken, New Jersey: Wiley.
12. Stegeman, G.I. and M. Segev, *Optical Spatial Solitons and Their Interactions: Universality and Diversity*. *Science*, 1999. **286**(5444): p. 1518-1523.
13. Silberberg, Y., *Collapse of optical pulses*. *Opt. Lett.*, 1990. **15**(22): p. 1282-1284.
14. Malomed, B.A., et al., *Spatiotemporal optical solitons*. *Journal of Optics B: Quantum and Semiclassical Optics*, 2005. **7**(5): p. R53-R72.
15. Fibich, G. and B. Ilan, *Optical light bullets in a pure Kerr medium*. *Opt. Lett.*, 2004. **29**(8): p. 887-889.
16. Mihalache, D., et al., *Stable Spinning Optical Solitons in Three Dimensions*. *Physical Review Letters*, 2002. **88**(7): p. 073902.
17. Edmundson, D.E. and R.H. Enns, *Robust bistable light bullets*. *Optics Letters*, 1992. **17**(8): p. 586-588.
18. Couairon, A., *Light bullets from femtosecond filamentation*. *Eur. Phys. J. D*, 2003. **27**(2): p. 159-167.
19. Aceves, A.B., et al., *Multidimensional solitons in fiber arrays*. *Optics Letters*, 1994. **19**(5): p. 329-331.
20. Panagiotopoulos, P., et al., *Intense dynamic bullets in a periodic lattice*. *Optics Express*, 2011. **19**(11): p. 10057-10062.
21. Durnin, J., J.J. Miceli, and J.H. Eberly, *Diffraction-free beams*. *Physical Review Letters*, 1987. **58**(15): p. 1499.
22. Gutiérrez-Vega, J.C., M.D. Iturbe-Castillo, and S. Chávez-Cerda, *Alternative formulation for invariant optical fields: Mathieu beams*. *Opt. Lett.*, 2000. **25**(20): p. 1493-1495.
23. Siviloglou, G.A., et al., *Observation of Accelerating Airy Beams*. *Physical Review Letters*, 2007. **99**(21): p. 213901-4.

24. Di Trapani, P., et al., *Spontaneously Generated X-Shaped Light Bullets*. Physical Review Letters, 2003. **91**(9): p. 093904.
25. Porras, M.A., et al., *Nonlinear Unbalanced Bessel Beams: Stationary Conical Waves Supported by Nonlinear Losses*. Physical Review Letters, 2004. **93**(15): p. 153902.
26. Chong, A., et al., *Airy-Bessel wave packets as versatile linear light bullets*. Nat Photon, 2010. **4**(2): p. 103-106.
27. Abdollahpour, D., et al., *Spatiotemporal Airy Light Bullets in the Linear and Nonlinear Regimes*. Physical Review Letters, 2010. **105**(25): p. 253901.
28. Feit, M.D. and J.J.A. Fleck, *Effect of refraction on spot-size dependence of laser-induced breakdown*. Applied Physics Letters, 1974. **24**(4): p. 169-172.
29. Schaffer, C.B., *Interaction of femtosecond laser pulses with transparent materials*, in *Department of Physics*. 2001, Harvard: Cambridge, Massachusetts.
30. Yu, P.Y. and M. Cardona, *Fundamentals of Semiconductors*. 4th ed. 2010, Heidelberg: Springer.
31. Mao, S.S., et al., *Dynamics of femtosecond laser interactions with dielectrics*. Applied Physics A: Materials Science & Processing, 2004. **79**(7): p. 1695-1709.
32. Loriot, V., et al., *Measurement of high order Kerr refractive index of major air components*. Opt. Express, 2009. **17**(16): p. 13429-13434.
33. B ejot, P., et al., *Higher-Order Kerr Terms Allow Ionization-Free Filamentation in Gases*. Physical Review Letters, 2010. **104**(Copyright (C) 2010 The American Physical Society): p. 103903.
34. Loriot, V., et al., *On negative higher-order Kerr effect and filamentation*. Laser Physics, 2011: p. 1-10.
35. Wahlstrand, J.K., et al., *Optical Nonlinearity in Ar and N₂ near the Ionization Threshold*. Physical Review Letters, 2011. **107**(10): p. 103901.
36. Kolesik, M., et al., *On the higher-order Kerr effect in femtosecond filaments*. Optics Letters, 2010. **35**(21): p. 3685-3687.
37. Teleki, A., E.M. Wright, and M. Kolesik, *Microscopic model for the higher-order nonlinearity in optical filaments*. Physical Review A, 2010. **82**(6): p. 065801.
38. Kolesik, M., E.M. Wright, and J.V. Moloney, *Femtosecond filamentation in air and higher-order nonlinearities*. Optics Letters, 2010. **35**(15): p. 2550-2552.
39. Polynkin, P., et al., *Experimental Tests of the New Paradigm for Laser Filamentation in Gases*. Physical Review Letters, 2011. **106**(15): p. 153902.
40. Stegeman, G., et al., *Nonlinear birefringence due to non-resonant, higher-order Kerr effect in isotropic media*. Optics Express, 2011. **19**(7): p. 6387-6399.
41. Braun, A., et al., *Self-channeling of high-peak-power femtosecond laser pulses in air*. Opt. Lett., 1995. **20**(1): p. 73-75.
42. La Fontaine, B., et al., *Filamentation of ultrashort pulse laser beams resulting from their propagation over long distances in air*. Physics of Plasmas, 1999. **6**(5): p. 1615-1621.
43. M echain, G., et al., *Long-range self-channeling of infrared laser pulses in air: a new propagation regime without ionization*. Applied Physics B: Lasers and Optics, 2004. **79**(3): p. 379-382.
44. Brodeur, A., F.A. Ilkov, and S.L. Chin, *Beam filamentation and the white light continuum divergence*. Optics Communications, 1996. **129**(3-4): p. 193-198.
45. Tzortzakis, S., et al., *Self-Guided Propagation of Ultrashort IR Laser Pulses in Fused Silica*. Physical Review Letters, 2001. **87**(21): p. 213902.

46. Brodeur, A. and S.L. Chin, *Ultrafast white-light continuum generation and self-focusing in transparent condensed media*. J. Opt. Soc. Am. B, 1999. **16**(4): p. 637-650.
47. Moloney, J.V. and M. Kolesik, *Full vectorial, intense ultrashort pulse propagators: derivation and applications*, in *Progress in Ultrafast Intense Laser Science*, K. Yamanouchi, et al., Editors. 2007, Springer: Berlin.
48. Couairon, A., et al., *Femtosecond filamentation in air at low pressures: Part I: Theory and numerical simulations*. Optics Communications, 2006. **259**(1): p. 265-273.
49. Chin, S.L., F. Théberge, and W. Liu, *Filamentation nonlinear optics*. Applied Physics B: Lasers and Optics, 2007. **86**(3): p. 477-483.
50. Ripoche, J.-F., et al., *Determination of the time dependence of n_2 in air*. Optics Communications, 1997. **135**(4-6): p. 310-314.
51. Nibbering, E.T.J., et al., *Determination of the inertial contribution to the nonlinear refractive index of air, N_2 , and O_2 by use of unfocused high-intensity femtosecond laser pulses*. J. Opt. Soc. Am. B, 1997. **14**(3): p. 650-660.
52. Couairon, A., *Filamentation length of powerful laser pulses*. Applied Physics B: Lasers and Optics, 2003. **76**(7): p. 789-792.
53. Courvoisier, F., et al., *Ultraintense light filaments transmitted through clouds*. Applied Physics Letters, 2003. **83**(2): p. 213-215.
54. Kolesik, M. and J.V. Moloney, *Self-healing femtosecond light filaments*. Optics Letters, 2004. **29**(6): p. 590-592.
55. Dubietis, A., et al., *Self-reconstruction of light filaments*. Optics Letters, 2004. **29**(24): p. 2893-2895.
56. Mlejnek, M., et al., *Optically Turbulent Femtosecond Light Guide in Air*. Physical Review Letters, 1999. **83**(15): p. 2938.
57. Méchain, G., et al., *Propagation of fs TW laser filaments in adverse atmospheric conditions*. Applied Physics B: Lasers and Optics, 2005. **80**(7): p. 785-789.
58. Kasparian, J., R. Sauerbrey, and S.L. Chin, *The critical laser intensity of self-guided light filaments in air*. Applied Physics B: Lasers and Optics, 2000. **71**(6): p. 877-879.
59. Méchain, G., et al., *Range of plasma filaments created in air by a multi-terawatt femtosecond laser*. Optics Communications, 2005. **247**(1-3): p. 171-180.
60. DeMartini, F., et al., *Self-Steepening of Light Pulses*. Physical Review, 1967. **164**(2): p. 312.
61. Suydam, B.R., *Self-Steepening of Optical Pulses*, in *The Supercontinuum Laser Source*, R.R. Alfano, Editor. 2006, Springer: New York.
62. Kasparian, J., et al., *Infrared extension of the super continuum generated by femtosecond terawatt laser pulses propagating in the atmosphere*. Opt. Lett., 2000. **25**(18): p. 1397-1399.
63. Nibbering, E.T.J., et al., *Spectral determination of the amplitude and the phase of intense ultrashort optical pulses*. J. Opt. Soc. Am. B, 1996. **13**(2): p. 317-329.
64. Nibbering, E.T.J., et al., *Conical emission from self-guided femtosecond pulses in air*. Opt. Lett., 1996. **21**(1): p. 62-65.
65. Kosareva, O.G., et al., *Conical emission from laser plasma interactions in the filamentation of powerful ultrashort laser pulses in air*. Opt. Lett., 1997. **22**(17): p. 1332-1334.
66. Luther, G.G., et al., *Short-pulse conical emission and spectral broadening in normally dispersive media*. Opt. Lett., 1994. **19**(11): p. 789-791.

67. Faccio, D., et al., *Conical Emission, Pulse Splitting, and X-Wave Parametric Amplification in Nonlinear Dynamics of Ultrashort Light Pulses*. Physical Review Letters, 2006. **96**(19): p. 193901.
68. Couairon, A., et al., *Self-compression of ultra-short laser pulses down to one optical cycle by filamentation*. Journal of Modern Optics, 2006. **53**(1): p. 75 - 85.
69. Tzortzakis, S., et al., *Coherent subterahertz radiation from femtosecond infrared filaments in air*. Opt. Lett., 2002. **27**(21): p. 1944-1946.
70. Houard, A., et al., *Strong Enhancement of Terahertz Radiation from Laser Filaments in Air by a Static Electric Field*. Physical Review Letters, 2008. **100**(25): p. 255006-4.
71. Manceau, J.M., et al., *Terahertz pulse emission optimization from tailored femtosecond laser pulse filamentation in air*. Opt. Lett., 2009. **34**(14): p. 2165-2167.
72. Manceau, J.-M., M. Massauti, and S. Tzortzakis, *Coherent control of THz pulses polarization from femtosecond laser filaments in gases*. Opt. Express, 2010. **18**(18): p. 18894-18899.
73. Manceau, J.M., M. Massauti, and S. Tzortzakis, *Strong terahertz emission enhancement via femtosecond laser filament concatenation in air*. Opt. Lett., 2010. **35**(14): p. 2424-2426.
74. Tzortzakis, S., et al., *Breakup and Fusion of Self-Guided Femtosecond Light Pulses in Air*. Physical Review Letters, 2001. **86**(Copyright (C) 2010 The American Physical Society): p. 5470.
75. Bergé, L., et al., *Multiple Filamentation of Terawatt Laser Pulses in Air*. Physical Review Letters, 2004. **92**(Copyright (C) 2010 The American Physical Society): p. 225002.
76. Méchain, G., et al., *Organizing Multiple Femtosecond Filaments in Air*. Physical Review Letters, 2004. **93**(3): p. 035003.
77. Dubietis, A., et al., *Multiple filamentation induced by input-beam ellipticity*. Opt. Lett., 2004. **29**(10): p. 1126-1128.
78. Kandidov, V.P., et al., *Towards a control of multiple filamentation by spatial regularization of a high-power femtosecond laser pulse*. Applied Physics B-Lasers and Optics, 2005. **80**(2): p. 267-275.
79. Fibich, G., et al., *Control of multiple filamentation in air*. Opt. Lett., 2004. **29**(15): p. 1772-1774.
80. Kasparian, J., et al., *White-Light Filaments for Atmospheric Analysis*. Science, 2003. **301**(5629): p. 61-64.
81. Rohwetter, P., et al., *Laser multiple filamentation control in air using a smooth phase mask*. Physical Review A, 2008. **77**(Copyright (C) 2010 The American Physical Society): p. 013812.
82. Stelmaszczyk, K., et al., *Long-distance remote laser-induced breakdown spectroscopy using filamentation in air*. Applied Physics Letters, 2004. **85**(18): p. 3977-3979.
83. Tzortzakis, S., D. Anglos, and D. Gray, *Ultraviolet laser filaments for remote laser-induced breakdown spectroscopy (LIBS) analysis: applications in cultural heritage monitoring*. Opt. Lett., 2006. **31**(8): p. 1139-1141.
84. Tzortzakis, S., et al., *Femtosecond laser-guided electric discharge in air*. Physical Review E, 2001. **64**(Copyright (C) 2010 The American Physical Society): p. 057401.
85. Rodriguez, M., et al., *Triggering and guiding megavolt discharges by use of laser-induced ionized filaments*. Opt. Lett., 2002. **27**(9): p. 772-774.

86. Ackermann, R., et al., *Influence of negative leader propagation on the triggering and guiding of high voltage discharges by laser filaments*. Applied Physics B: Lasers and Optics, 2006. **82**(4): p. 561-566.
87. Kasparian, J. and J.-P. Wolf, *Physics and applications of atmospheric nonlinear optics and filamentation*. Optics Express, 2008. **16**(1): p. 466-493.
88. Gattass, R.R. and E. Mazur, *Femtosecond laser micromachining in transparent materials*. Nat Photon, 2008. **2**(4): p. 219-225.
89. Sowa, S., et al., *Filamentary cavity formation in poly(methyl methacrylate) by single femtosecond pulse*. Applied Physics A: Materials Science & Processing, 2005. **81**(8): p. 1587-1590.
90. Shimotsuma, Y., et al., *Self-Organized Nanogratings in Glass Irradiated by Ultrashort Light Pulses*. Physical Review Letters, 2003. **91**(24): p. 247405.
91. Bhardwaj, V.R., et al., *Optically Produced Arrays of Planar Nanostructures inside Fused Silica*. Physical Review Letters, 2006. **96**(5): p. 057404-4.
92. Kapteyn, H.C., et al., *Prepulse energy suppression for high-energy ultrashort pulses using self-induced plasma shuttering*. Opt. Lett., 1991. **16**(7): p. 490-492.
93. Thaury, C., et al., *Coherent dynamics of plasma mirrors*. Nat Phys, 2008. **4**(8): p. 631-634.
94. Suntsov, S., et al., *Femtosecond laser induced plasma diffraction gratings in air as photonic devices for high intensity laser applications*. Applied Physics Letters, 2009. **94**(25): p. 251104-3.
95. Goodman, J.W., *Introduction to Fourier Optics*. Second Edition ed. 1996: McGraw-Hill. 441.
96. Lатычевская, Т. and H.-W. Fink, *Solution to the Twin Image Problem in Holography*. Physical Review Letters, 2007. **98**(23): p. 233901-4.
97. Geindre, J.P., et al., *Single-shot spectral interferometry with chirped pulses*. Optics Letters, 2001. **26**(20): p. 1612-1614.
98. Tokunaga, E., A. Terasaki, and T. Kobayashi, *Frequency-domain interferometer for femtosecond time-resolved phase spectroscopy*. Optics Letters, 1992. **17**(16): p. 1131-1133.
99. Geindre, J.P., et al., *Frequency-domain interferometer for measuring the phase and amplitude of a femtosecond pulse probing a laser-produced plasma*. Opt. Lett., 1994. **19**(23): p. 1997-1999.
100. Audebert, P., et al., *Space-Time Observation of an Electron Gas in SiO₂*. Physical Review Letters, 1994. **73**(14): p. 1990.
101. Tzortzakis, S., et al., *Time- and space-resolved X-ray absorption spectroscopy of aluminum irradiated by a subpicosecond high-power laser*. Journal of Quantitative Spectroscopy and Radiative Transfer, 2006. **99**(1-3): p. 614-626.
102. Marquès, J.R., et al., *Temporal and Spatial Measurements of the Electron Density Perturbation Produced in the Wake of an Ultrashort Laser Pulse*. Physical Review Letters, 1996. **76**(19): p. 3566.
103. Rebibo, S., et al., *Single-shot spectral interferometry of femtosecond laser-produced plasmas*. Laser and Particle Beams, 2001. **19**(01): p. 67-73.
104. Kim, K.Y., I. Alexeev, and H.M. Milchberg, *Single-shot supercontinuum spectral interferometry*. Applied Physics Letters, 2002. **81**(22): p. 4124-4126.

105. Tzortzakis, S., et al., *Time-evolution of the plasma channel at the trail of a self-guided IR femtosecond laser pulse in air*. Optics Communications, 2000. **181**(1-3): p. 123-127.
106. Sun, Q., et al., *Measurement of the collision time of dense electronic plasma induced by a femtosecond laser in fused silica*. Optics Letters, 2005. **30**(3): p. 320-322.
107. Gopal, A., S. Minardi, and M. Tatarakis, *Quantitative two-dimensional shadowgraphic method for high-sensitivity density measurement of under-critical laser plasmas*. Optics Letters, 2007. **32**(10): p. 1238-1240.
108. Centurion, M., et al., *Holographic recording of laser-induced plasma*. Opt. Lett., 2004. **29**(7): p. 772-774.
109. Centurion, M., Y. Pu, and D. Psaltis, *Holographic capture of femtosecond pulse propagation*. Journal of Applied Physics, 2006. **100**(6): p. 063104-9.
110. Centurion, M., et al., *Dynamics of filament formation in a Kerr medium*. Physical Review A, 2005. **71**(6): p. 063811.
111. Centurion, M., et al., *Erratum: Dynamics of filament formation in a Kerr medium [Phys Rev. A [bold 71], 063811 (2005)]*. Physical Review A (Atomic, Molecular, and Optical Physics), 2006. **74**(6): p. 069902-1.
112. Liu, Z., et al., *Holographic recording of fast events on a CCD camera*. Opt. Lett., 2002. **27**(1): p. 22-24.
113. Rodriguez, G., et al., *In-line holographic imaging and electron density extraction of ultrafast ionized air filaments*. J. Opt. Soc. Am. B, 2008. **25**(12): p. 1988-1997.
114. Eisenmann, S., A. Pukhov, and A. Zigler, *Fine Structure of a Laser-Plasma Filament in Air*. Physical Review Letters, 2007. **98**(15): p. 155002-4.
115. Akturk, S., et al., *Generation of long plasma channels in air by focusing ultrashort laser pulses with an axicon*. Optics Communications, 2009. **282**(1): p. 129-134.
116. Polynkin, P., et al., *Generation of extended plasma channels in air using femtosecond Bessel beams*. Opt. Express, 2008. **16**(20): p. 15733-15740.
117. Abdollahpour, D., et al., *Long spatio-temporally stationary filaments in air using short pulse UV laser Bessel beams*. Opt. Express, 2009. **17**(7): p. 5052-5057.
118. Vujičić, N., et al., *Low-density plasma channels generated by femtosecond pulses*. Applied Physics B: Lasers and Optics, 2006. **82**(3): p. 377-382.
119. Abdollahpour, D., et al., *Measuring easily electron plasma densities in gases produced by ultrashort lasers and filaments*. Optics Express, 2011. **19**(18): p. 16866-16871.
120. Polynkin, P., M. Kolesik, and J. Moloney, *Extended filamentation with temporally chirped femtosecond Bessel-Gauss beams in air*. Opt. Express, 2009. **17**(2): p. 575-584.
121. Hosseini, S.A., et al., *Multi-parameter characterization of the longitudinal plasma profile of a filament: a comparative study*. Applied Physics B: Lasers and Optics, 2004. **79**(4): p. 519-523.
122. Papazoglou, D.G. and S. Tzortzakis, *In-line holography for the characterization of ultrafast laser filamentation in transparent media*. Applied Physics Letters, 2008. **93**(4): p. 041120-3.
123. Abdollahpour, D., D. Papazoglou, and S. Tzortzakis, *Four-dimensional visualization of single and multiple laser filaments using in-line holographic microscopy*. Physical Review A (Atomic, Molecular, and Optical Physics), 2011. **xx**: p. xxxxxx.
124. Pedrini, G., W. Osten, and Y. Zhang, *Wave-front reconstruction from a sequence of interferograms recorded at different planes*. Opt. Lett., 2005. **30**(8): p. 833-835.
125. Gabor, D., *A New Microscopic Principle*. Nature, 1948. **161**: p. 777-778.

126. Montgomery Smith, L., D.R. Keefer, and S.I. Sudharsanan, *Abel inversion using transform techniques*. Journal of Quantitative Spectroscopy and Radiative Transfer, 1988. **39**(5): p. 367-373.
127. Bespalov, V.I. and V.I. Talanov, *Filamentary structure of light beams in nonlinear liquids*. JETP Letters, 1966. **3**: p. 471-476.
128. Becker, A., et al., *Intensity clamping and re-focusing of intense femtosecond laser pulses in nitrogen molecular gas*. Applied Physics B: Lasers and Optics, 2001. **73**(3): p. 287-290.
129. Sudrie, L., et al., *Study of damage in fused silica induced by ultra-short IR laser pulses*. Optics Communications, 2001. **191**(3-6): p. 333-339.
130. Sudrie, L., et al., *Writing of permanent birefringent microlayers in bulk fused silica with femtosecond laser pulses*. Optics Communications, 1999. **171**(4-6): p. 279-284.
131. Hnatovsky, C., et al., *Pulse duration dependence of femtosecond-laser-fabricated nanogratings in fused silica*. Applied Physics Letters, 2005. **87**(1): p. 014104-3.
132. Taylor, R., C. Hnatovsky, and E. Simova, *Applications of femtosecond laser induced self-organized planar nanocracks inside fused silica glass*. Laser & Photonics Review, 2008. **2**(1-2): p. 26-46.
133. Mills, J.D., et al., *Embedded anisotropic microreflectors by femtosecond-laser nanomachining*. Applied Physics Letters, 2002. **81**(2): p. 196-198.
134. Hnatovsky, C., et al., *Polarization-selective etching in femtosecond laser-assisted microfluidic channel fabrication in fused silica*. Opt. Lett., 2005. **30**(14): p. 1867-1869.
135. Kazansky, P.G., et al., *Anomalous Anisotropic Light Scattering in Ge-Doped Silica Glass*. Physical Review Letters, 1999. **82**(10): p. 2199.
136. Rajeev, P.P., et al., *Memory in Nonlinear Ionization of Transparent Solids*. Physical Review Letters, 2006. **97**(25): p. 253001.
137. Rajeev, P.P. and et al., *Transient nanoplasmonics inside dielectrics*. Journal of Physics B: Atomic, Molecular and Optical Physics, 2007. **40**(11): p. S273.
138. Papazoglou, D.G. and S. Tzortzakis, *Physical mechanisms of fused silica restructuring and densification after femtosecond laser excitation [Invited]*. Opt. Mater. Express, 2011. **1**(4): p. 625-632.
139. Papazoglou, D.G., I. Zergioti, and S. Tzortzakis, *Plasma strings from ultraviolet laser filaments drive permanent structural modifications in fused silica*. Opt. Lett., 2007. **32**(14): p. 2055-2057.
140. Sudrie, L., et al., *Femtosecond Laser-Induced Damage and Filamentary Propagation in Fused Silica*. Physical Review Letters, 2002. **89**(18): p. 186601.
141. Vogel, A., et al., *Mechanisms of femtosecond laser nanosurgery of cells and tissues*. Applied Physics B: Lasers and Optics, 2005. **81**(8): p. 1015-1047.
142. Schaffer, C., et al., *Dynamics of femtosecond laser-induced breakdown in water from femtoseconds to microseconds*. Opt. Express, 2002. **10**(3): p. 196-203.
143. Minardi, S., et al., *Time-resolved refractive index and absorption mapping of light-plasma filaments in water*. Opt. Lett., 2008. **33**(1): p. 86-88.
144. Hauge, E., S.A. Naroo, and W.N. Charman, *Poly(methyl methacrylate) model study of optical surface quality after excimer laser photorefractive keratectomy*. Journal of Cataract & Refractive Surgery, 2001. **27**(12): p. 2026-2035.
145. Shen, J.H., et al., *Ablation rate of PMMA and human cornea with a frequency-quintupled Nd:YAG laser (213 nm)*. Lasers in Surgery and Medicine, 1997. **21**(2): p. 179-185.

146. Watanabe, W., et al., *Three-Dimensional Waveguides Fabricated in Poly(methyl methacrylate) by a Femtosecond Laser*. Japanese Journal of Applied Physics, 2006. **45**(Copyright (C) 2006 The Japan Society of Applied Physics): p. L765.
147. Watanabe, W., *Femtosecond filamentary modifications in bulk polymer materials*. Laser Physics, 2009. **19**(2): p. 342-345.
148. Kallepalli, D.L.N., N.R. Desai, and V.R. Soma, *Fabrication and optical characterization of microstructures in poly(methylmethacrylate) and poly(dimethylsiloxane) using femtosecond pulses for photonic and microfluidic applications*. Applied Optics, 2010. **49**(13): p. 2475-2489.
149. Elles, C.G., *Excitation-energy dependence of the mechanism for two-photon ionization of liquid H₂O and D₂O from 8.3 to 12.4 eV*. J. Chem. Phys., 2006. **125**(4): p. 044515.
150. Lian, R., R.A. Crowell, and I.A. Shkrob, *Solvation and Thermalization of Electrons Generated by above-the-Gap (12.4 eV) Two-Photon Ionization of Liquid H₂O and D₂O*. The Journal of Physical Chemistry A, 2005. **109**(8): p. 1510-1520.
151. Siefermann, K.R. and B. Abel, *The Hydrated Electron: A Seemingly Familiar Chemical and Biological Transient*. Angewandte Chemie International Edition, 2011. **50**(23): p. 5264-5272.
152. Nikogosyan, D.N., A.A. Oraevsky, and V.I. Rupasov, *Two-photon ionization and dissociation of liquid water by powerful laser UV radiation*. Chemical Physics, 1983. **77**(1): p. 131-143.
153. Wiesenfeld, J.M. and E.P. Ippen, *Dynamics of electron solvation in liquid water*. Chemical Physics Letters, 1980. **73**(1): p. 47-50.
154. Babin, A., et al., *Shock-wave generation upon axicon focusing of femtosecond laser radiation in transparent dielectrics*. Jetp Letters, 2004. **80**(5): p. 298-302.
155. Backus, S., et al., *16-fs, 1- μ J ultraviolet pulses generated by third-harmonic conversion in air*. Opt. Lett., 1996. **21**(9): p. 665-667.
156. Fedotov, A.B., et al., *Saturation of third-harmonic generation in a plasma of self-induced optical breakdown due to the self-action of 80-fs light pulses*. Optics Communications, 1997. **133**(1-6): p. 587-595.
157. Peatross, J., et al., *Spectral-spatial measurements of fundamental and third-harmonic light of intense 25-fs laser pulses focused in a gas cell*. J. Opt. Soc. Am. B, 1998. **15**(1): p. 186-192.
158. Naudeau, M.L., et al., *Observation of nonlinear optical phenomena in air and fused silica using a 100 GW, 1.54 μ m source*. Optics Express, 2006. **14**(13): p. 6194-6200.
159. Aközbek, N., et al., *Third-Harmonic Generation and Self-Channelling in Air Using High-Power Femtosecond Laser Pulses*. Physical Review Letters, 2002. **89**(14): p. 143901.
160. Théberge, F., et al., *Conical emission and induced frequency shift of third-harmonic generation during ultrashort laser filamentation in air*. Optics Communications, 2007. **276**(2): p. 298-304.
161. Xiong, H., et al., *Spectral evolution of angularly resolved third-order harmonic generation by infrared femtosecond laser-pulse filamentation in air*. Physical Review A (Atomic, Molecular, and Optical Physics), 2008. **77**(4): p. 043802-4.
162. Siders, C.W., et al., *Blue-shifted third-harmonic generation and correlated self-guiding during ultrafast barrier suppression ionization of subatmospheric density noble gases*. J. Opt. Soc. Am. B, 1996. **13**(2): p. 330-335.

163. Lange, H.R., et al., *High-Order Harmonic Generation and Quasiphase Matching in Xenon Using Self-Guided Femtosecond Pulses*. Physical Review Letters, 1998. **81**(8): p. 1611.
164. Kortsalioudakis, N., et al., *Enhanced harmonic conversion efficiency in the self-guided propagation of femtosecond ultraviolet laser pulses in argon*. Applied Physics B: Lasers and Optics, 2005. **80**(2): p. 211-214.
165. Marcus, G., A. Zigler, and Z. Henis, *Third-harmonic generation at atmospheric pressure in methane by use of intense femtosecond pulses in the tight-focusing limit*. J. Opt. Soc. Am. B, 1999. **16**(5): p. 792-800.
166. Mao, G., Y. Wu, and K.D. Singer, *Third harmonic generation in self-focused filaments in liquids*. Opt. Express, 2007. **15**(8): p. 4857-4862.
167. Théberge, F., et al., *Third harmonic beam profile generated in atmospheric air using femtosecond laser pulses*. Optics Communications, 2005. **245**(1-6): p. 399-405.
168. Kolesik, M., et al., *Simulation of third-harmonic and supercontinuum generation for femtosecond pulses in air*. Applied Physics B: Lasers and Optics, 2006. **85**(4): p. 531-538.
169. Kolesik, M., E.M. Wright, and J.V. Moloney, *Supercontinuum and third-harmonic generation accompanying optical filamentation as first-order scattering processes*. Opt. Lett., 2007. **32**(19): p. 2816-2818.
170. Suntsov, S., et al., *Efficient third-harmonic generation through tailored IR femtosecond laser pulse filamentation in air*. Opt. Express, 2009. **17**(5): p. 3190-3195.
171. Suntsov, S., et al., *Filamentation-induced third-harmonic generation in air via plasma-enhanced third-order susceptibility*. Physical Review A, 2010. **81**(Copyright (C) 2010 The American Physical Society): p. 033817.
172. Tzortzakis, S., et al., *Nonlinear propagation of subpicosecond ultraviolet laser pulses in air*. Opt. Lett., 2000. **25**(17): p. 1270-1272.
173. Fedotov, A.B., et al., *Highly efficient frequency tripling of laser radiation in a low-temperature laser-produced gaseous plasma*. J. Opt. Soc. Am. B, 1991. **8**(2): p. 363-366.
174. Tsang, T.Y.F., *Optical third-harmonic generation at interfaces*. Physical Review A, 1995. **52**(Copyright (C) 2009 The American Physical Society): p. 4116.
175. Stoker, D., M.F. Becker, and J.W. Keto, *Optical third-harmonic generation using ultrashort laser pulses*. Physical Review A, 2005. **71**(6): p. 061802.
176. Xi, T.-T., X. Lu, and J. Zhang, *Enhancement of third harmonic emission by interaction of two colored filament with droplet in air*. Optics Communications, 2009. **282**(15): p. 3140-3143.
177. Zhang, Z., et al., *Enhancement of third-harmonic emission from femtosecond laser filament screened partially by a thin fiber*. Opt. Lett., 2010. **35**(7): p. 974-976.
178. Ganeev, R.A., et al., *Third-harmonic generation in air by use of femtosecond radiation in tight-focusing conditions*. Applied Optics, 2006. **45**(4): p. 748-755.
179. Ward, J.F. and G.H.C. New, *Optical Third Harmonic Generation in Gases by a Focused Laser Beam*. Physical Review, 1969. **185**(1): p. 57.
180. Boyd, R., *Nonlinear Optics*. 578 ed. 2003: Academic Press.
181. Birch, K.P. and M.J. Downs, *Correction to the Updated Edlén Equation for the Refractive Index of Air*. Metrologia, 1994. **31**(4): p. 315.

182. Kuo, C.C., et al., *Enhancement of Relativistic Harmonic Generation by an Optically Preformed Periodic Plasma Waveguide*. Physical Review Letters, 2007. **98**(3): p. 033901-4.
183. Dahiya, D., V. Sajal, and A.K. Sharma, *Phase-matched second- and third-harmonic generation in plasmas with density ripple*. Physics of Plasmas, 2007. **14**(12): p. 123104-7.
184. Couairon, A., et al., *Infrared femtosecond light filaments in air: simulations and experiments*. J. Opt. Soc. Am. B, 2002. **19**(5): p. 1117-1131.
185. Rodríguez, C., et al., *Characterization of laser-induced air plasmas by third harmonic generation*. Optics Express, 2011. **19**(17): p. 16115-16125.
186. Kim, K.Y., et al., *Coherent control of terahertz supercontinuum generation in ultrafast laser-gas interactions*. Nat Photon, 2008. **2**(10): p. 605-609.
187. Kapteyn, H.C. and M.M. Murnane, *Relativistic pulse compression*. J. Opt. Soc. Am. B, 1991. **8**(8): p. 1657-1662.
188. Gibbon, P., *Plasma physics: Cleaner petawatts with plasma optics*. Nat Phys, 2007. **3**(6): p. 369-370.
189. Teubner, U. and et al., *Sub-10 fs gating of optical pulses*. Journal of Physics B: Atomic, Molecular and Optical Physics, 2001. **34**(15): p. 2993.
190. Rolland, C. and P.B. Corkum, *Generation of 130-fsec midinfrared pulses*. J. Opt. Soc. Am. B, 1986. **3**(12): p. 1625-1629.
191. Plaja, L. and L. Roso, *Analytical description of a plasma diffraction grating induced by two crossed laser beams*. Physical Review E, 1997. **56**(6): p. 7142.
192. Sheng, Z.M., J. Zhang, and D. Umstadter, *Plasma density gratings induced by intersecting laser pulses in underdense plasmas*. Applied Physics B: Lasers and Optics, 2003. **77**(6): p. 673-680.
193. Wu, H.C., et al., *Controlling ultrashort intense laser pulses by plasma Bragg gratings with ultrahigh damage threshold*. Laser and Particle Beams, 2005. **23**(04): p. 417-421.
194. Wu, H.-C., Z.-M. Sheng, and J. Zhang, *Chirped pulse compression in nonuniform plasma Bragg gratings*. Applied Physics Letters, 2005. **87**(20): p. 201502-3.
195. Rax, J.M. and N.J. Fisch, *Third-harmonic generation with ultrahigh-intensity laser pulses*. Physical Review Letters, 1992. **69**(5): p. 772.
196. Panagiotopoulos, P., et al., *Tailoring the filamentation of intense femtosecond laser pulses with periodic lattices*. Physical Review A, 2010. **82**(6): p. 061803.
197. Kogelnik, H., *Coupled wave theory for thick hologram gratings*. The Bell System Technical Journal, 1969. **48**: p. 2909.
198. Ciapurin, I.V., L.B. Glebov, and V.I. Smirnov, *Modeling of phase volume diffractive gratings, part 1: transmitting sinusoidal uniform gratings*. Optical Engineering, 2006. **45**(1): p. 015802.
199. Couairon, A., H.S. Chakraborty, and M.B. Gaarde, *From single-cycle self-compressed filaments to isolated attosecond pulses in noble gases*. Physical Review A (Atomic, Molecular, and Optical Physics), 2008. **77**(5): p. 053814-10.
200. Couairon, A., et al., *Pulse self-compression to the single-cycle limit by filamentation in a gas with a pressure gradient*. Optics Letters, 2005. **30**(19): p. 2657-2659.
201. Xie, X., J. Dai, and X.C. Zhang, *Coherent Control of THz Wave Generation in Ambient Air*. Physical Review Letters, 2006. **96**(7): p. 075005.

202. Calegari, F., et al., *Rotational Raman Effects in the Wake of Optical Filamentation*. Physical Review Letters, 2008. **100**(12): p. 123006.
203. Cai, H., et al., *Elongation of femtosecond filament by molecular alignment in air*. Opt. Express, 2009. **17**(23): p. 21060-21065.
204. Papazoglou, D.G., et al., *Tunable intense Airy beams and tailored femtosecond laser filaments*. Physical Review A, 2010. **81**(6): p. 061807.
205. Weinstein, M., *Modulational stability of ground states of nonlinear Schrödinger equations*. SIAM J. Appl. Math., 1985. **16**(3): p. 472.
206. Mezentsev, V.K., et al., *Two-dimensional solitons in discrete systems*. JETP Letters, 1994. **60**: p. 829.
207. Flach, S., K. Kladko, and R.S. MacKay, *Energy Thresholds for Discrete Breathers in One-, Two-, and Three-Dimensional Lattices*. Physical Review Letters, 1997. **78**(7): p. 1207.
208. Fleischer, J.W., et al., *Observation of Discrete Solitons in Optically Induced Real Time Waveguide Arrays*. Physical Review Letters, 2003. **90**(Copyright (C) 2010 The American Physical Society): p. 023902.
209. Yang, J. and Z.H. Musslimani, *Fundamental and vortex solitons in a two-dimensional optical lattice*. Optics Letters, 2003. **28**(21): p. 2094-2096.
210. Fleischer, J.W., et al., *Observation of two-dimensional discrete solitons in optically induced nonlinear photonic lattices*. Nature, 2003. **422**(6928): p. 147-150.
211. Efremidis, N.K., et al., *Discrete solitons in photorefractive optically induced photonic lattices*. Physical Review E, 2002. **66**(4): p. 046602.
212. Lederer, F., et al., *Discrete solitons in optics*. Physics Reports, 2008. **463**(1-3): p. 1.
213. Dubietis, A., et al., *Axial emission and spectral broadening in self-focusing of femtosecond Bessel beams*. Optics Express, 2007. **15**(7): p. 4168-4175.
214. Polesana, P., et al., *Filamentation in Kerr media from pulsed Bessel beams*. Physical Review A (Atomic, Molecular, and Optical Physics), 2008. **77**(4): p. 043814-11.
215. Polynkin, P., et al., *Curved Plasma Channel Generation Using Ultraintense Airy Beams*. Science, 2009. **324**(5924): p. 229-232.
216. Polynkin, P., M. Kolesik, and J. Moloney, *Filamentation of Femtosecond Laser Airy Beams in Water*. Physical Review Letters, 2009. **103**(Copyright (C) 2010 The American Physical Society): p. 123902.
217. Kasparian, J. and J.P. Wolf, *Curved plasma channels: Kerr lens and Airy prism*. J. Europ. Opt. Soc. Rap. Public. , 2009. **4**: p. 09039.
218. Lotti, A., et al., *Stationary nonlinear Airy beams*. Physical Review A, 2011. **84**(2): p. 021807.
219. Christodoulides, D.N. and R.I. Joseph, *Discrete self-focusing in nonlinear arrays of coupled waveguides*. Opt. Lett., 1988. **13**(9): p. 794-796.
220. Eisenberg, H.S., et al., *Discrete Spatial Optical Solitons in Waveguide Arrays*. Physical Review Letters, 1998. **81**(16): p. 3383.
221. Efremidis, N.K., et al., *Two-Dimensional Optical Lattice Solitons*. Physical Review Letters, 2003. **91**(21): p. 213906.
222. McLeod, J.H., *The Axicon: A New Type of Optical Element*. J. Opt. Soc. Am., 1954. **44**(8): p. 592-592.
223. Minardi, S., et al., *Accurate retrieval of pulse-splitting dynamics of a femtosecond filament in water by time-resolved shadowgraphy*. Opt. Lett., 2009. **34**(19): p. 3020-3022.

224. Varma, S., Y.H. Chen, and H.M. Milchberg, *Trapping and Destruction of Long-Range High-Intensity Optical Filaments by Molecular Quantum Wakes in Air*. Physical Review Letters, 2008. **101**(20): p. 205001.
225. Tsangaris, C.L., G.H.C. New, and J. Rogel-Salazar, *Unstable Bessel beam resonator*. Optics Communications, 2003. **223**(4-6): p. 233-238.
226. McLeod, J.H., *Axicons and Their Uses*. J. Opt. Soc. Am., 1960. **50**(2): p. 166-166.
227. Vasara, A., J. Turunen, and A.T. Friberg, *Realization of general nondiffracting beams with computer-generated holograms*. J. Opt. Soc. Am. A, 1989. **6**(11): p. 1748-1754.
228. Koronkevich, V.P., et al., *Lensacon*. Appl. Opt., 1995. **34**(25): p. 5761-5772.
229. Chen, F., *Introduction to plasma physics and controlled fusion*. Second ed. 2006: Springer.
230. Berry, M.V. and N.L. Balazs, *Nonspreading wave packets*. American Journal of Physics, 1979. **47**(3): p. 264-267.
231. Siviloglou, G.A. and D.N. Christodoulides, *Accelerating finite energy Airy beams*. Opt. Lett., 2007. **32**(8): p. 979-981.
232. Vallee, O. and M. Soares, *Airy functions and applications to physics*. 2004: World Scientific.
233. Bandres, M.A., *Accelerating beams*. Opt. Lett., 2009. **34**(24): p. 3791-3793.
234. Bandres, M.A., J.C. Gutiérrez-Vega, and S. Chávez-Cerda, *Parabolic nondiffracting optical wave fields*. Opt. Lett., 2004. **29**(1): p. 44-46.
235. Gori, F., G. Guattari, and C. Padovani, *Bessel-Gauss beams*. Optics Communications, 1987. **64**(6): p. 491-495.
236. Siviloglou, G.A., et al., *Observation of discrete quadratic surface solitons*. Optics Express, 2006. **14**(12): p. 5508-5516.
237. Schiff, L.I., *Quantum Mechanics*. 3rd ed. 1968, New York: McGraw-Hill.
238. Siviloglou, G.A., et al., *Ballistic dynamics of Airy beams*. Opt. Lett., 2008. **33**(3): p. 207-209.
239. Baumgartl, J., M. Mazilu, and K. Dholakia, *Optically mediated particle clearing using Airy wavepackets*. Nat Photon, 2008. **2**(11): p. 675-678.
240. Christodoulides, D.N., *Optical trapping: Riding along an Airy beam*. Nat Photon, 2008. **2**(11): p. 652-653.
241. Broky, J., et al., *Self-healing properties of optical Airy beams*. Opt. Express, 2008. **16**(17): p. 12880-12891.
242. Allen, L., et al., *Orbital angular momentum of light and the transformation of Laguerre-Gaussian laser modes*. Physical Review A, 1992. **45**(11): p. 8185.
243. Ellenbogen, T., et al., *Nonlinear generation and manipulation of Airy beams*. Nat Photon, 2009. **3**(7): p. 395-398.
244. Born, M. and E. Wolf, *Principles of Optics*. 7th ed. 1999, Cambridge: Cambridge University Press.
245. Chen, R.-P., et al., *Effect of Kerr nonlinearity on an Airy beam*. Physical Review A, 2010. **82**(4): p. 043832.
246. Porras, M.A. and P. Di Trapani, *Localized and stationary light wave modes in dispersive media*. Physical Review E, 2004. **69**(6): p. 066606.
247. Faccio, D., A. Couairon, and P. Di Trapani, *Conical Wave, Filaments and Nonlinear Filamentation Optics*. 2007: ARACNE editrice

248. White, W.E., et al., *Compensation of higher-order frequency-dependent phase terms in chirped-pulse amplification systems*. Opt. Lett., 1993. **18**(16): p. 1343-1345.
249. Trager, F.E., *Handbook of Laser and Optics*. 2007, New York: Springer.
250. D'Amore, F., et al., *Enhancement of PMMA nonlinear optical properties by means of a quinoid molecule*. Optical Materials, 2004. **24**(4): p. 661-665.
251. Abramowitz, M. and I. Stegun, eds. *Handbook of Mathematical Functions* 1972, Dover: New York.
252. Polesana, P., et al., *Near-field dynamics of ultrashort pulsed Bessel beams in media with Kerr nonlinearity*. Physical Review E (Statistical, Nonlinear, and Soft Matter Physics), 2006. **73**(5): p. 056612-4.
253. Dubietis, A., et al., *Measurement and calculation of nonlinear absorption associated with femtosecond filaments in water*. Applied Physics B: Lasers and Optics, 2006. **84**(3): p. 439-446.
254. Kolesik, M., E.M. Wright, and J.V. Moloney, *Dynamic Nonlinear X Waves for Femtosecond Pulse Propagation in Water*. Physical Review Letters, 2004. **92**(25): p. 253901.
255. Polesana, P., et al., *Observation of Conical Waves in Focusing, Dispersive, and Dissipative Kerr Media*. Physical Review Letters, 2007. **99**(22): p. 223902-4.
256. Moll, K.D., A.L. Gaeta, and G. Fibich, *Self-Similar Optical Wave Collapse: Observation of the Townes Profile*. Physical Review Letters, 2003. **90**(20): p. 203902.
257. Bhuyan, M.K., et al., *High aspect ratio nanochannel machining using single shot femtosecond Bessel beams*. Applied Physics Letters, 2010. **97**(8): p. 081102-3.
258. Belgiorno, F., et al., *Hawking Radiation from Ultrashort Laser Pulse Filaments*. Physical Review Letters, 2010. **105**(20): p. 203901.
259. Thirolf, P.G., et al., *Signatures of the Unruh effect via high-power, short-pulse lasers*. The European Physical Journal D - Atomic, Molecular, Optical and Plasma Physics, 2009. **55**(2): p. 379-389.

List of Publications

- [1]. D. Abdollahpour, P. Panagiotopoulos, M. Turconi, O. Jedrkiewicz, D Faccio, P. Di Trapani, A. Couairon, D. Papazoglou, S. Tzortzakis, “*Long Spatio-temporally stationary filaments in air using short pulse UV laser Bessel beams,*” *Optics Express* **17**, 5052 (2009).
- [2]. S. Sunstov, D. Abdollahpour, D. G. Papazoglou, S. Tzortzakis, “*Efficient third-harmonic through tailored IR femtosecond laser pulse filamentation in air,*” *Optics Express* **17**, 1390 (2009).
- [3]. S. Sunstov, D. Abdollahpour, D. G. Papazoglou, S. Tzortzakis, “*femtosecond laser induced plasma diffraction gratings in air as photonic devices for high intensity laser applications,*” *Applied Physics Letters* **94**, 251104 (2009).
- [4]. S. Sunstov, D. Abdollahpour, D. G. Papazoglou, S. Tzortzakis, “*Filamentation-induced third-harmonic generation in air via plasma-enhanced third-order susceptibility,*” *Physical Review A* **81**, 033817 (2010).
- [5]. D. G. Papazoglou, S. Sunstov, D. Abdollahpour, S. Tzortzakis, “*Tunable intense Airy beams and tailored femtosecond laser filaments,*” *Physical Review A* **81**, 061807 (R) (2010).
- [6]. D. Abdollahpour, S. Sunstov, D. G. Papazoglou, S. Tzortzakis, “*Spatiotemporal Airy Light Bullets in the Linear and Nonlinear Regimes,*” *Physical Review Letters* **105**, 253901 (2010).
- [7]. D. Abdollahpour, S. Sunstov, D. G. Papazoglou, S. Tzortzakis, “*Measuring easily electron plasma densities in gases produced by ultrashort lasers and filaments,*” *Optics Express* **19**, 16866 (2011).
- [8]. A. Lotti, D. Faccio, A. Couairon, D. G. Papazoglou, P. Panagiotopoulos, D. Abdollahpour, S. Tzortzakis, “*Stationary nonlinear Airy beams,*” *Physical Review A* **84**, 021807 (R) (2011).
- [9]. D. Abdollahpour, D. G. Papazoglou, S. Tzortzakis, “*Four-dimensional visualization of single and multiple laser filaments using in-line holographic microscopy,*” *Physical Review A*, *In press*.
- [10]. S. Sunstov, D. Abdollahpour, D.G. Papazoglou, P. Panagiotopoulos, A. Couairon, S. Tzortzakis, “*Tailoring femtosecond laser pulse filamentation in water using a plasma lattice,*” *Submitted*.
- [11]. P. Panagiotopoulos, D. Abdollahpour, A. Lotti, A. Couairon, D. Faccio, D. G. Papazoglou, S. Tzortzakis, “*Nonlinear propagation dynamics of finite energy Airy beams,*” *In preparation*.

- [12]. D. Abdollahpour, D. G. Papazoglou, S. Georgiou, S. Tzortzakis, “*Dynamics of filamentation in the femtosecond laser irradiation in polymers,*” *In preparation.*
- [13]. D. G. Papazoglou, D. Abdollahpour, S. Tzortzakis, “*Plasma strings form nanostructures in fused silica,*” *In preparation.*